FATIGUE BEHAVIOR OF AN ADVANCED SIC/SIC COMPOSITE WITH AN OXIDATION INHIBITED MATRIX AT 1200°C IN AIR AND IN STEAM

THESIS

Delapasse Jacob, Captain, USAF
AFIT/GAE/ENY/10-M07

DEPARTMENT OF THE AIR FORCE
AIR UNIVERSITY

AIR FORCE INSTITUTE OF TECHNOLOGY

Wright-Patterson Air Force Base, Ohio

AFIT/GAE/ENY/10-M07

FATIGUE BEHAVIOR OF AN ADVANCED SIC/SIC COMPOSITE WITH AN OXIDATION INHIBITED MATRIX AT 1200°C IN AIR AND IN STEAM

THESIS

Presented to the Faculty

Department of Aeronautics and Astronautics

Graduate School of Engineering and Management

Air Force Institute of Technology

Air University

Air Education and Training Command

In Partial Fulfillment of the Requirements for the

Degree of Master of Science in Aeronautical Engineering

Jacob Delapasse, B.S.

Captain, USAF

March 2010

AFIT/GAE/ENY/10-M07

FATIGUE BEHAVIOR OF AN ADVANCED SIC/SIC COMPOSITE WITH AN OXIDATION INHIBITED MATRIX AT 1200°C IN AIR AND IN STEAM

Jacob Delapasse, B.S.

Captain, USAF

Approved:

_____/signed/_____ _____
Marina Ruggles-Wrenn, PhD (Chairman) Date

_____/signed/_____ _____
Geoff Fair, PhD (Member) Date

_____/signed/_____ _____
Randall Hay, PhD (Member) Date

Abstract

The fatigue behavior of an advanced Silicon Carbide/Silicon Carbide (SiC/SiC) ceramic matrix composite (CMC) with oxidation inhibited matrix was investigated at 1200˚C in laboratory air and in steam environments. The composite consisted of an oxidation inhibited SiC matrix reinforced with Hi-Nicalon fibers coated with pyrolytic carbon (PyC) with a boron carbide overlay woven into eight-harness-satin (8HS) weave plies. Tensile stress-strain behavior and tensile properties were evaluated at 1200˚C. Tension-tension fatigue tests were conducted in both laboratory air and in steam at 1200˚C at frequencies of 0.1 Hz, 1.0 Hz, and 10 Hz. The tension-tension fatigue tests had a ratio of minimum stress to maximum stress of R = 0.05, with maximum stresses ranging from 100 to 140 MPa in air and in steam. Fatigue run-out was defined as 10^5 cycles for the 0.1 Hz tests and as 2 x 10^5 cycles for the 1.0 Hz and 10 Hz tests. Strain accumulation with cycles and modulus evolution with cycles were analyzed for each fatigue test. The presence of steam degraded the fatigue resistance of the material at 0.1 Hz and 10 Hz. At 1.0 Hz, the presence of steam appeared to have little influence on the fatigue resistance for the fatigue stress levels < 140 MPa. The presence of steam degraded the fatigue performance of the CMC at 1.0 Hz for the fatigue stress level of 140 MPa. Fatigue limit was 100 MPa (32.6% UTS) in air and steam at 1.0 Hz and in steam at 0.1 Hz. Fatigue limit was 140 MPa (45.6%) in air at 10 Hz. Specimens that achieved run-out were subjected to tensile tests to failure to characterize the retained tensile properties. Specimens tested in air retained 42-61% of their tensile strength and specimen tested in steam retained 59-75% of their tensile strength.

The modulus loss in air and in steam was limited to 56%. The microstructural investigation revealed pronounced oxidation on the fracture surfaces of specimens tested in steam. The self sealing matrix cracks were also observed.

Acknowledgments

I would like to express my appreciation to the following people for helping me with repairs and maintenance of the lab equipment used in this research: Lab technicians Sean Miller, Barry Page, and Chris Zickefoose. I would like to also offer my heartfelt thanks to the following individuals who aided in the completion of this research: Dr. Ruggles-Wrenn for her advice and support throughout the entirety of this work, Dr. Geoff Fair for his time and expertise in the field of ceramics, Capt Devon Christensen for leading the way in this research effort, and Lt Brad Diedrick for his help in the lab. Finally, I would like to thank my wife for her love and support throughout this effort.

Table of Contents

Page

List of Figures

Page

Page

Page

Page

Page

Page

Page

Page

List of Tables

Page

Page

FATIGUE BEHAVIOR OF AN ADVANCED SIC/SIC COMPOSITE WITH AN OXIDATION INHIBITED MATRIX AT 1200°C IN AIR AND IN STEAM

I. Introduction

Ceramic matrix composites are the advanced material that will boost aircraft engine performance and efficiency into new heights. In today's world, aircraft users want an aircraft that can fly higher, faster, and longer while being more fuel efficient and safer. Aircraft engines play a major role in achieving these requirements since they propel the aircraft forward. Without a doubt, the materials that make up internal engine components are the limiting factor to achieving these goals [5:71]. The metals currently being used as internal engines parts are at their temperature performance limits and can no longer meet the raised demands [20]; however, advanced materials such as ceramic matrix composites (CMCs) have demonstrated a promising future in meeting the structural needs.

Throughout the history of aircraft, the advancement of materials has been well documented. In the beginning, aircraft were made from wood and fabric and would later advance to metals such as steel and aluminum. Currently, composites are changing the aircraft industry by providing a strong, low density, and high temperature material. Until recently, composites were used mostly on aircraft structural components. Now, composites are being introduced into aircraft engine industry. The designs of current aircraft engines are being motivated by performance needs, economical constraints, and international environmental regulations. These three objectives are driven by weight savings and increased gas temperature [17:327]. As the weight of an aircraft is decreased, the less thrust is needed to fly

at given speed and altitude. As the combustion temperature is increased, the better burn is achieved inside the combustion chamber resulting in better engine efficiency [5:71]. In other words, a higher internal engine temperature provides more thrust per pound of gas. Overall, these two factors increase the thrust to weight ratio of the aircraft providing a more efficient aircraft which ultimately saves money on fuel.

In order to achieve weight savings and increased gas temperatures, engine designers can no longer turn to metals. Metal's strength decreases dramatically at the higher temperatures the new engines are being asked to perform [17:327]. Therefore, a new advanced material having versatile mechanical properties must be considered. First, the material must maintain its strength at high temperatures. Second, it must be able to resist fatigue (material damage caused by cyclic loading) at high temperatures. Third, it must have a low density. Finally, it must resist environmental effects such as oxidation [1:17; 6:9]. Currently, many materials are being tested to see if they meet these stringent materials properties.

CMCs may be the perfect fit for internal engine parts because it is on the verge of meeting the raised structural demands. Table 1 shows the strengths that make CMCs a prime candidate but also shows the weaknesses that CMCs must overcome to meet engine needs. The main limitation of CMCs is in the unavailability of fibers to maintain high-elastic moduli and strength, chemical stability, and oxidation resistance at elevated temperatures [1:17]. The purpose of this research is to test silicon carbide fiber/silicon carbide matrix (SiC/SiC) ceramic

matrix composite at 1200˚C in steam and air to see if it could be a possible candidate for internal engine components.

Table 1: Advantages and disadvantages of ceramic matrix composites [1:17].

• Advantages
- high to very high temperature capability (500 - 1500˚C)
- low density
- low conductivity
- low thermal expansion
- resistant to aggressive environments
• Disadvantages
- fabrication can be costly and difficult
- joining difficult
- relatively low fracture toughness
- matrix microcrack at low strain levels

II. Background

2.1 Ceramics

Throughout the last century there have been large advances in making ceramic materials, and it is suitable to categorize ceramics into two classes. These classes consist of traditional and advanced ceramics [6:2]. Traditional ceramics are typically monolithic. Examples include bricks, tiles, and pottery. Advanced or high performance ceramics are usually crated by a sophisticated chemical process. Examples include oxides, nitrides, and carbides of silicon, aluminum, titanium, and zirconium. Advanced ceramics contain combine some very desirable characteristics such as high strength and hardness, excellent high temperature capability, chemical inertness, wear resistant, and low density which are all very advantageous for engine components. Because of its superior properties, the high performance ceramics is the class of ceramics used for CMCs. Table 2 shows the properties of some high performance ceramics that are used in CMCs.

Table 2: Properties of some high performance ceramic materials [5:111].

Ceramic	Density (g/cm^3)	Elastic Modulus (GPa)	Flexural Strength at 25 ˚C (MPa)	Estimated Max Temp (˚C)
Alumina	4.0	400	550	900
Silicon Carbide	3.1	300	380	1400
Silicon Nitride	3.1	240	420	1000
Toughened Zirconia	5.7	210	600	900
Alumina/SiC whickers	3.7	380	640	900

The biggest drawback to ceramics is that it has a very low tolerance to crack defects resulting in low fracture toughness. A ceramic will break catastrophically if there is a minute defect such as a crack. When compared to other aircraft applicable materials, aluminum and steel are on the order of 20-100 times the fracture toughness of ceramics. In Table 3, fracture toughness of high performance ceramics are compared to polymers and metals.

Table 3: Typical fracture toughness values for some materials [6:8].

Material	K_{ic}, MPa $m^{1/2}$
Polymers	
Polyethylene	1-2
Nylon	3
Epoxy, Polyester	0.5
Matals	
Pure metals (copper, nickel, aluminum)	100-300
Aluminum Alloys	20-50
Titanium Alloys	50-110
Low Carbon Steel	50
Cast Iron	40278
Ceramics	
Sodalime glass	0.5-1
Magnesium Oxide	3
Alumina	1-3
Silicon Oxide	2-4
Silicon Nitride	3-5

Since the largest single cause of component failures in modern military aircraft gas turbine engines is high cycle fatigue [9:147], the materials making up these components must be resistant to fatigue. In the early 1980s, major engine demonstration programs were stalled because ceramics were unreliable due to their low fracture toughness [13:183]. Engine components made of ceramics had short lifetime and would fail catastrophically. Since catastrophic failure was not an option for primary structure of an aircraft engine, increasing the

toughness of ceramics was a must. To obtain this goal, ceramics have been incorporated into composites providing a material with all the favorable characteristics of ceramics but also having higher fracture toughness.

2.2 Composites

A composite material is a structural material that consists of two or more combined constituents that are combined at a microscopic level and are not soluble in each other [16:2]. One constituent is the matrix phase and other is the reinforcement phase. The reinforcement phase may come in the form of fibers, particles, or flakes. The matrix phase is usually a continuous material. The matrix phase is usually weaker while the reinforcement phase provides much of the strength to the material.

Composites are classified by matrix material characterization. For example, composites that have a polymer matrix are called polymer matrix composites (PMC). Others include metal matrix composites (MMC) and ceramics matrix composites (CMC). The reinforcement material can also be a metal, polymer, or ceramic. The choice for the reinforcement and matrix material depends on the material behavior goal to be reached. The interface between the matrix and fiber also plays a large role in material behavior [17:49]. For the most part, composites are made to provide a better or different characteristic than the individual materials that make up the composite. For the case of CMCs in this research, the composite provides a better toughness characteristic than ceramics the make up the fiber and matrix. Later sections will discuss the science behind the increase fracture toughness.

2.3 Ceramic-Matrix Composites

2.3.1 Traditional Ceramic-Matrix Composites

Ceramic Matrix Composites (CMCs) are a new class of quasi-ductile ceramic material designed for applications in severe environments. CMCs were made to toughen ceramics by incorporating fibers in them and thus exploiting the attractive high-temperature and environmental resistance of ceramics without risking catastrophic failure [7:212]. As illustrated in Figure 1, CMCs maintain their strength when subjected to extreme temperatures when compared to aluminum, titanium, and nickel based alloys.

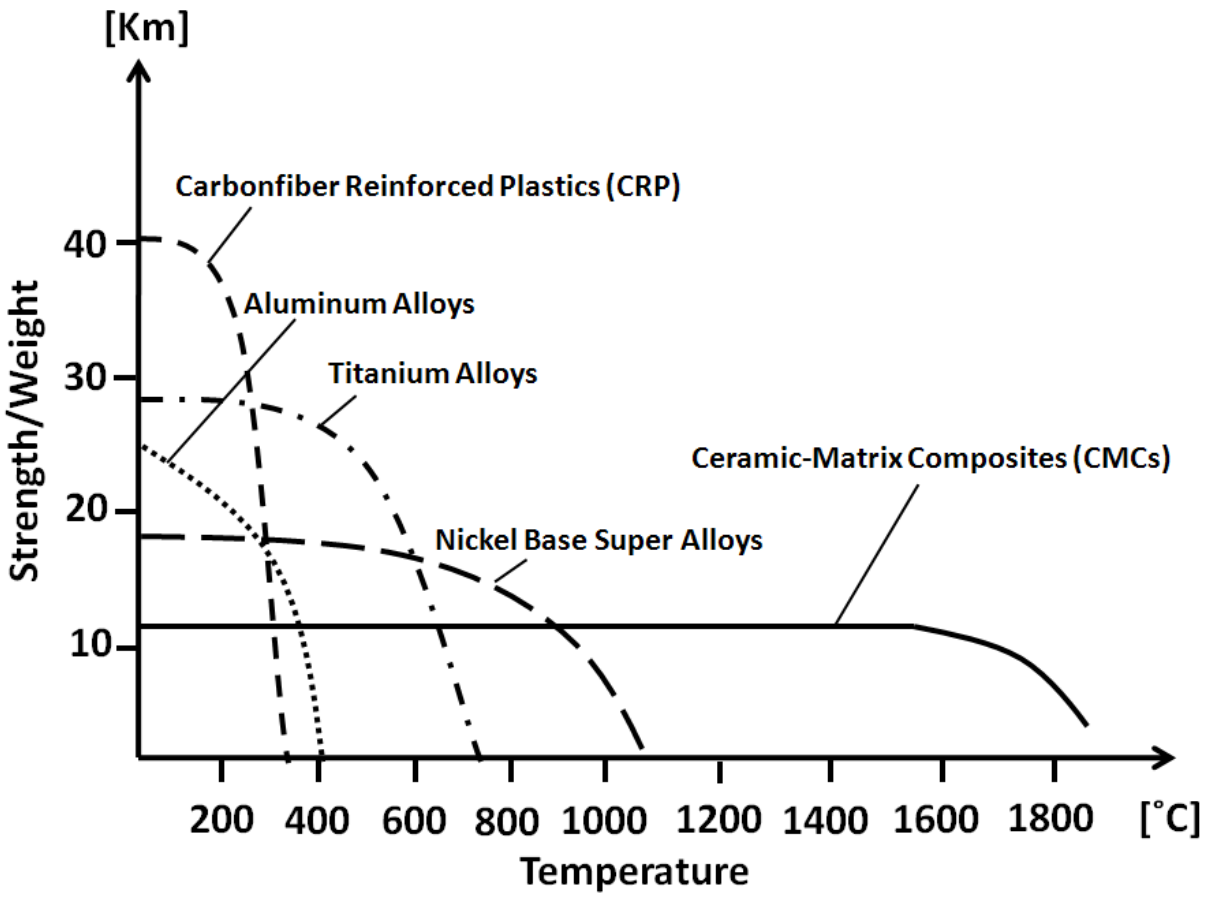

Figure 1: Strength to weight ratio versus temperatures for various materials [26].

CMCs present many differences compared to nonceramic composites. The general philosophy behind nonceramic matrix composites is to have the fiber bear the majority of the applied load. The load partitioning between the matrix and fiber depends on the ratio of their elastic moduli, E_f / E_m. In nonceramic matrix composites this ratio is usually very high (generally 10-100), while the ratio in CMCs is very low and usually close to unity [7:212]. In the case of CMCs, to increase strength is not the objective because the ceramics themselves are already strong. The objective is improved fracture toughness. Furthermore, the fibers and the matrix of CMCs have similar thermal expansion properties [1:18]. If the fiber and the matrix

experience a thermal shock and do not expand at the same rate, internal stress will be applied to the material causing premature cracking and maybe even fracture. Another important feature in CMCs is there must be a mechanism to increase fracture toughness. Toughness is introduced to the composite by way of a porous matrix or weak interface between the fiber and the matrix.

2.3.2 Oxide versus Non-oxide

The ability to maintain material properties while at high temperatures makes CMCs a prime candidate for internal engine parts; however, CMCs do come with some drawbacks which include poor damage tolerances due to oxidation, fatigue, and creep. These damage tolerance mechanisms vary between CMCs based on the fiber and matrix material and the design of the composite [10:6; 23:31]. The two main types of ceramics used for the reinforcement and matrix phases are oxides and non-oxides. Both have their advantages and disadvantages. Oxides, which are mostly based on Al_2O_3 or Al_2O_3/SiO_2, possess high values for tensile strength and modulus and are stable against oxidation at high temperatures [17:9]. Unfortunately, even the best oxide fibers are prone to creep and losing strength under loading at 1100˚C [29; 17:9]. Efforts have been made to improve creep resistance of oxides, but it comes with the price of strength and stiffness reduction [22]. On the other hand, non-oxides, which are based on SiC, exhibit high values for tensile strength and modulus (higher than oxides) and due to their structure, which is crystalline, possess lower creep rates at high temperatures. The disadvantage, however, is that SiC is very susceptible to oxidation. Through testing, SiC's rate of kinetic oxidation increased as the content of water vapor increased [21;14].

Oxidation resistant attempts have been successful by lowering the oxygen level content in SiC fibers, but SiC material comes at a higher cost. Current research efforts are focused on the development of oxide fibers with enhanced creep properties as well as non-oxide fibers with improved oxidation stability and lower production cost.

Oxides have a higher thermal expansions and a lower thermal conductivity than SiC. Component designs for high thermal gradients and transients are therefore more difficult to design with oxide/oxide composites [17:187].

In general, both oxide/oxide composites and non-oxide/non-oxide composites require a mechanism to overcome fatigue. There are two types of ways to increase fracture toughness. The more conventional approach used by SiC/SiC CMCs involves the use of fiber coatings such as carbon or boron nitride to promote crack deflection and frictional sliding along fiber-matrix interfaces. The coatings create a weak interface that will lead to debonding at the interface, followed by crack deflection, crack bridging, fiber fracture, and finally fiber pullout. These additional energy absorbing phenomena lead to the CMCs having increased fracture toughness and most importantly a non-catastrophic failure [6:147]. A strong bond between the fiber and matrix will allow an oncoming crack to travel through the interface into the fiber resulting in a brittle failure. An example of a weak and strong interface is seen in Figure 2. The weak interface allows the development of multiple matrix cracks, which in turn produce inelastic strain during tensile loading [30:15]. On the other hand, since oxide/oxide CMCs are resistant to oxidation environments, they are capable of using a porous matrix to deflect matrix cracking. This approach uses a controlled amount of fine scale matrix porosity, which alleviates the need

for a fiber coating. Crack deflection occurs in this instance because of the low fracture toughness of the porous interface [30:15]. The advantage of a porous matrix is the crack deflection mechanism is independent of an interface that may be susceptible to environmental attack [15:6]. The interface for SiC/SiC composites has a tendency to breakdown in oxidizing environments. This is a limitation for SiC/SiC composites. Other disadvantages of porous matrices are low interlaminar strength and poor resistance to wear.

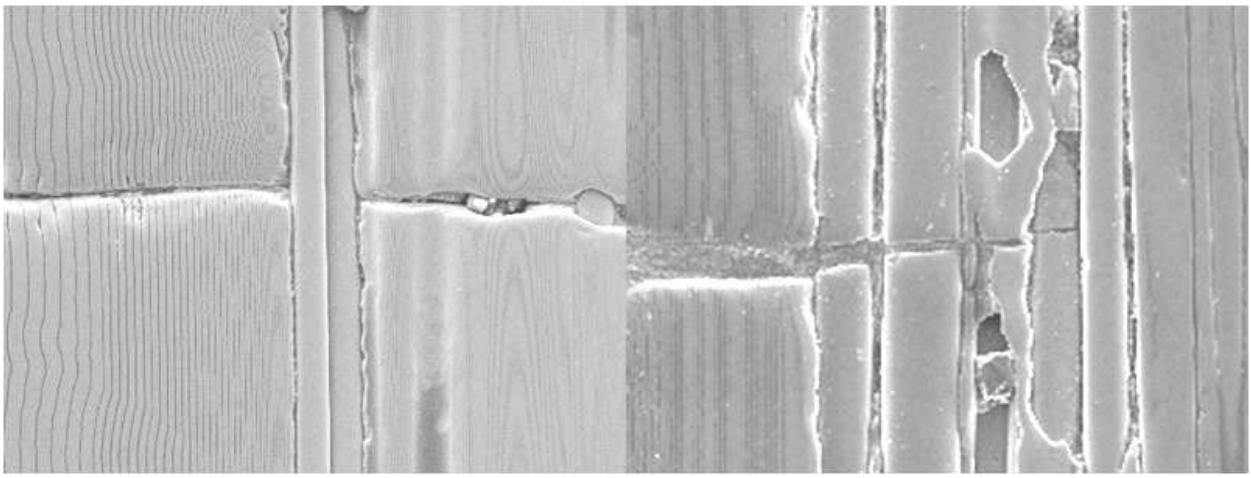

Figure 2: Propagating crack through the matrix for weak (left) and strong (right) matrix interfaces.

Overall, SiC/SiC CMCs can do one thing that oxide/oxide CMCs cannot do and that is it can keep its strength at higher temperatures. It important to find the right combination SiC/SiC composites that will maintain its strength even in oxidative environments. The motive of this research is to test a form of SiC/SiC composite to see if it can survive the harsh oxidative environment at elevated temperatures.

2.3.3 SiC/SiC Ceramic Matrix Composites Prior Research

Prior research has seen the presence of steam cause a noticeable degradation in fatigue performance in SiC/SiC CMCs at elevated temperatures. In Sharma's research, two types of SiC/SiC CMCs were tested in laboratory air and steam at 1300˚C [27]. Both materials were classified as SiC-SiNC CMCs. The two composites were processed by using polymer infiltration and pyrolysis (PIP). The first composite (C1) tested was a 5HSW fiber fabric reinforced with Sylramic fibers and coated with a proprietary dual-layer interface. The composite was infiltrated with a mixture of polymer, filler particles, and solvent. During pyrolysis under nitrogen at high temperatures, the polymer was pyrolyzed to an amorphous SiNC ceramic matrix. The second composite (C2) varied from the first in that it consisted of a Sylramic-iBN fiber, but contained the same proprietary dual-layer interface in a modified PIP SiNC matrix. Tensile test and tension-tension fatigue test at 1.0 Hz ranging from 100 to 180 MPa at 1300˚C were accomplished by Sharma. He noticed that fatigue limit based on a run-out condition of 2 x 10^5 cycles in both air and steam for C1 was 100 MPa (53% UTS at 1300˚C). The fatigue limit for C2 was 160 MPa (66% UTS) in air and 140 MPa (58% UTS) in steam. As the maximum stress for fatigue test was increased, the specimens tested in steam had shorter lifetimes than in air. Both specimens maintained 100% tensile strength in air, while only maintaining 90% of their tensile strength in steam for specimens achieving run-out. The data for this analysis can be seen in Figure 3.

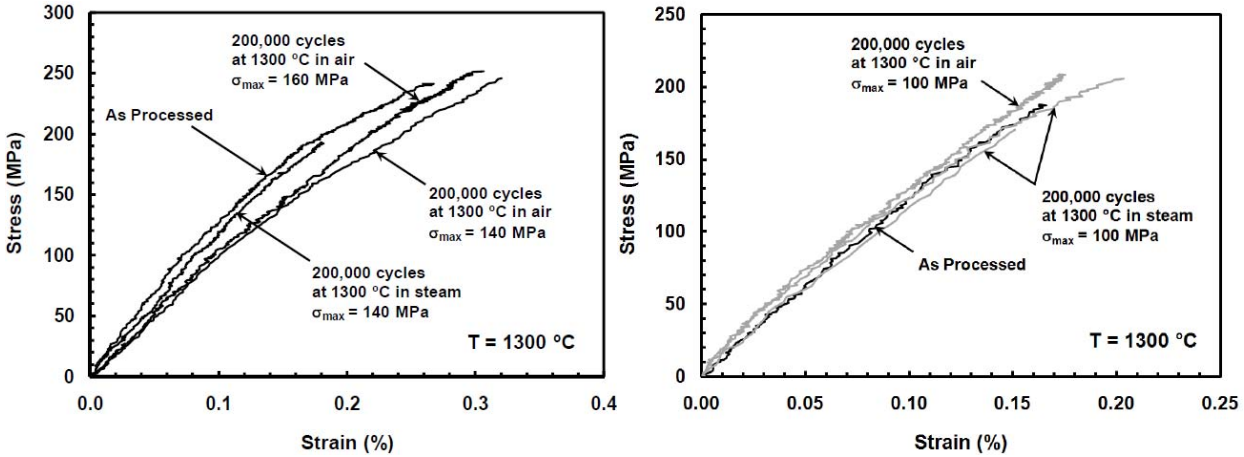

Figure 3: The effects of prior fatigue at 1300˚C in air and steam for C1 (right) and C2 (left) [27]

Furthermore, Sharma showed that there was very little ratcheting (strain accumulated during fatigue cycles) observed in composite C1 in steam and virtually no ratcheting in all test conducted in air (Figure 4). The maximum strains accumulated in fatigue test by composite C1 were limited to .16 %, which is also the failure strain obtained in tension test. Composite C2 however showed more ratcheting in both air and steam (Figure 5). The maximum strains accumulated by composite C2 were limited to .24% which is also the failure strain obtained in tension test [27]. The fiber/matrix interface and the stiffness of fibers used in Sharma's research contributed to the minimal amounts of ratcheting observed for composite C1 and C2.

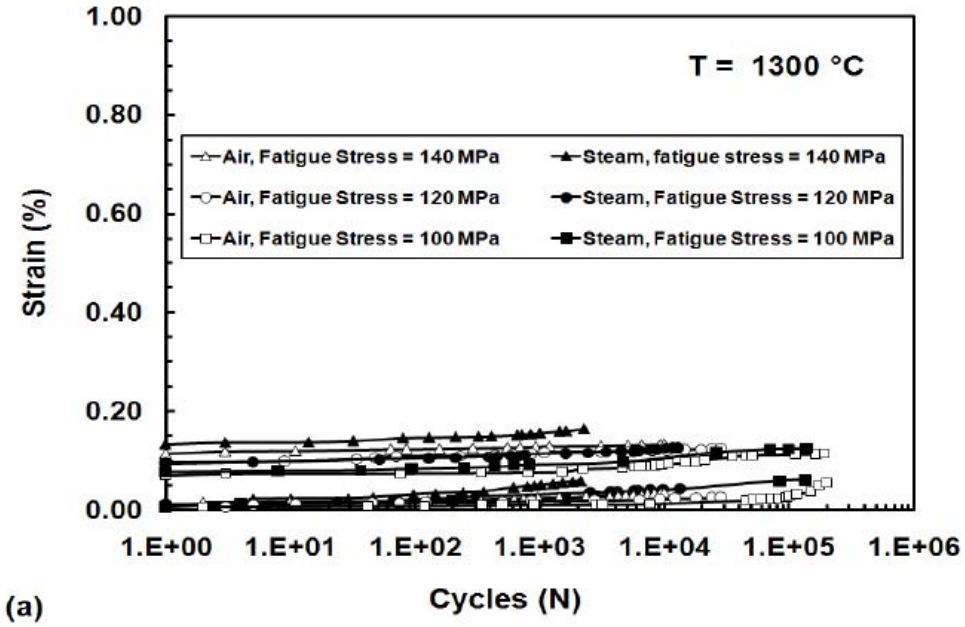

Figure 4: Maximum and minimum strains versus number of cycles in air and steam at 1300˚C for composite C1 [27].

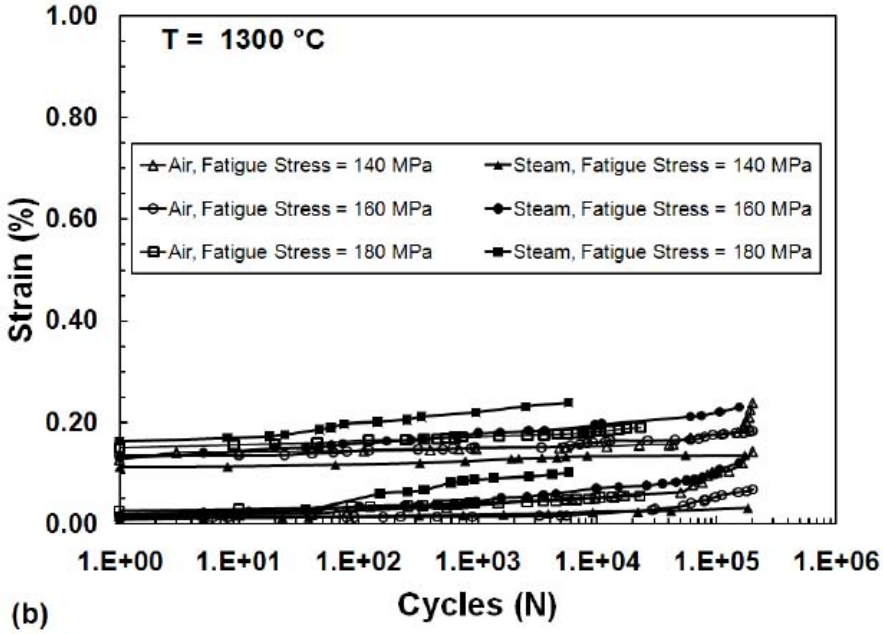

Figure 5: Maximum and minimum strains versus number of cycles in air and steam at 1300˚C for composite C2 [27].

Research on SiC/SiC CMCs was also accomplished by Christensen [8]. The composite tested by Christensen consisted of a SiC matrix reinforced with a Boron Nitride (BN) coated Hi-Nicalon fibers woven into an eight-harness-satin weave. This SiC matrix was densified using the chemical vapor infiltration process. Tensile test and tension-tension fatigue test were conducted at 1200˚C. The fatigue tests were conducted in laboratory air and steam at 1200˚C at frequencies of 0.1 Hz, 1.0 Hz, and 10 Hz with a max stress ranging from 80-120 MPa in air and 60-110 MPa in steam. The fatigue limit was 100 MPa (46% UTS) and 80 MPa (37% UTS) in air and steam respectfully. With run-out defined at 2 x 10^5 cycles for 1.0 Hz and 10 Hz test and 10^5, all specimens in air retained 100% of their tensile strength and only one specimen in steam showed minor strength degradation as seen in Figure 6. In Figure 6, there is a noticeable bend in the stress versus strain curve. The bend is where matrix cracking occurs and the majority of the load is transferred to the fibers. In Sharma's work, C1 and C2 had a less noticeable bilinear effect due to the weakness of the PIP matrix. In materials tested by Sharma and Christensen, the bend indicates vulnerability of the internal composite to the outside environment due to matrix cracking. It is at this point where the presence of steam has degraded the performance of CMCs as seen in both Christensen and Sharma's work.

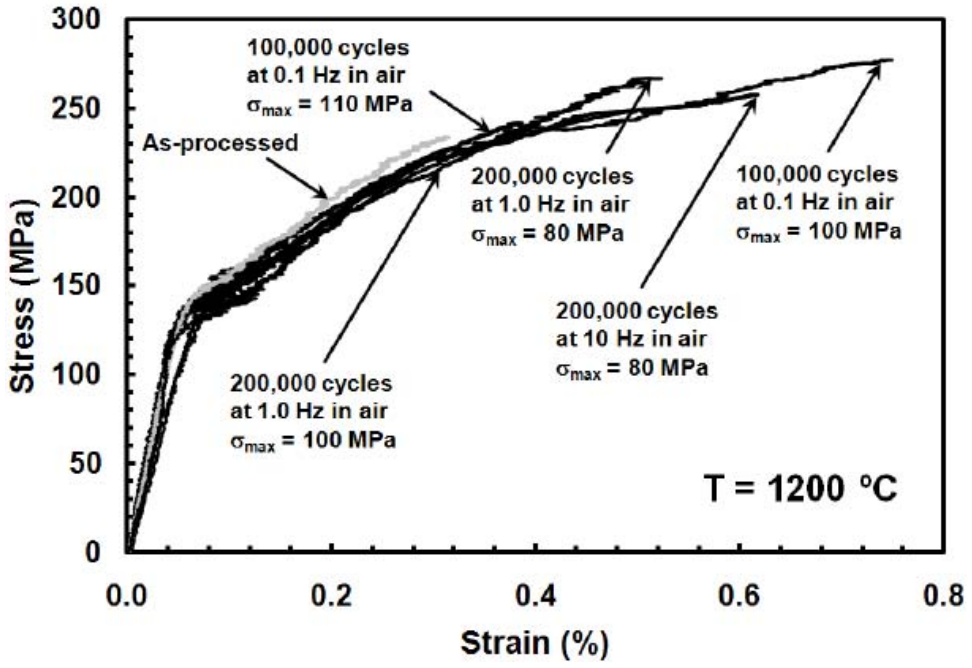

Figure 6: Stress-strain response of Hi-Nicalon/BN/SiC specimens fatigue in air at 1200˚C then subjected to a monotonic tensile test to failure in laboratory air at 1200˚C at displacement rate of 0.05 mm/s [8].

As the max stress level passed the proportional limit, fatigue tests for both research efforts saw the lifetime in steam become shorter than air. Both research efforts also showed how the choice in material and fiber/matrix interface play a large role in the tensile and fatigue material properties of the composite. Finding the right combination of material and fiber/matrix interface has been the driver for many CMC research efforts.

III. Material and Test Specimen

3.1 Material

The material studied in this research effort was manufactured by Hyper-Therm High-Temperature Composites, Inc., Huntington Beach CA, by chemical vapor infiltration (CVI) of HyprSiC oxidation inhibited matrix material into the woven Hi-Nicalon fiber preforms. The composite was supplied in the form of three 3.1 mm thick plates. The composite consisted of eight plies of Hi-Nicalon [0°/90°] fabric woven in an 8 harness satin weave (8HSW) (Figure 7). To produce the laminated preforms, the 8 [0°/90°] plies were laid-up symmetric about mid-plane with warp and fill plies alternated. Prior to matrix densification, the preforms were coated with pyrolytic carbon with boron carbide overlay in order to decrease interface bonding between fibers and matrix, thereby increasing composite strength and toughness. The thickness of the pyrolytic carbon fiber coating was ~0.40 μm and the thickness of the boron carbide overlay was ~1.0 μm. The HyprSiC oxidation inhibited matrix was densified by CVI. The volume fraction of the fibers was 34.8% and the density of the composite was 2.56 g/cm^3. The tensile specimens (dimensions are given in Section 3.2 below) had an outer seal coating of HyprSiC that was applied by chemical vapor deposition (CVD) after the specimens had been machined. Specifications for the as-processed Hi-Nicalon/PyC/HyprSiC panels are summarized in Table 4.

Table 4: Specifications for Hi-Nicalon 8HS/PyC/HyprSiC material.

Panel ID	Mass (g)	Planform Size (in x in)	Average thickness (in)	Density (g/cm^3)	Fiber Volume (%)
9C-316-P5	211.17	6.30 x 6.30	0.126	2.58	33.8
9C-316-P6	205.82	6.30 x 6.30	0.122	2.59	34.9
9C-316-P7	194.74	6.30 x 6.30	0.119	2.52	35.8

Average Density: 2.56 g/cm^3
Average Fiber Volume: 34.8%

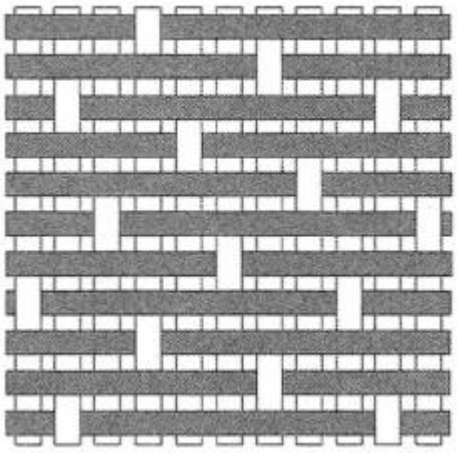

Figure 7: 8 Harness satin weave.

The oxidation inhibited matrix is made of Silicon Carbide (SiC) along with materials that discourage oxidation. SiC is a very hard and abrasive material. It has excellent resistance to erosion and chemical attack in reducing environments while keeping its strength; however, it can be oxidized at very high temperatures [6:30]. Although SiC oxidizes, SiC does have an upside in that it forms silica in high temperature oxidizing atmospheres. The silica can act as a self healing layer when cracks are formed. Figure 8 shows the oxidation inhibited matrix of a

polished as-processed specimen through a scanning electron microscope (SEM). To help depress oxidation, at least one other material has been added to the matrix which can be seen through the layering of the matrix as seen in the figure.

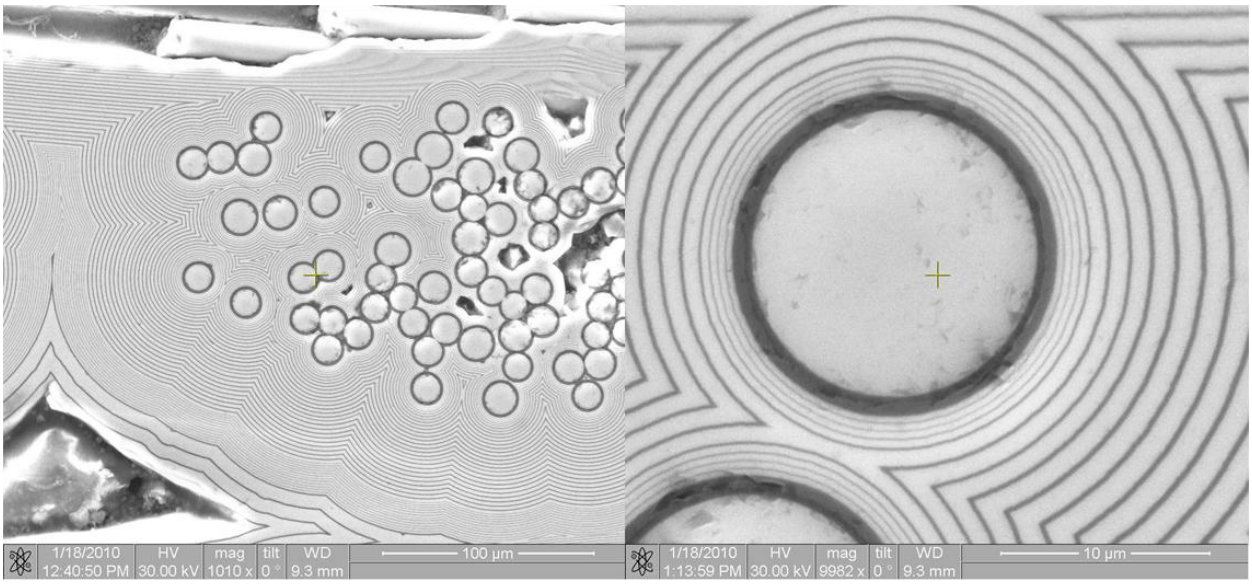

Figure 8: Hi-Nicalon/PyC/HyprSiC oxidation inhibited matrix

The SiC matrix was applied to the composite through chemical vapor infiltration (CVI). The CVI process is similar to the well-established process of chemical vapor deposition, which is used to apply coatings to materials. The only difference is CVI is used to infiltrate and form a matrix. In CVI, a solid (in this case SiC) is deposited within the open volume of a porous structure (fibers) by the reaction of composition of gases or vapors. The process starts when a porous perform of fibers is placed into a high temperature furnace. Reactants gases are then pumped into the chamber and flow around and decompose onto the fibers. As the process continues the apparent fiber diameter increases and eventually fills the available porosity resulting in a completed matrix formation as depicted in Figure 9 [4: 483]. The drawback to CVI

processing of the matrix is voids within fiber tows. The vapors react with the first surfaces contacted resulting in sealing-off interior pores of the preform as seen in the last picture in Figure 9. The majority of pore volume in a SiC matrix is within the fiber bundle, but can also be found between cloth layers. Alleviating porosity is very important because as seen in this research many cracks begin at stress concentrations developed from porosity.

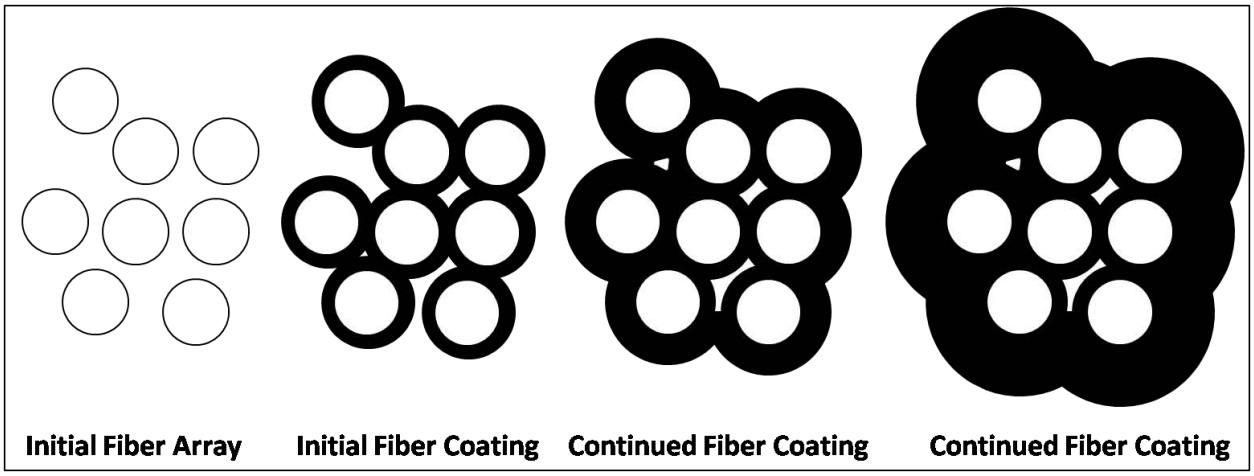

Figure 9: Chemical Vapor Infiltration Growth

The fiber of the research material is made of Hi-Nicalon. Hi-Nicalon fiber has a desirable combination of tensile strength, elastic modulus, density, and retention of these properties at elevated temperatures [2]. Nicalon commercially produced consist of a mixture of β-SiC, free carbon, and SiO_2. The designation "Hi" indicates having low oxygen. The first fiber coating of pyrolytic carbon is intended to optimize the fiber/matrix interface to guarantee sufficient debonding of the fibers in the matrix resulting in high fracture toughness and strength. The second coating of boron carbide, which is a low density; high melting point; and high hardness ceramic, is intended to protect the fiber from oxidative environments. At elevated temperatures and in oxidative atmospheres, boron carbide forms into boron oxide which can

act as a self-healing layer. This layer of boron carbide is important because it can self heal at lower temperatures (700˚C-1000˚C) when SiC can only self heal at higher temperatures (above 1000˚C) [17:90]. A close up of the fiber coatings is shown Figure 10.

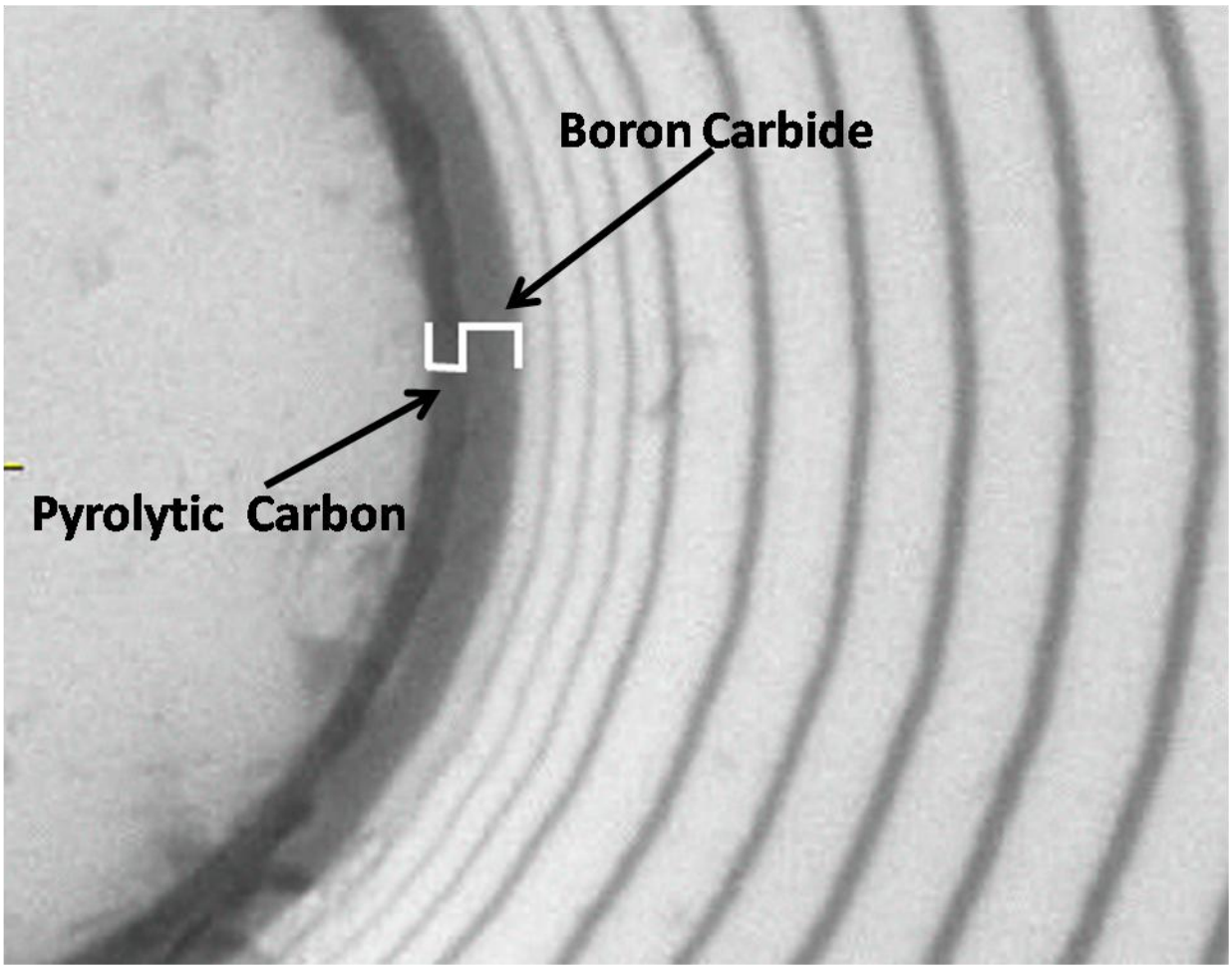

Figure 10: Hi-Nicalon fiber coated with pyrolytic carbon at ~0.4 µm and boron carbide at ~1.0µm

3.2 Test Specimen

Nine test specimens were cut from each panel by Bomas Machine Specialies, Inc. using diamond grinding resulting in 27 specimens. The specimens were cut in accordance with the

specification in Figure 11. The length and width of the specimens were cut in the direction of the fibers.

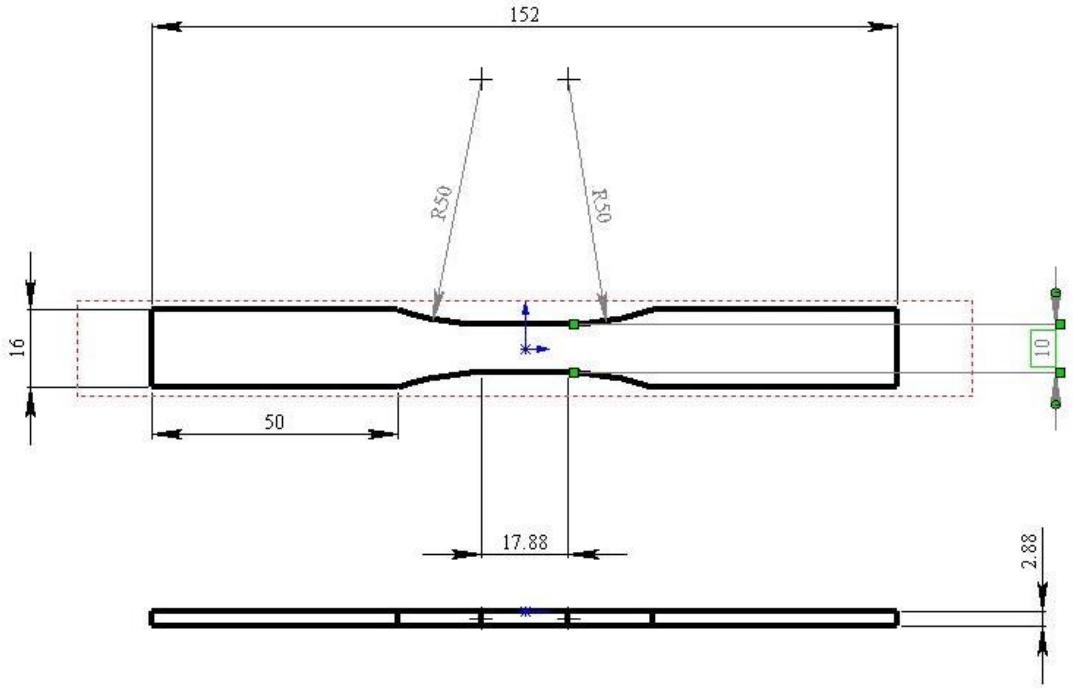

Figure 11: Test Specimen Specifications

A traditional dog bone shape was used to concentrate the maximum stress at the gauge part of the specimen ensuring the failure will occur at this location. The ends of the specimen are larger to provide grip surface area to pull the specimen apart. After the specimens were cut the width and thickness of the gauge area were measured using a Mitutoyo Corporation Digital Micrometer. Minor perturbations during the cutting introduced a small variation in the cross section area of the test section. The dimensions and the identification of each test specimen can be seen in Table 5 through Table 7. The largest variation between specimens was in the thickness due to the weave of the fibers. All dimensions are in millimeters.

Table 5: Dimensions for Specimens from Panel 5

Identification	Width (mm)	Thickness (mm)	Area (mm^2)
P5-1	10.24	3.65	37.38
P5-2	10.29	3.65	37.52
P5-3	10.17	3.49	35.52
P5-4	10.19	3.39	34.51
P5-5	10.18	3.51	35.78
P5-6	10.29	3.47	35.67
P5-7	10.29	3.59	36.94
P5-8	10.28	3.66	37.65
P5-9	10.23	3.66	37.41

Table 6: Dimensions for Specimens from Panel 6

Identification	Width (mm)	Thickness (mm)	Area (mm^2)
P6-1	10.10	3.54	35.78
P6-2	10.10	3.52	35.55
P6-3	10.07	3.48	35.00
P6-4	9.96	3.55	35.40
P6-5	10.09	3.41	34.45
P6-6	10.05	3.59	36.09
P6-7	10.04	3.56	35.75
P6-8	10.04	3.47	34.85
P6-9	10.06	3.63	36.52

Table 7: Dimensions for Specimens from Panel 7

Identification	Width (mm)	Thickness (mm)	Area (mm^2)
P7-1	10.12	3.31	33.53
P7-2	10.12	3.28	33.16
P7-3	10.08	3.26	32.89
P7-4	10.11	3.21	32.44
P7-5	10.10	3.29	33.27
P7-6	10.12	3.24	32.79
P7-7	10.06	3.32	33.37
P7-8	10.12	3.36	33.99
P7-9	10.12	3.37	34.06

Before testing each specimen was fitted with fiberglass tabs to protect the specimen from the grips from the MTS machine. The red tabs were attached using M-bond adhesive. Each tab was then marked for orientation when mounted into the MTS machine. UR, UL, LR, and LL were used for upper right, lower left, lower right, and lower left respectfully. The final specimen before testing can be seen in Figure 12.

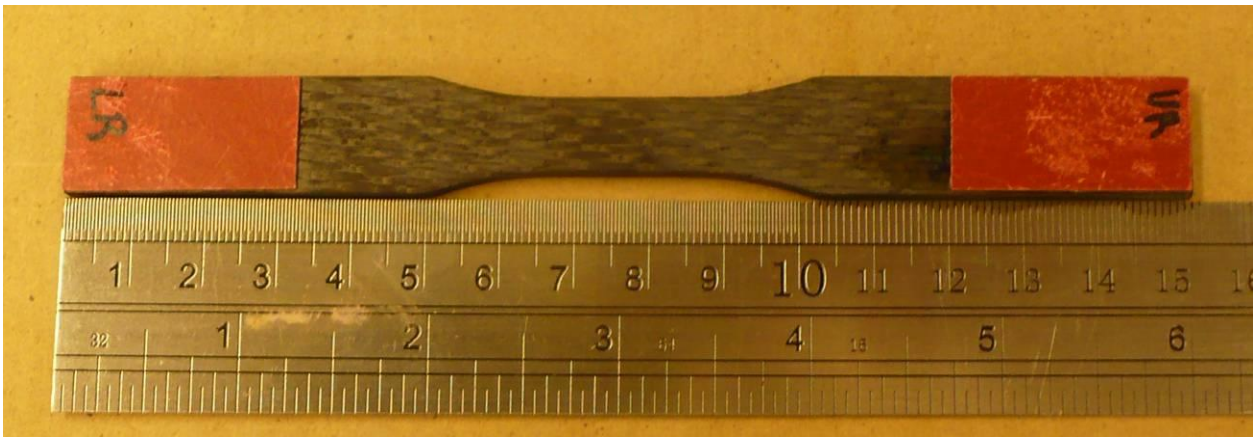

Figure 12: Final Test Specimen

VI. Experimental Arrangements and Procedures

4.1 Test Equipment and Setup

A servo-hydraulic controlled MTS mechanical testing machine (5 kip machine) equipped with hydraulic water-cooled collet grips, a compact two-zone resistance-heater furnace, and two temperature controllers was used in all tests (Figure 13).

Figure 13: MTS 5 Kip machine.

The maximum force available on this unit is 5 kip (approximately 25 kN). Before any tests were run, the 5 kip machines hydraulic system had to be warmed up, which was accomplished by inputting a .25in magnitude sin waveform input as the displacement command for 20 minutes.

A test set up in laboratory air began by mounting the test specimen in MTS Series 647 hydraulic wedge grips ensuring the specimen was parallel to the loading direction. The grips were surfaced with a Surfalloy grip texture to prevent slippage. The wedge grip pressure was raised to 10 MPa to prevent slippage without crushing the test specimen. The grips were also cleaned after each test to insure proper function. The grips were cooled using 15 ˚C water from the Naslab model HX-75 chiller. In steam, the specimens were placed in an alumina susceptor (Figure 14) before mounted onto the MTS mechanical testing machine. Steam was generated by an AMTECO Steam Generator entered the susceptor from the backside to create a near 100% steam environment.

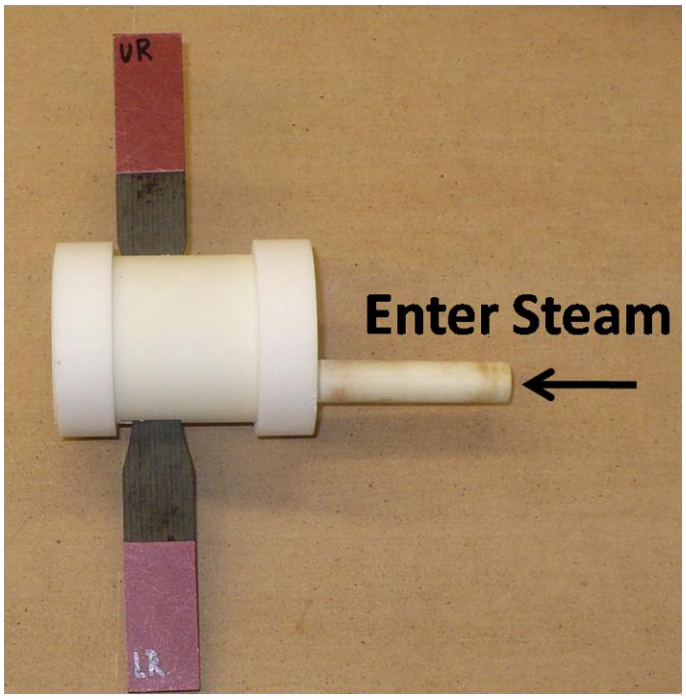

Figure 14: Test specimen inside alumina susceptor.

After the specimens were mounted, a high temperature extensometer, MTS Model 632.53 E-14, was placed on the specimen as seen in Figure 15 to measure strain throughout the test.

Figure 15: Test specimen mounted for steam (left) and air (right) with extensometer attached

Next, the test specimens were enclosed by an AMTECO Hot Rail two zone furnace system (Figure 16). The furnace was controlled by an MTS Model 409.83B Temperature Controller. The controller managed two segregated furnace systems known as the left and right zones.

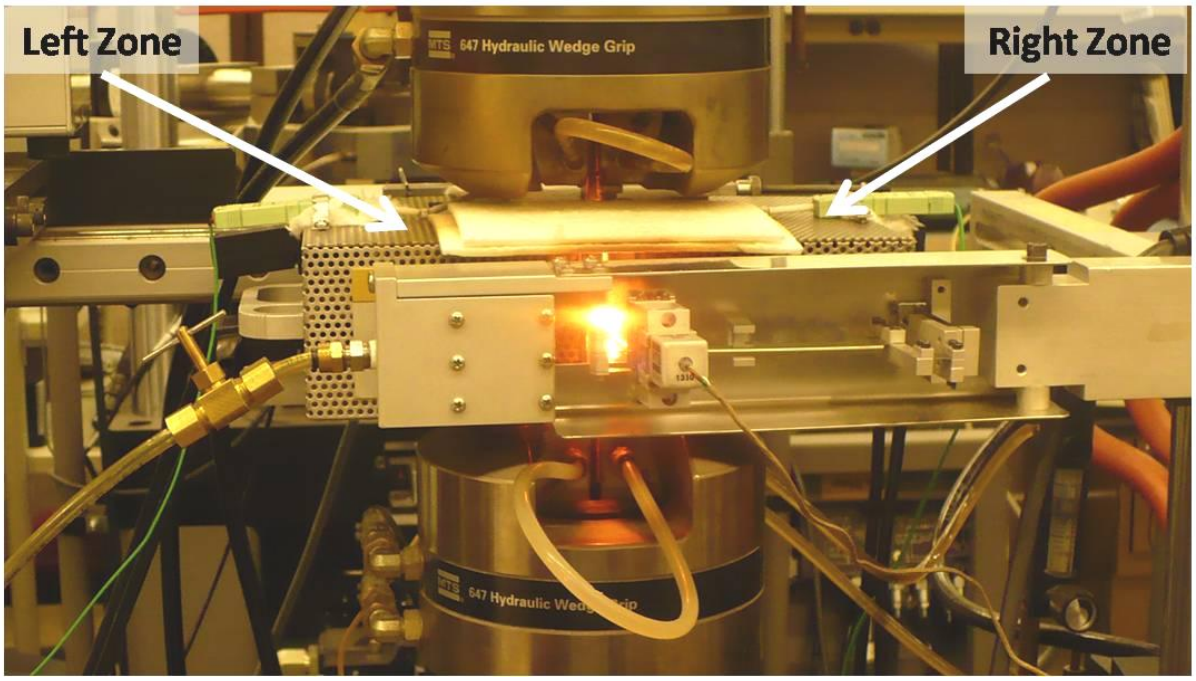

Figure 16: Final test configuration.

The zones were calibrated to ensure correct temperature at the gauge section of the specimen by inserting a test specimen with two R-Type thermocouples in both air and steam environments. While in load command, both furnace temperatures were slowly increased until the Omega CL3515A digital, hand thermometer display read a temperature of 1200˚C. Once 1200˚C was held for 2 hours without much perturbation, the temperature output on the MTS Temperature Controller for the left and right zones for both steam and air conditions were recorded. These temperatures were to be used for all testing for their respective conditions. Throughout testing heating elements would burn out and have to be replaced. Since heating elements perform differently, the furnace had to be recalibrated after each heating element change. Once the test set up was completed, testing began as depicted in section 4.3.

4.2 Microstructural Characterization

Once fractured, the test specimens were investigated by means of a Zeiss Stemi SV II optical microscope equipped with a Zeiss AxioCam HRc digital camera and the Quanta 200 scanning electron microscope (SEM) (Figure 17).

Figure 17: Zeiss Stemi SV II optical microscope (left) and Quanta 200 scanning electron microscope (right).

Before cutting the specimens for the SEM, the two fracture surfaces for all specimens were viewed under the optical microscope. A total of 8 micrographs were taken for each test specimen. The pictures included two side views, a front, and a back view for the two sides of the fracture surface. After microscopy, one side of select specimens was cut approximately 4mm behind the fracture surface using a diamond coated blade. The fracture surface was then mounted to a metallic SEM sample tab by carbon double sided tape (Figure 19). The other fracture surface for each specimen was cut into two sections. The cuts were made according to Figure 18. The two pieces were then mounted into phenolic pucks using Buehler specimen preparation machine. One section was mounted damage side up while the other was mounted internal thickness side up as seen in the Figure 18.

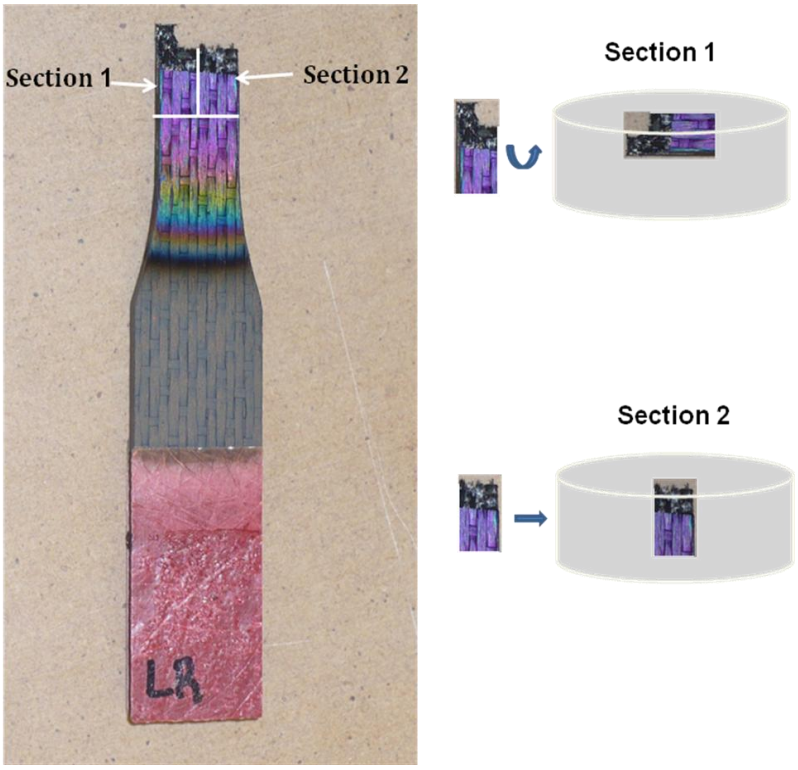

Figure 18: Phenolic mount orientation for fractured specimens.

Figure 19: Hi-Nicalon/PyC/SiC specimens prepared for SEM observation.

The samples were then polished on a Buehler AutoMet Specimen polisher using progressively finer Metadi Diamond Suspension polishing fluids. The steps are outlined in Table 8. After accomplishing two consecutive steps, specimens were inspected under the SEM to

ensure proper polishing before proceeding to next polishing step. If a specimen was not ready, the two steps were repeated.

Table 8: Polishing sample process.

Polishing Media Grit Size	Polishing Pressure (Lbs)	Polishing Time (min)
400	6	10
600	6	10
45μ	4	8
30μ	4	8
15μ	4	8
6μ	3	6
3μ	3	6
1μ	3	6
1/4μ	1	4

4.3 Test Procedures

4.3.1 Monotonic Testing

A specimen from each panel was tested under monotonic tensile loading providing baseline material properties for Hi-Nicalon/PyC/HyprSiC. With the MTS 5 kip machine at zero load condition, the temperature was raised to 1200˚C at a rate of 1.0 °C/s. Once the specimens reached 1200˚C, the temperature dwelled for 20 minutes with no more than a five degree variation. If temperature perturbations were more than 5 degrees the dwell period would start over. Once the dwell period was over, the specimens were loaded using the displacement command of .05 mm per second until failure. Throughout the entire test, the data recorded was strain, load, oven temperature, displacement, displacement command, and time.

4.3.2 Fatigue Test

Tension-tension fatigue test were conducted at .1 Hz, 1 Hz, and 10 Hz with a maximum load to minimum load ratio (R) equal to .05 in both air and steam environments. With the MTS 5 kip machine at no load condition, temperature was raised to 1200˚C at a rate of 1.0 °C/s. Once the specimens reached 1200˚C, the temperature dwelled for 20 minutes with no more than a five degree variation. After the dwell period, specimens were loaded to the minimum stress level in 20 seconds. Once the minimum stress was reached, the fatigue cycles began. The fatigue run-out was 2×10^5 cycles in tests conducted at 1.0 Hz and at 10 Hz, and to 10^5 cycles in tests conducted at 0.1 Hz. If specimens achieved run-out, they were brought to zero load and ran through the same tensile test described in section 3.4.1. The data collected included strain, load, load command, displacement, cycle number, temperature and time. The data was collected in four different data files titled “Specimen,” “Cycle,” “Peak and Valley,” and “Tensile.” The “Specimen” file collected data during the warm up, dwell period, and ramp to minimum stress. The “Cycle” file collected data during the following cycles: i) cycles 1 to 25, ii) every tenth cycle between cycles 30 and 100, iii) every 100^{th} cycle between cycles 100 and 1000, iv) every 1000^{th} cycle between cycles 1000 and 10000, and v) every 10000^{th} cycle between cycles 10000 and run-out. The “Peak and Valley” file collected data at every peak and valley during cycling. The “Tensile” files collected data during the tensile test for specimens that achieved run-out. A screen shot of the program used to input the test procedures is in Figure 20.

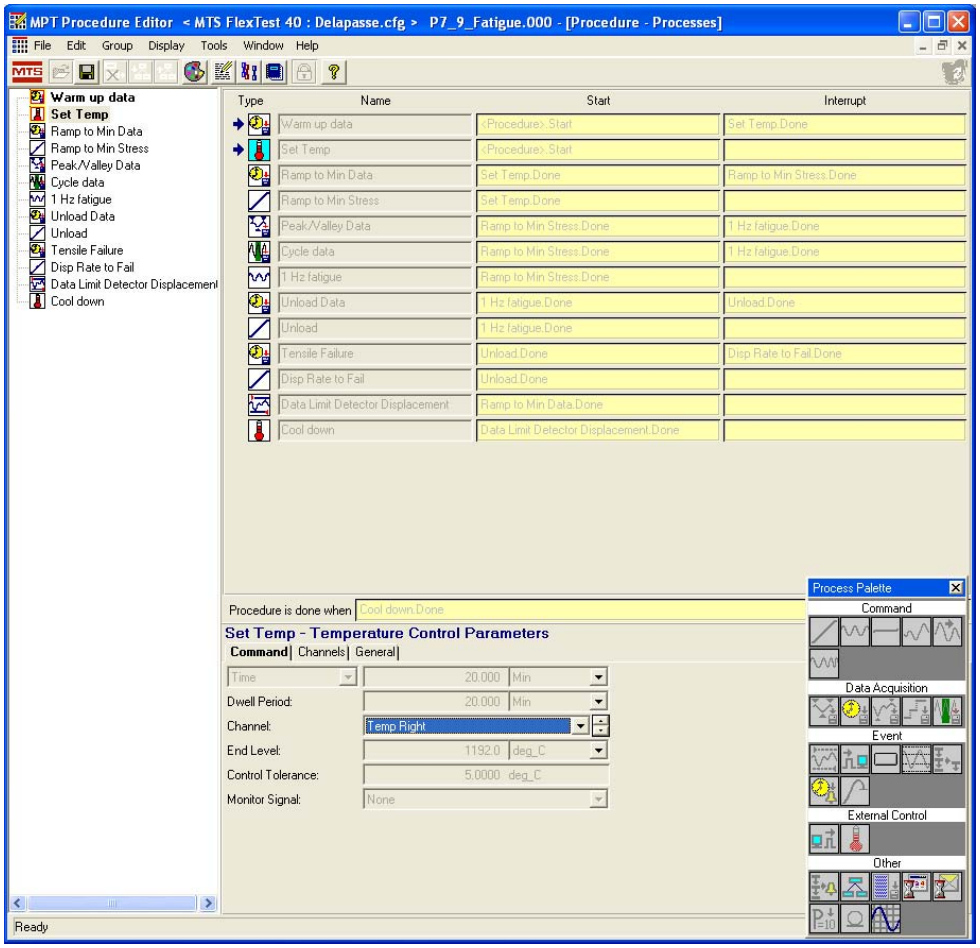

Figure 20: Screen shot of procedures for cyclic loading test.

The scope function was used to ensure the test procedures were running as intended. During warm up the thermal strain was observed through the scope function (Figure 21A) to ensure the extensometer was working properly and to ensure the thermal strain was comparable to previous test. Once cyclic loading began, the strain and force were observed though the scope (Figure 21B) to ensure the peaks and valleys of the strain and force functions were occurring simultaneously.

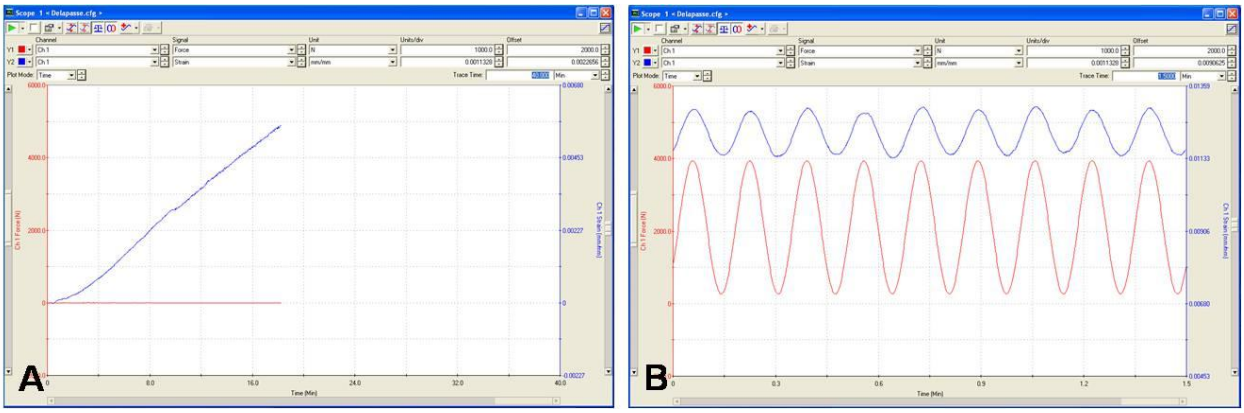

Figure 21: Scope function showing load and strain during warm up (A) and cycling (B).

V. Results and Discussion

5.1 Chapter Overview

The following chapter discusses results of all tests. Section 5.2 presents the thermal strain and linear coefficient of thermal expansion for each specimen. Section 5.3 presents results of the monotonic tension-to-failure tests for specimens from each panel. Section 5.4 presents results of the tension-tension fatigue tests conducted in air. Section 5.5 presents results of the tension-tension fatigue tests conducted in steam. Section 5.6 presents results of the tension-to-failure tests conducted on specimens that achieved fatigue run-out. Section 5.6 presents the composite microstructure. Throughout all sections, test results obtained in this research effort are compared to test results on Hi-Nicalon/BN/SiC composite reported by Christensen [8]. For comparison, the composite investigated by Christensen [8] is identified as "Hi-Nicalon/BN/SiC" or the "baseline CMC" and the material tested in this research is identified as "Hi-Nicalon/PyC/HyperSiC" or "CMC with oxidation inhibited matrix."

Specimen numbers contain reference to the panel number. For example, specimen P5-3 refers to specimen 3 from panel P5. Fatigue run-out was defined as $2x10^5$ cycles for tests performed at the frequencies of 1 Hz and 10 Hz, and was 10^5 for test performed at 0.1 Hz. The results of all tests are summarized in Table 9. Values shown in Table 9 were determined from experimental data in accordance with the procedures in ASTM Standard C 1359 [28].

Table 9: Summary of Hi-Nicalon/PyC/HyprSiC specimen data. All tests conducted at 1200˚C.

Specimen	Fatigue Frequency (Hz)	Test Environment	Maximum Stress (MPa)	Elastic Modulus (GPa)	Cycles to Failure (N)	Time to Failure (h)	Failure Strain (%)
Tensile Test							
P5-1	-	Air	-	253.0	-	-	-
P5-2	-	Air	-	237.9	-	-	0.62
P6-1	-	Air	-	230.8	-	-	0.67
P6-2	-	Air	-	179.6	-	-	0.67
P7-1	-	Air	-	176.9	-	-	0.78
Tension-Tension Fatigue Tests							
P6-7	0.1	Air	140	188.6	30,712	85.3	0.64
P7-3	0.1	Air	130	172.6	42,449	117.9	1.38
P7-9	0.1	Air	120	230.9	41,918	116.4	2.01
P7-4	0.1	Air	100	205.5	67,607[b]	187.8[b]	-
P5-8	0.1	Air	100	172.4	24,925	69.2	2.64
P6-8	0.1	Steam	140	175.2	11,323	31.5	0.42
P6-9	0.1	Steam	130	201.4	19,542	54.3	0.46
P7-7	0.1	Steam	120	212.6	79,532	220.9	0.68
P7-8	0.1	Steam	100	186.1	100000[a]	277.8[a]	0.34
P6-3	1.0	Air	140	203.1	63,458	17.6	0.50
P5-7	1.0	Air	130	231.7	70,309	19.5	0.57
P7-5	1.0	Air	130	222.6	95,712	26.6	0.39
P5-3	1.0	Air	120	200.0	119,530	33.2	0.26
P7-6	1.0	Air	120	209.0	92,468	25.7	0.32
P5-4	1.0	Air	100	210.4	200000[a]	55.6[a]	0.14
P6-4	1.0	Steam	140	206.4	36,679	10.2	0.27
P5-9	1.0	Steam	130	181.8	98,462	27.4	0.49
P5-6	1.0	Steam	120	234.9	119,931	33.3	-
P7-2	1.0	Steam	120	186.6	134,512	37.4	0.31
P5-5	1.0	Steam	100	261.6	200,000[a]	55.6[a]	0.18
P6-5	10.0	Air	140	231.1	200,000[a]	2.8[a]	0.19
P6-6	10.0	Steam	140	195.9	39,849	1.1	0.15

[a] Run-out, failure of the specimen did not occur when the test was terminated

[b] Failure of the specimen occurred due to equipment malfunction

The result obtained in the 120 MPa fatigue tests conducted at 0.1 Hz in air appears anomalous. The author is not aware of anything in the specimen history that would explain this anomaly. It is recommended that this test be repeated.

The specimen tested at 100 MPa and 0.1 Hz in air also produced a surprisingly short fatigue lifetime. In this case the explanation for such an exceptionally poor fatigue performance and an early failure may be found in the microstructure of this particular specimen (Figure 22). Optical micrographs in Figure 22 reveal that the surface of the specimen (along the thickness) exhibits multiple large voids. Furthermore numerous cracks are seen initiating at the voids and propagating throughout the specimen surface. Such profuse surface cracking was not observed in any other specimen tested in this effort. The surface cracks provided an easy access into the specimen interior for the oxidizing air environment, which resulted in rapid environmental degradation and an early failure. This particular specimen also had a greater thickness than any other specimens used in this research. Consequently, a higher load was used to produce the fatigue stress of 100 MPa. Yet it appears that while the thickness was higher, the density of this particular specimen was lower. This further contributed to the early failure. Therefore the result of this particular test may not be reliable. It is recommended that this test be repeated and the results be re-assessed.

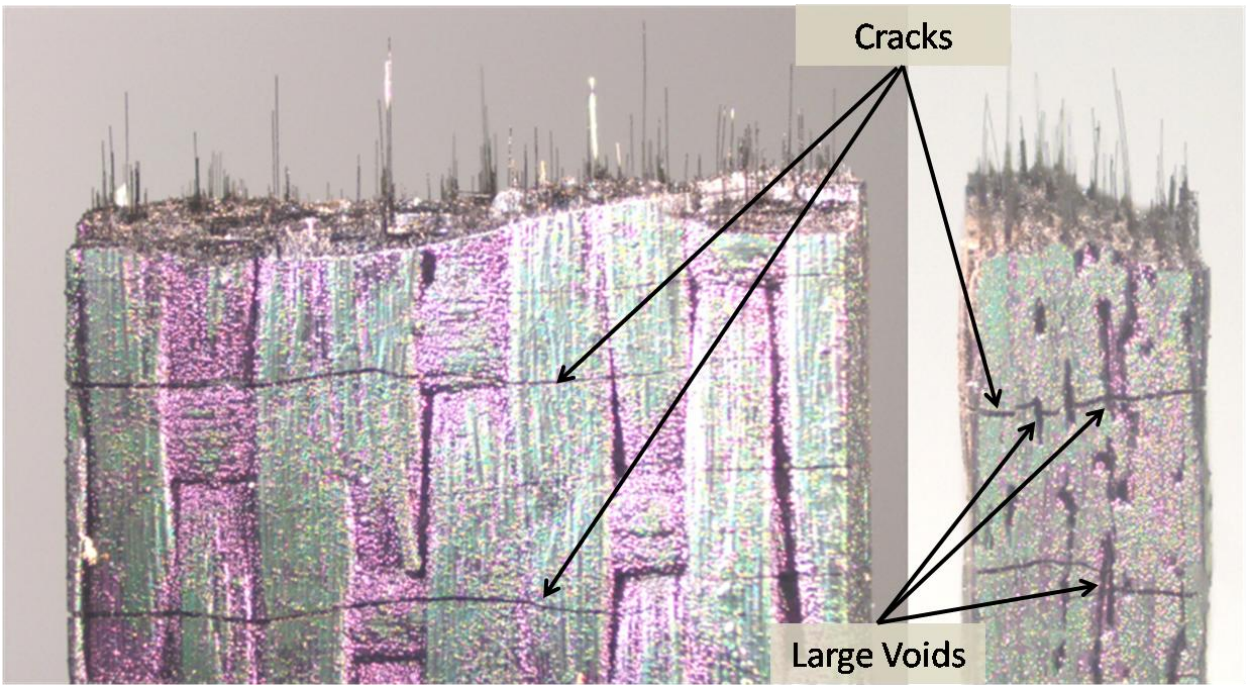

Figure 22: Optical micrographs of specimen P5-8 tested in fatigue at 0.1 Hz in air at 1200˚C, σ_{max} = 100 MPa, N_f = 24,925, t_f = 69.2 h.

5.2 Thermal Expansion

All tests were performed at 1200°C. In all tests, a specimens were heated to test temperature at a rate of 1.0 °C/s and held at temperature for additional 20 min prior to testing. While the temperature increased, no load was applied to each specimen to allow thermal strain. Thermal strain was recorded during ramp-up to test temperature. Then, the thermal strain values were used to calculate the coefficient of thermal expansion (CTE), α, using the equation:

$$\alpha_t = \frac{\varepsilon_t}{\Delta T}$$

where ε_t is the thermal strain in m/m and ΔT is the change in temperature in degrees Celsius. Thermal strain measurements and coefficients of linear thermal expansion are summarized in Table 10. For the specimens tested in this effort, thermal strains varied between .53% and .62%. The average coefficient of thermal expansion was 4.82×10^{-6} 1/°C, which is slightly higher than the CTE reported for the baseline CMC by Christensen [8] as seen in Table 11.

Table 10: **Thermal strains produced by Hi-Nicalon/PyC/HyprSiC CMC due to temperature rise from 23˚C to 1200˚C and corresponding coefficients of linear thermal expansion.**

Specimen	Thermal Strain (%)	Coefficient of Linear Thermal Expansion, α ($10^{-6}/^{\circ}C$)
P5-1	0.57	4.88
P5-2	0.59	5.01
P5-3	0.53	4.54
P5-4	0.55	4.65
P5-5	0.57	4.84
P5-6	0.57	4.88
P5-7	0.59	5.01
P5-8	0.61	5.20
P5-9	0.55	4.66
Average	0.57	4.85
Standard Deviation	0.02	0.20
P6-1	0.58	4.90
P6-2	0.57	4.88
P6-3	0.57	4.80
P6-4	0.58	4.92
P6-5	0.55	4.71
P6-6	0.53	4.52
P6-7	0.53	4.47
P6-8	0.55	4.70
P6-9	0.54	4.55
Average	0.56	4.72
Standard Deviation	0.02	0.16
P7-1	0.55	4.69
P7-2	0.62	5.23
P7-3	0.55	4.69
P7-4	0.55	4.68
P7-5	0.60	5.06
P7-6	0.61	5.14
P7-7	0.58	4.89
P7-8	0.58	4.94
P7-9	0.57	4.81
Average	0.58	4.90
Standard Deviation	0.02	0.19

Table 11: Thermal strains produced by Hi-Nicalon/PyC/HyprSiC and Hi-Nicalon/BN/SiC temperature rise from 23˚C to 1200˚C and corresponding coefficients of linear thermal expansion. Data for Hi-Nicalon/BN/SiC from Christensen [8].

Plate	Average Thermal Strain (%)	Average α (10-6/˚C)	Standard Deviation α (10-6/˚C)
Hi-Nicalon/PyC/HyprSiC			
Plate 5	0.57	4.85	0.20
Plate 6	0.56	4.72	0.16
Plate 7	0.58	4.90	0.19
Average	0.57	4.82	0.18
Hi-Nicalon/BN/SiC			
Plate 1	0.51	4.35	0.14
Plate 2	0.51	4.37	0.86
Plate 3	0.52	4.42	0.25
Average	0.52	4.38	0.42

5.3 Monotonic Tension

At least one specimen from each panel was subjected to a monotonic tensile test to failure to determine the tensile properties at 1200˚C. The results of the tensile tests are summarized in Table 12. The tensile stress-strain curves are shown in Figure 23. The average ultimate tensile strength (UTS) was 307 MPa, the average elastic modulus was 206 GPa, and the average failure strain was 0.69%. The proportional limit was determined as the stress at which the stress-strain curve departs from linearity (see Figure 24). The average proportional limit was 116 MPa, which is approximately 38% of the average UTS. Near the proportional limit a noticeable knee is observed in the stress-strain curve. Such knee in the stress-strain curve indicates that matrix cracking is taking place. At this point a larger portion of the load is being transferred to the fibers resulting in a marked change in the slope of the stress-strain curve. As seen in Figure 23, the tensile stress-

strain curves are nearly bi-linear. The bi-linear character of the tensile stress-strain curves is typical for CMCs with the dense matrix.

Table 12: Tensile properties obtained for Hi-Nicalon/PyC/HyprSiC composite at 1200˚C in laboratory air at a constant displacement rate of 0.05 mm/s.

Specimen	Elastic Modulus (GPa)	Proportional Limit (MPa)	Ultimate Strength (MPa)	Failure Strain (%)
P5-2	237.9	110.0	276.8	0.621
P6-1	230.8	100.0	308.4	0.672
P6-2	179.6	125.0	297.9	0.668
P7-1	176.9	130.0	344.1	0.784
Average	206.3	116.3	306.8	0.686

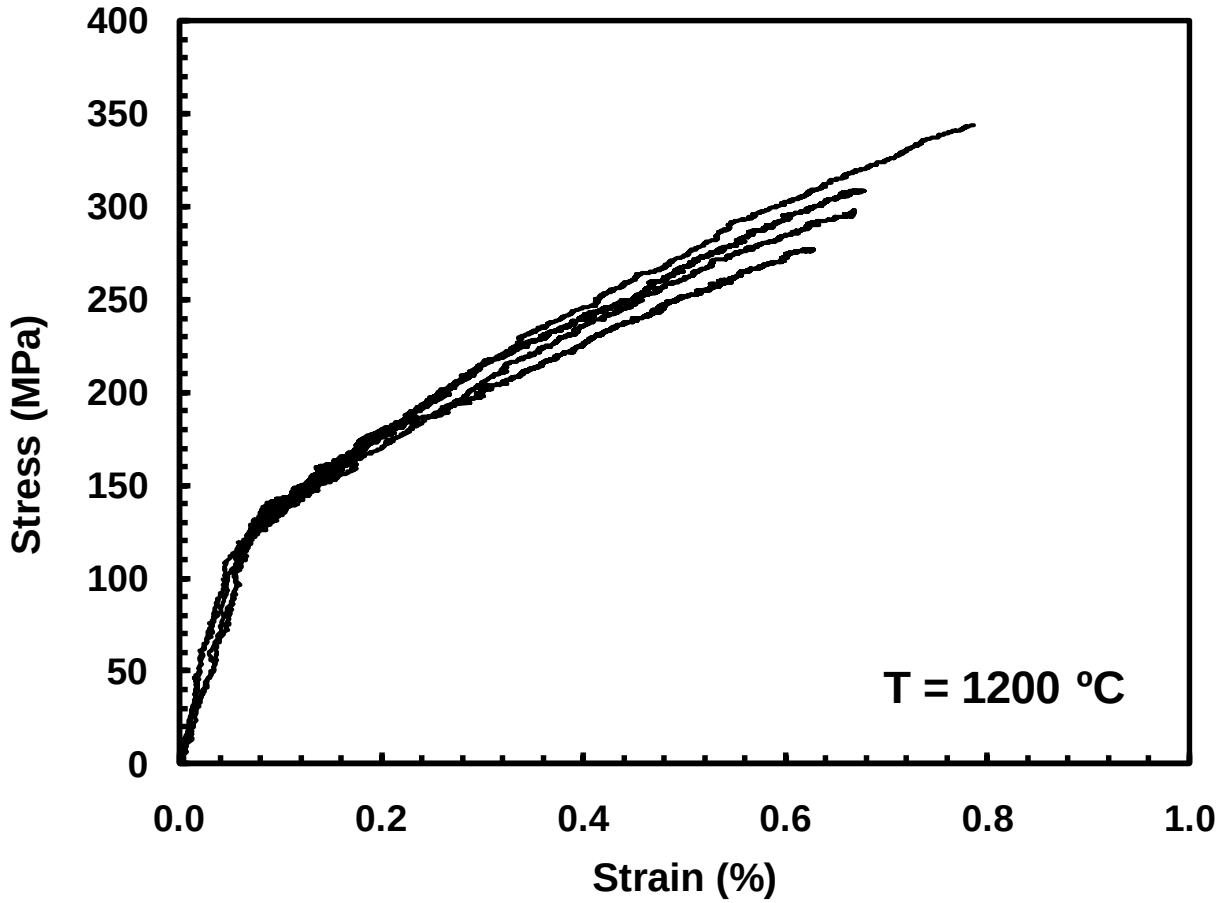

Figure 23: Tensile stress-strain curves for Hi-Nicalon/PyC/HyprSiC Ceramic composite at 1200˚C in air.

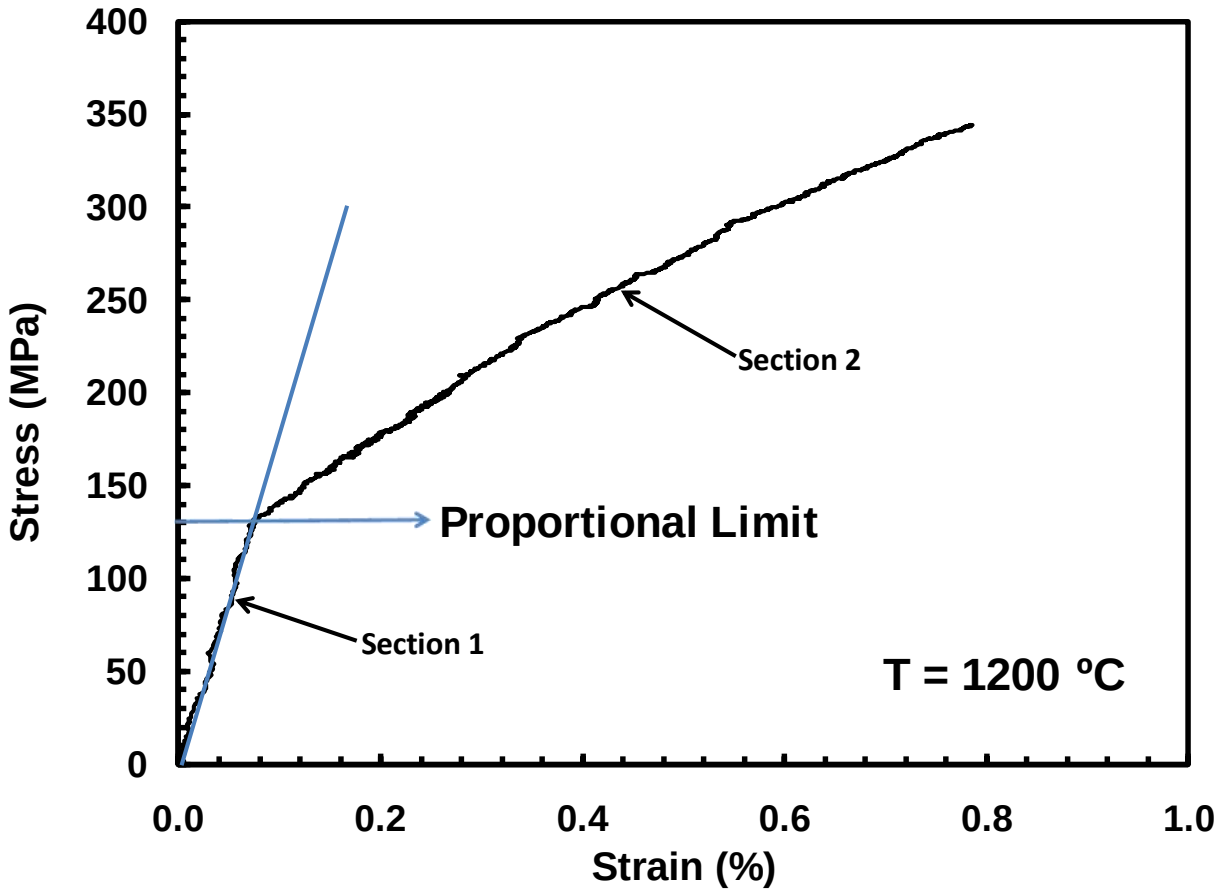

Figure 24: Tensile stress-strain curve obtained for the Hi-Nicalon/PyC/HyprSiC composite at 1200°C showing the proportional limit. The bilinear nature of the stress-strain curve is evident.

The tensile properties and the tensile stress-strain curves obtained for the Hi-Nicalon/ PyC/HyprSiC in this study are compared to those reported for the baseline CMC [8] in Table 13 and in Figure 25, respectively. It is seen that the Hi-Nicalon/PyC/HyprSiC composite produced a higher UTS and a larger failure strain than the baseline material. However, the elastic modulus of the Hi-Nicalon/PyC/HyprSiC material is lower than that of the baseline CMC. The baseline composite also exhibits a higher proportional limit stress than the composite with the oxidation inhibited matrix investigated in this effort. The most notable difference in the stress-strain behaviors of the two

materials is seen in the latter portion (Section 2) of the bilinear stress-strain curve. In the case of the Hi-Nicalon/ PyC/HyprSiC composite, 90% of the failure strain is accumulated during Section 2. Conversely in the case of the baseline material, only 75% of the failure strain is accumulated in Section 2.

Table 13: Summary of tensile properties for Hi-Nicalon/PyC/HyprSiC and Hi-Nicalon/BN/SiC composite at 1200˚C in laboratory air at a constant displacement rate of 0.5mm/s. Data for Nicalon/BN/SiC from Christensen [8].

Material	Elastic Modulus (GPa)	Proportional Limit (MPa)	Ultimate Strength (MPa)	Failure Strain (%)
Hi-Nicalon/PyC/HyperSiC	206.3	116.3	306.8	0.686
Hi-Nicalon/BN/SiC	246.5	110.0	217.0	0.250

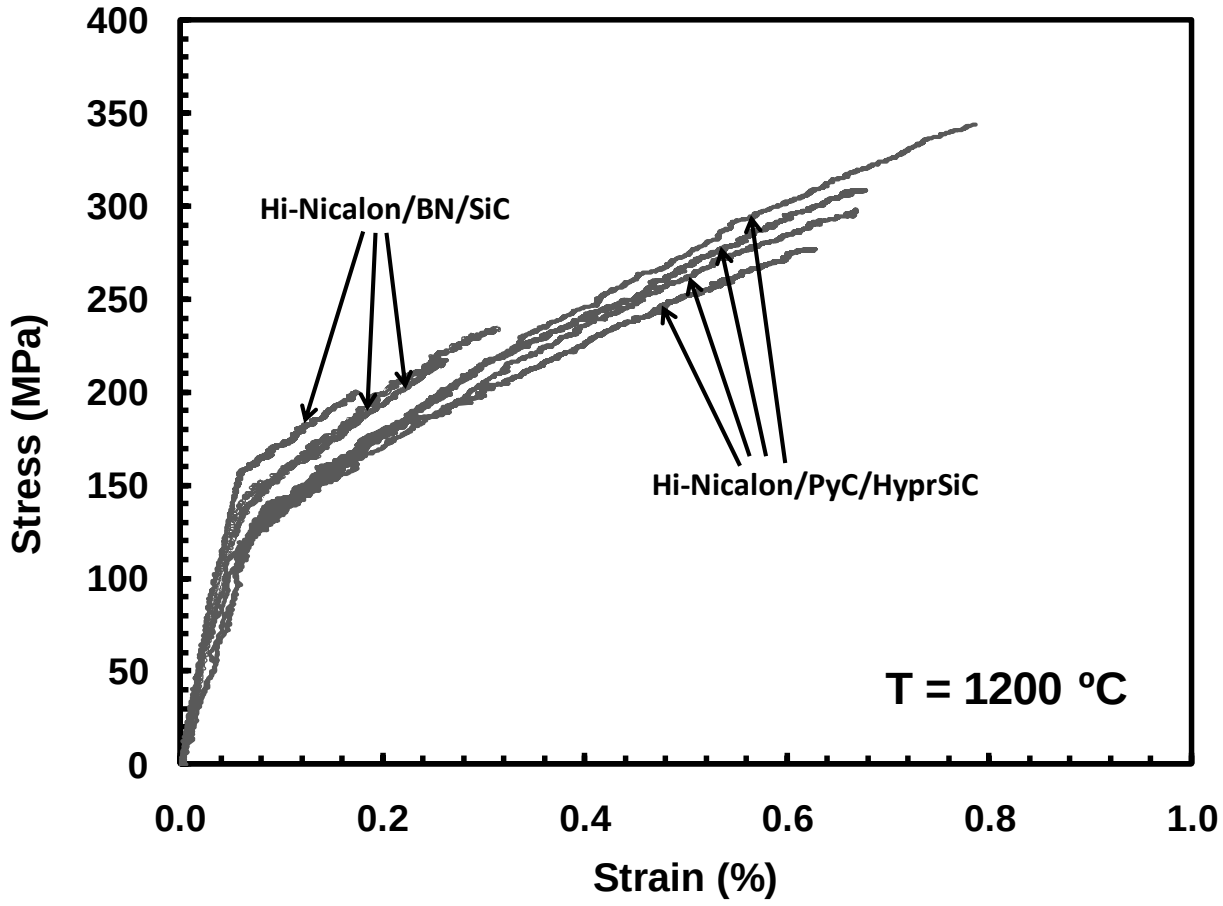

Figure 25: Tensile stress-strain curves obtained for the Hi-Nicalon/PyC/HyprSiC and Hi-Nicalon/BN/SiC CMCs at 1200°C. Data for Hi-Nicalon/BN/SiC from Christensen [8].

5.4 Tension-Tension Fatigue Test at 1200˚C in Air

Tension-tension fatigue tests were conducted at loading frequencies of 0.1, 1.0, and 10.0 Hz at 1200˚C in laboratory air. The maximum stress levels ranged from 100 to 140 MPa and the R-ratio was 0.05. Fatigue run-out was set to 2 x 10^5 cycles in tests conducted at 1.0 Hz and at 10 Hz, and to 10^5 cycles in tests conducted at 0.1 Hz. These run-out conditions are consistent with the

number of loading cycles expected in aerospace applications at 1200°C. Results are summarized in Table 14. Results are also presented in Figure 26 as stress vs. cycles to failure curves.

Table 14: Summary of fatigue results for the Hi-Nicalon/PyC/HyprSiC composite at 1200˚C in laboratory air.

Test Environment	Max Stress (MPa)	Cycles to Failure (N)	Time to Failure (h)	Failure Strain (%)
Fatigue at 0.1 Hz				
Laboratory Air	140	30,712	85.3	0.64
Laboratory Air	130	42,449	117.9	1.38
Laboratory Air	120	41,918	116.4	2.01
Laboratory Air	100	24,925	69.2	2.64
Fatigue at 1.0 Hz				
Laboratory Air	140	63,458	17.6	0.50
Laboratory Air	130	70,309	19.5	0.57
Laboratory Air	130	95,712	26.6	0.39
Laboratory Air	120	119,530	33.2	0.26
Laboratory Air	120	92,468	25.7	0.32
Laboratory Air	100	200,000[a]	55.6[a]	0.14
Fatigue at 10 Hz				
Laboratory Air	140	200,000[a]	2.8[a]	0.19

[a] Run-out, failure of the specimen did not occur when the test was terminated

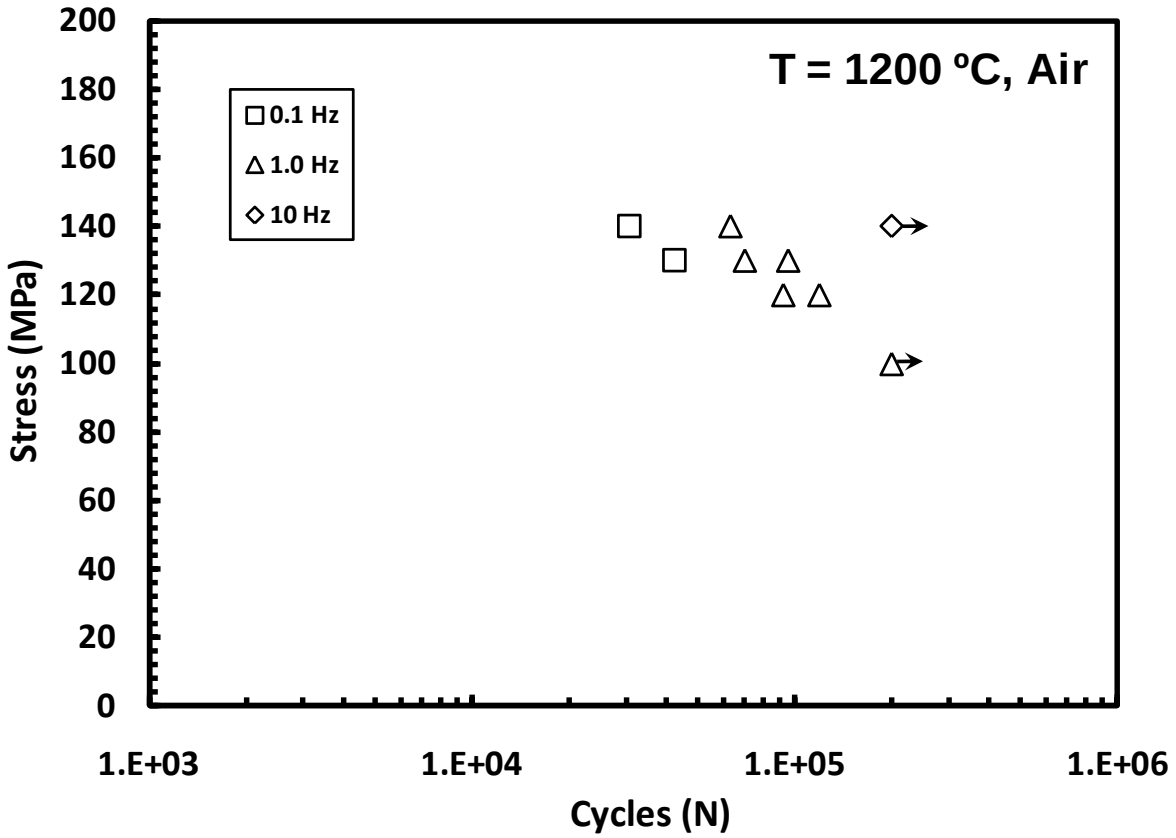

Figure 26: Fatigue S-N diagram for the Hi-Nicalon/PyC/HyprSiC composite at 1200˚C in laboratory air.

The data in

Table 14 and in Figure 26 shows that the loading frequency has a significant effect on fatigue performance in air. When considering cycles to failure, fatigue performance improves considerably with increasing loading frequency. At 10 Hz, the fatigue run-out stress was 140 MPa. At 1.0 Hz the fatigue run-out stress was a lower 100 MPa. The fatigue lifetimes are further reduced as the frequency decreases to 0.1 Hz. For a given fatigue stress of 130 MPa (or 140 MPa) the decrease in frequency from 1.0 Hz to 0.1 Hz results in reduction in fatigue life by nearly a factor of 2. Note that the fatigue limit of 140 MPa produced at 10 Hz is considerably

above the average proportional limit obtained in tensile tests. This indicates that at 10 Hz the fatigue limit is greater than the stress of matrix cracking. In contrast, at 1.0 Hz the fatigue limit was only 100 MPa, which is slightly below the average proportional limit or the stress of matrix cracking.

When considering maximum stress versus time to failure, the specimens tested at lower frequencies had a longer lifetime than those tested at higher frequencies as seen in Figure 27. The specimen tested at 0.1 Hz with a maximum stress of 130 had a lifetime of 117.9 h.

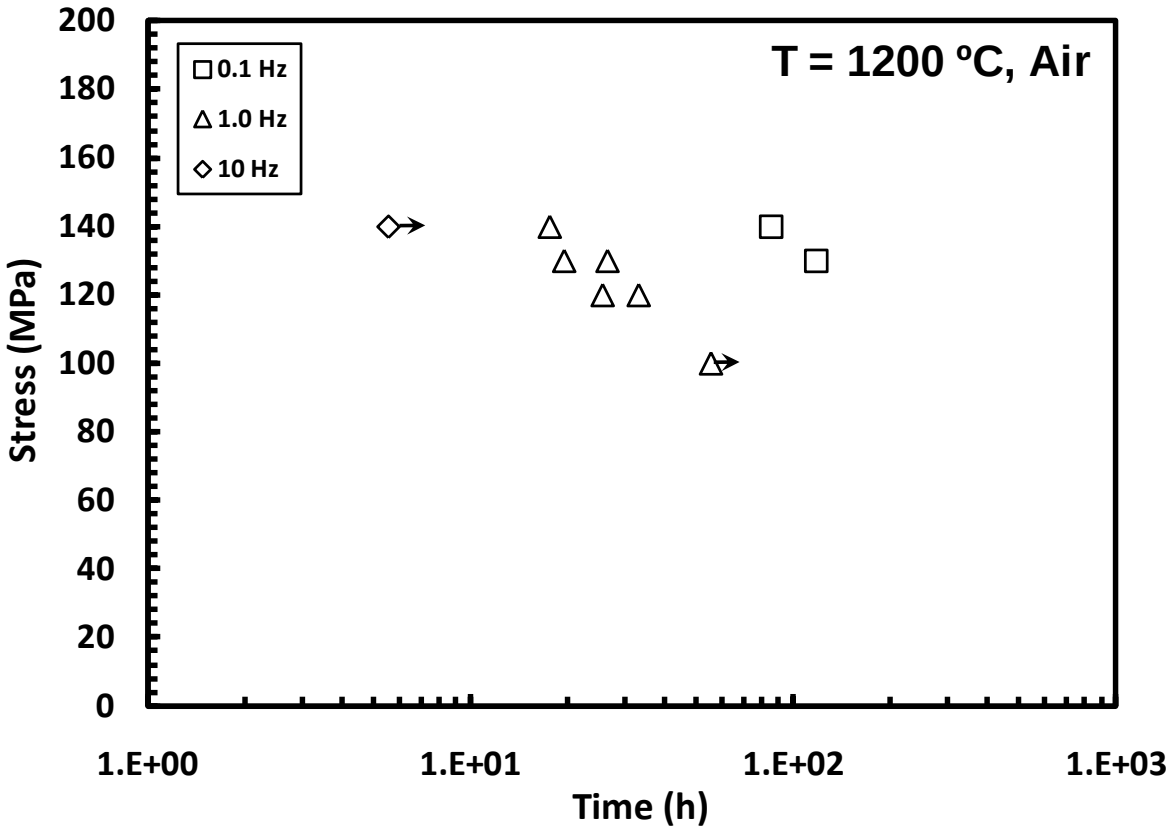

Figure 27: Fatigue stress vs. time to failure for Hi-Nicalon/PyC/HyprSiC composite at 1200˚C in laboratory air.

The fatigue results obtained for the Hi-Nicalon/PyC/HyprSiC composite in this study are compared with the results obtained for the baseline material [8] in Figure 28. Results in Figure 28 reveal that the Hi-Nicalon/PyC/HyprSiC composite exhibits an overall better fatigue performance than the baseline material. This is particularly apparent at the low frequency of 0.1 Hz. At the maximum stress of 120 MPa, the baseline material failed after 3,780 cycles while the Hi-Nicalon/PyC/HyprSiC composite survived over 40,000 cycles. It is noteworthy that the baseline material exhibits an opposite trend as regards the dependence of the cyclic life on the loading frequency. Results reported by Christensen [8] reveal that the cyclic life of the baseline material degrades with increasing frequency.

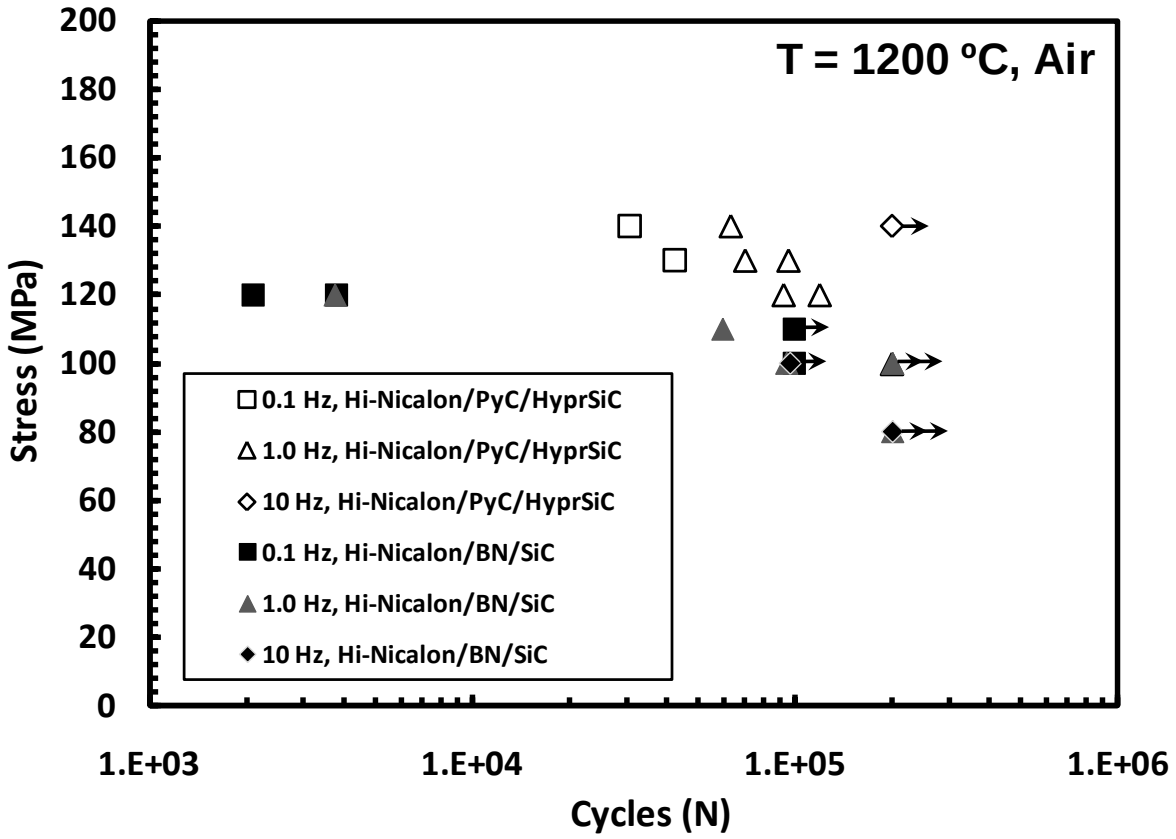

Figure 28: Fatigue S-N diagram for the Hi-Nicalon/PyC/HyprSiC and Hi-Nicalon/BN/SiC CMCs at 1200˚C in laboratory air. Data for Hi-Nicalon/BN/SiC from Christensen [8].

The fatigue versus time to failure for the Hi-Nicalon/PyC/HyprSiC composite in this study is compared with the results obtained for the baseline material [8] in Figure 29. Both materials had longer lifetimes with specimens tested at lower frequencies for a given maximum stress.

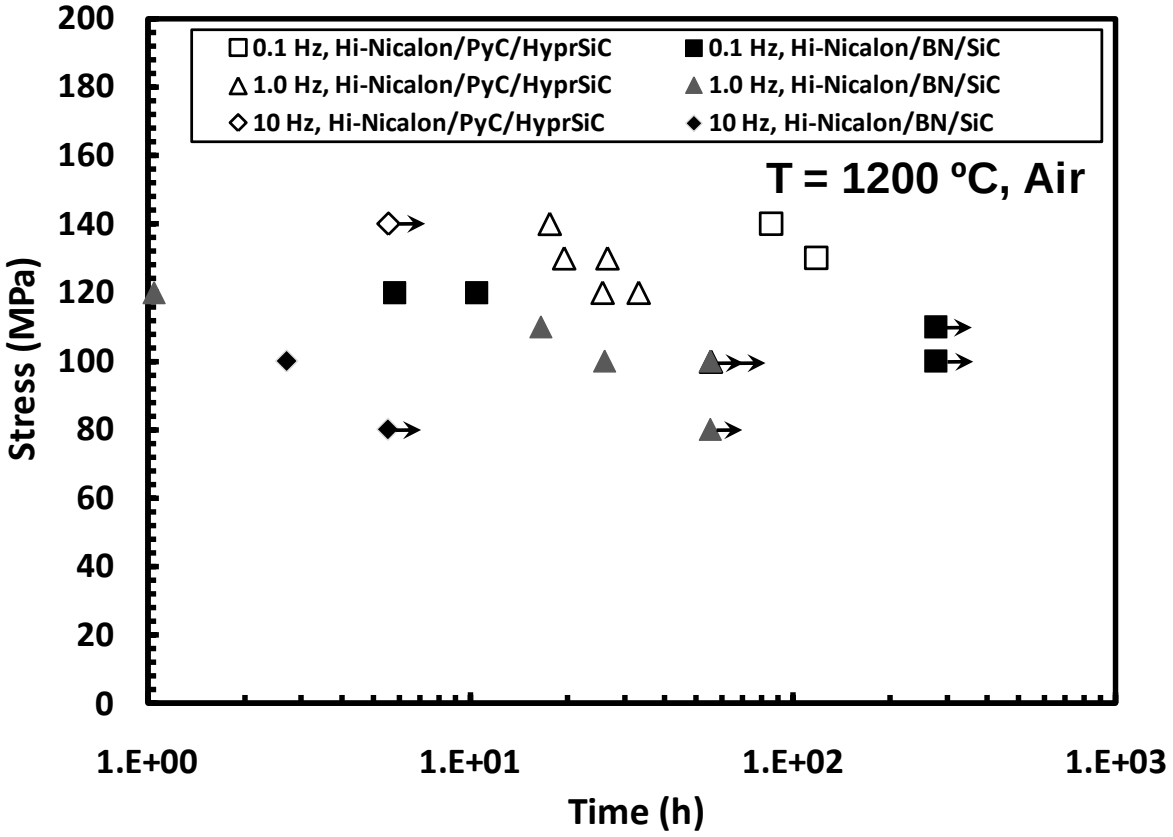

Figure 29: Fatigue stress vs. time to failure for Hi-Nicalon/PyC/HyprSiC and Hi-Nicalon/BN/SiC CMCs at 1200˚C in laboratory air. Data for Hi-Nicalon/BN/SiC from Christensen [8].

Of importance in cyclic fatigue is the reduction in stiffness (hysteresis modulus determined from the maximum and minimum stress-strain data points during a load cycle), which reflects the damage development during fatigue cycling. Modulus evolution with fatigue cycles is shown in Figure 30, where normalized modulus (i.e. modulus normalized by the modulus obtained in the first cycle) is plotted vs. fatigue cycles. A decrease in normalized modulus with cycling was observed for all specimens tested at 1200°C in air, including the specimens that achieved fatigue run-out. The modulus loss was affected by the fatigue stress

level as well as by the loading frequency. Results in Figure 30 show that modulus decreased at a faster rate in test conducted with higher maximum stress and in tests conducted at lower frequency. In some cases reductions in hysteresis modulus reached 90%.

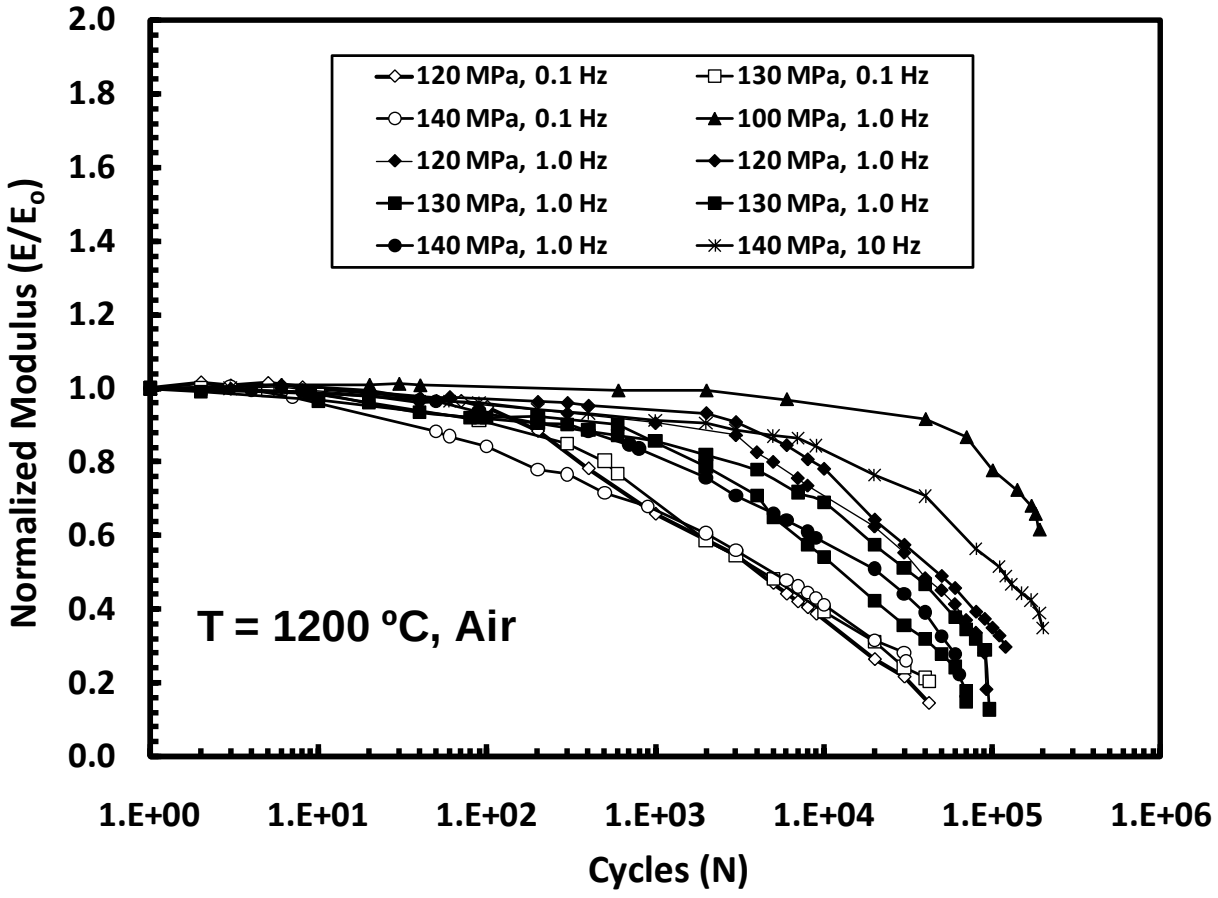

Figure 30: Normalized modulus vs. fatigue cycles for the Hi-Nicalon/PyC/HyprSiC ceramic composite at 1200˚C in laboratory.

Modulus evolution with fatigue cycles recorded for the Hi-Nicalon/PyC/HyprSiC composite is compared with the results obtained for the Hi-Nicalon/BN/SiC CMC by Christensen [8] in Figure 31. Note that a larger decrease in hysteresis modulus with fatigue cycles is seen

for the Hi-Nicalon/PyC/HyprSiC composite than for the baseline material. This observation can be made for all fatigue stress levels and for all fatigue frequencies. While in the 120 MPa test at 0.1 Hz the Hi-Nicalon/BN/SiC composite exhibited a modulus loss of 26%, the Hi-Nicalon/ PyC/HyprSiC material showed a modulus decrease of 86%. Likewise, in the 120 MPa test at 1.0 Hz the modulus loss was 20% for the baseline material and 82% for the composite with the oxidation inhibited matrix.

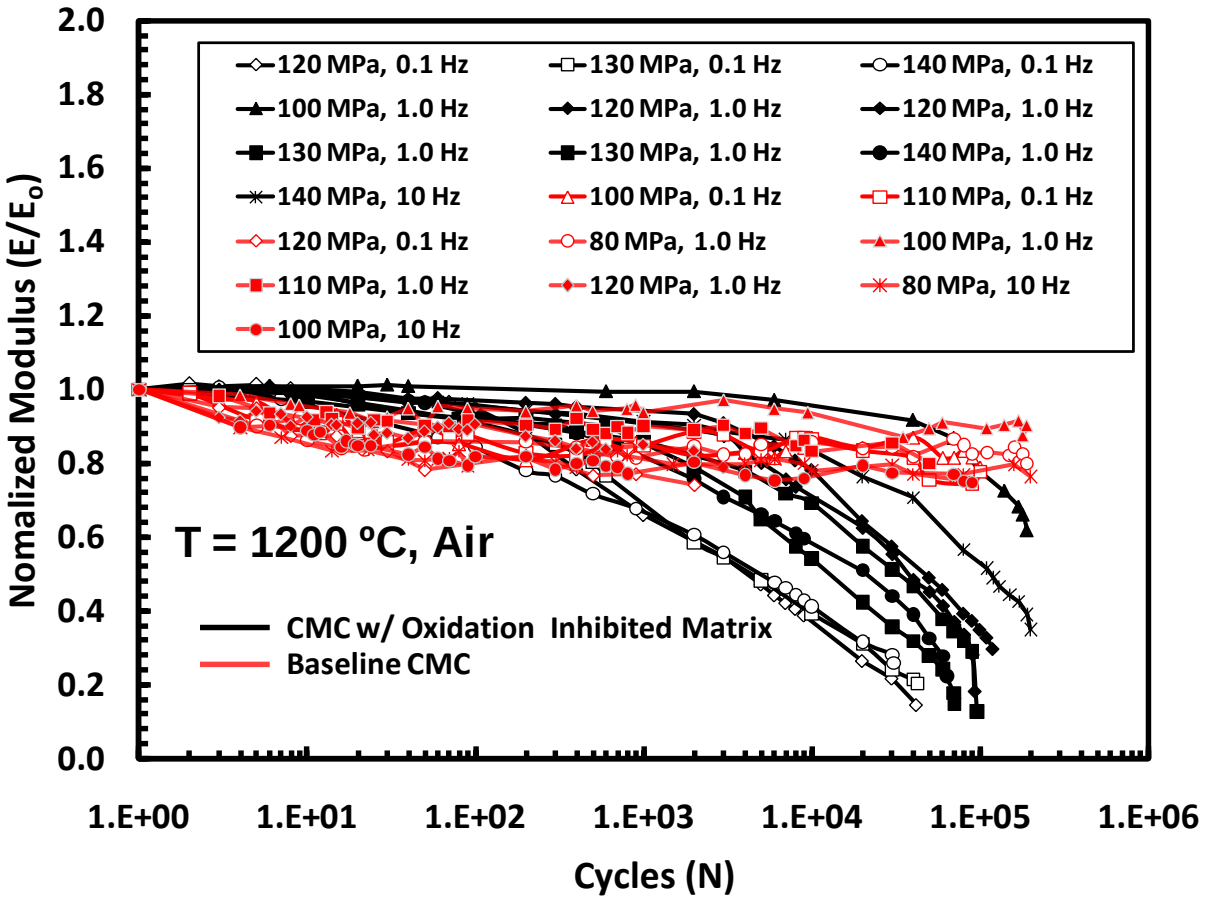

Figure 31: Normalized modulus vs. fatigue cycles for the Hi-Nicalon/PyC/HyprSiC and Hi-Nicalon/BN/SiC ceramic composites at 1200˚C in laboratory air. Data for Hi-Nicalon/BN/SiC from Christensen [8].

Accumulated strains as functions of fatigue cycles are presented in Figure 32. It is seen that at 1200°C in air continual strain accumulation with cycling occurs until failure or run-out. The loading frequency has a noticeable effect on the rate of strain accumulation or on the accumulated strains. Larger strains are accumulated during cycling with a lower frequency. In tests conducted at 0.1 Hz strain accumulation can reach 2.0%. In contrast, all strains accumulated in fatigue tests conducted at 1.0 Hz and at 10 Hz are below 0.6%.

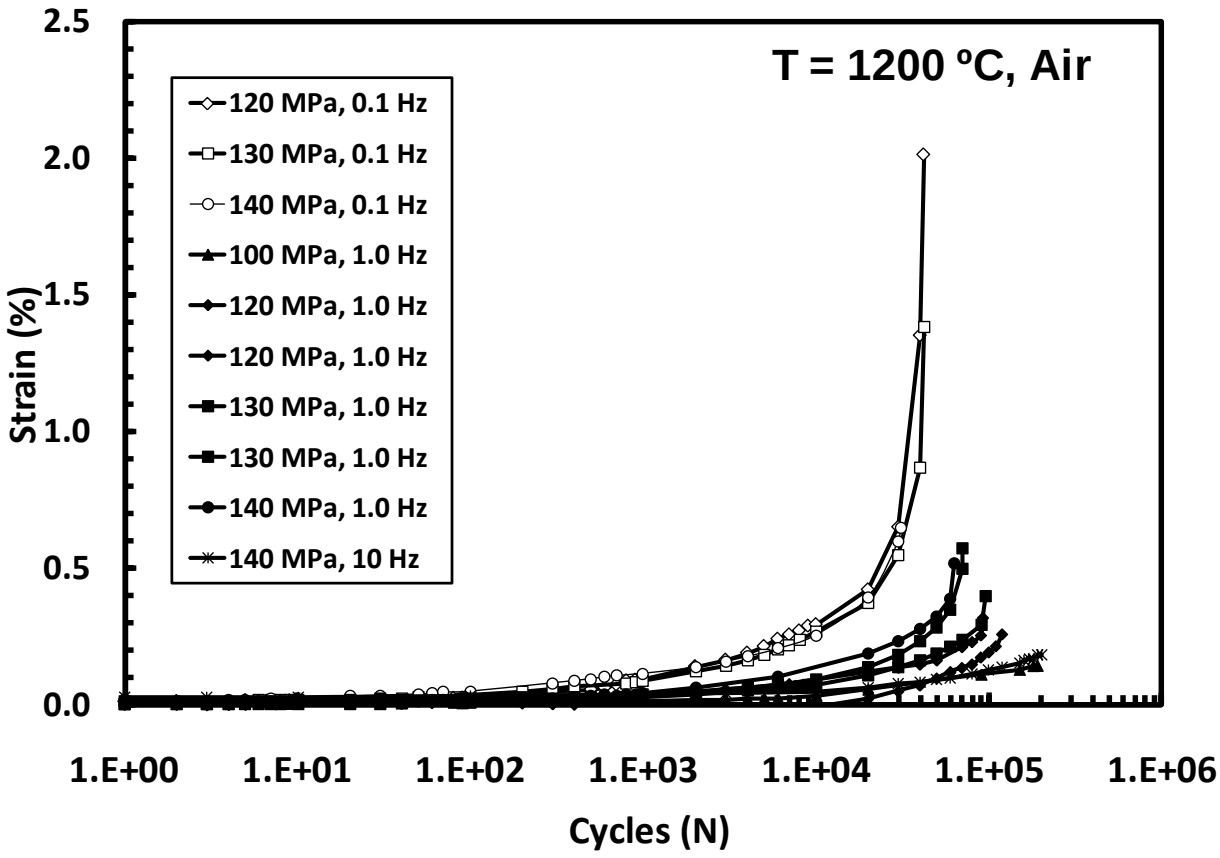

Figure 32: Accumulated strain vs. fatigue cycles for the Hi-Nicalon/PyC/HyprSiC ceramic composite at 1200˚C in laboratory air.

Strain accumulation with fatigue cycles recorded for the Hi-Nicalon/PyC/HyprSiC composite is compared with the results obtained for the Hi-Nicalon/BN/SiC CMC by Christensen [8] in Figure 33. Clearly much larger strains are accumulated by the Hi-Nicalon/ PyC/HyprSiC CMC than by the baseline material. Strains accumulated by the Hi-Nicalon/ PyC/HyprSiC composite range from 0.14% (100 MPa test at 1.0 Hz) to 2.01% (120 MPa test at 0.1 Hz). Conversely, all strains accumulated by the baseline material at 1200°C in air are below 0.1%. Furthermore, while loading frequency had a significant effect on the rate of strain accumulation in the case of the Hi-Nicalon/PyC/HyprSiC composite, it had little influence on the rate of strain accumulation or on the accumulated strains in the case of the Hi-Nicalon/BN/SiC CMC.

A possible reason for the larger strain accumulation by the CMC with the oxidation inhibited matrix may be dependent on the type of loading conditions applied. In specimens tested at 140 MPa, the bulk of the load is carried by the fibers due to matrix cracking. In this case creep would be dominated by the fibers and the increase strain during fatigue is due to the improved fiber coatings (PyC and B_4C). At lower maximum stresses, the matrix is not fully cracked and still supports a load. Here the strain accumulation is due to the both the fibers and the matrix. The additions to the SiC matrix may contribute to increased strain when compared to an ordinary SiC matrix. Because of this, a creep study of the oxidation inhibited matrix should be considered. On the other hand, the baseline CMC has a single fiber coating of boron nitride which breaks down when exposed to oxidative environments when matrix cracking occurs. At this point the BN coating no longer provides a weak fiber/matrix interface to deflect matrix cracking resulting in lower strain accumulations.

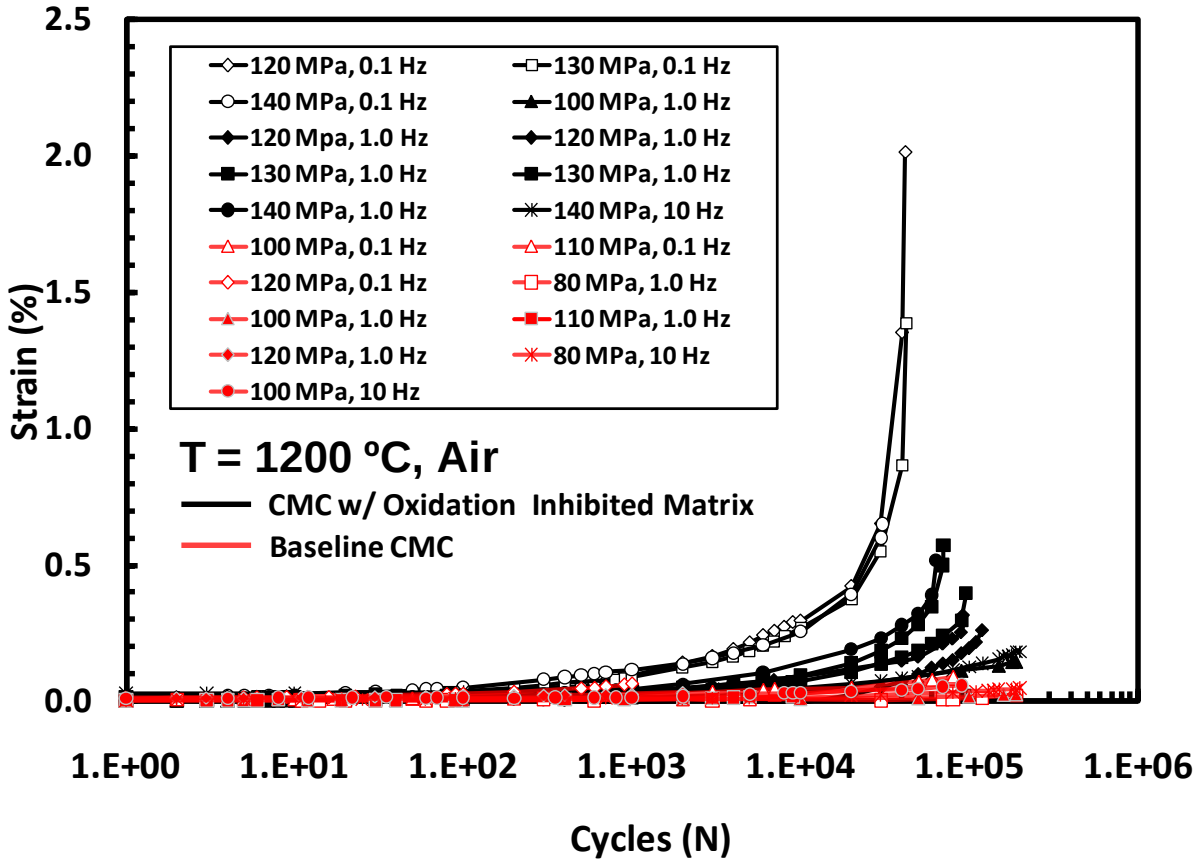

Figure 33: Accumulated strain vs. fatigue cycles for the Hi-Nicalon/PyC/HyprSiC and Hi-Nicalon/BN/SiC ceramic composites at 1200˚C in laboratory air. Data for Hi-Nicalon/BN/SiC from Christensen [8].

Evolution of the hysteresis response of Hi-Nicalon/PyC/HyprSiC with fatigue cycles is typified in Figure 34 and Figure 35, which show hysteresis stress-strain loops for tests conducted in laboratory air at 140 MPa, at 0.1 Hz and 1.0 Hz, respectively. The results reveal that ratcheting, defined as progressive increase in accumulated strain with increasing number of cycles, continues throughout cycling. The results also confirm the modulus decreases as

cycles increase. Cycle 1 exhibits a higher modulus than cycle 30,000. Results in Figure 34 and Figure 35 also confirm that larger permanents strains are produced at lower frequencies. At 0.1 Hz the permanent strain produced at 30,000 cycles amounts to 0.60%, while at 1.0 Hz the permanent strain at 30,000 cycles amounts to 0.37%.

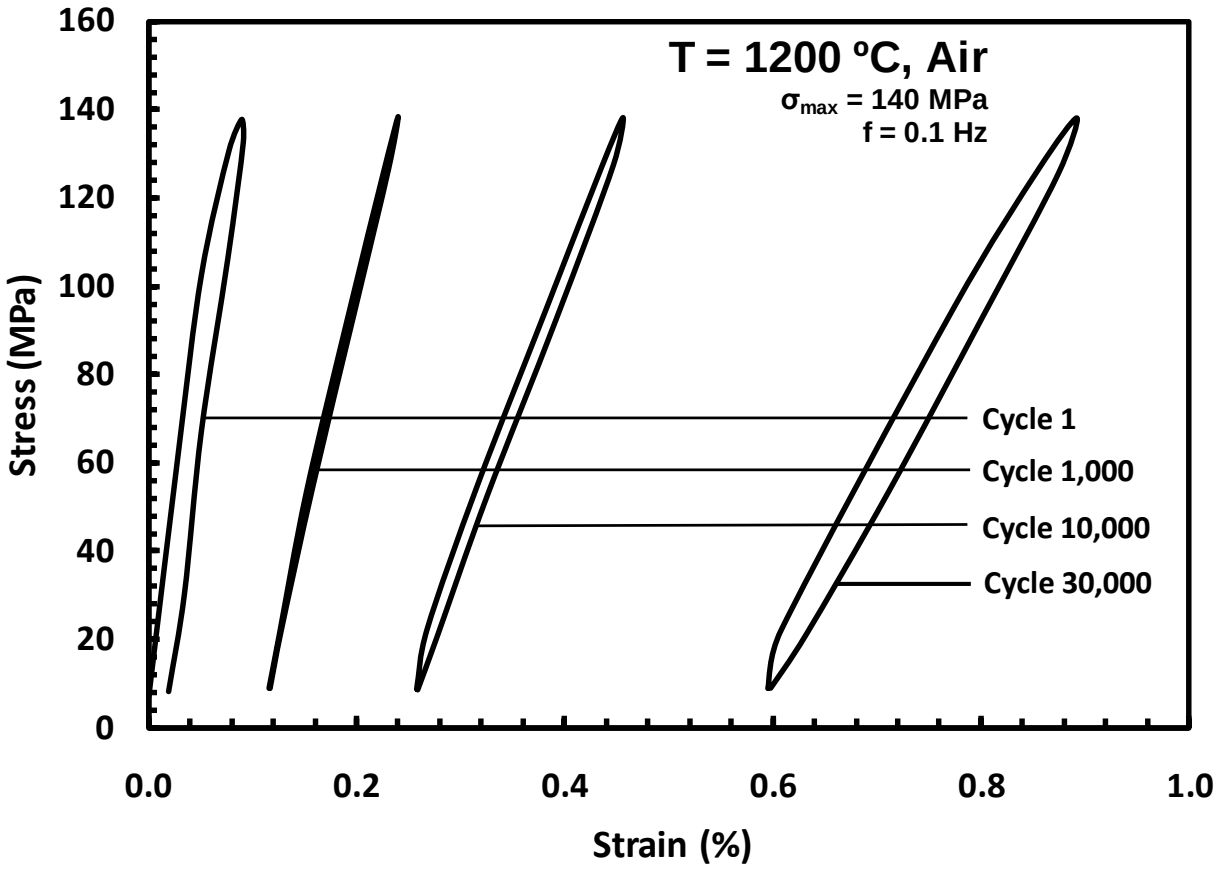

Figure 34: Evolution of Stress-Strain hysteresis response of Hi-Nicalon/PyC/HyprSiC ceramic composite with fatigue cycles in air at 1200˚C at 0.1 Hz and σ_{max} = 140 MPA.

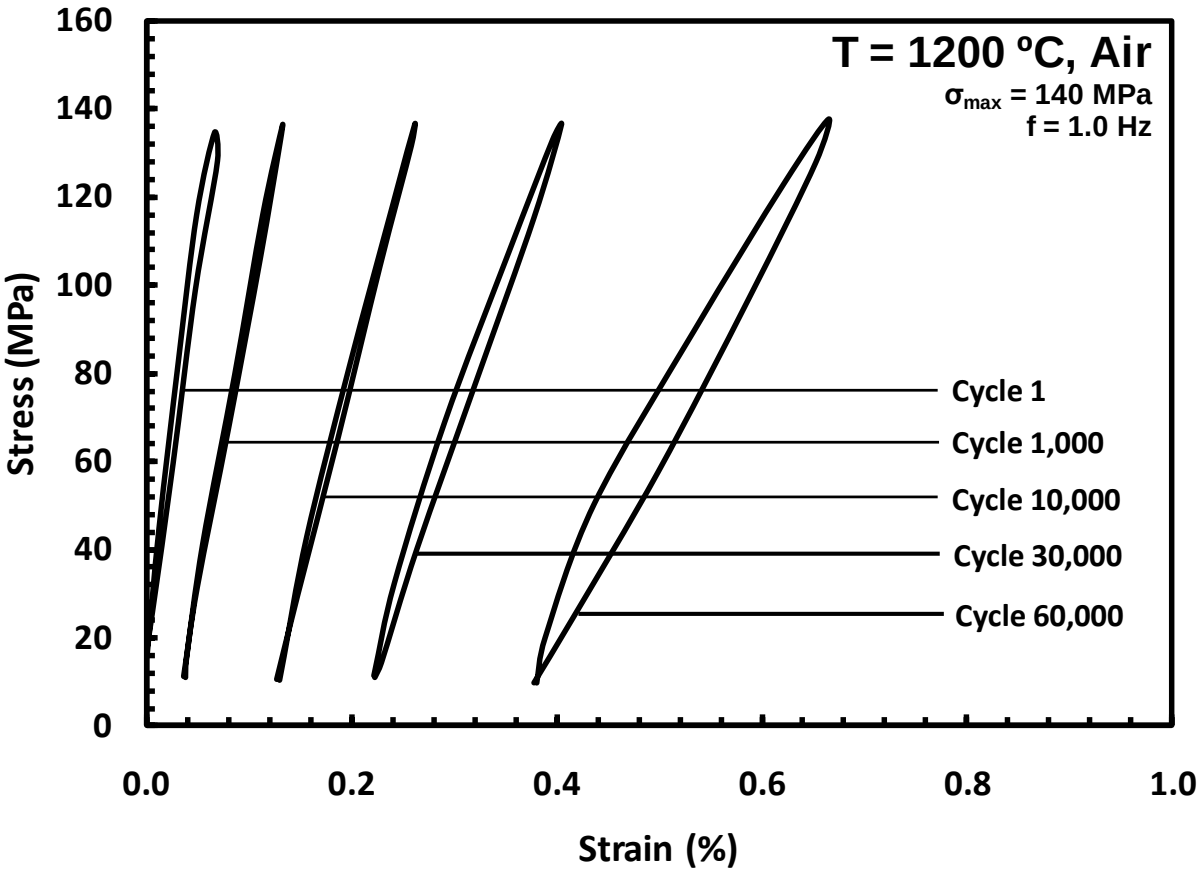

Figure 35: Evolution of Stress-Strain hysteresis response of Hi-Nicalon/PyC/HyprSiC ceramic composite with fatigue cycles in air at 1200˚C at 1.0 Hz and σ_{max} = 140 MPA.

Maximum and minimum cyclic strains as function of cycle number for fatigue tests conducted at 1200°C in laboratory air at 140 MPa and at frequencies of 0.1 Hz and 1.0 Hz are shown in Figure 36 and Figure 37, respectively. It is seen in Figure 36 and Figure 37 that the difference between the maximum and minimum strains for a given cycle increases with cycle number. The cyclic softening is evident.

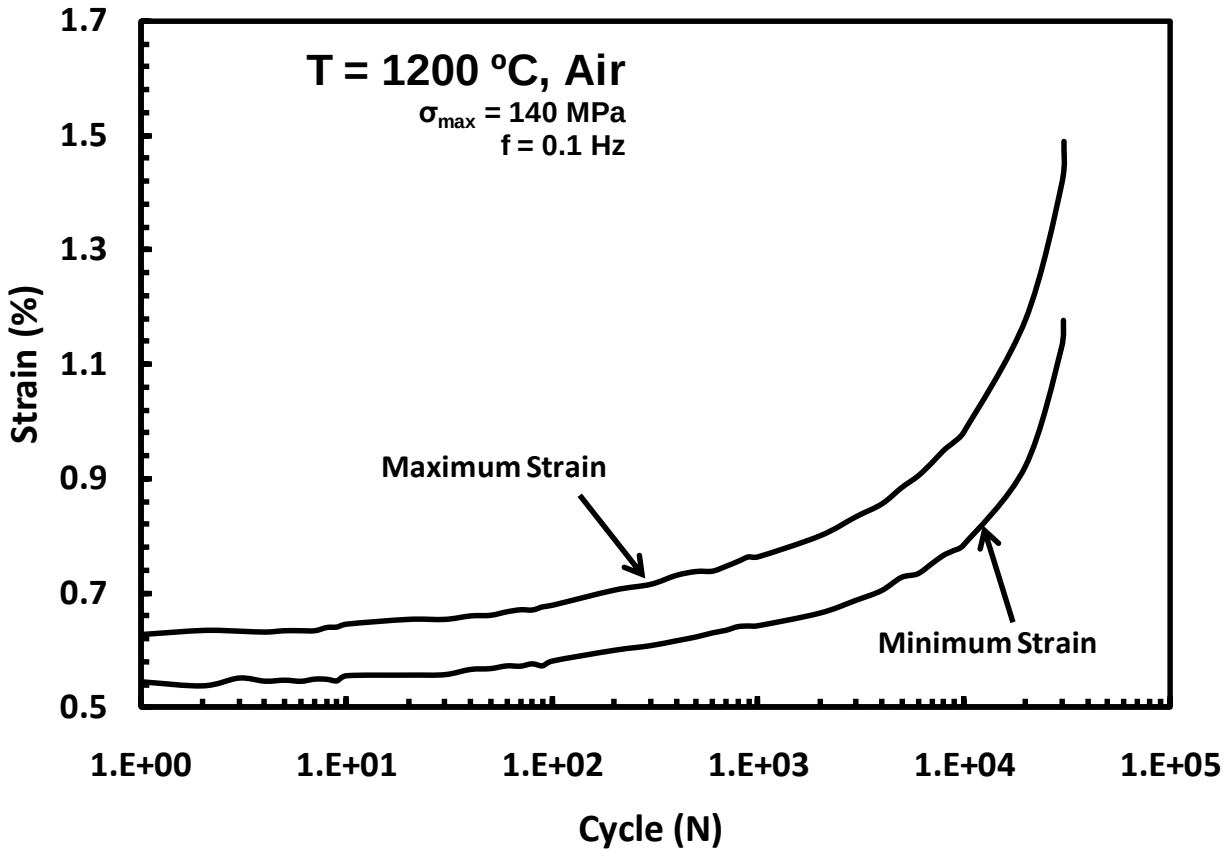

Figure 36: Maximum and minimum strains vs. fatigue cycles for the Hi-Nicalon/ PyC/HyprSiC ceramic composite at 0.1 Hz and 140 MPa, at 1200˚C in laboratory air.

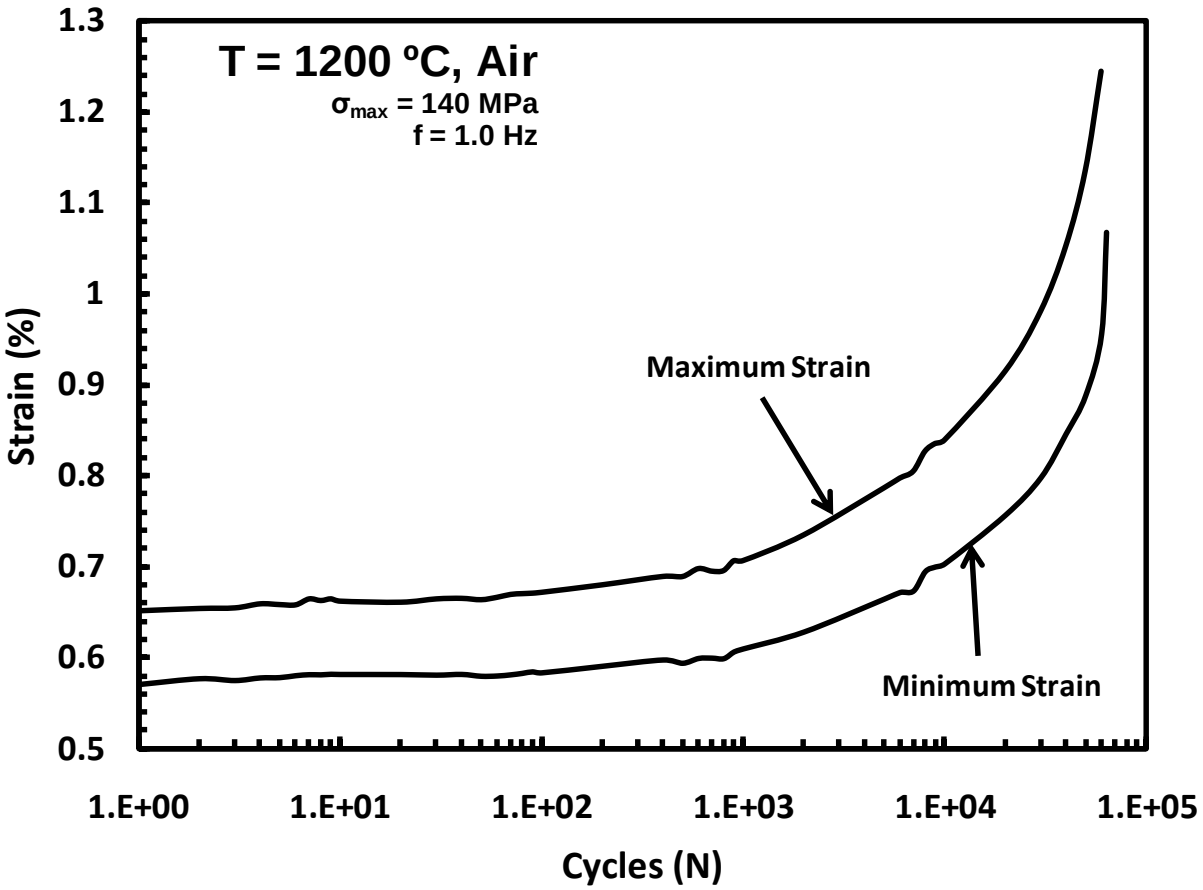

Figure 37: Maximum and minimum strains vs. fatigue cycles for the Hi-Nicalon/ PyC/HyprSiC ceramic composite at 1.0 Hz and 140 MPa, at 1200˚C in laboratory air.

5.5 Tension-Tension Fatigue at 1200˚C in Steam

Tension-tension fatigue tests were conducted at 1200˚C in steam with loading frequencies of 0.1, 1.0, and 10.0 Hz. The maximum stress levels ranged from 100 to 140 MPa and the R-ratio was 0.05. Fatigue run-out was set to 2 x 10^5 cycles in tests conducted at 1.0 Hz and at 10 Hz, and to 10^5 cycles in tests conducted at 0.1 Hz. Results are summarized in Table 15 where the results obtained at 1200°C in air are included for comparison. Results are also presented in Figure 38 as stress vs. cycles to failure curves.

Table 15: Summary of fatigue results for the Hi-Nicalon/PyC/HyprSiC ceramic composite at 1200˚C in laboratory air and in steam environment.

Test Environment	Max Stress (MPa)	Cycles to Failure (N)	Time to Failure (h)	Failure Strain (%)
Fatigue at 0.1 Hz				
Laboratory Air	140	30,712	85.3	0.64
Laboratory Air	130	42,449	117.9	1.38
Laboratory Air	120	41,918	116.4	2.01
Laboratory Air	100	24,925	69.2	2.64
Steam	140	11,323	31.5	0.42
Steam	130	19,542	54.3	0.46
Steam	120	79,532	220.9	0.68
Steam	100	100000[a]	277.8[a]	0.34
Fatigue at 1.0 Hz				
Laboratory Air	140	63,458	17.6	0.50
Laboratory Air	130	70,309	19.5	0.57
Laboratory Air	130	95,712	26.6	0.39
Laboratory Air	120	119,530	33.2	0.26
Laboratory Air	120	92,468	25.7	0.32
Laboratory Air	100	200000[a]	55.6[a]	0.14
Steam	140	36,679	10.2	0.27
Steam	130	98,462	27.4	0.49
Steam	120	119,931	33.3	-
Steam	120	134,512	37.4	0.31
Steam	100	200,000[a]	55.6[a]	0.18
Fatigue at 10 Hz				
Laboratory Air	140	200,000[a]	2.8[a]	0.19
Steam	140	39,849	1.1	0.15

[a] Run-out, failure of the specimen did not occur when the test was terminated

Results in Table 15 and in Figure 38 demonstrate that at the frequency of 1.0 Hz and the fatigue stress levels < 140 MPa, the test environment has little effect on the fatigue performance. The cyclic lifetimes obtained in steam are similar to those produced in air. However, in the case of the fatigue stress level of 140 MPa conducted at 1.0 Hz, the presence of

steam resulted in a 42% loss in cyclic life. Likewise a noticeable degradation in cyclic life due to the presence of steam was observed in the 140 MPa fatigue test conducted at 10 Hz. In this case, the loss of fatigue life reached 80%. At the frequency of 0.1 Hz, the influence of the steam environment becomes dramatic. At 0.1 Hz degradation of fatigue performance is seen at all fatigue stress levels. At 140 MPa the loss of fatigue life due to steam was 63%.

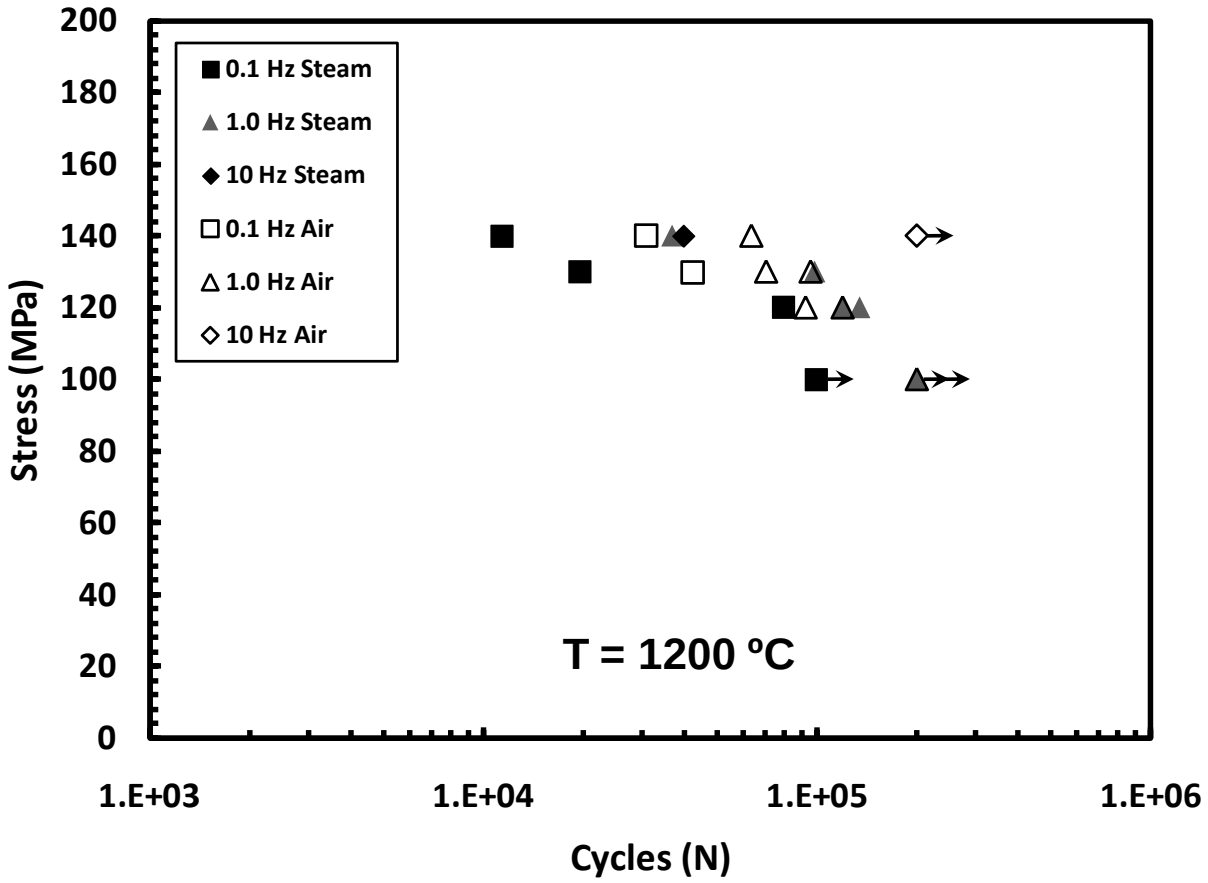

Figure 38: Fatigue S-N curves for the Hi-Nicalon/PyC/HyprSiC composite at 1200°C in laboratory air and steam.

When considering maximum stress versus time to failure for specimens tested in steam and air, the specimens tested at 0.1 had longer lifetimes. The specimen tested at 0.1 in steam with a maximum stress of 130 MPa had a lifetime of 54.3 h, while the specimen tested at 0.1 in air with a maximum stress of 130 MPa had a lifetime of 117.9 h.

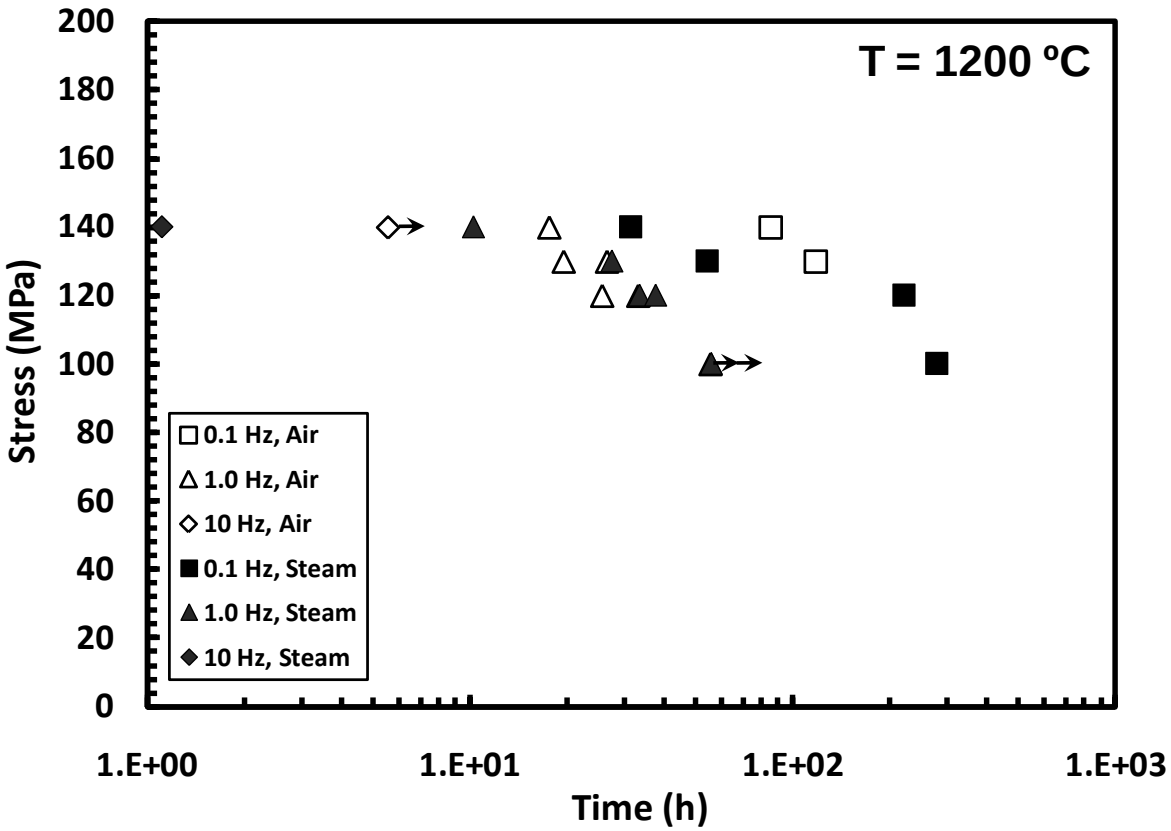

Figure 39: Fatigue stress vs. time to failure for Hi-Nicalon/PyC/HyprSiC composite at 1200°C in laboratory air and steam.

The fatigue results obtained for the Hi-Nicalon/PyC/HyprSiC composite at 1200°C in steam are compared with the corresponding results obtained for the baseline material [8] in Figure 40.

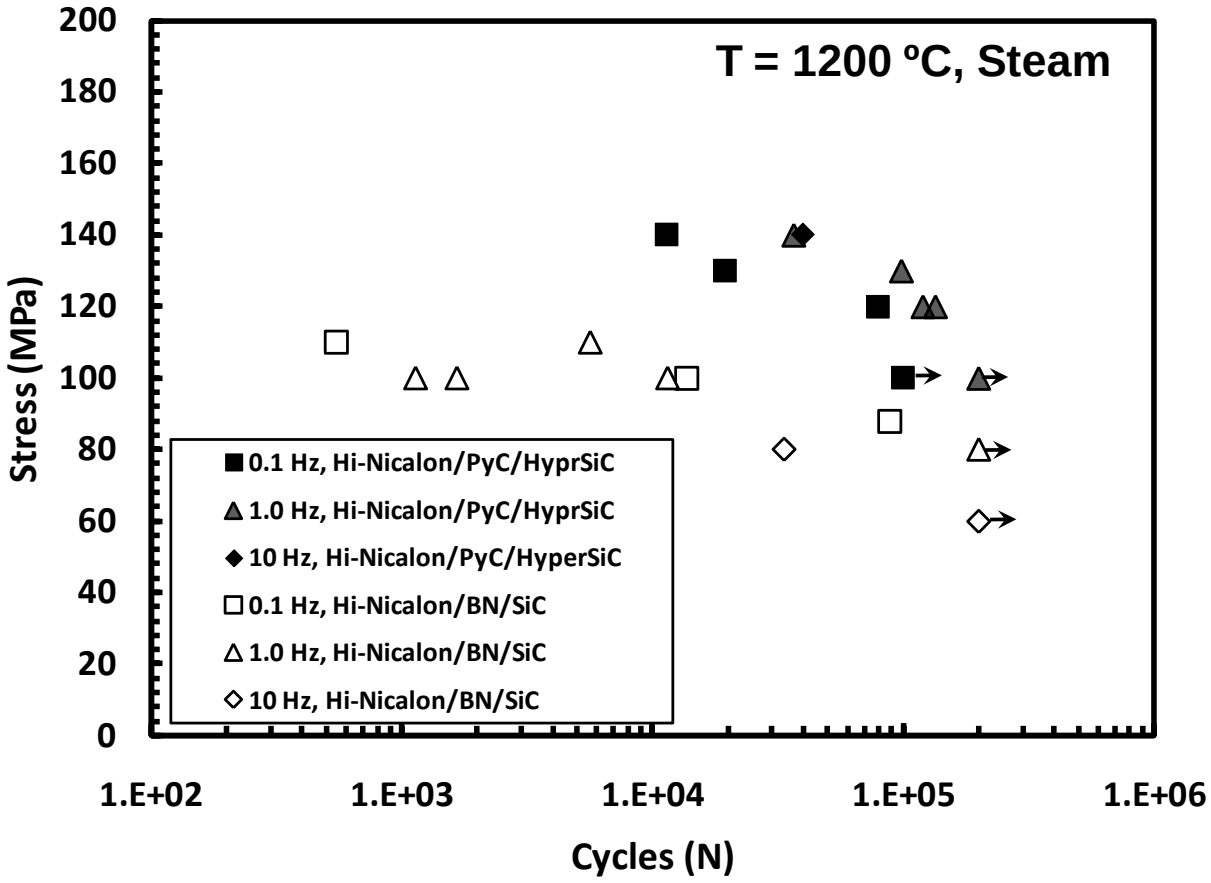

Figure 40: Fatigue S-N curves for the Hi-Nicalon/PyC/HyprSiC and Hi-Nicalon/BN/SiC CMCs at 1200°C in steam. Data for Hi-Nicalon/BN/SiC from Christensen [8].

Maximum stress versus time to failure obtained for the Hi-Nicalon/PyC/HyprSiC composite at 1200°C in steam are compared with the corresponding results obtained for the baseline material [8] in Figure 41.

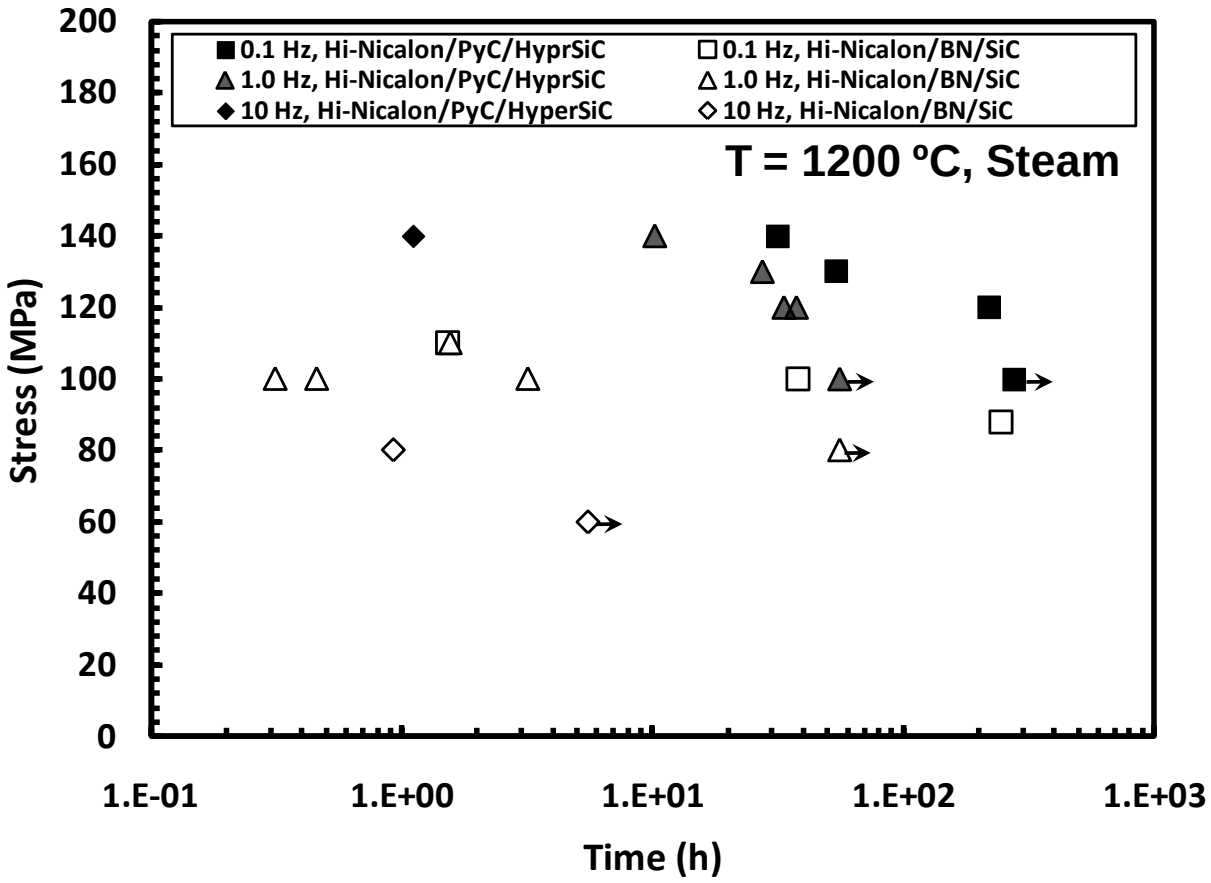

Figure 41: Fatigue stress vs. time to failure for Hi-Nicalon/PyC/HyprSiC and Hi-Nicalon/BN/SiC CMCs at 1200°C in steam. Data for Hi-Nicalon/BN/SiC from Christensen [8].

It is seen that at 1200°C in steam the Hi-Nicalon/PyC/HyprSiC composite performs much better than the baseline material. In the case of the baseline material Christensen [8] reported 90% reduction in fatigue life due to steam in tests performed at 1.0 Hz with the maximum stress levels of 100 and 110 MPa. In contrast, the Hi-Nicalon/PyC/HyprSiC composite exhibited no loss in fatigue life due to steam in tests performed at 1.0 Hz with the maximum stress levels ≤ 130 MPa. Only for the fatigue stress of 140 MPa at 1.0 Hz was life reduction due to the presence of steam observed. At 0.1 Hz both the Hi-Nicalon/PyC/HyprSiC composite and the baseline CMC exhibited loss of fatigue life in the presence of steam. However, the degradation

was less severe in the case of the Hi-Nicalon/PyC/HyprSiC composite than in the case of the baseline material. At 0.1 Hz and at 100 MPa (110 MPa), Hi-Nicalon/BN/SiC composite exhibited 86% (90%) reduction in fatigue life due to steam [8]. In the case of the Hi-Nicalon/PyC/HyprSiC composite tested at 0.1 Hz the loss of fatigue life due to steam was limited to 63%. The loss of fatigue life in the presence of steam for both CMCs is quantified in the Table 16.

Table 16: Reduction in life cycles due to the presence in steam for Hi-Nicalon/PyC/HyprSiC and Hi-Nicalon/BN/SiC. Data for Hi-Nicalon/BN/SiC from Christensen [8].

Max Stress (MPa)	Cycles to Failure (n) Air	Steam	Reduction in Fatigue Life (%)
Fatigue at 0.1 Hz			
Hi-Nicalon/PyC/HyprSiC			
140	30,712	11,323	63.1
130	42,449	19,542	54.0
120	41,918	79,532	None
Hi-Nicalon/BN/SiC			
110	100,000[a]	548	99.5
100	100,000[a]	13,726	86.3
Fatigue at 1.0 Hz			
Hi-Nicalon/PyC/HyprSiC			
140	63,458	36,679	42.2
130	95,712	98,462	None
120	119,530	119,931	None
100	200,000[a]	200,000[a]	None
Hi-Nicalon/BN/SiC			
110	59,641	5,620	90.6
100	200,000[a]	11,447	94.3
80	200,000[a]	200,000[a]	None
Fatigue at 10 Hz			
Hi-Nicalon/PyC/HyprSiC			
140	200,000[a]	39,849	80.1
Hi-Nicalon/BN/SiC			
80	200,000[a]	33,451	83.3

[a] Run-out, failure of specimen did not occur due to run-out

The change in hysteresis modulus (determined from the maximum and minimum stress-strain data points during a load cycle) with fatigue cycling at 1200˚C in steam was assessed. Results are presented in Figure 42 where normalized modulus (i. e. modulus normalized by the modulus obtained in the first cycle) is plotted vs. fatigue cycles. As was the case at 1200°C in air, a noticeable decrease in modulus with cycles was observed at 1200°C in steam. However, the total modulus loss in steam was less than that in air. The modulus loss in steam was limited

to 65% (obtained in the 120 MPa test at 0.1 Hz) while the modulus loss in air reached 87% (obtained in the 30 MPa test at 1.0 Hz).

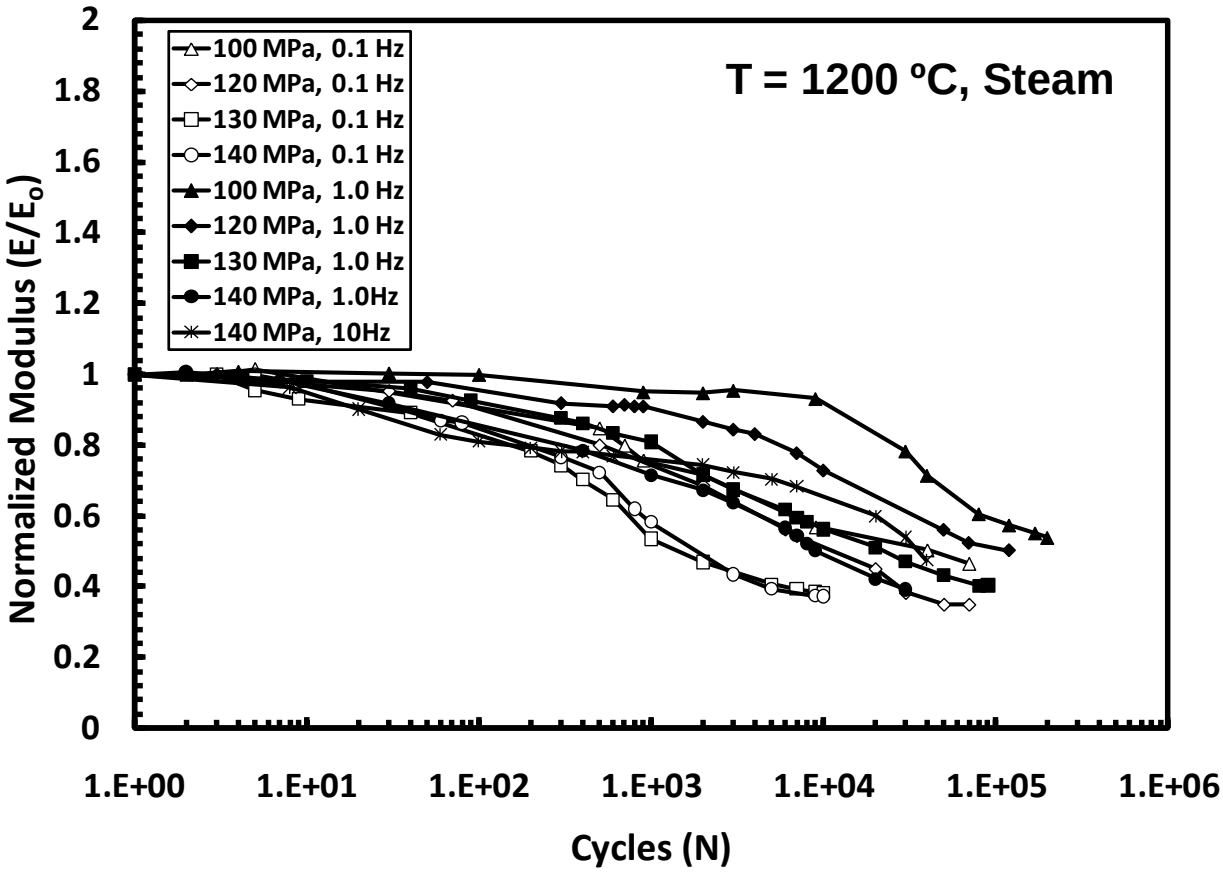

Figure 42: Normalized modulus vs. fatigue cycles for the Hi-Nicalon/PyC/HyprSiC ceramic composite at 1200°C in steam.

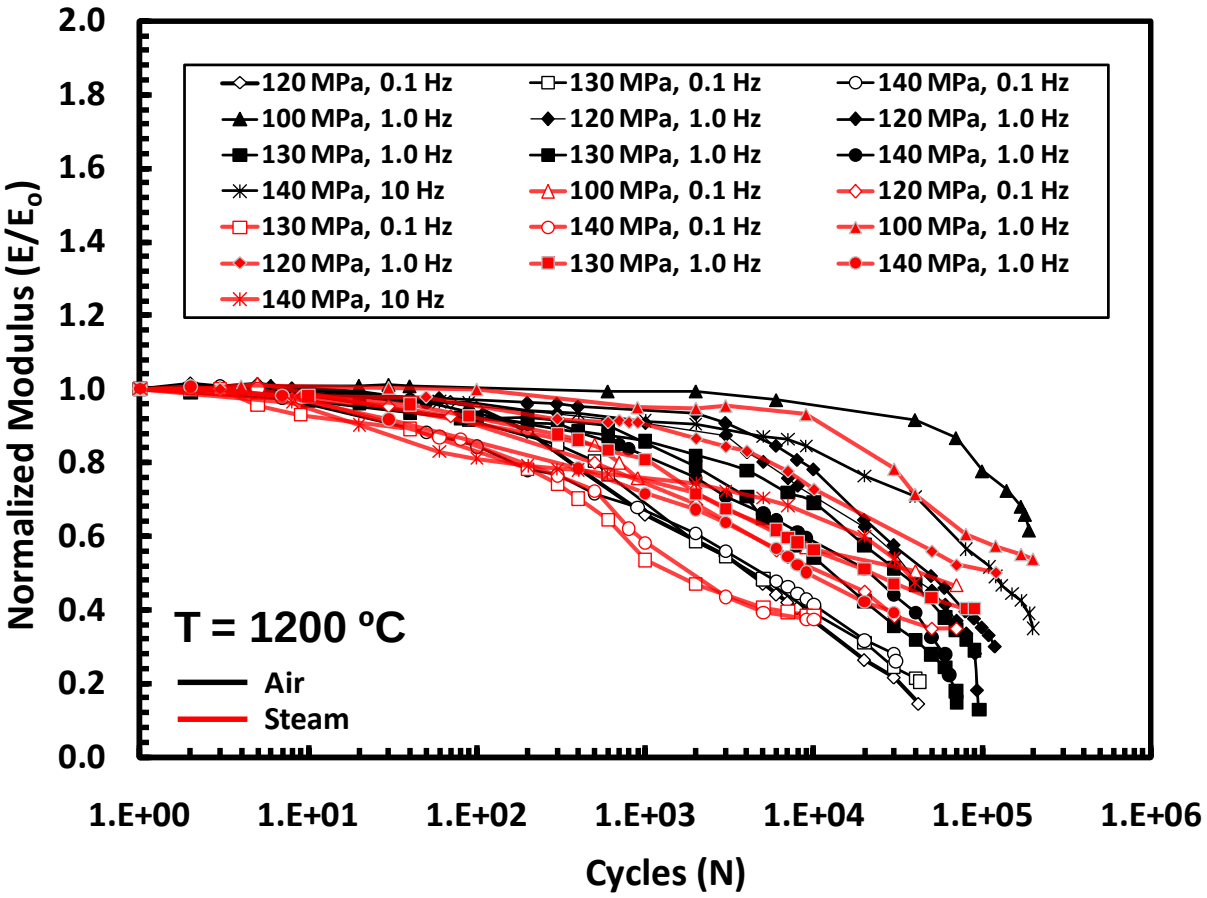

Figure 43: Normalized modulus vs. fatigue cycles for the Hi-Nicalon/PyC/HyprSiC ceramic composites at 1200°C in laboratory air and steam.

Figure 44 presents a comparison of the modulus evolution with fatigue cycles at 1200°C in steam for the Hi-Nicalon/PyC/HyprSiC composite and for the Hi-Nicalon/BN/SiC CMC at [8]. It is seen that the Hi-Nicalon/BN/SiC CMC showed greater decrease in modulus in steam than in air. Conversely, the Hi-Nicalon/PyC/HyprSiC composite showed greater decrease in modulus in air. Yet, at 1200°C in steam the modulus loss exhibited by the Hi-Nicalon/PyC/ HyprSiC composite was 25 to 40% higher than that exhibited by the baseline material.

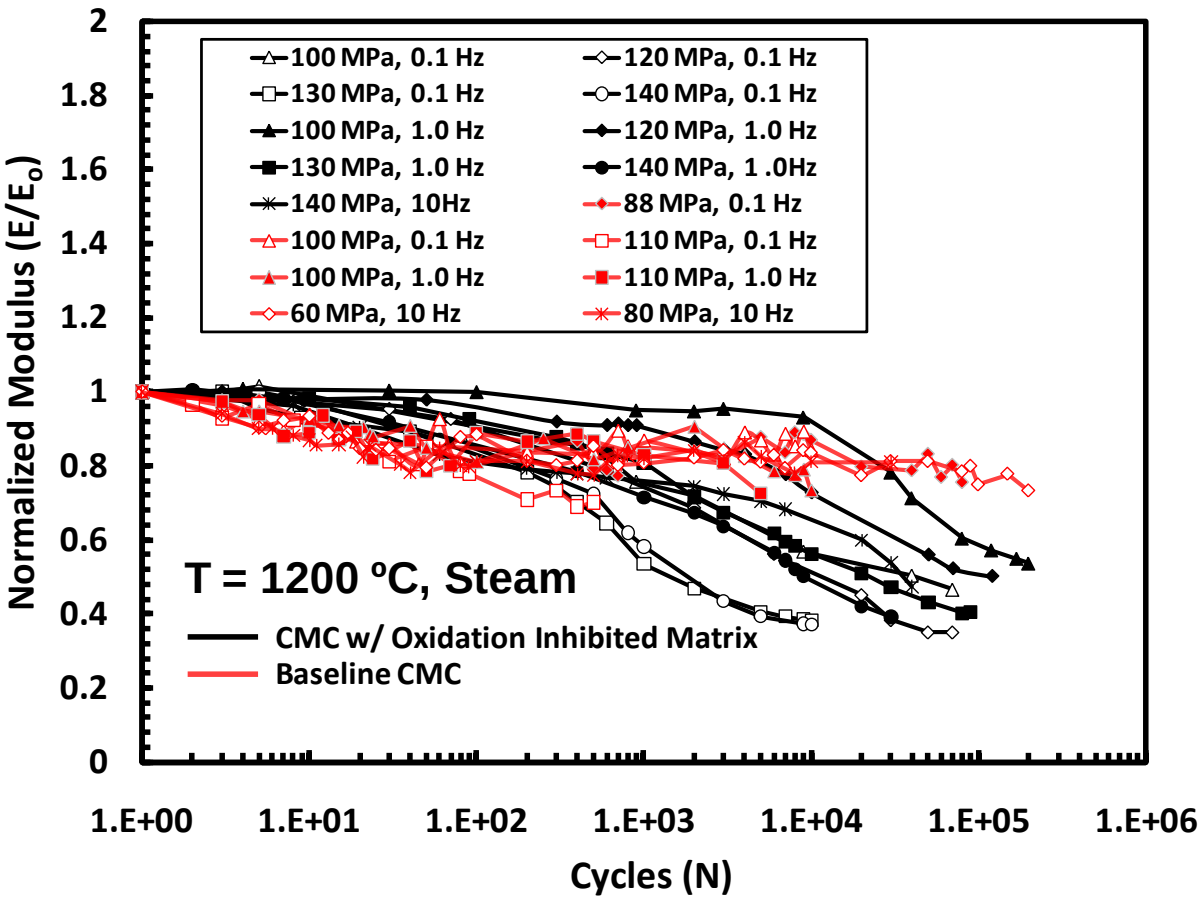

Figure 44: Normalized modulus vs. fatigue cycles for the Hi-Nicalon/PyC/HyprSiC and Hi-Nicalon/BN/SiC ceramic composites at 1200°C in steam. Data for Hi-Nicalon/BN/SiC from Christensen [8].

Next, strain accumulation with fatigue cycles recorded for the Hi-Nicalon/PyC/HyprSiC composite at 1200°C in steam was evaluated (see Figure 45 and Figure 46). It is seen that less strain was accumulated during the fatigue lifetimes in steam than in air. In steam, the largest strain of 0.68% was accumulated in the 120 MPa test at 0.1 Hz. Contrastingly, in air the largest strain accumulation was 2.02%, also produced in the 120 MPa test at 0.1 Hz.

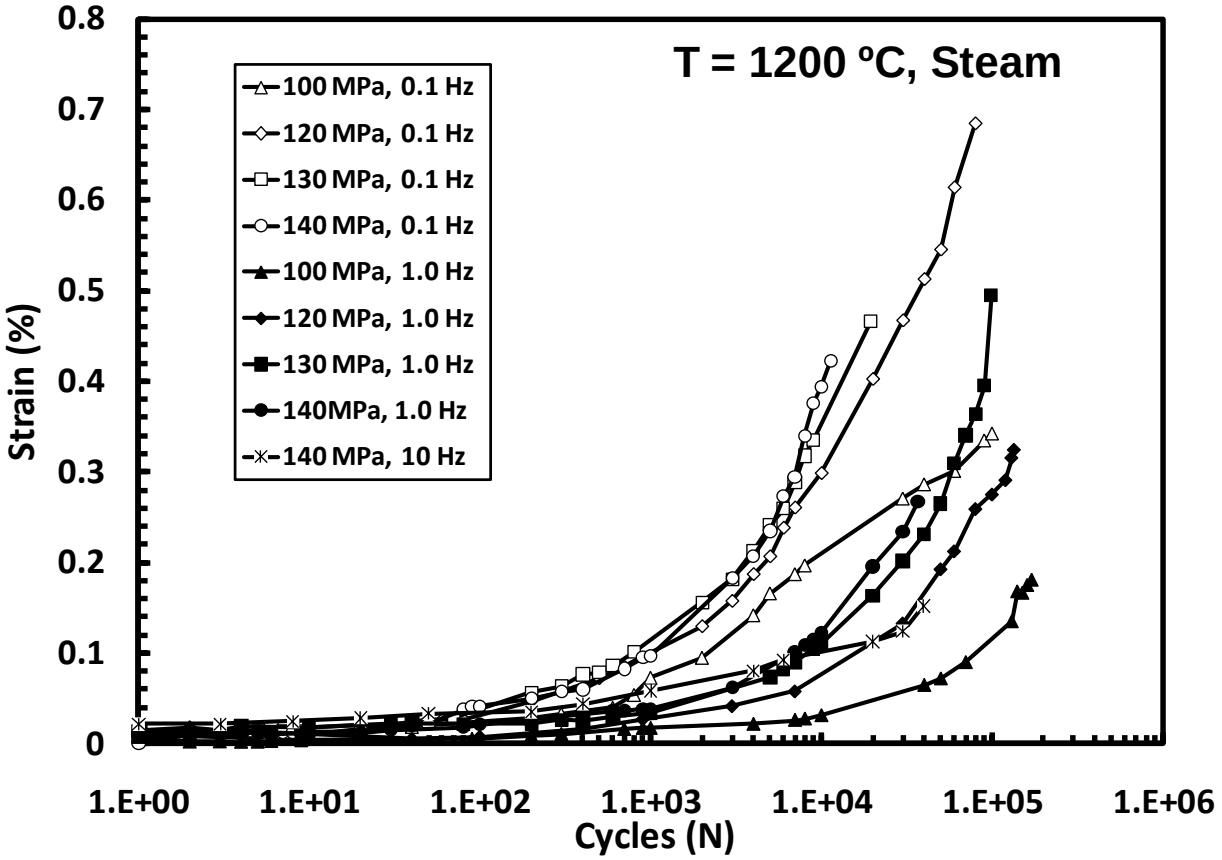

Figure 45: Accumulated strain vs. fatigue cycles for the Hi-Nicalon/PyC/HyprSiC ceramic composite at 1200°C in steam.

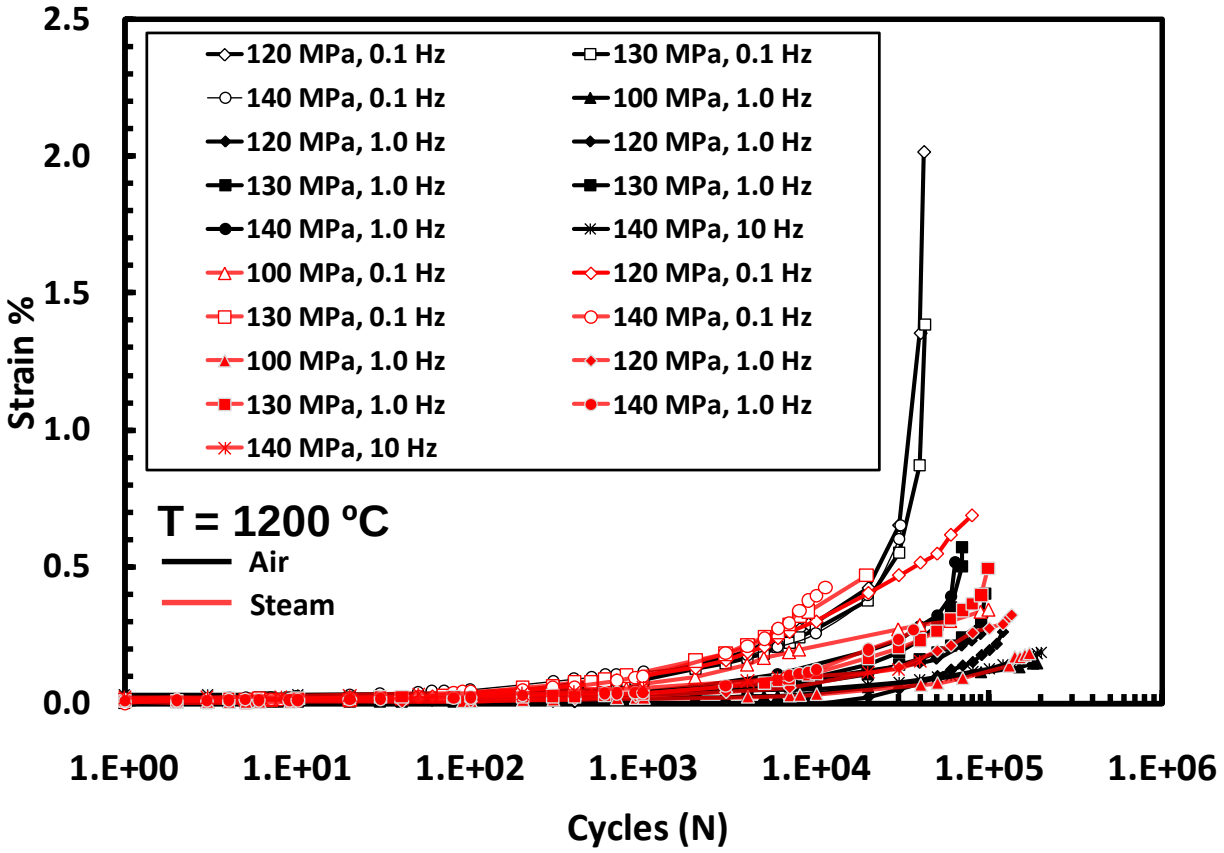

Figure 46: Accumulated strain vs. fatigue cycles for the Hi-Nicalon/PyC/HyprSiC ceramic composite at 1200°C in laboratory air and steam.

Strain accumulation with fatigue cycles recorded for the Hi-Nicalon/PyC/HyprSiC composite at 1200°C in steam is compared with the results obtained for the Hi-Nicalon/BN/SiC CMC by Christensen [8] in Figure 47.

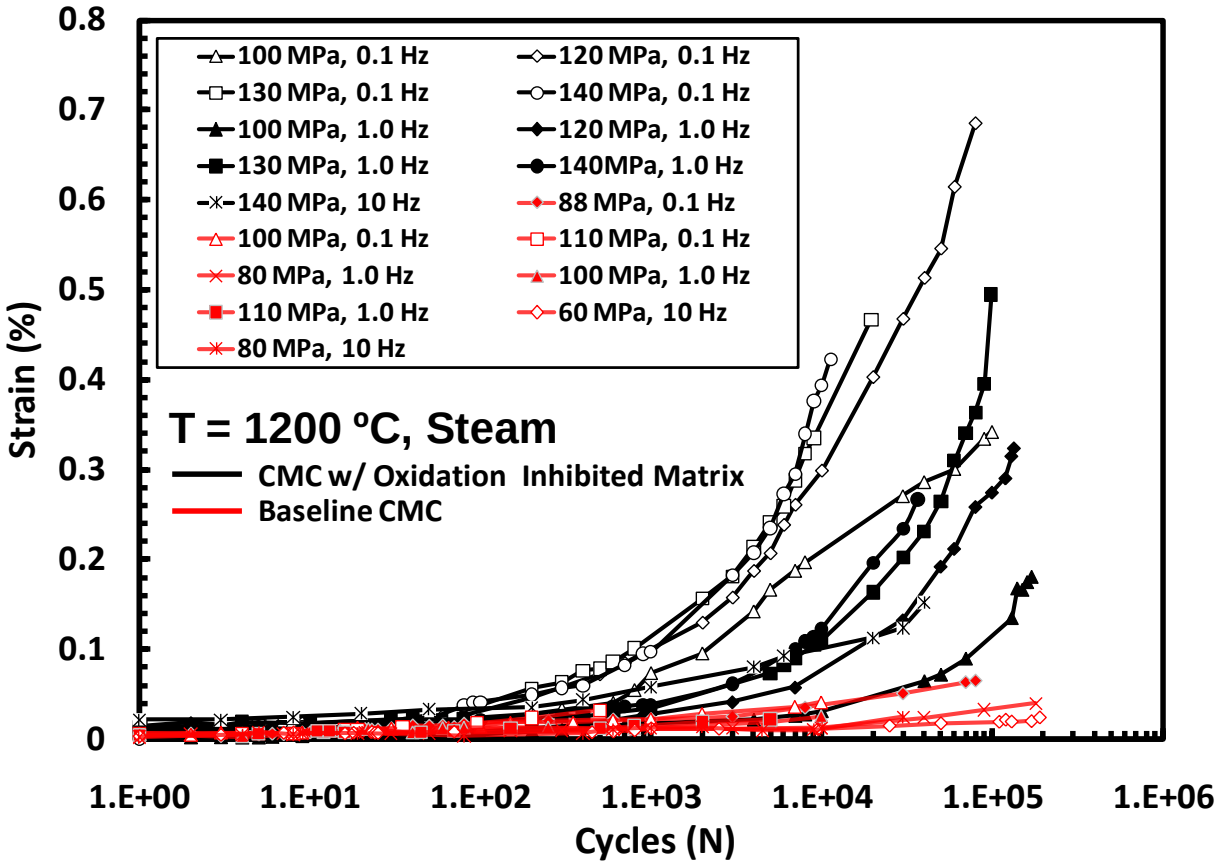

Figure 47: Accumulated strain vs. fatigue cycles for the Hi-Nicalon/PyC/HyprSiC and Hi-Nicalon/BN/SiC ceramic composites at 1200°C in steam. Data for Hi-Nicalon/BN/SiC from Christensen [8].

As was the case at 1200°C in air, in steam much larger strains are accumulated by the Hi-Nicalon/ PyC/HyprSiC CMC than by the baseline material. The strains accumulated by the Hi-Nicalon/ PyC/HyprSiC composite reached 0.68% (120 MPa test at 0.1 Hz), while the largest strain accumulated by the baseline material was only 0.06% (88 MPa test at 0.1 Hz).

Evolution of the hysteresis response of Hi-Nicalon/PyC/HyprSiC with fatigue cycles is typified in Figure 48 and Figure 49, which show hysteresis stress-strain loops for tests conducted in steam at 140 MPa with the frequency of 0.1 Hz and 1.0 Hz, respectively. As in the

case of air environment, the results reveal that ratcheting continues throughout cycling at 1200°C in steam. Furthermore, the results in Figure 48 and Figure 49 demonstrate that the modulus decreases with cycling. As was the case in air, the data in Figure 48 and Figure 49 show that at lower frequencies larger strains are accumulated during a fixed number of cycles. For example consider strains accumulated during 10,000 cycles in tests conducted with different frequencies. The strain accumulated during 10,000 cycles in the 140 MPa test performed at 0.1 Hz approaches 0.4%, while the strain accumulated in the 140 MPa test at 1.0 H is only ~ 0.1%. Note that the rate of strain accumulation with cycling was higher in steam than in air. Specimen tested at 140 MPa at 0.1 Hz in steam accumulated the strain of 0.4% during 10,000 cycles. Conversely the specimen subjected to the 140 MPa test at 0.1 Hz in air accumulated a strain of only 0.25% during the 10,000 cycles.

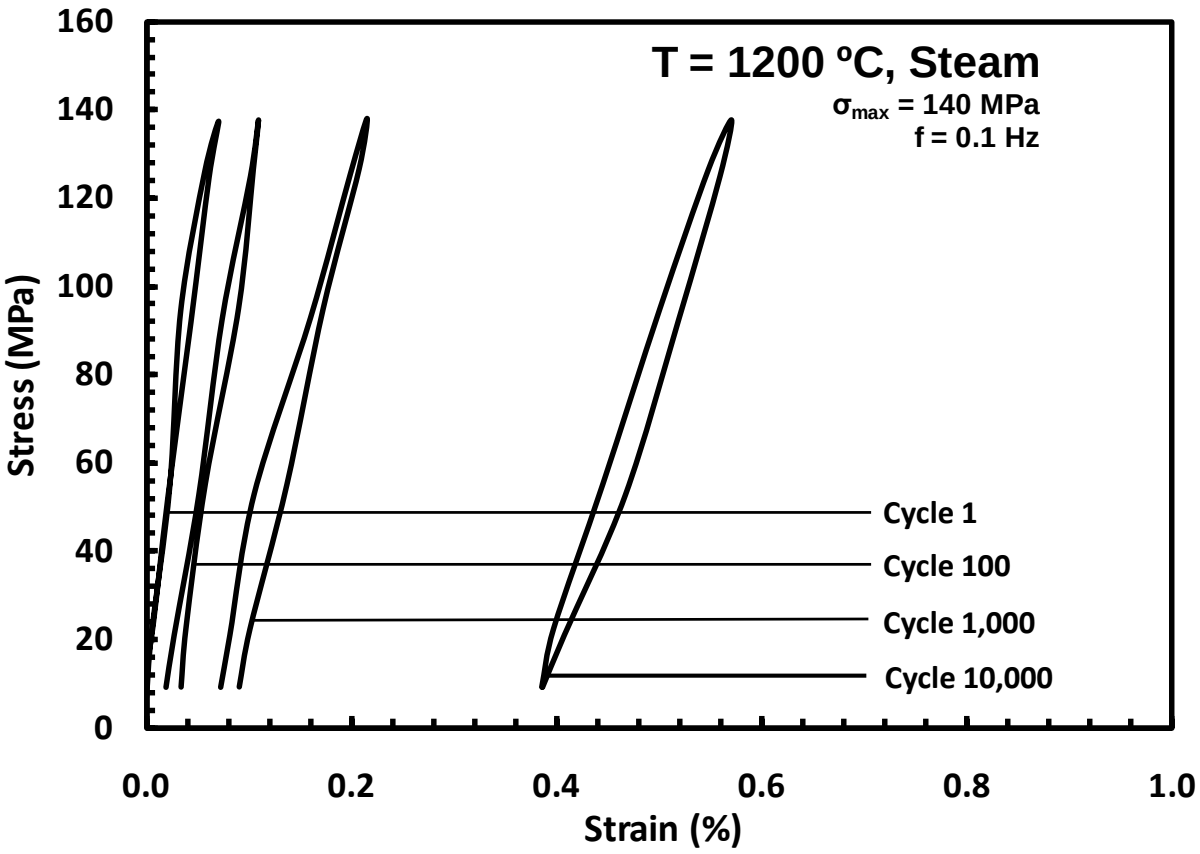

Figure 48: Evolution of Stress-Strain hysteresis response of Hi-Nicalon/PyC/HyprSiC with fatigue cycles in steam at 1200˚C at 0.1 Hz and σ_{max} = 140 MPA.

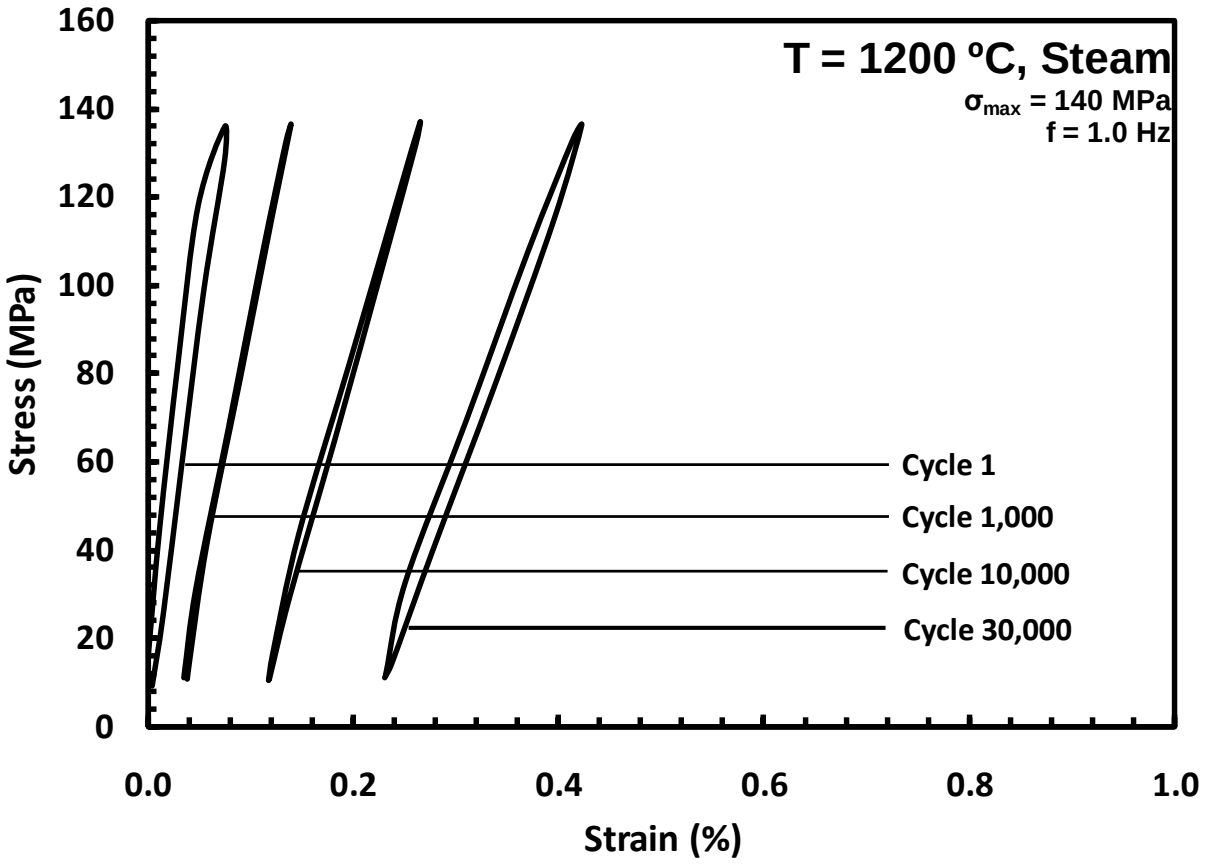

Figure 49: Evolution of Stress-Strain hysteresis response of Hi-Nicalon/PyC/HyprSiC with fatigue cycles in steam at 1200˚C at 0.1 Hz and σ_{max} = 140 MPA.

Maximum and minimum cyclic strains as function of cycle number for fatigue tests conducted at 1200°C in steam at 140 MPa and at frequencies of 0.1 Hz and 1.0 Hz are shown in Figure 50 and Figure 51, respectively. It is seen in Figures x and y that the difference between the maximum and minimum strains for a given cycle increases with continued cycling. The cyclic softening is taking place.

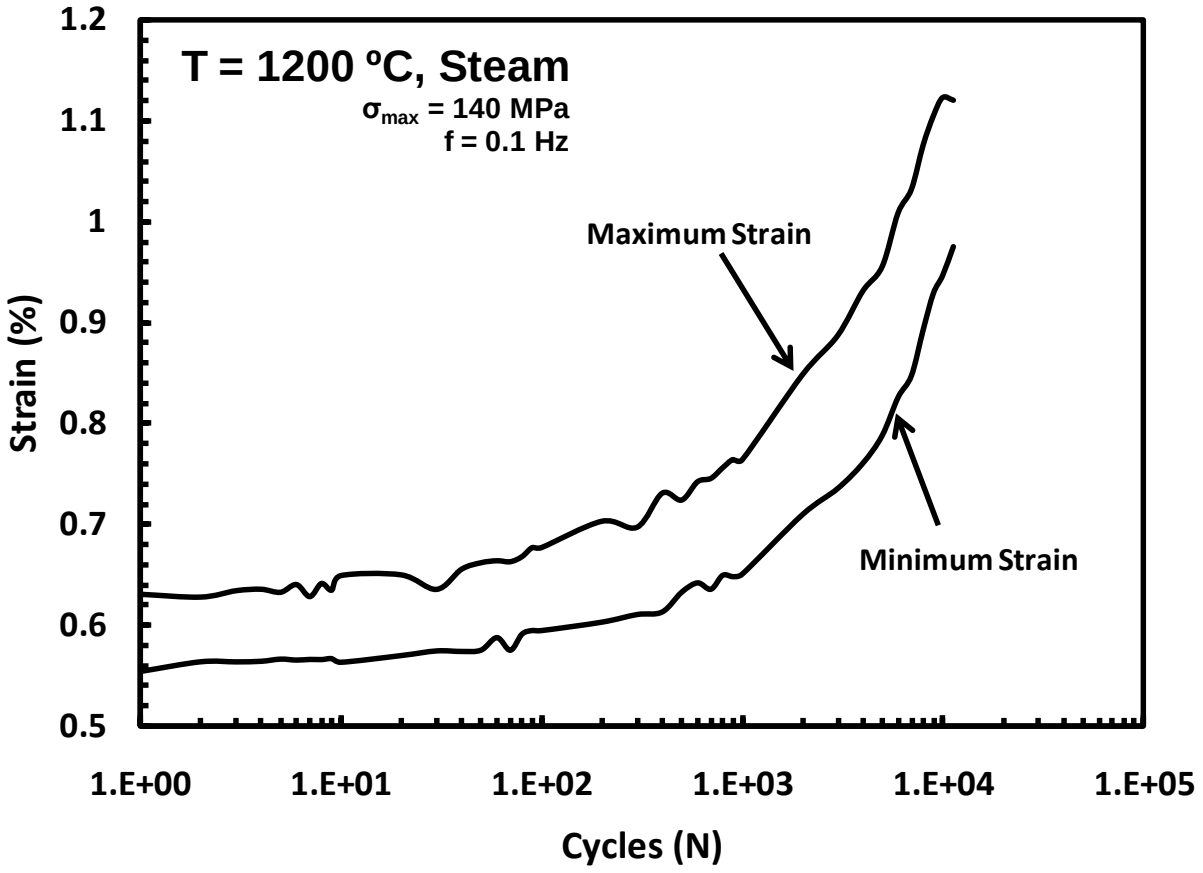

Figure 50: Maximum and minimum strain as a function of cycling at 0.1 Hz in steam at 1200˚C, σ_{max} = 140 MPa.

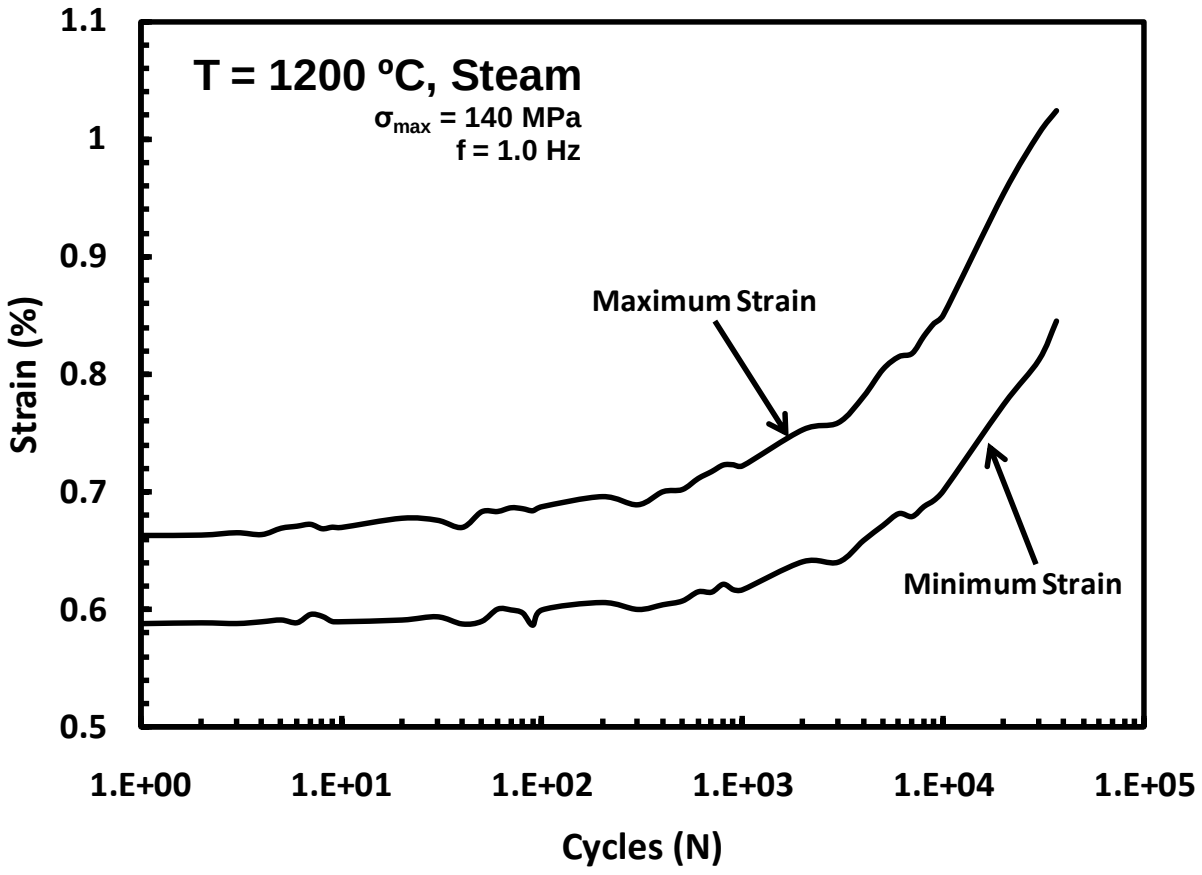

Figure 51: Maximum and minimum strain as a function of cycling at 1.0 Hz in steam at 1200˚C, σ_{max} = 140 MPa.

5.6 Effect of Prior Fatigue on Tensile Properties

All specimens that achieved fatigue run-out were subjected to tensile tests to failure in order to measure the retained tensile properties. The tensile tests on the run-out specimens were performed at 1200°C in air. Retained strength and stiffness of the run-out specimens are summarized in Table 17. It is seen that all specimens subjected to prior fatigue suffered a

considerable loss of strength. The specimen subjected to prior fatigue at 100 MPa and 0.1 Hz in steam retained 74.8% of its tensile strength. The specimen subjected to prior fatigue at 100 MPa and 1.0 Hz in air retained 42% of its tensile strength. The specimens subjected to prior fatigue at 100 MPa and 1.0 Hz in steam retained 60% of its tensile strength. The specimen pre-fatigued at 10 Hz in air also retained 60% of its tensile strength. Stiffness loss was observed in all cases. Stiffness reduction was 17% for specimen pre-fatigued at 100 MPa and 1.0 Hz in air and nearly 32% for specimen pre-fatigued at 100 MPa and 1.0 Hz in steam. In the case of specimen pre-fatigued at 10 Hz, the stiffness loss was a significant 56%.

Table 17: Retained properties of the Hi-Nicalon/PyC/HyprSiC specimens subjected to prior fatigue in laboratory air and in steam at 1200˚C.

Fatigue Stress (MPa)	Fatigue Environment	Retained Strength (MPa)	Strength Retention (%)	Retained Modulus (GPa)	Modulus Retention (%)	Strain at Failure (%)
Prior fatigue at 0.1 Hz						
100	Steam	229.4	74.8	129	62.5	0.604
Prior fatigue at 1.0 Hz						
100	Air	130.0	42.4	171.5	83.1	0.196
100	Steam	183.1	59.7	141.6	68.6	0.345
Prior fatigue at 10 Hz						
140	Air	186.7	60.9	91.0	44.1	0.374

The tensile stress-strain curves obtained for the pre-fatigued specimens are presented in Figure 52 together with the stress-strain curves obtained for the as-processed specimens. The tensile stress-strain curves obtained for the pre-fatigued specimens are qualitatively similar to those produced by the as-processed specimens. The stress-strain curve produced by the specimen pre-fatigue at 10 Hz represents an exception. In this case the stress-strain curve does

not have a distinctive bi-linear character. Since the pre-fatigue maximum stress (140 MPa) was much higher than the proportional limit, the majority of the matrix cracking occurred during the pre-fatigue test which eliminated the bilinear appearance in the stress-strain diagram for the tension to failure test. From this, it appears that fatigue at 10 Hz caused significant damage to the matrix, which is consistent with the low retained modulus.

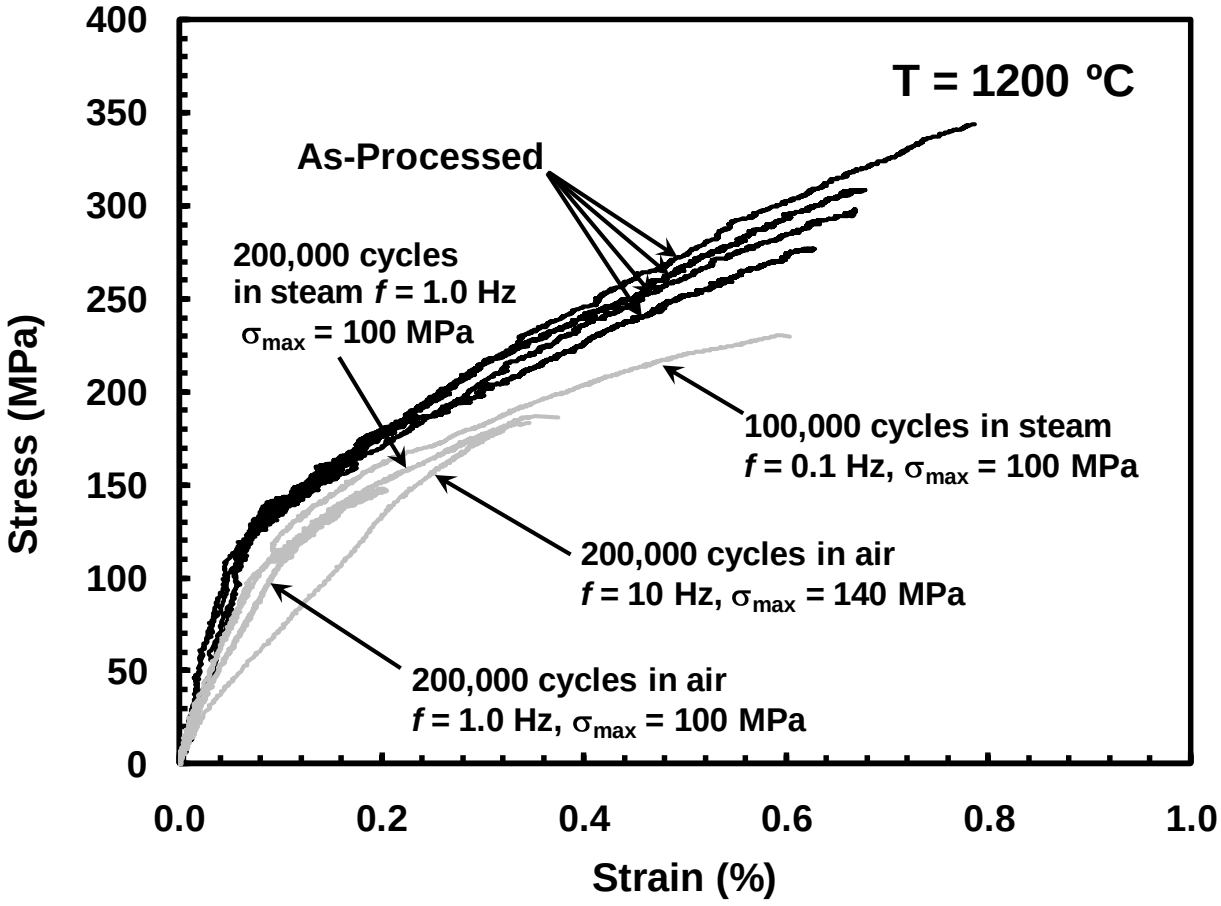

Figure 52: Tensile stress-strain curves obtained for the Hi-Nicalon/ PyC/HyprSiC specimens subjected to prior fatigue at 1200°C. Tensile stress-strain curves for the as-processed specimens are shown for comparison.

The retained properties measured for the Hi-Nicalon/PyC/HyprSiC specimens are compared with those reported by Christensen [8] for the baseline material in Table 18. Data in Table 18 reveals that the baseline material shows much better strength retention than the CMC with the oxidation inhibited matrix. Nearly all baseline specimens subjected to prior fatigue retained 100% of their tensile strength, irrespective of the fatigue stress level, test environment, or fatigue frequency. In contrast, the pre-fatigued Hi-Nicalon/PyC/HyprSiC specimens lost 25 to 60% of their tensile strength. The baseline composite also exhibited higher retained stiffness. Stiffness loss was limited to 12% in the case of the Hi-Nicalon/BN/SiC specimens. Yet, the pre-fatigued Hi-Nicalon/PyC/HyprSiC specimens lost 17 to 66% of their stiffness.

Table 18: Retained tensile properties of the Hi-Nicalon/ PyC/HyprSiC and Hi-Nicalon/BN/SiC specimens subjected to prior fatigue in laboratory air and in steam environment at 1200°C. Data for Hi-Nicalon/BN/SiC from Christensen [8].

Fatigue Stress (MPa)	Fatigue Environment	Retained Strength (MPa)	Strength Retention (%)	Retained Modulus (GPa)	Modulus Retention (%)	Strain at Failure (%)
Prior fatigue at 0.1 Hz						
Hi-Nicalon/PyC/HyprSiC						
100	Steam	229.4	74.8	129	62.5	0.604
Hi-Nicalon/BN/SiC						
110	Air	242.5	100	248.5	100	0.384
100	Air	277.5	100	229.8	97.3	0.746
Prior fatigue at 1.0 Hz						
Hi-Nicalon/PyC/HyprSiC						
100	Air	130.0	42.4	171.5	83.1	0.196
100	Steam	183.1	59.7	141.6	68.6	0.345
Hi-Nicalon/BN/SiC						
100	Air	248.2	100	208.3	88.2	0.496
80	Air	267	100	224.1	94.9	0.503
80	Steam	229.3	100	221	93.6	0.395
Prior fatigue at 10 Hz						
Hi-Nicalon/PyC/HyprSiC						
140	Air	186.7	60.9	91.0	44.1	0.374
Hi-Nicalon/BN/SiC						
80	Air	257.9	100	273.8	100	0.614
60	Steam	205.3	94.6	211.4	89.5	0.305

The tensile stress-strain curves produced by the pre-fatigued Hi-Nicalon/PyC/HyprSiC specimens are compared to those produced by the pre-fatigued Hi-Nicalon/BN/SiC specimens in Figure 53. It is seen that prior fatigue had no qualitative effect on the bi-linear nature of the tensile stress-strain curves in the case of the baseline CMC. The same observation can be made for the Hi-Nicalon/PyC/HyprSiC composite. Of course, as stated above, the Hi-

Nicalon/PyC/HyprSiC specimen pre-fatigued at 10 Hz represents an exception. Results in Figure 53 further emphasize a much better strength retention exhibited by the baseline CMC.

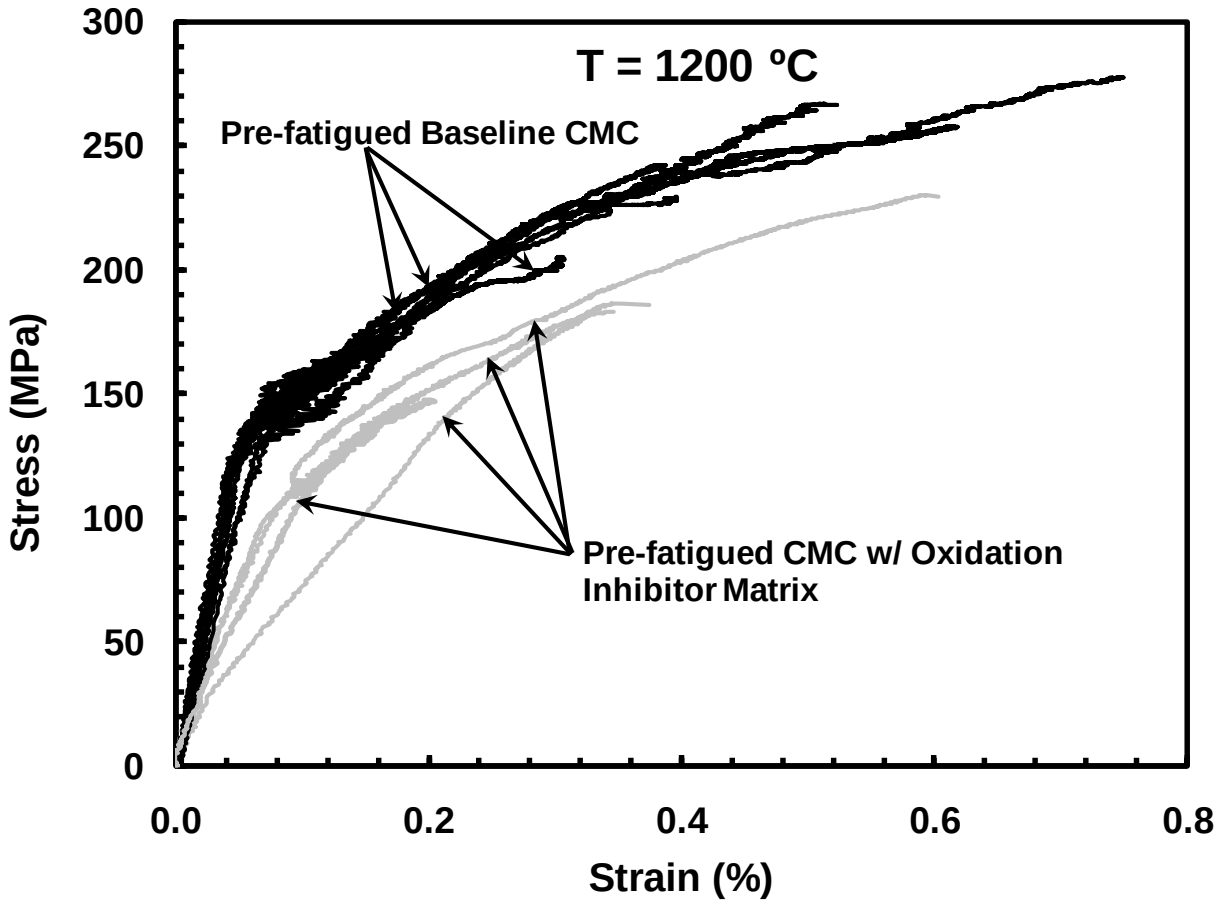

Figure 53: Tensile stress-strain curves obtained for the Hi-Nicalon/ PyC/HyprSiC and Hi-Nicalon/BN/SiC specimens subjected to prior fatigue at 1200°C. Data for Hi-Nicalon/BN/SiC from Christensen [8].

5.7 Microstructural Characterization

The following sections present a qualitative analysis of the fracture surfaces of the selected Hi-Nicalon/PyC/HyprSiC failed specimens as well of the as-processed untested material, which was accomplished using both an optical microscope and a scanning electron microscope (SEM).

5.7.1 Microstructure of the As-Processed Material

Sections of material from the three original panels were mounted and polished for examination under the SEM. Similar microstructural characteristics were noted for all three panels (see Figure 54 through Figure 56). Large voids are seen in all as-processed samples. In addition, a layered matrix structure can be seen in all as-processed specimens (see Figure 55B). A dual-layer coating of boron carbide and pyrolytic carbon is also seen in all as-processed specimens (Figure 54B).

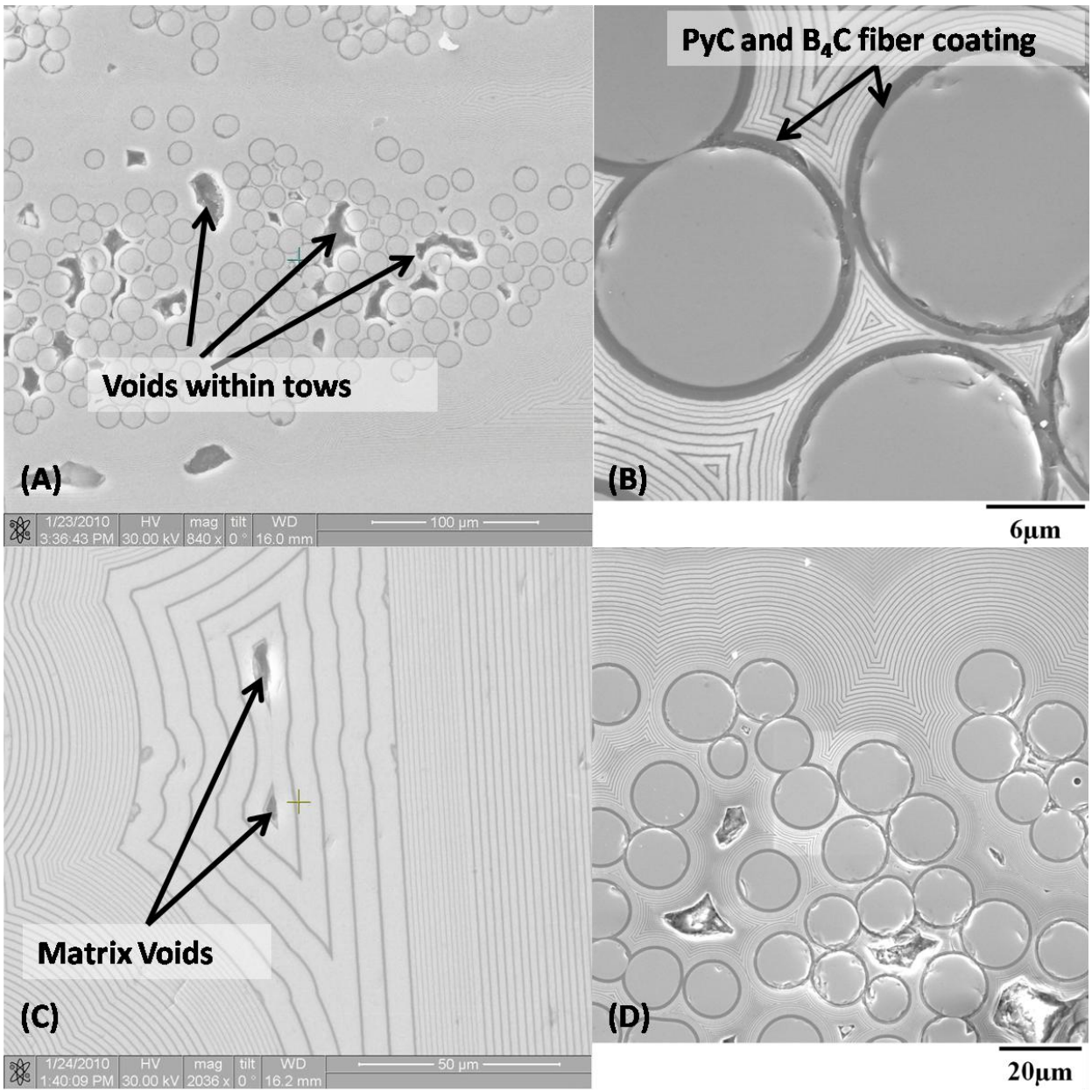

Figure 54: SEM micrographs of the as-processed material from Panel 5 showing: A) voids between fiber tows, B) duel-layer BC and PyC fiber coating, C) matrix voids and layer matrix structure, and D) fibers and layered structure of matrix.

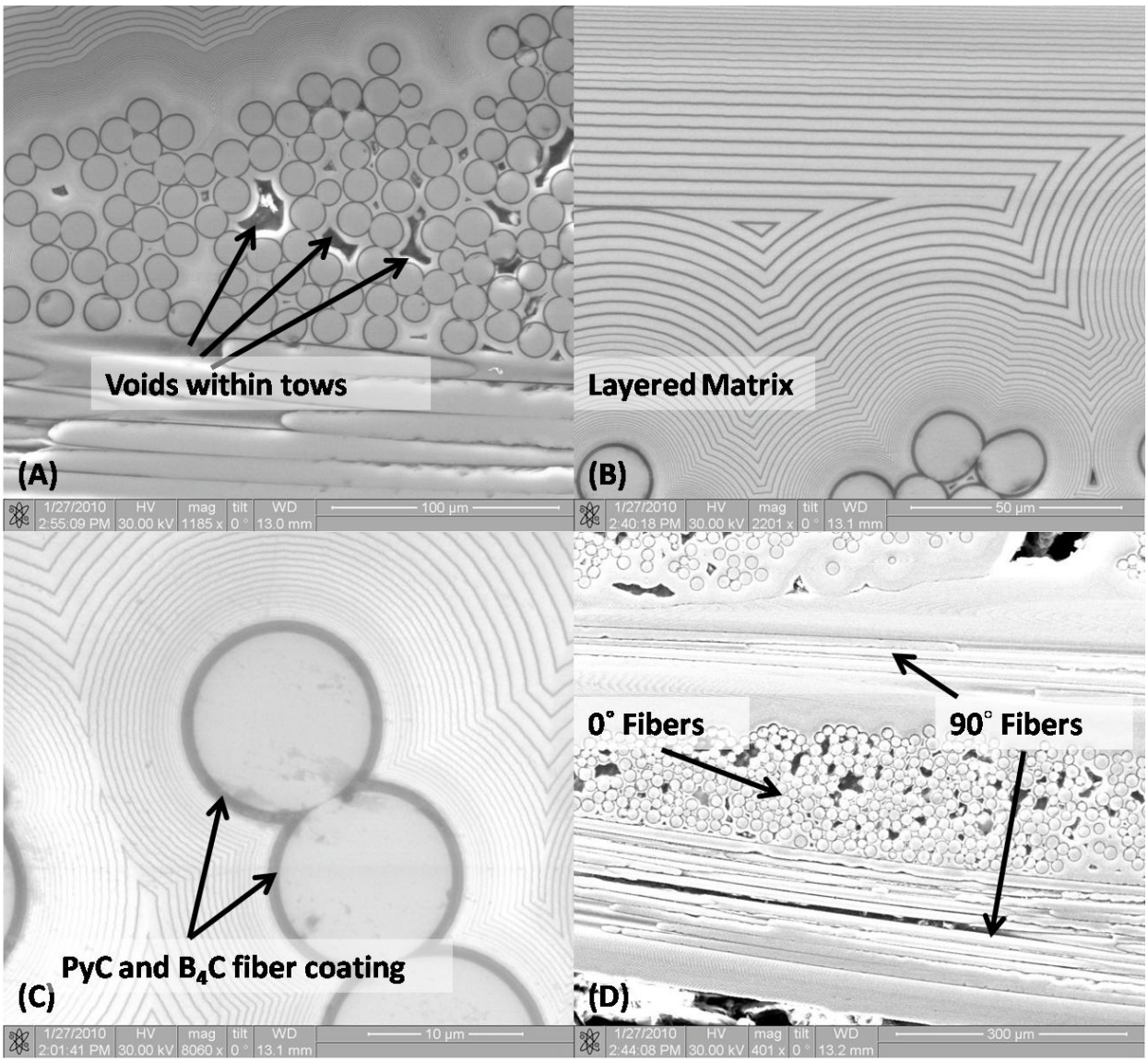

Figure 55: SEM micrographs of the as-processed material from Panel 6 showing: A) voids between fiber tows, B) layered matrix structure, C) duel-layer BC and PyC fiber coating, and D) 0˚ and 90˚ fibers.

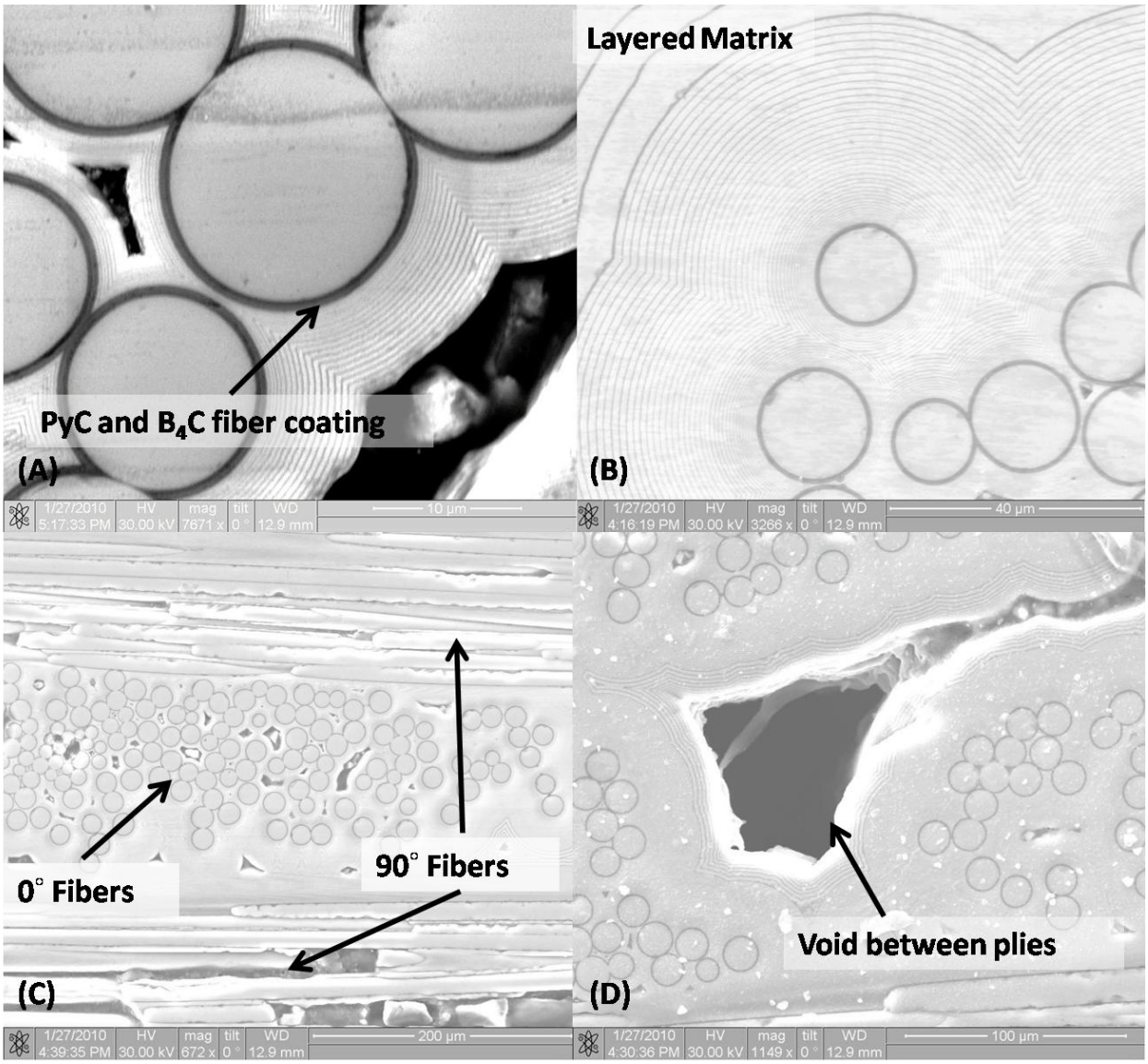

Figure 56: SEM micrographs of the as-processed material from Panel 7 showing: A) duel-layered BC and PyC fiber coating, B) the layered matrix structure, C) 0˚ and 90˚ fibers, D) a large void between plies.

5.7.2 Microstructure of Specimens Tested in Tension to Failure

The fracture surfaces of specimens subjected to tension to failure tests were examined using the optical microscope and the SEM. The optical micrographs are shown in Figure 57 through Figure 60. It is noteworthy that only minimal fiber pull-out is seen in fracture surfaces.

The fracture surfaces are nearly normal to the loading direction (or the 0° fiber tows). The side views of the tensile specimens in Figure 57 through Figure 60 show no signs of delamination.

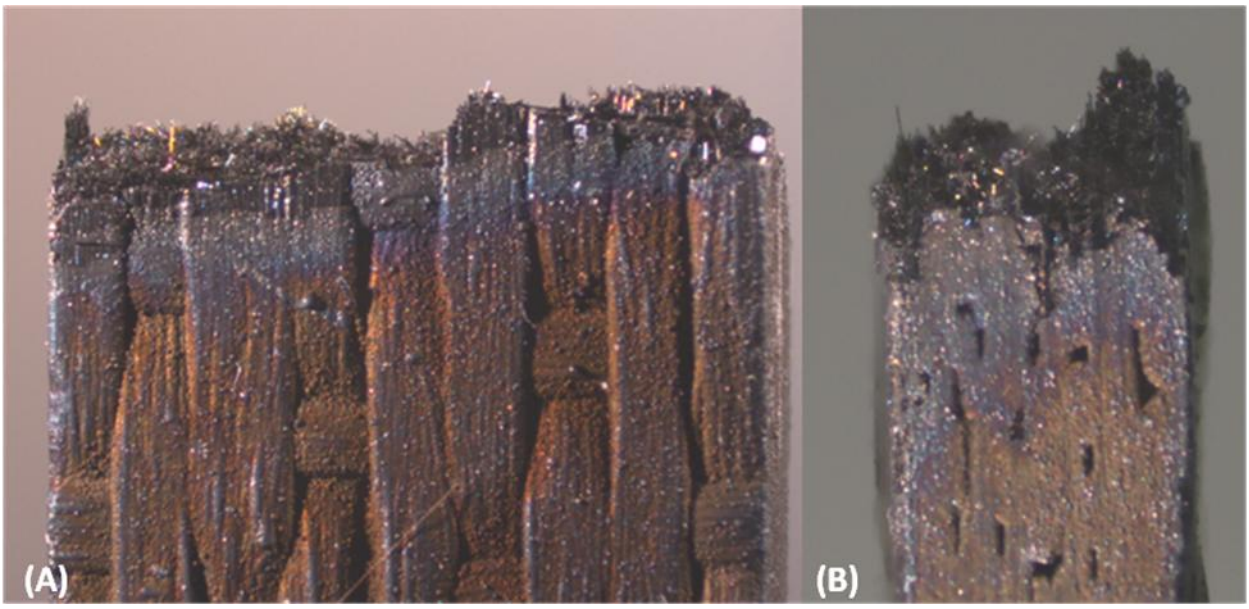

Figure 57: Optical micrographs of the fracture surfaces produced in tensile test to failure conducted at 0.05 mm/s at 1200°C in air on specimen P5-2.

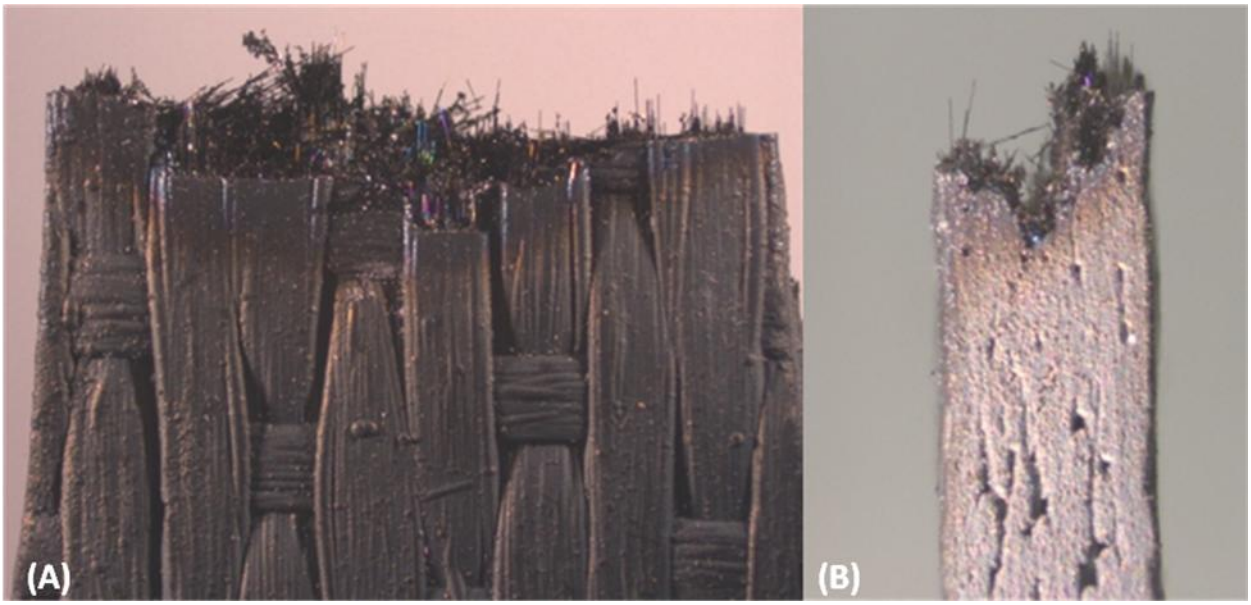

Figure 58: Optical micrographs of the fracture surfaces produced in tensile test to failure conducted at 0.05 mm/s at 1200°C in air on specimen P6-1.

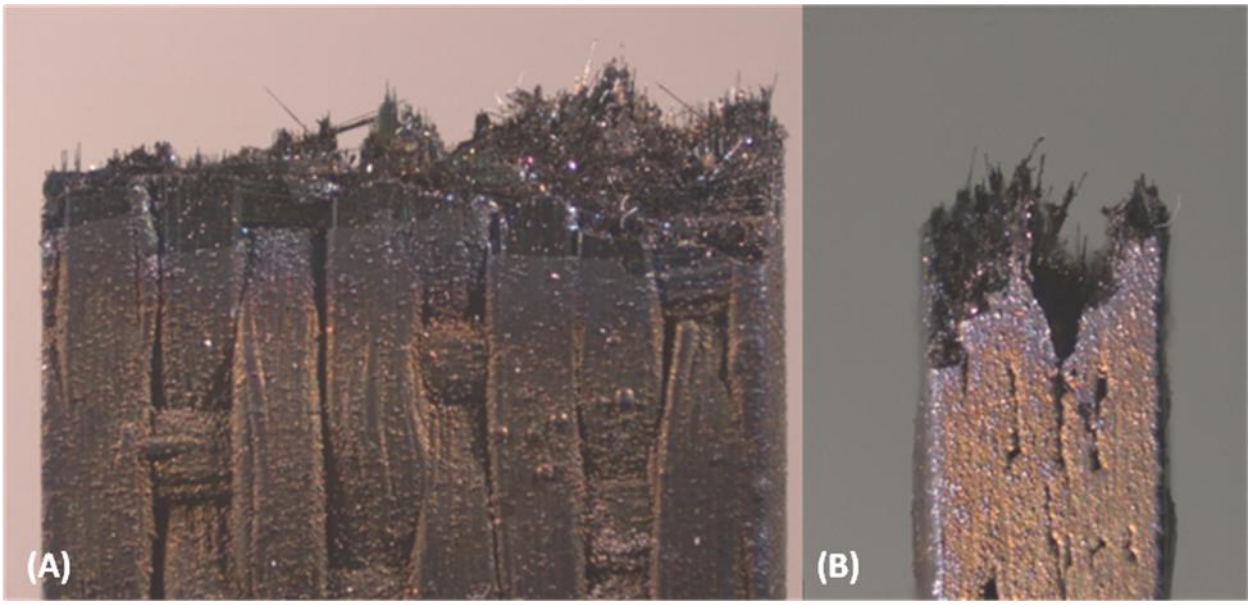

Figure 59: Optical micrographs of the fracture surfaces produced in tensile test to failure conducted at 0.05 mm/s at 1200°C in air on specimen P6-2.

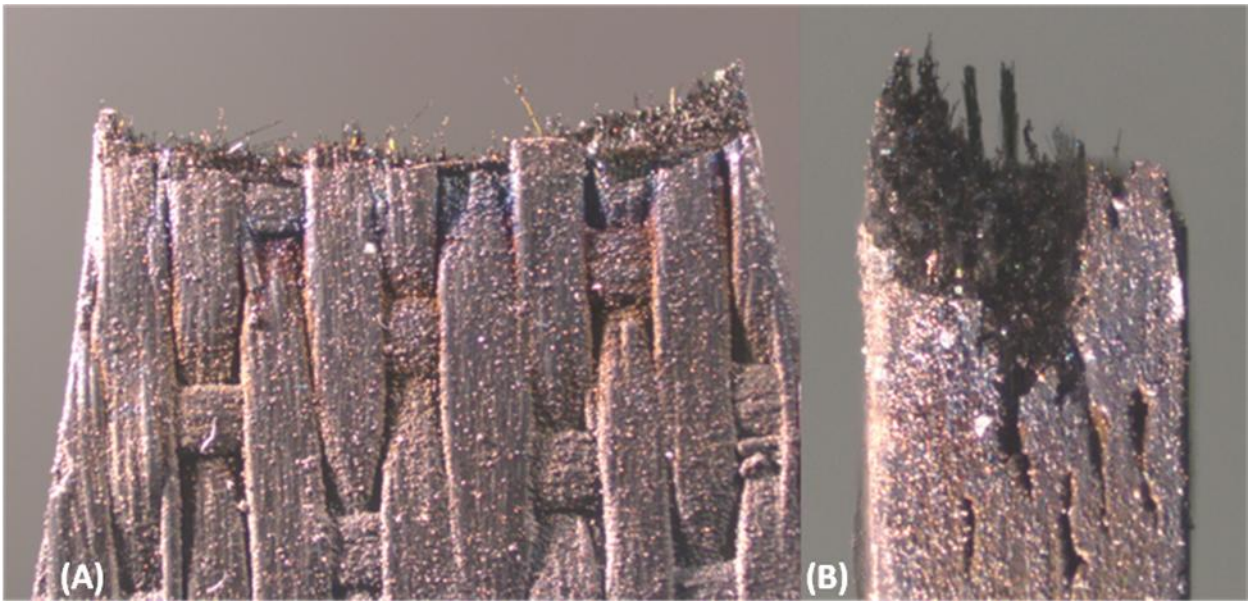

Figure 60: Optical micrographs of the fracture surfaces produced in tensile test to failure conducted at 0.05 mm/s at 1200°C in air on specimen P7-1.

The SEM micrographs of the fracture surface obtained in the tensile test to failure on specimen P6-1 is shown in Figure 61. The fracture surface in Figure 61 shows little evidence of

oxidation. Note that only minimal oxidation could be expected in this case because of the short (< 10 s) duration of the tensile test.

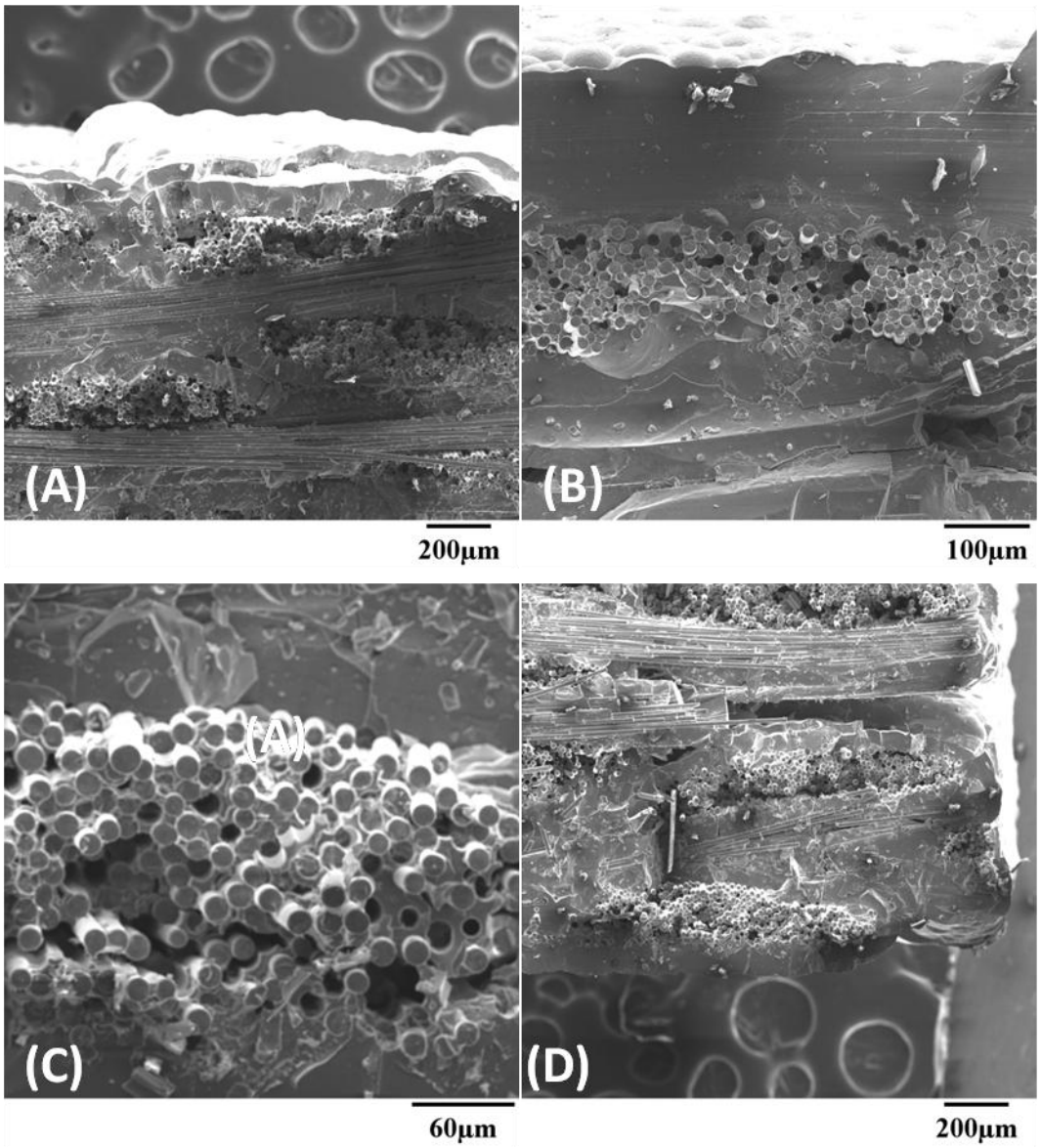

Figure 61: SEM micrograph of the fracture surfaces produced in tensile test to failure conducted at 0.05 mm/s at 1200°C in air on specimen P6-1.

To evaluate the progression of oxidation throughout the specimen P6-1 more thoroughly, the specimen was cut along the specimen axis (also the loading direction). The cut surface was polished and observed under the SEM (see Figure 62 and Figure 63). Figure 62 shows an overview of the specimen microstructure. As expected, only a few minor matrix cracks can be seen in Figure 62. Figure 63 shows a higher magnification view of the interior surface shown in Figure 62. Matrix cracks are clearly visible in Figure 63. SEM micrograph in Figure 63A shows a crack propagating through the matrix and to a fiber, which in turn appears to be more affected by the oxidizing environment (i. e. air at 1200°C). It appears that glass has formed around this particular fiber.

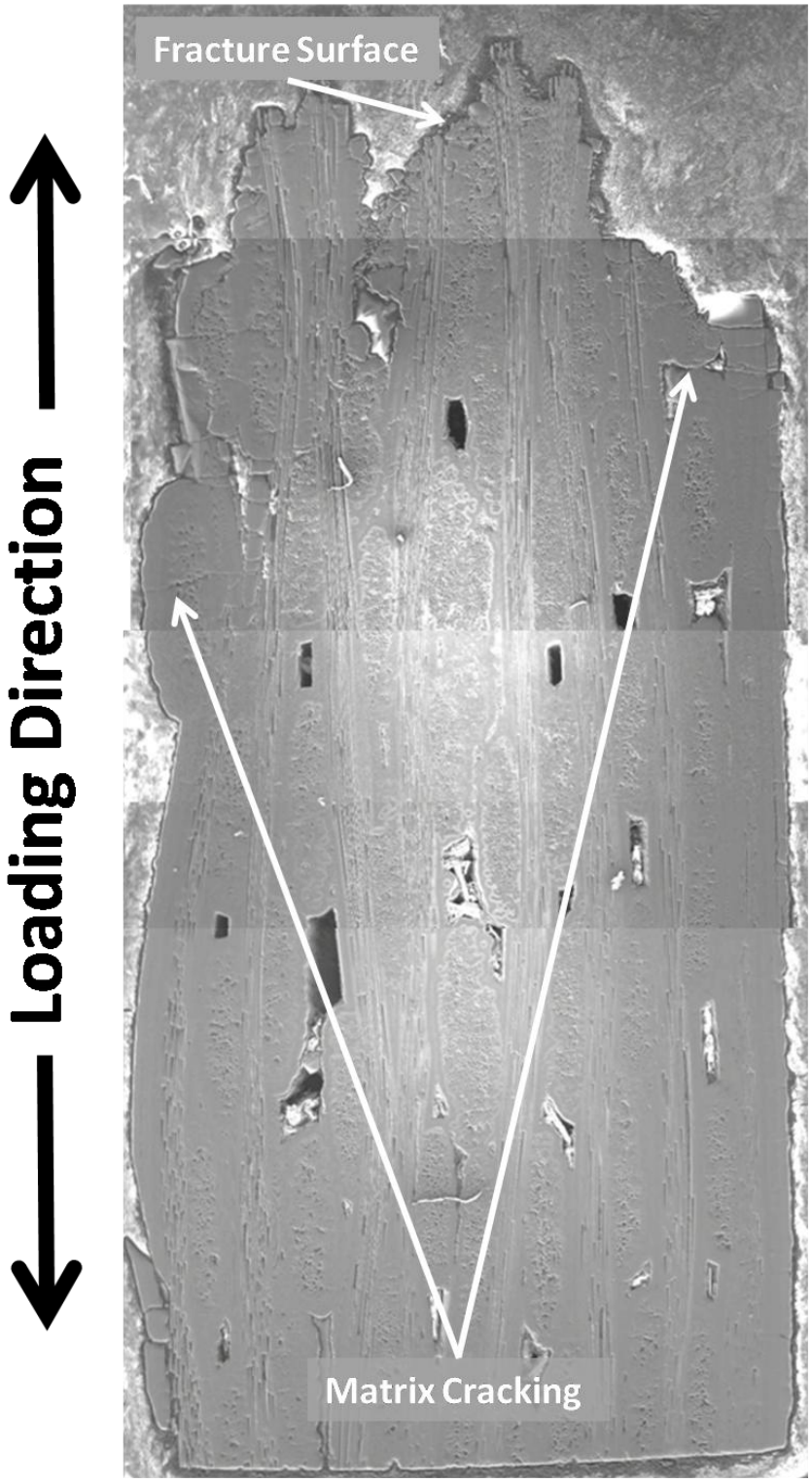

Figure 62: SEM micrograph of the specimen P6-1 tested in tension to failure at 1200°C showing an interior surface parallel to the specimen axis.

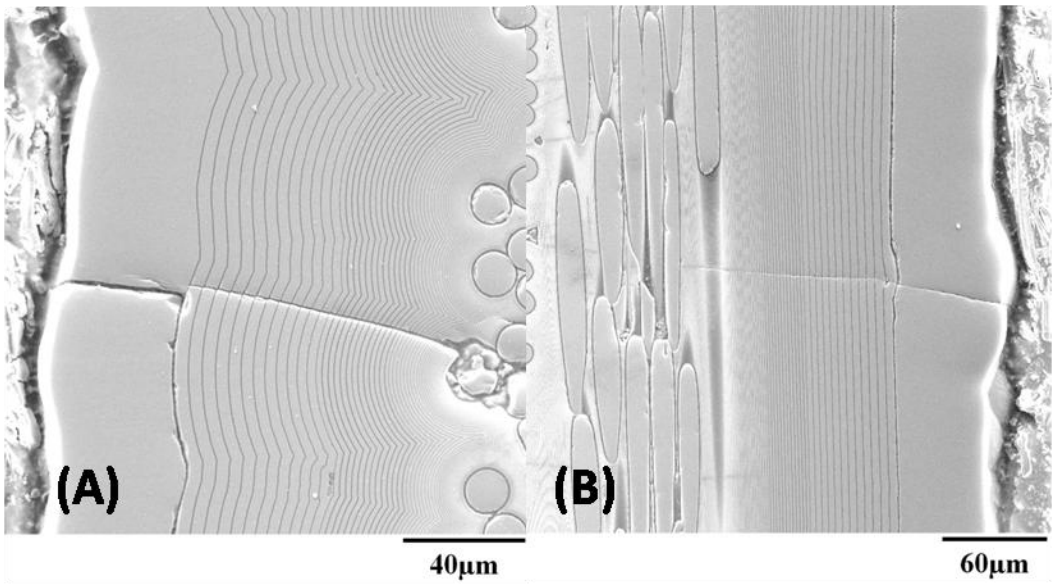

Figure 63: Higher magnification SEM micrographs of the specimen P6-1 tested in tension to failure at 1200°C showing an interior surface parallel to the specimen axis.

5.7.3 Microstructure of the Specimens Tested at 0.1 Hz

The fracture surfaces of specimens subjected to fatigue at 0.1 Hz with the maximum stress of 140 MPa were examined. The optical micrographs of the specimen P6-7 tested in air are shown in Figure 64. The optical micrographs of the specimen P6-8 tested in steam are shown in Figure 65. The fracture surface of all specimens tested at 0.1 Hz (also see Appendix A) shows more fiber pullout than specimens tested at 1.0 and 10 Hz. A possible reason for more fiber pullout at 0.1 Hz stems from the ability of the fiber coatings to perform as intended. As the load is applied at 0.1 Hz, matrix cracks are opened for a longer period of time allowing the crack surface to be exposed to the outside environment longer. The longer exposure to the oxidative environment results in the oxidation inhibited matrix forming more glass which seals off the fibers and fiber coatings from the outside environment. This allows the fibers and the

fiber coatings to perform as intended which is to create a weak fiber/matrix interface. Since the weak fiber/matrix interface stays intact longer more fiber pullout is observed at 0.1 Hz.

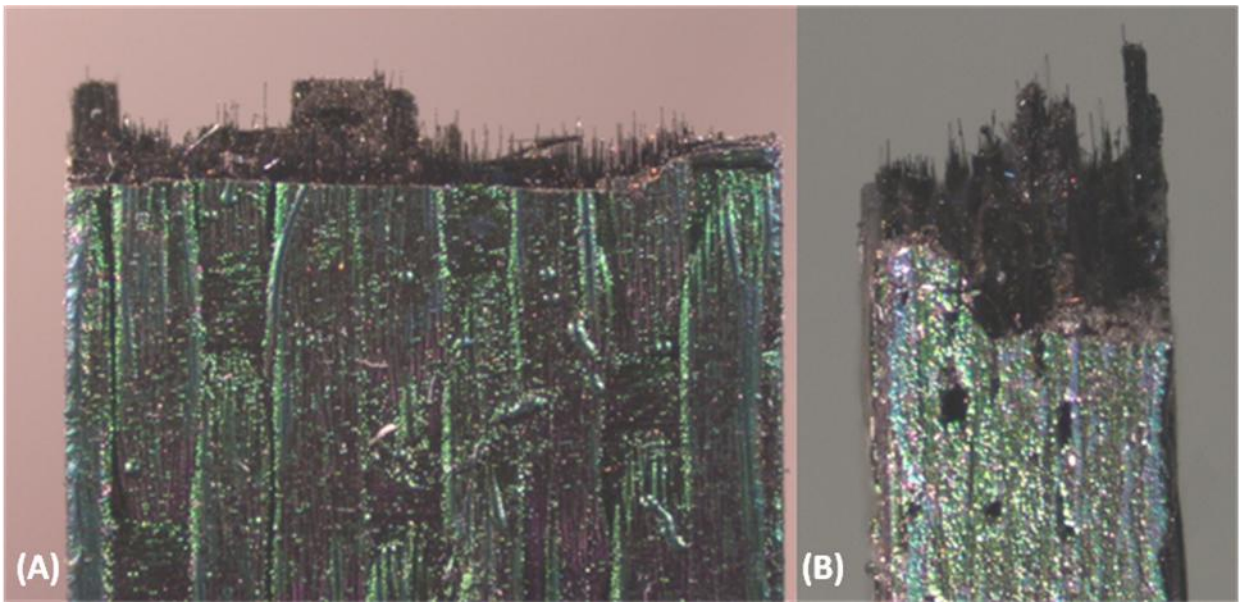

Figure 64: Optical micrographs of specimen P6-7 tested in fatigue at 0.1 Hz in air at 1200˚C. σ_{max} = 140 MPa, N_f = 30,712, t_f = 85.3 h.

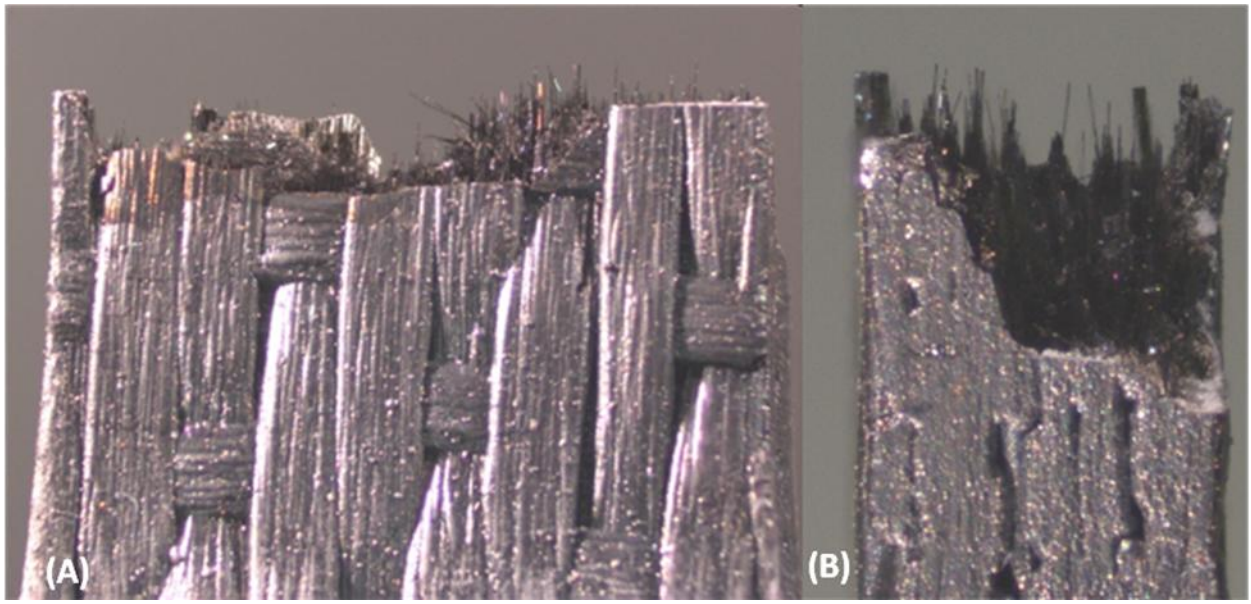

Figure 65: Optical micrograph of specimen P6-8 fatigue tested at 0.1 Hz in steam at 1200˚C. σ_{max} = 140 MPa, N_f = 11,323, t_f = 31.5 h.

The SEM micrographs of the fracture surfaces produced in the 140 MPa fatigue tests conducted at 0.1 Hz in air and in steam are shown in Figure 66 and Figure 67, respectively. Figure 66 B, C, and D show some areas of relatively fibrous fracture in the interior of the fracture surface. Figure 66A shows signs of oxidation near the edges of the fracture surface. Micrographs in Figure 67 show considerable amount of oxidative damage in the fracture surface of specimen P6-8 tested in steam. It is seen in Figure 67A that glass has formed near the edges of the fracture surface. Glass formations are also seen in Figure 67 B, C, and D. Glass (or silica) is a product of oxidation occurring in the Si-containing material tested steam in, a highly oxidizing environment.

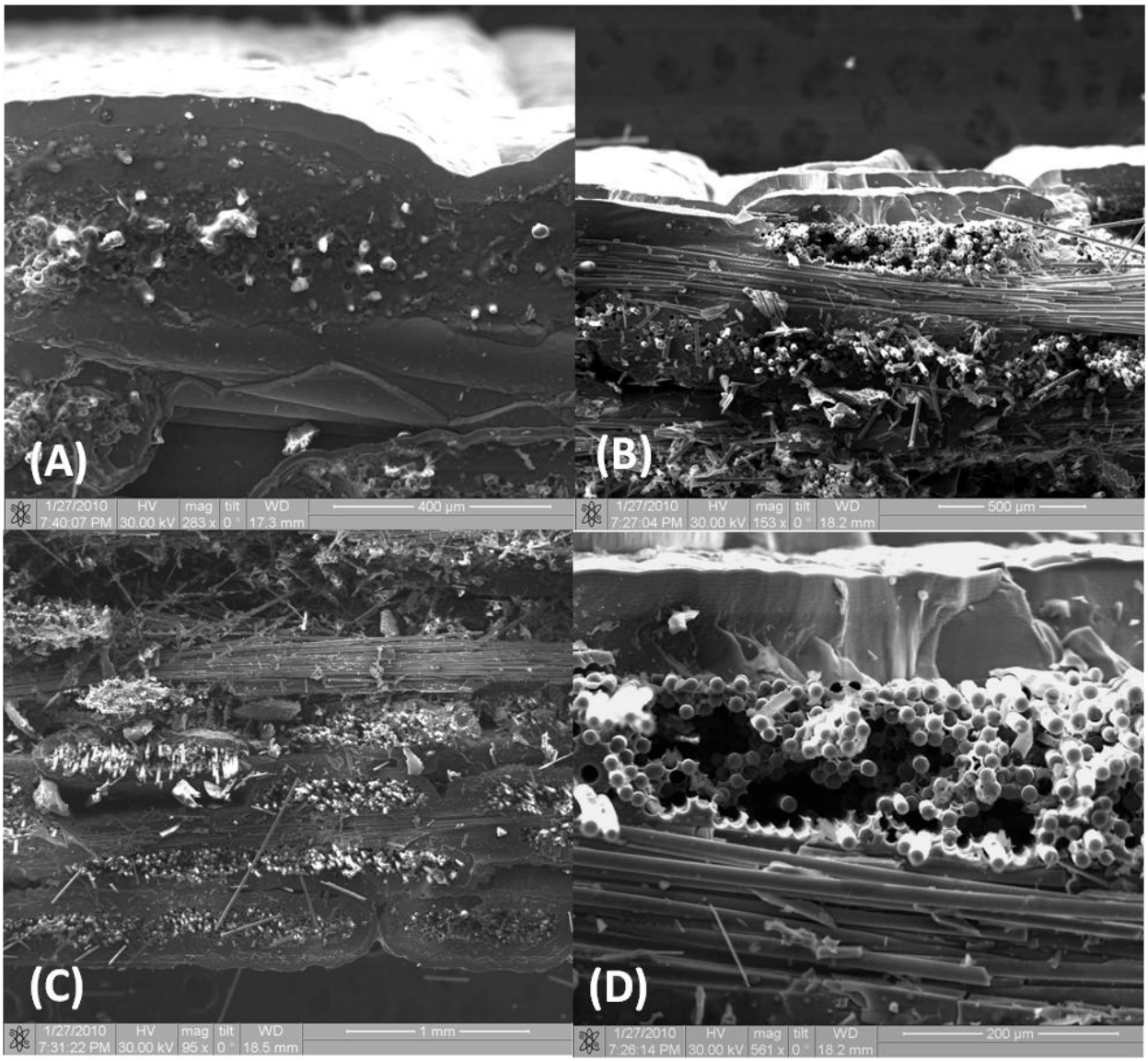

Figure 66: SEM micrographs of fracture surface for specimen P6-7 tested in fatigue at 0.1 Hz in air at 1200˚C, σ_{max} = 140 MPa, N_f = 30,712, t_f = 85.3 h.

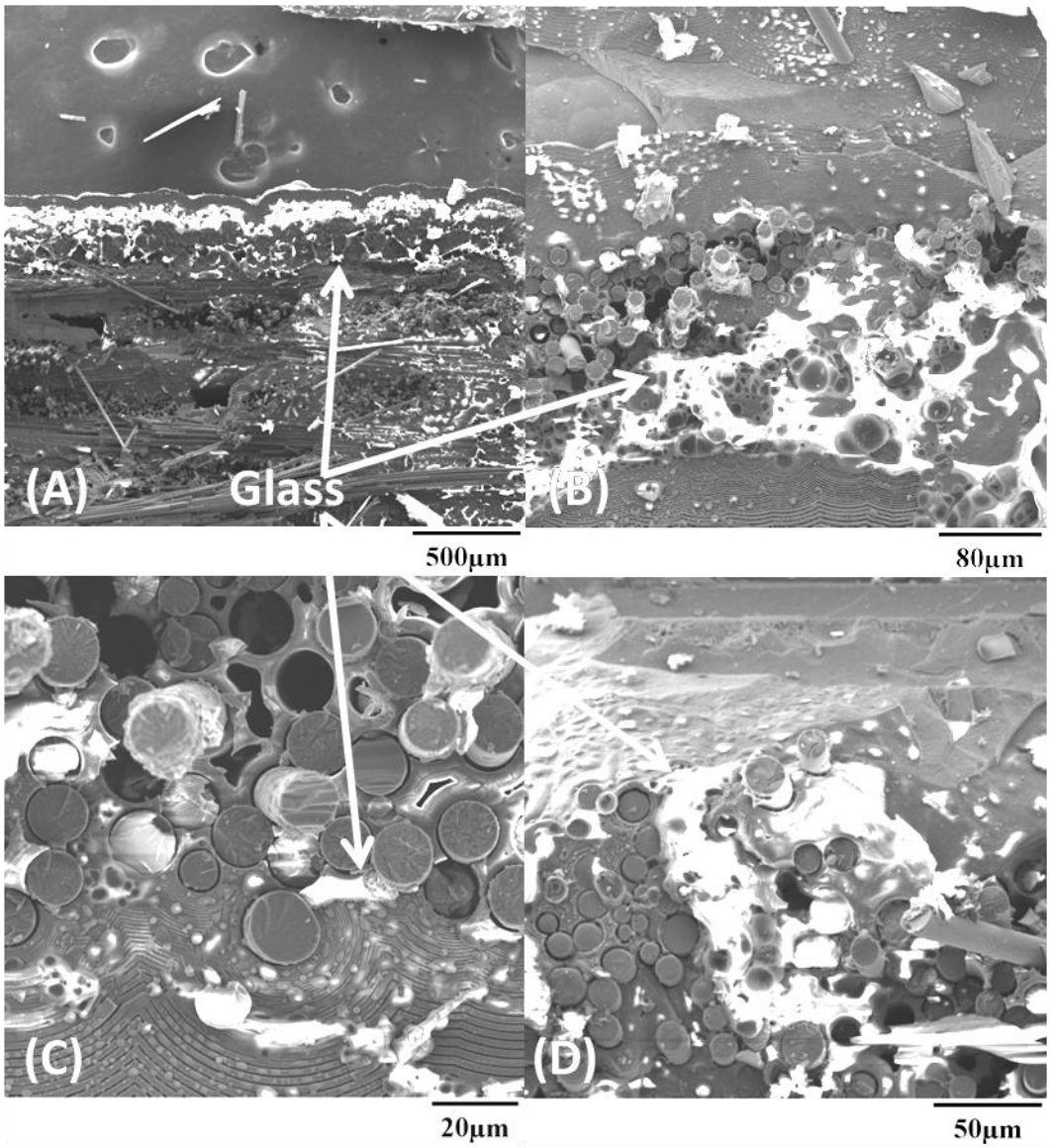

Figure 67: SEM micrograph of fracture surface of specimen P6-8 tested in fatigue at 0.1 Hz in steam at 1200˚C. σ_{max} = 140 MPa, N_f = 11,323, t_f = 31.5 h.

Presented in Figure 68 is an SEM micrograph of a polished interior surface of specimen P6-7 subjected to the 140 MPa fatigue test at 0.1 Hz at 1200°C in air. In this case the specimen was cut along the specimen axis (also the loading direction) in order to assess the damage development throughout the specimen. Figure 68 shows an abundance of matrix cracks in the interior of the specimen P6-7. Recall that this specimen was tested with the fatigue stress of

140 MPa, which exceeds the proportional limit. Therefore considerable matrix cracking should be expected. Figure 69 shows a higher magnification view of the interior surface shown in Figure 68. A crack initiating at the voids between the fiber tows can be seen in Figure 69A. Matrix cracks are also seen in Figure 69B.

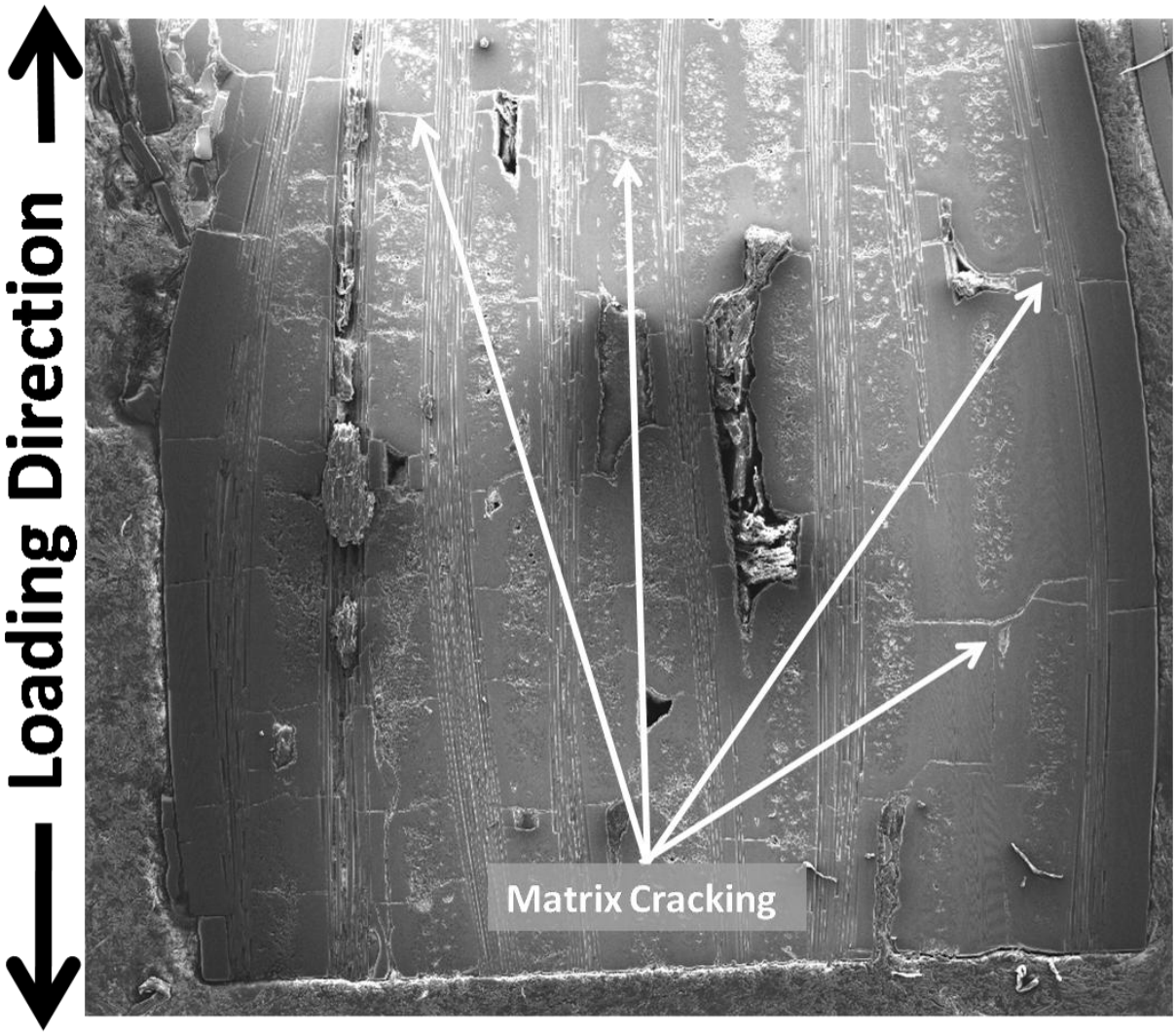

Figure 68: SEM micrograph of the specimen P6-7 tested in fatigue at 0.1 Hz at 1200°C in air showing an interior surface parallel to the specimen axis. σ_{max} = 140 MPa, N_f = 30,712, t_f = 85.3 h.

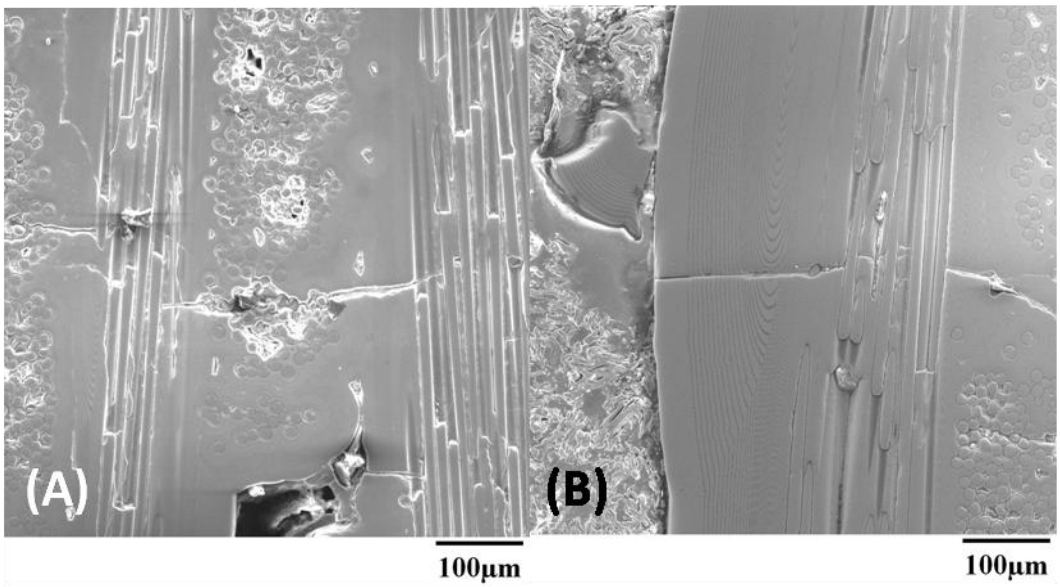

Figure 69: Higher magnification SEM micrographs of the specimen P6-7 tested in fatigue at 0.1 Hz at 1200°C in air showing an interior surface parallel to the specimen axis. σ_{max} = 140 MPa, N_f = 30,712, t_f = 85.3 h.

Figure 70 shows an SEM micrograph of a polished interior surface of specimen P6-8 subjected to the 140 MPa fatigue test at 0.1 Hz at 1200°C in steam. This specimen was also cut along the specimen axis (also the loading direction) in order to assess the damage development throughout the specimen. Figure 70 shows a profusion of matrix cracks in the interior of the specimen P6-8. The SEM micrograph in Figure 71 shows a close-up view of the interior surface of specimen P6-8. The signs of oxidation are readily seen in Figure 71. A matrix crack seen in Figure 71 propagates into the interior of the composite. As the crack opens and grows it provides a pathway for the steam environment, which causes oxidation of the SiC matrix. As the SiC oxidizes, silica forms on the faces of the crack. The matrix crack filled with silica deposits shown in Figure 71 is typical and representative of the matrix cracks seen near the edge of specimen 6-8. The majority of matrix cracks growing near the edge of specimen P6-8 are filled with silica deposits caused by the oxidation of the SiC matrix exposed to steam

environment. Conversely, no silica deposits were seen in the matrix cracks in Specimen P6-7 tested in air. Figure 72 shows other matrix cracks growing near the edge of the specimen P6-8, which are filled with silica deposits formed due to the oxidation of the SiC matrix in steam. A crack seen in Figure 72B propagates through the outer layer of the matrix and is then deflected around an interior matrix layer.

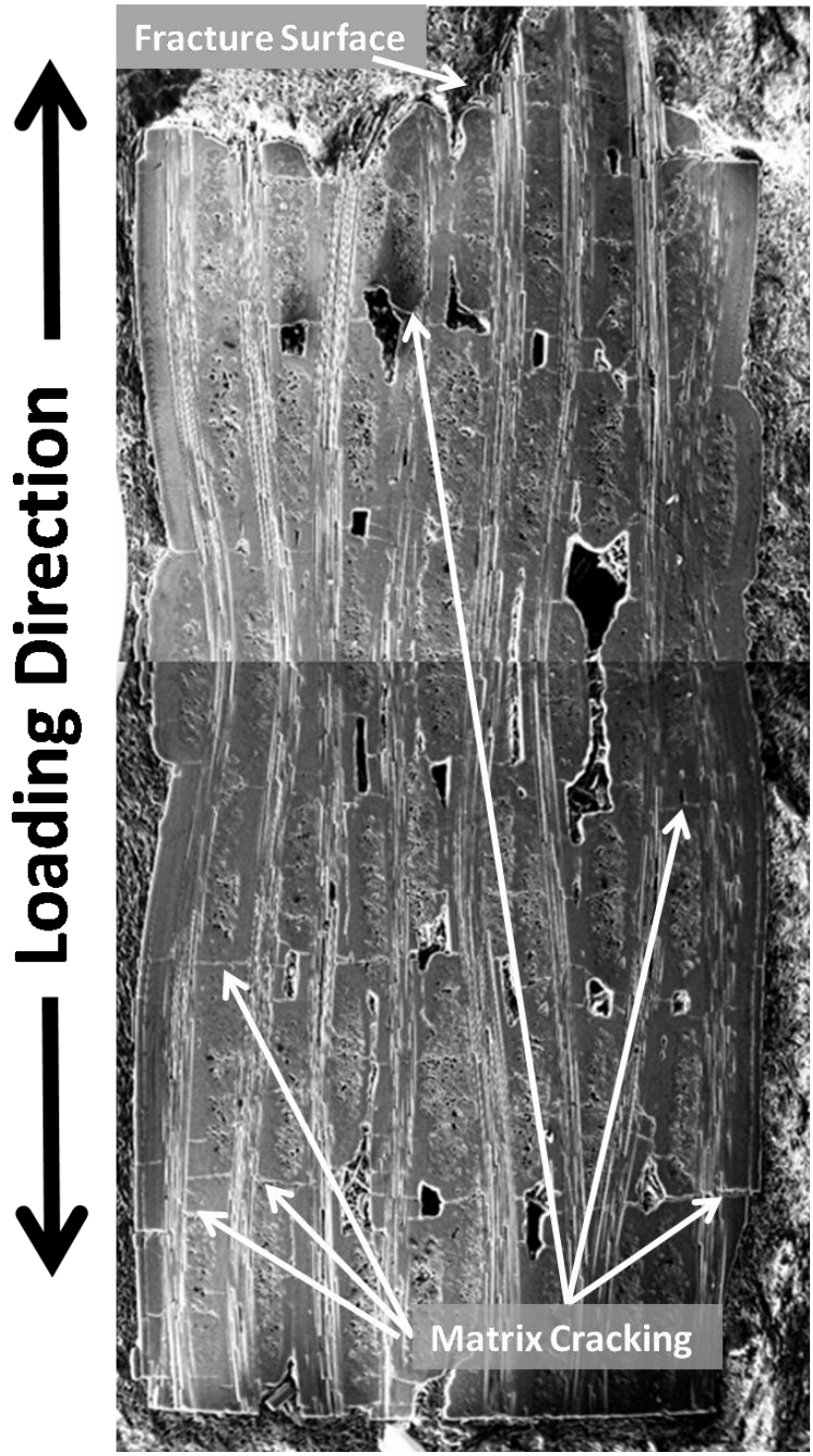

Figure 70: SEM micrograph of the specimen P6-8 tested in fatigue at 0.1 Hz at 1200°C in steam showing an interior surface parallel to the specimen axis. σ_{max} = 140 MPa, N_f = 11,323, t_f = 31.5 h.

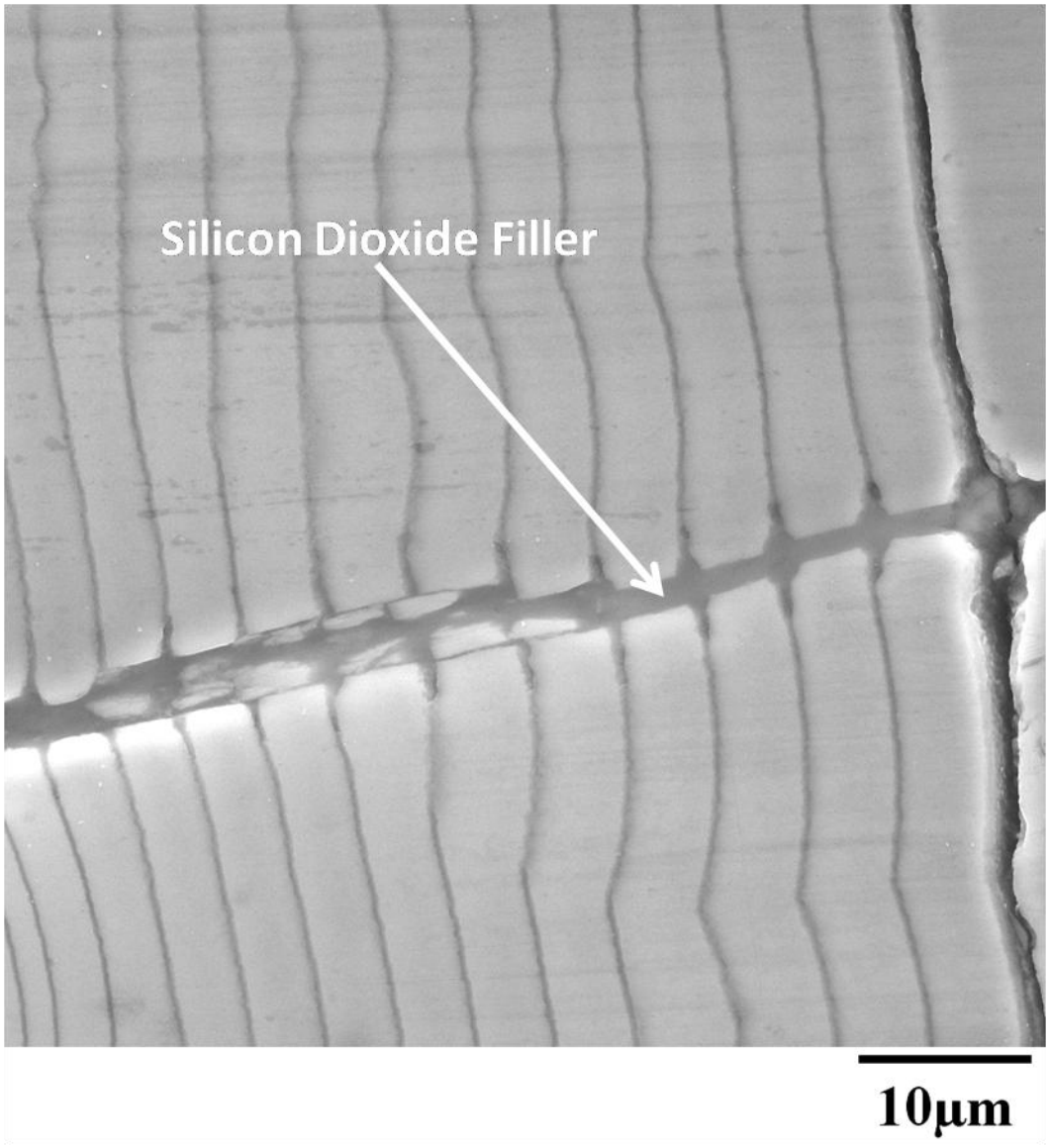

Figure 71: Higher magnification SEM micrograph of the specimen P6-8 tested in fatigue at 0.1 Hz at 1200°C in steam showing an interior surface parallel to the specimen axis. σ_{max} = 140 MPa, N_f = 11,323, t_f = 31.5 h. Matrix crack with silica deposits formed by oxidation are evident.

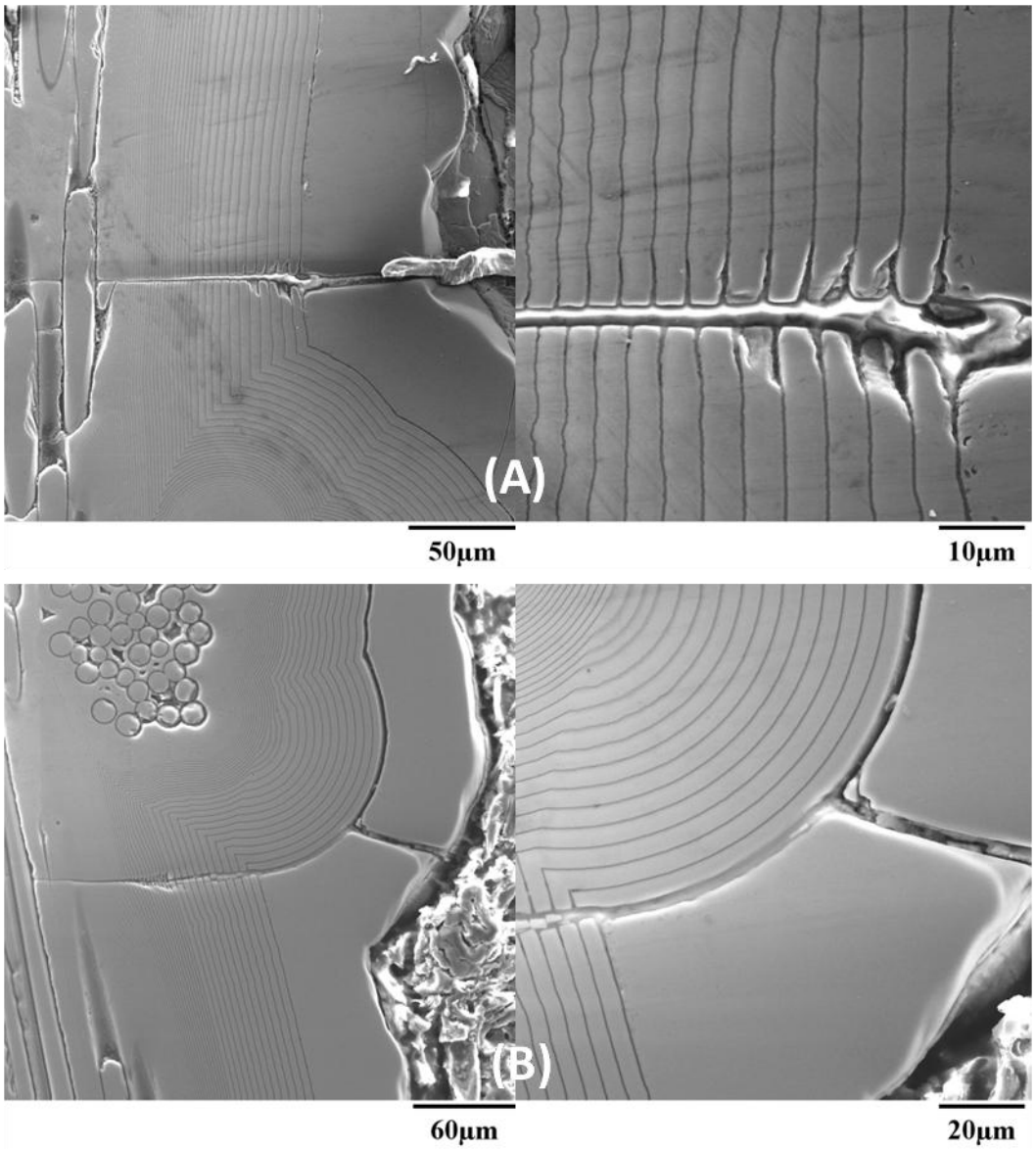

Figure 72: SEM micrographs of the specimen P6-8 tested in fatigue at 0.1 Hz at 1200°C in steam showing an interior surface parallel to the specimen axis. σ_{max} = 140 MPa, N_f = 11,323, t_f = 31.5 h. Matrix cracks with silica deposits formed by oxidation are evident.

5.7.4 Microstructure of the Specimens Tested in Fatigue at 1.0 Hz

Optical micrographs of the fracture surfaces for specimens tested in fatigue with the maximum stress of 100 MPa at 1.0 Hz in air and in steam are presented in Figure 73 and Figure

74, respectively. Optical micrographs of the fracture surfaces for specimens tested in fatigue with the maximum stress of 140 MPa at 1.0 Hz in air and in steam are presented in Figure 75 and Figure 76, respectively. The fracture surfaces in Figure 73 through Figure 76 have similar appearance. All show minimal fiber pull-out and exhibit no ply delamination.

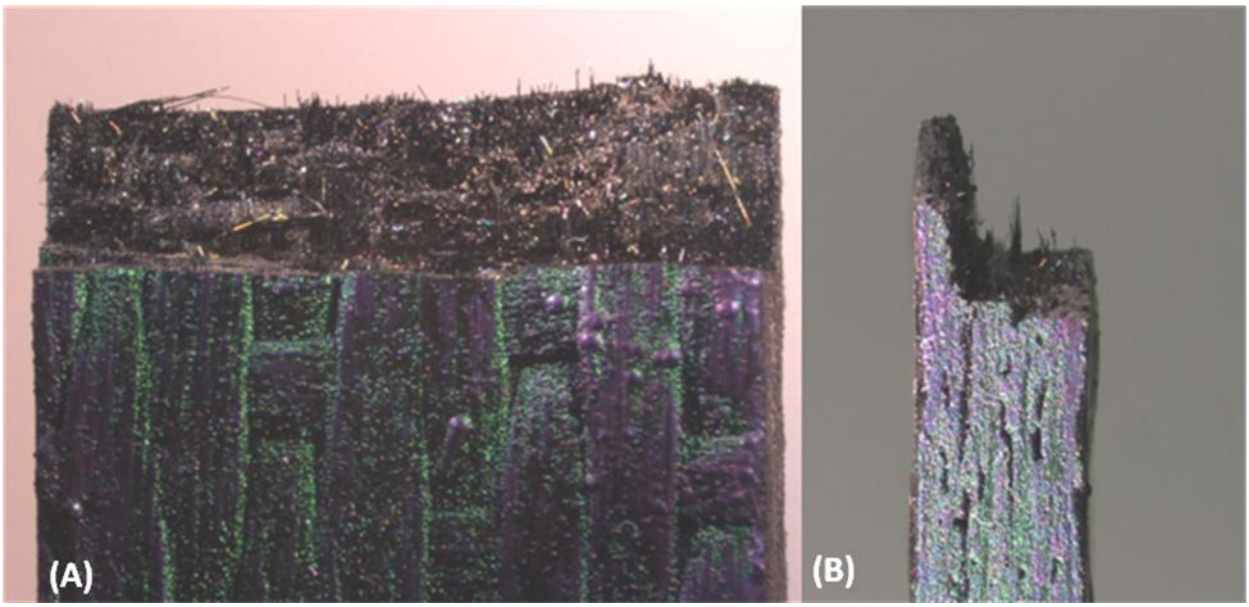

Figure 73: Optical micrographs of specimen P5-4 tested in fatigue at 1.0 Hz in air at 1200˚C. σ_{max} = 100 MPa, N_f = 200,000, t_f = 55.6 h.

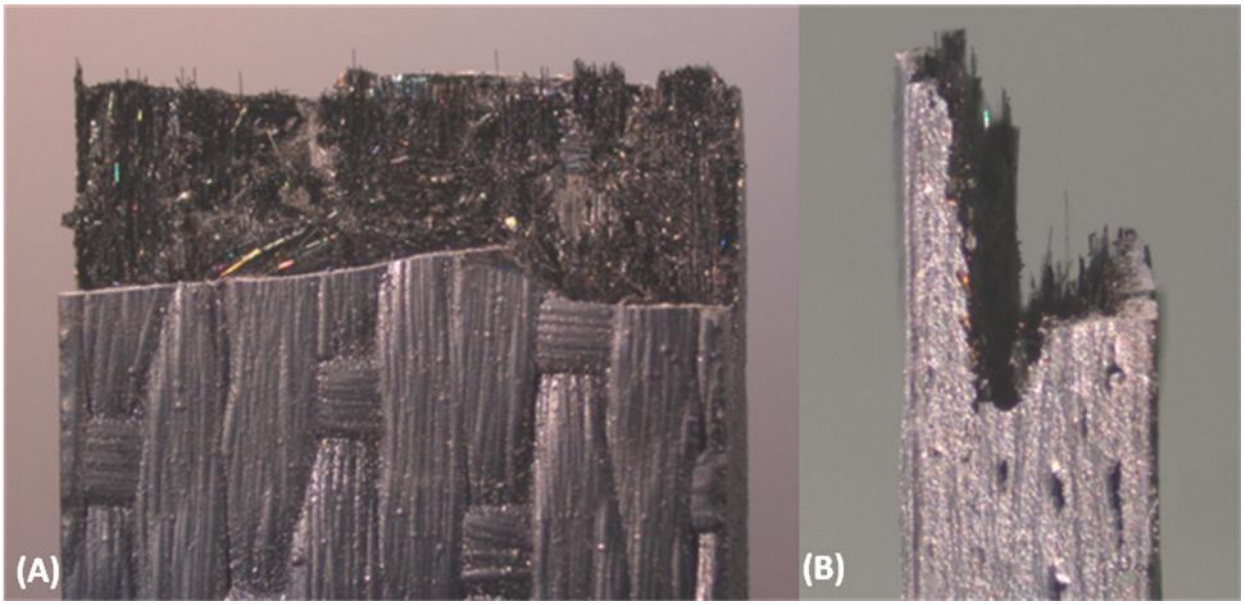

Figure 74: Optical micrographs of specimen P5-4 tested in fatigue at 1.0 Hz in air at 1200˚C. σ_{max} = 100 MPa, N_f = 200,000, t_f = 55.6 h.

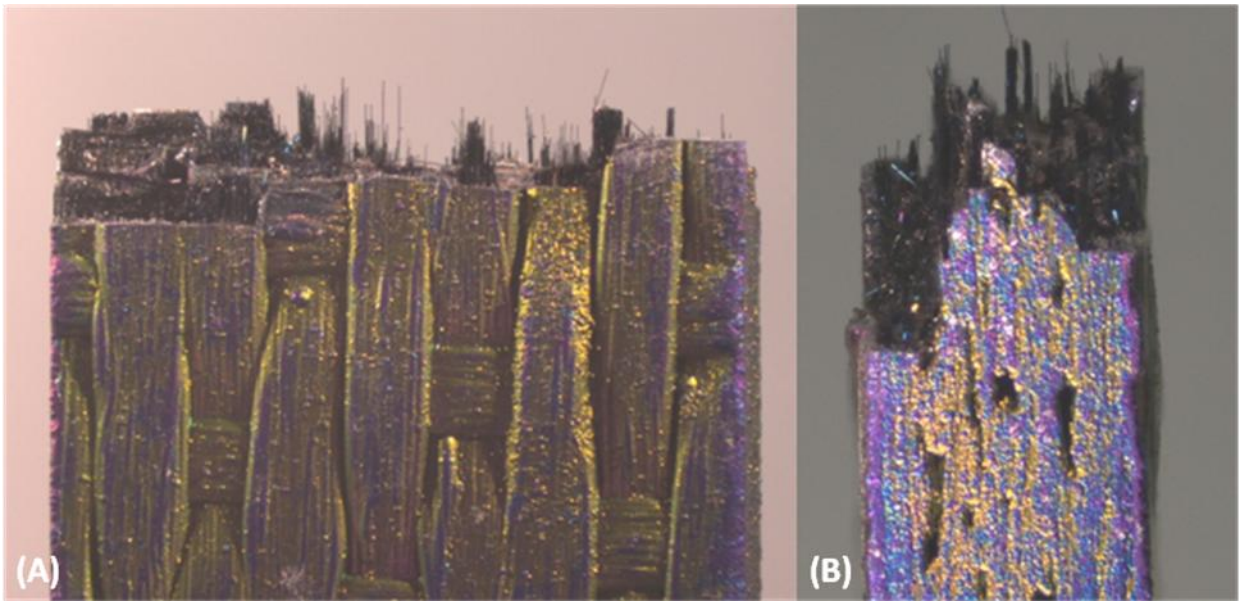

Figure 75: Optical micrographs of specimen P6-3 tested in fatigue at 1.0 Hz in air at 1200˚C. σ_{max} = 140 MPa, N_f = 63,458, t_f = 17.6 h.

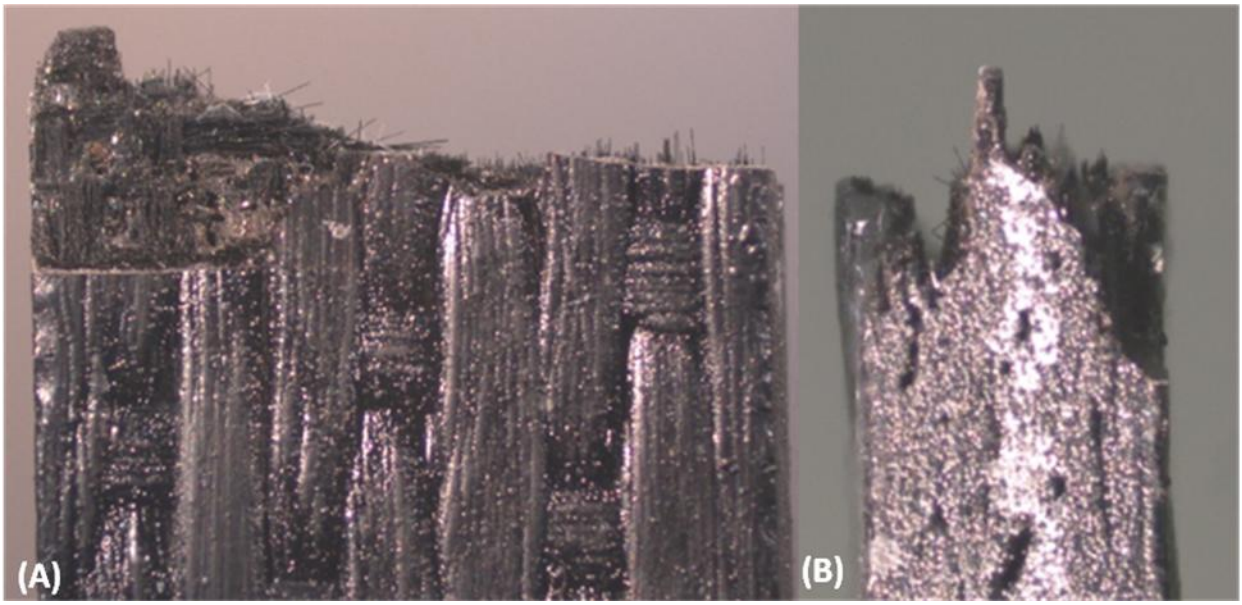

Figure 76: Optical micrographs of specimen P6-4 tested in fatigue at 1.0 Hz in air at 1200˚C. σ_{max} = 140 MPa, N_f = 36,679, t_f = 10.2 h.

The SEM micrographs of the fracture surfaces for specimens tested in fatigue with the maximum stress of 100 MPa at 1.0 Hz in air and in steam are presented in Figure 77 and Figure 78, respectively.

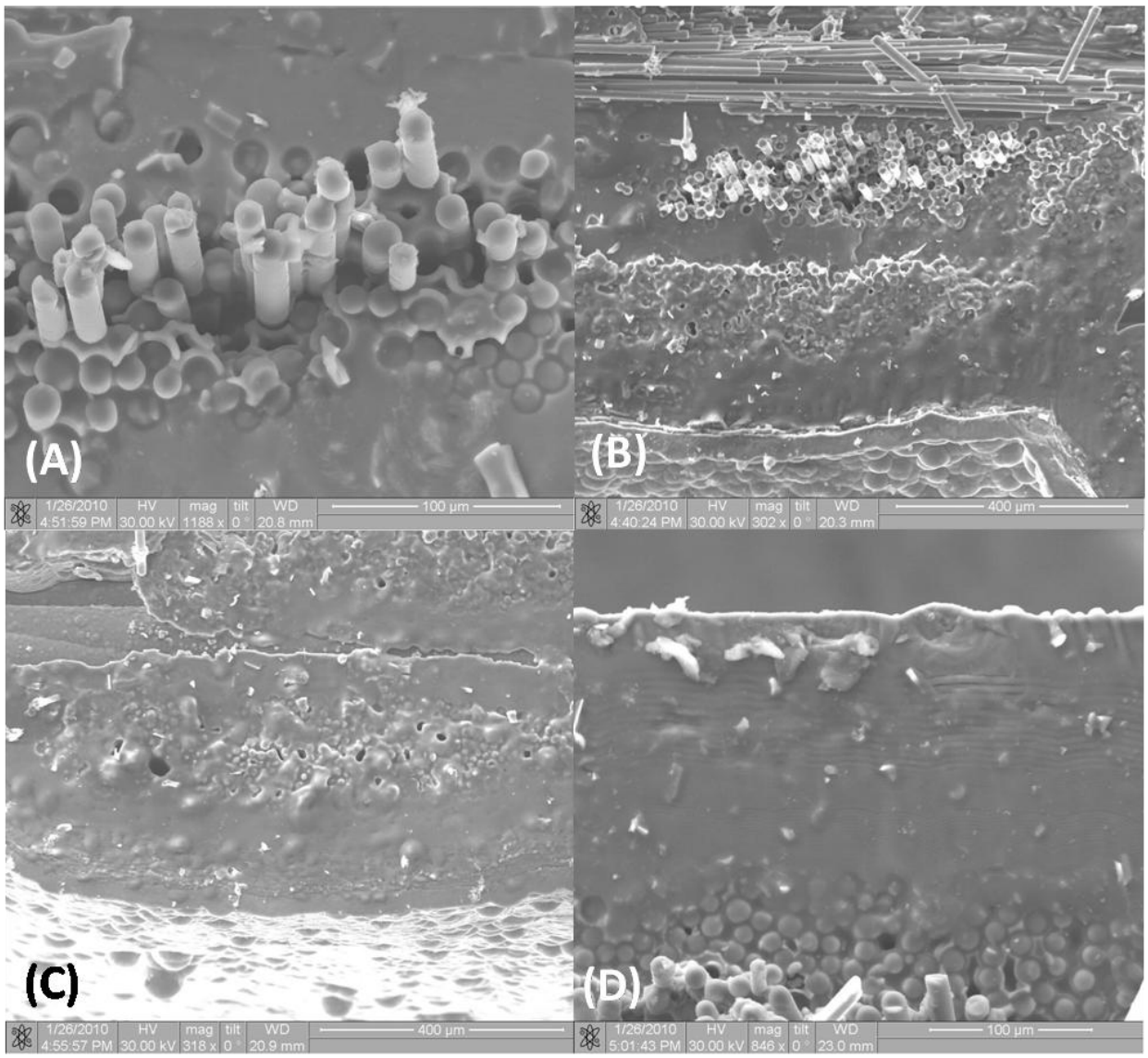

Figure 77: SEM micrographs of the fracture surface of specimen P5-4 tested in fatigue at 1.0 Hz at 1200°C in air. σ_{max} = 100 MPa, N_f > 200,000, t_f > 55.6 h.

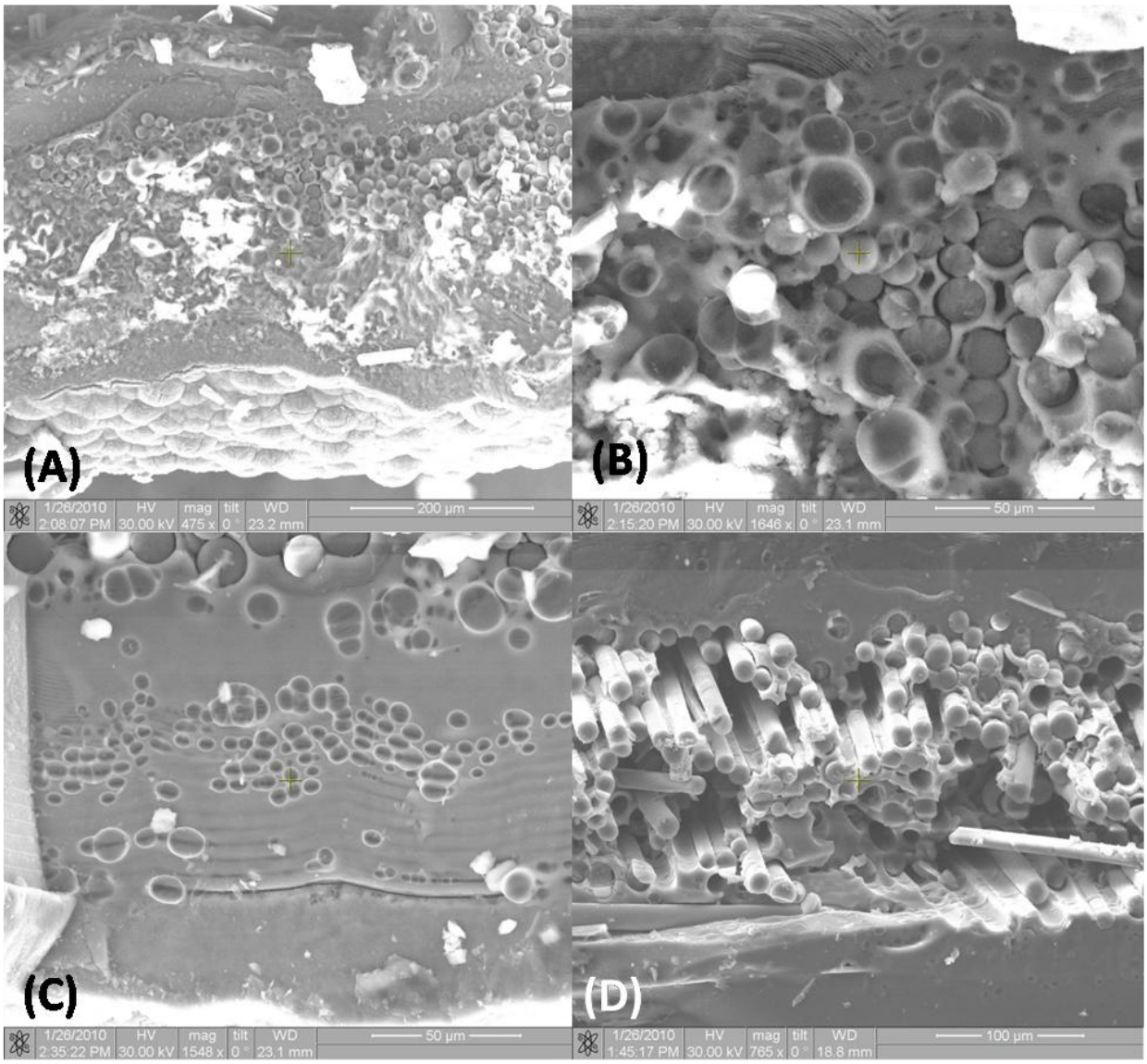

Figure 78: SEM micrographs of the fracture surface of specimen P5-5 tested in fatigue at 1.0 Hz at 1200°C in steam. σ_{max} = 100 MPa, N_f > 200,000, t_f > 55.6 h.

The fracture surfaces of both specimens in Figure 77 and Figure 78 show oxidation near the edges. Figure 77A shows a small area of fiber-pull adjacent to an area with clear signs of oxidation. It appears that oxidation occurred at the edge of the fiber tow with minimal fiber pull-out occurring in the middle of the fiber tow. Figure 77B shows fibers near the edge of the fracture surface experiencing greater oxidation than the fibers in the interior of the specimen,

where some fiber pull-out is observed. Fracture surface in Figure 78A, B, and C show glass bubbles that formed by oxidation. Yet some fiber pull-out can be seen in the interior of the fracture surface in Figure 78D.

The SEM micrographs of the fracture surfaces obtained for specimens tested in fatigue with the maximum stress of 140 MPa at 1.0 Hz in air and in steam are presented in Figure 79 and Figure 80, respectively. The fracture surfaces in Figure 79 and Figure 80 show signs of oxidation. However, the oxidation appears to be more pronounced in the case of the specimen tested in steam (Figure 80). The fracture surfaces in Figure 79 and Figure 80 also exhibit areas of fiber pull-out in the interior of the specimen, where fewer signs of oxidation are generally observed. Nevertheless, Figure 79A shows fibers in the interior of the specimen, which experienced degradation by oxidation than those near the edge of the specimen. This is likely due to the presence of a large void between the plies seen in top right corner of the micrograph in Figure 79A. It is likely that the moisture traveled through the voids and attacked the fibers in the interior of the specimen.

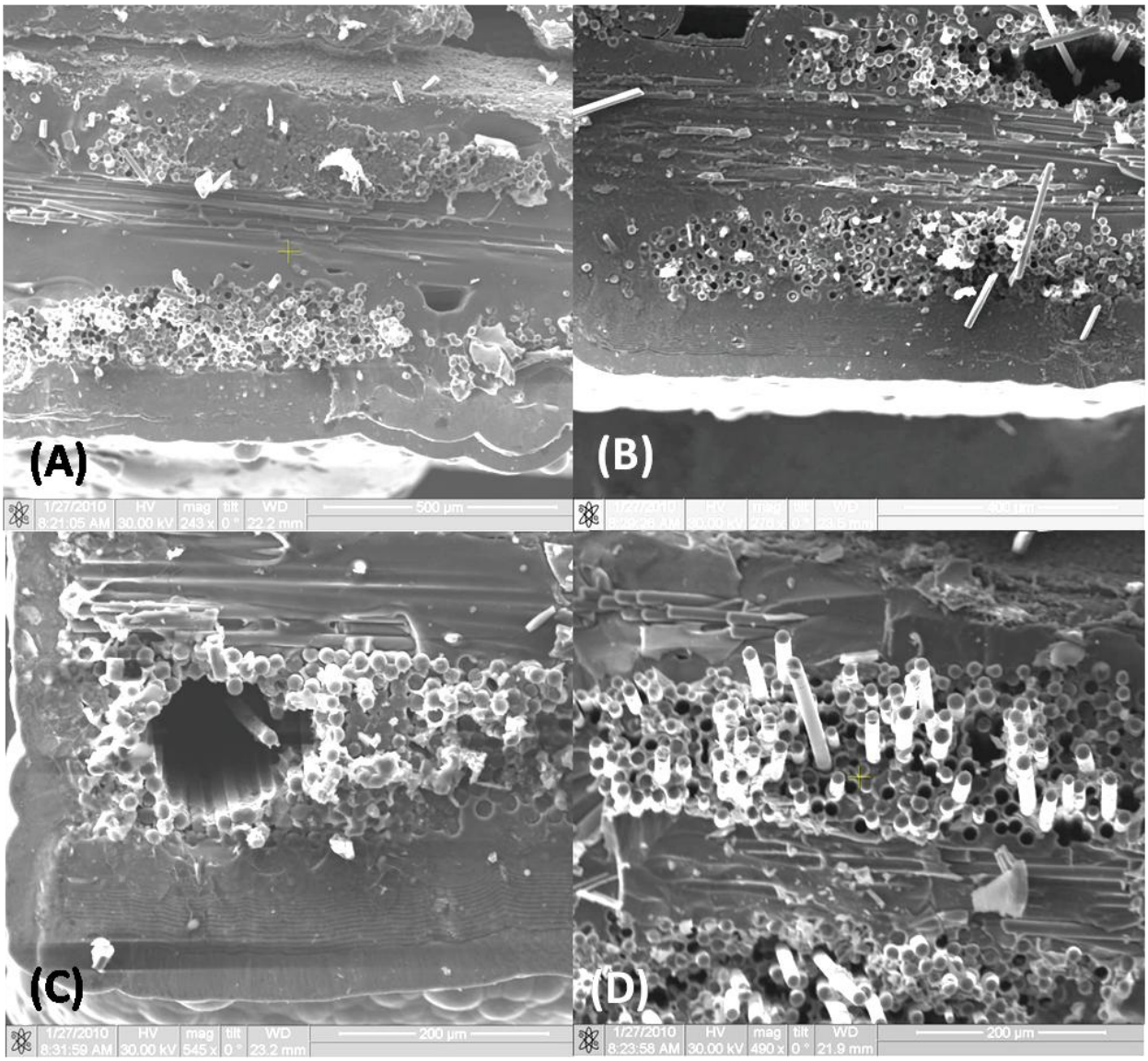

Figure 79: SEM micrographs of specimen P6-3 tested in fatigue at 1.0 Hz at 1200°C in air. σ_{max} = 140 MPa, N_f = 63,458, t_f = 17.6 h.

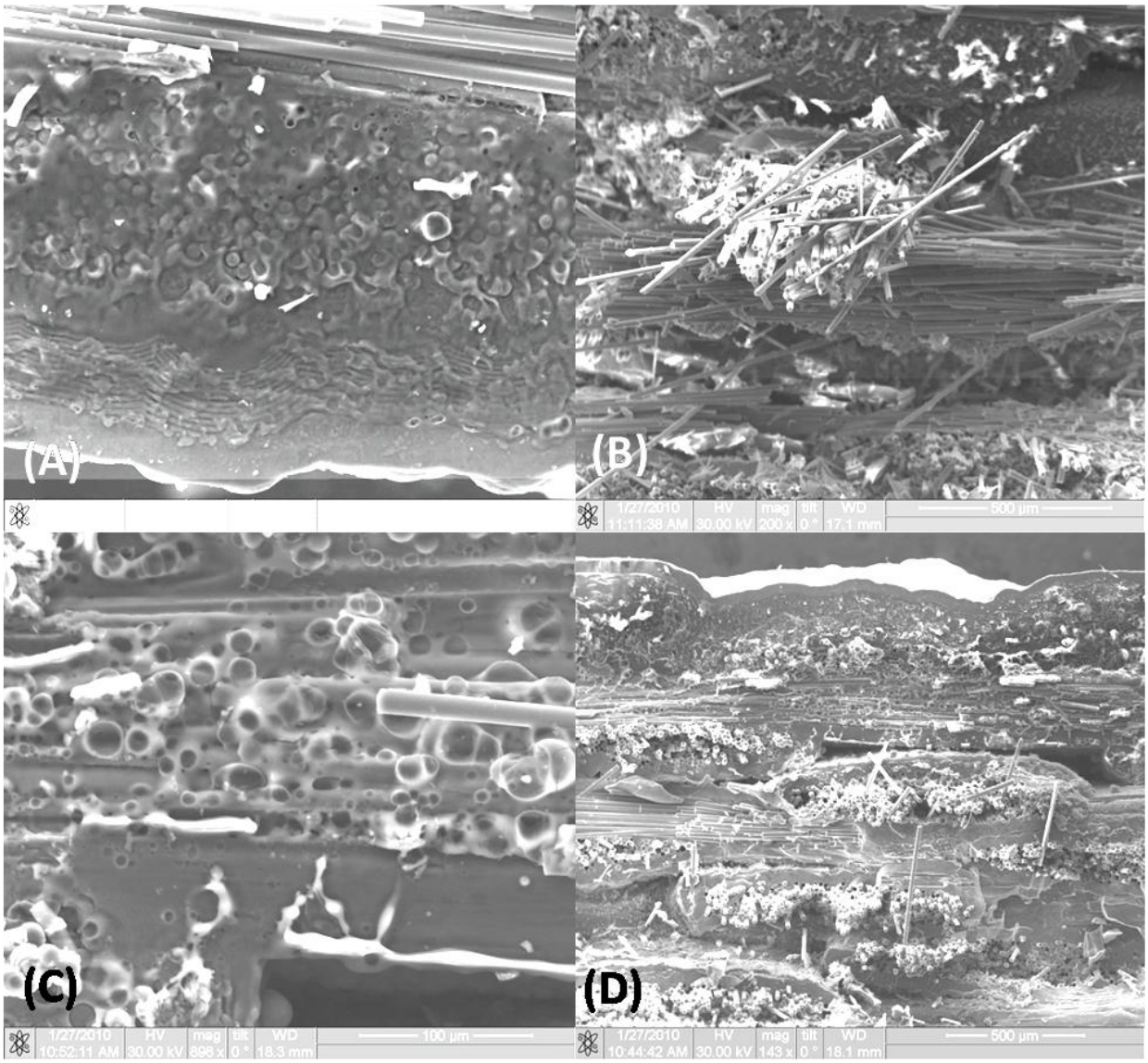

Figure 80: SEM micrographs of specimen P6-4 tested in fatigue at 1.0 Hz at 1200°C in steam. σ_{max} = 140 MPa, N_f = 36,679, t_f = 10.2 h.

Figure 81 shows an SEM micrograph of a polished interior surface of specimen P5-4 subjected to the 100 MPa fatigue test at 1.0 Hz at 1200°C in air. Specimen P5-4 was cut along the specimen axis (also the loading direction) in order to assess the damage development throughout the specimen. A few matrix cracks can be seen in Figure 81. The limited amount of matrix cracking is most likely due to the low fatigue stress of 100 MPa, which is below the

proportional limit for this material. Figure 82 shows a higher magnification view of the interior surface shown in Figure 81. A small amount of glass can be seen forming in the crack.

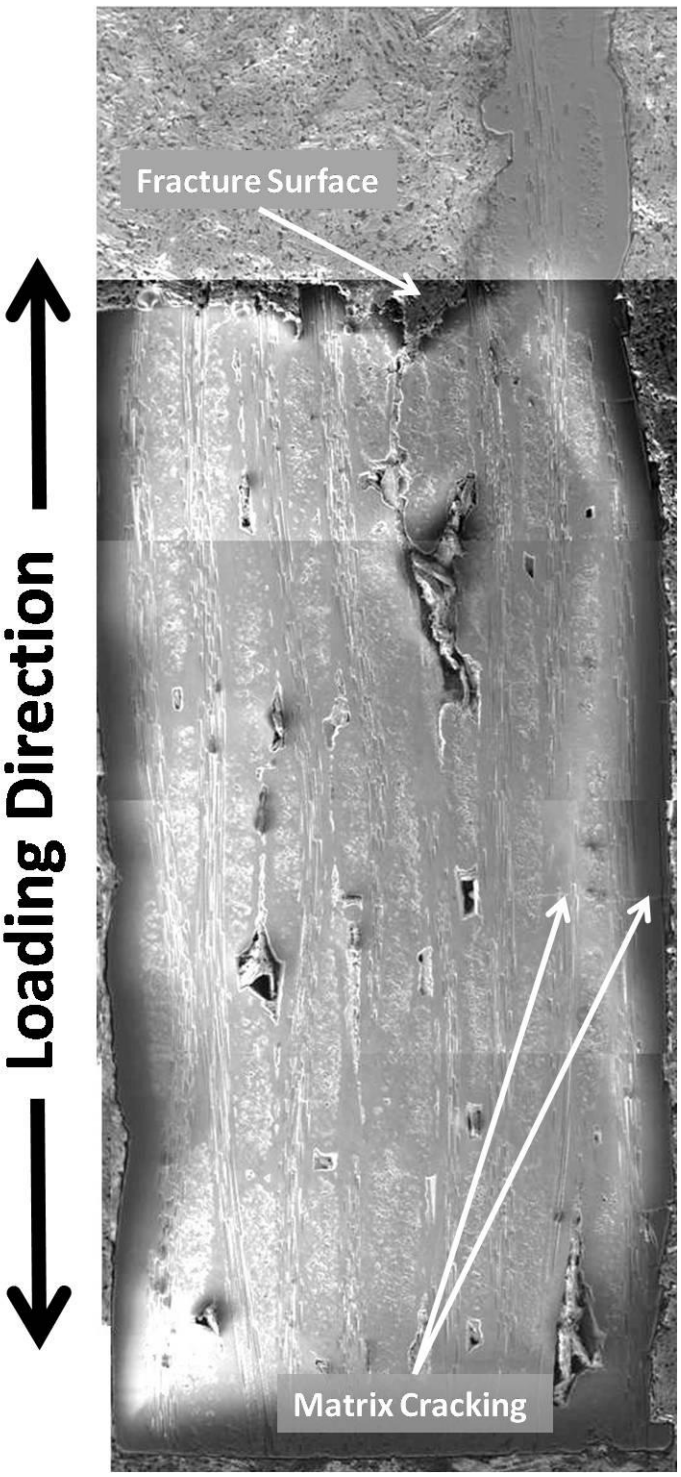

Figure 81: SEM micrograph of the specimen P5-4 tested in fatigue at 1.0 Hz at 1200°C in air showing an interior surface parallel to the specimen axis. σ_{max} = 100 MPa, N_f > 200,000, t_f > 55.6 h.

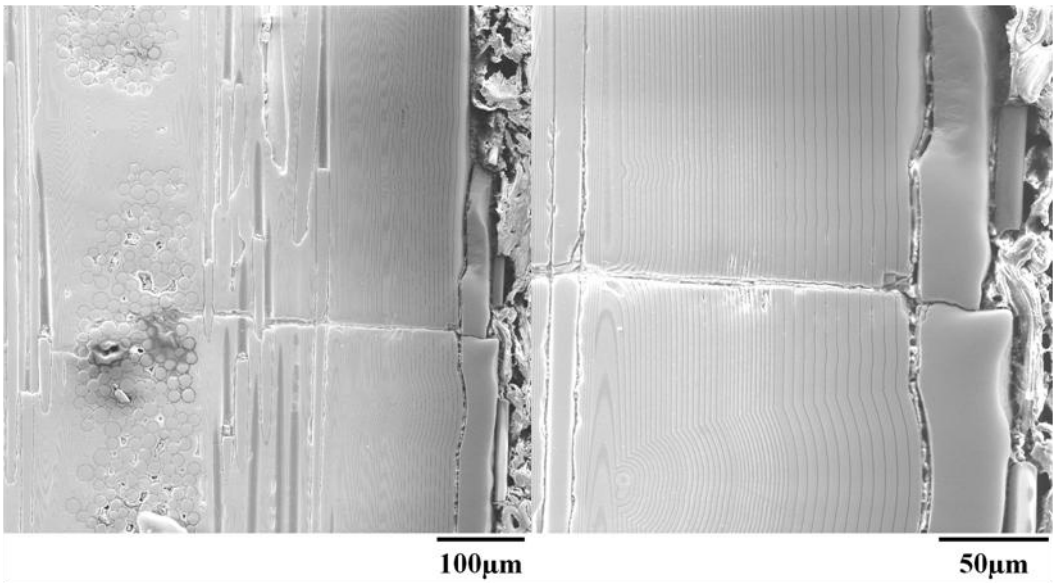

Figure 82: Higher magnification SEM micrographs of the specimen P5-4 tested in fatigue at 1.0 Hz at 1200°C in air showing an interior surface parallel to the specimen axis. σ_{max} = 100 MPa, N_f > 200,000, t_f > 55.6 h.

Figure 83 shows an SEM micrograph of a polished interior surface of specimen P5-5 subjected to the 100 MPa fatigue test at 1.0 Hz at 1200°C in steam. Specimen P5-5 was cut along the specimen axis (also the loading direction) in order to assess the damage development throughout the specimen. Fewer matrix cracks are observed in this case than in the case of a specimen tested with a higher fatigue stress. Figure 84 shows a higher magnification view of the interior surface shown in Figure 83. Glass is seen forming in the matrix voids in Figure 84. Glass deposits are also observed along the crack faces. Even though this specimen achieved fatigue run-out, oxidation damage is evident. The pronounced oxidation in this case can be accounted for by a prolonged exposure to steam at 1200°C during a 55.6-h fatigue test.

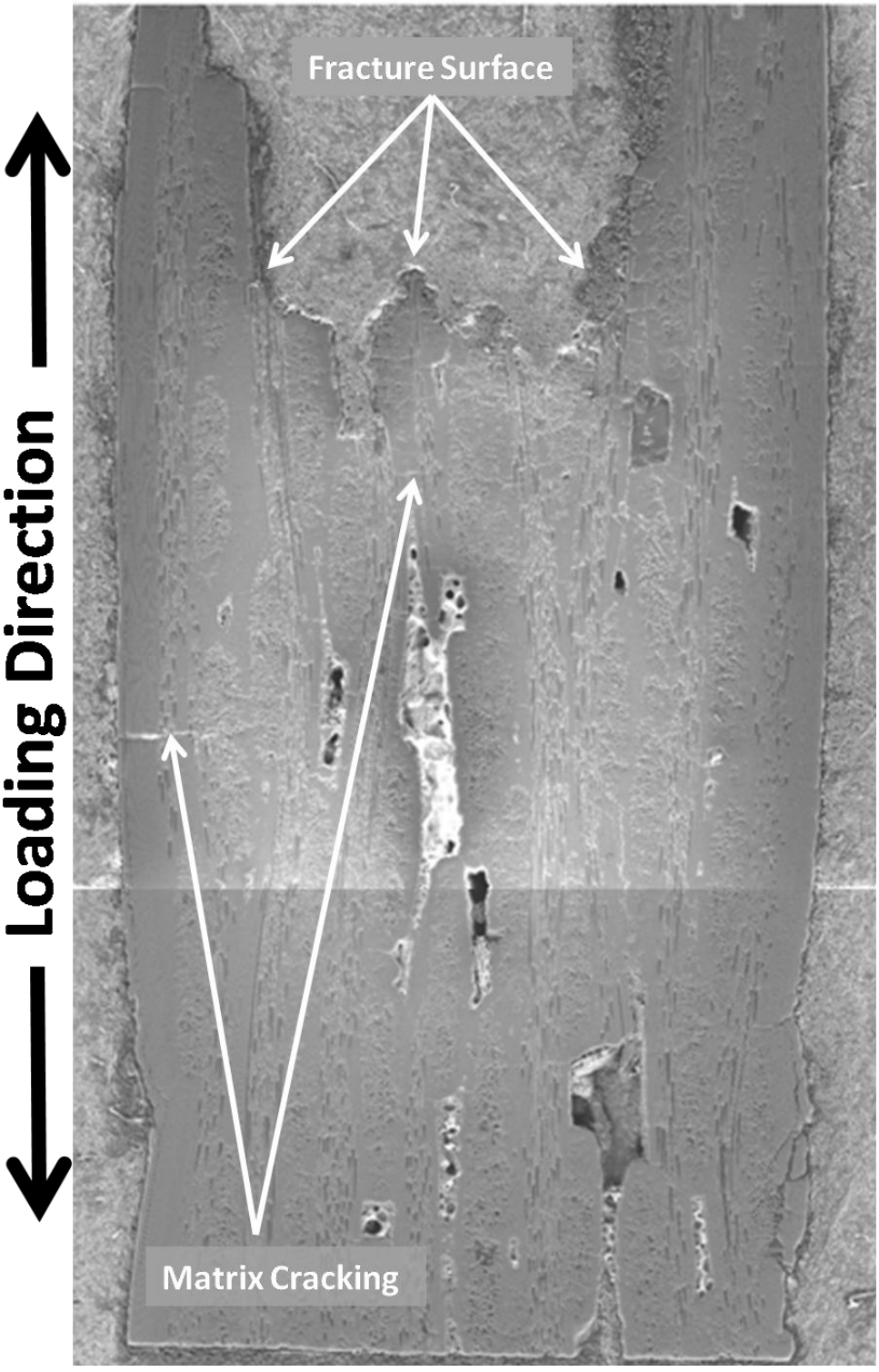

Figure 83: SEM micrograph of the specimen P5-5 tested in fatigue at 1.0 Hz at 1200°C in steam showing an interior surface parallel to the specimen axis. σ_{max} = 100 MPa, N_f > 200,000, t_f > 55.6 h.

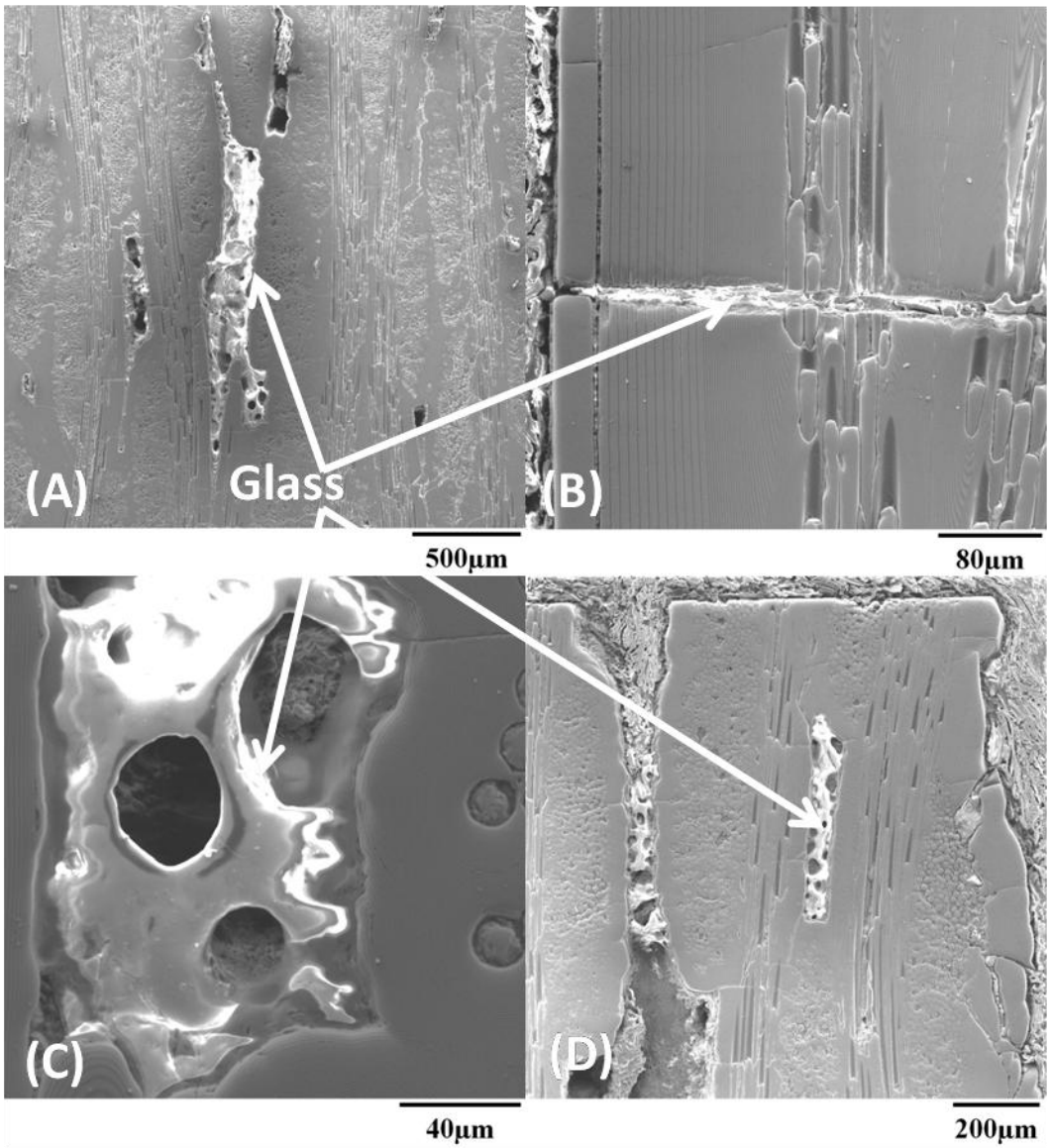

Figure 84: Higher magnification SEM micrographs of the specimen P5-5 tested in fatigue at 1.0 Hz at 1200°C in steam showing an interior surface parallel to the specimen axis. σ_{max} = 100 MPa, N_f > 200,000, t_f > 55.6 h.

Figure 85 shows an SEM micrograph of a polished interior surface of specimen P6-3 subjected to the 140 MPa fatigue test at 1.0 Hz at 1200°C in air. Specimen P6-3 was cut along the specimen axis (also the loading direction) in order to assess the damage development throughout the specimen. Note that more matrix cracks are observed in this case than in the

case of the specimens tested with a lower fatigue stress of 100 MPa. Figure 86-Figure 88 show higher magnification views of the interior surface shown in Figure 85. A crack can be seen initiating at the corners of a matrix void in Figure 86. Figure 87 shows a matrix crack propagating around the fiber. Crack deflection is aided by a weak fiber-matrix interface. Matrix cracks are seen to propagate along the matrix layers in Figure 88.

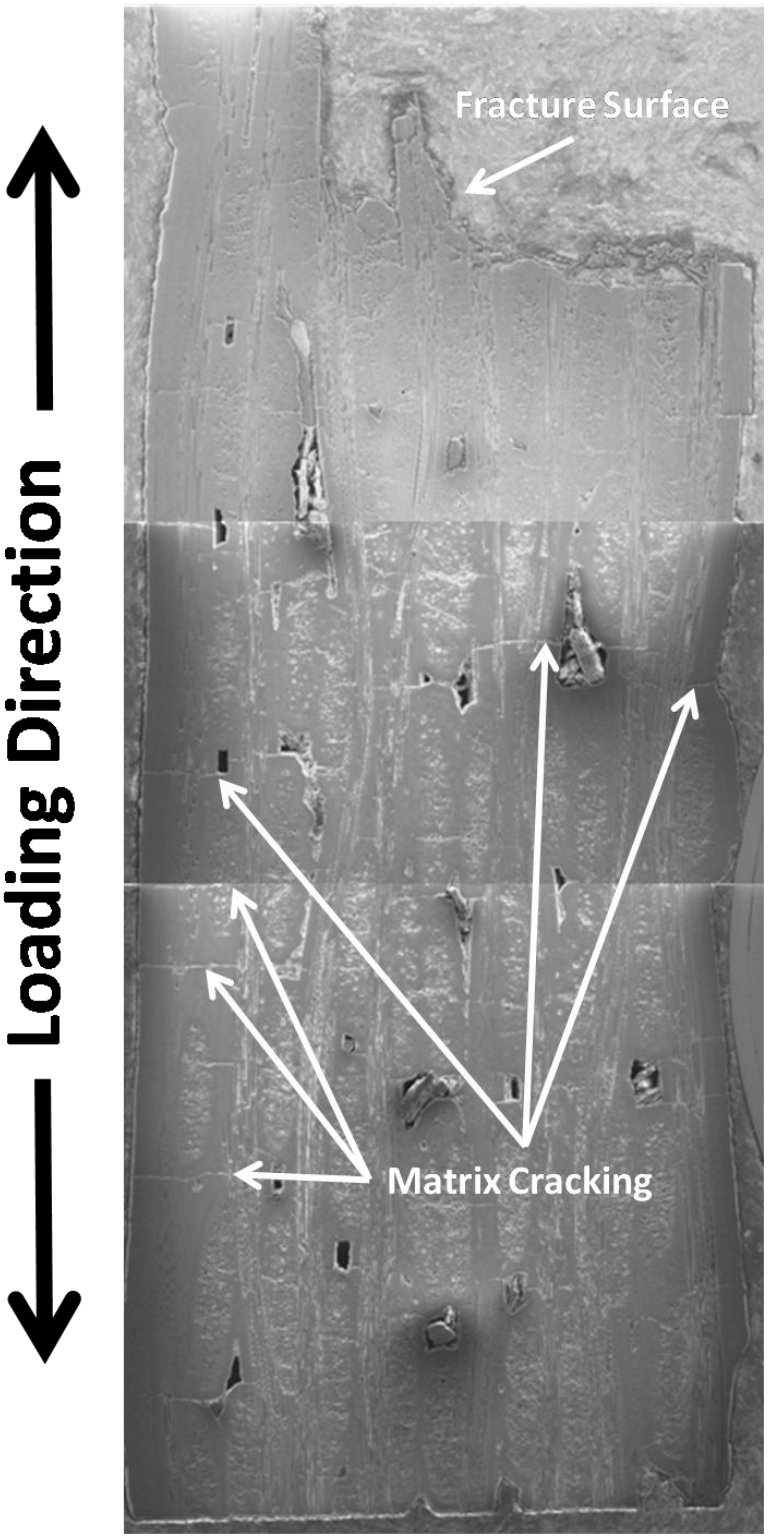

Figure 85: SEM micrograph of the specimen P6-3 tested in fatigue at 1.0 Hz at 1200°C in air showing an interior surface parallel to the specimen axis. σ_{max} = 140 MPa, N_f = 63,458, t_f = 17.6 h.

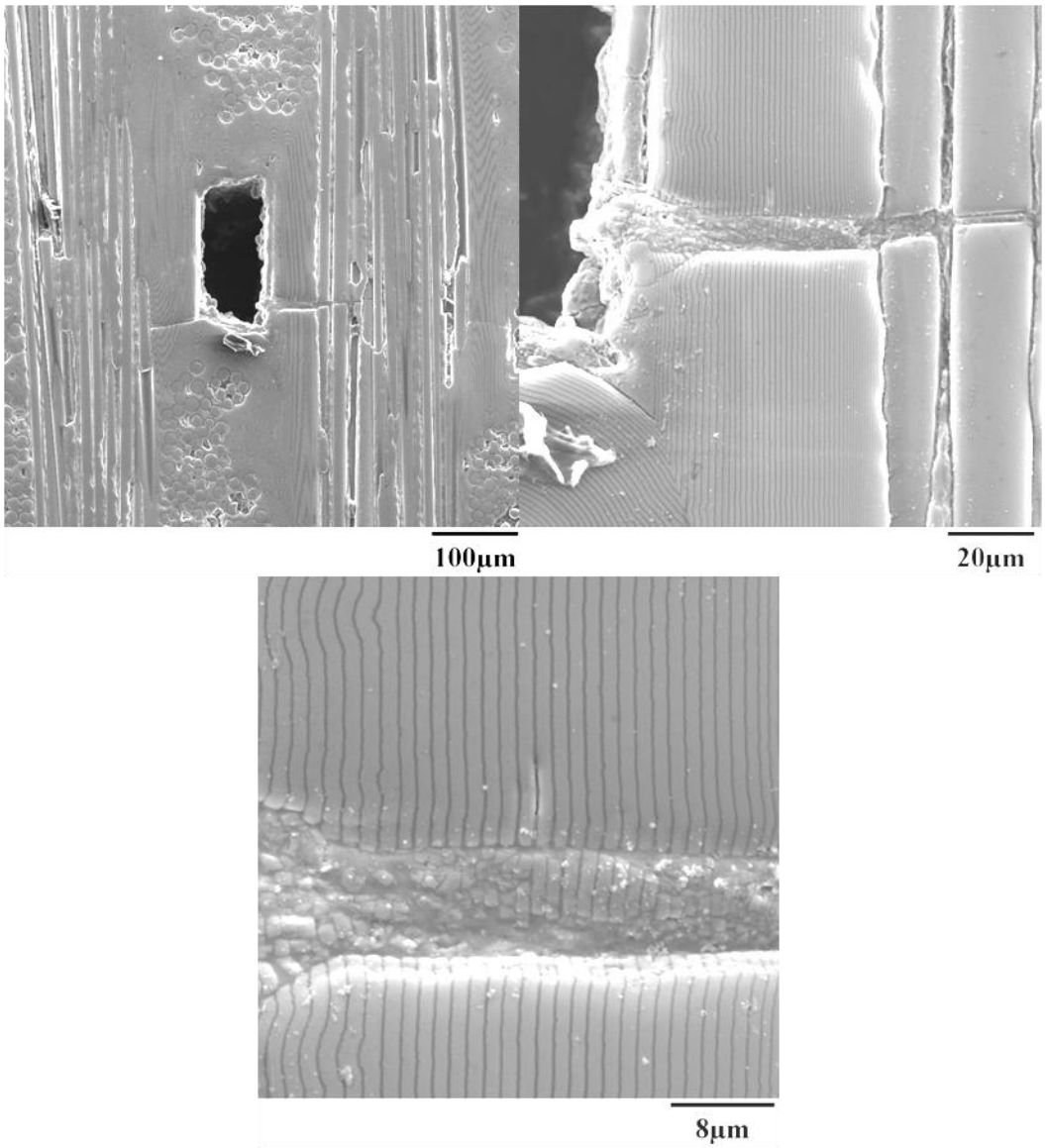

Figure 86: Higher magnification SEM micrographs of the specimen P6-3 tested in fatigue at 1.0 Hz at 1200°C in air showing an interior surface parallel to the specimen axis. Matrix cracks are seen to initiate at the corners of a matrix void. σ_{max} = 140 MPa, N_f = 63,458, t_f = 17.6 h.

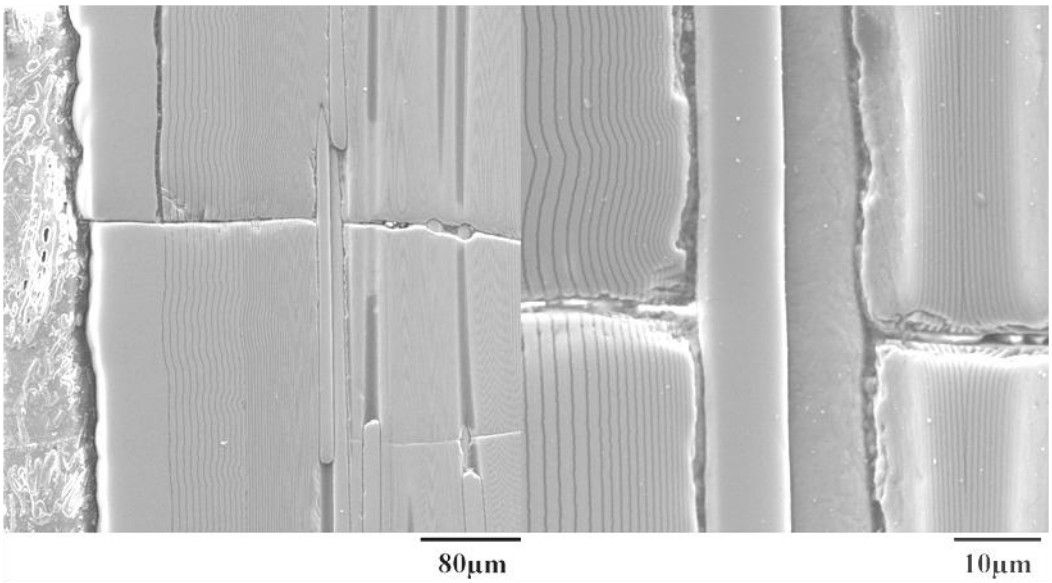

Figure 87: Higher magnification SEM micrographs of the specimen P6-3 tested in fatigue at 1.0 Hz at 1200°C in air showing an interior surface parallel to the specimen axis. A matrix crack is seen to propagate around the fiber. Crack deflection is aided by a weak fiber-matrix interface. σ_{max} = 140 MPa, N_f = 63,458, t_f = 17.6 h.

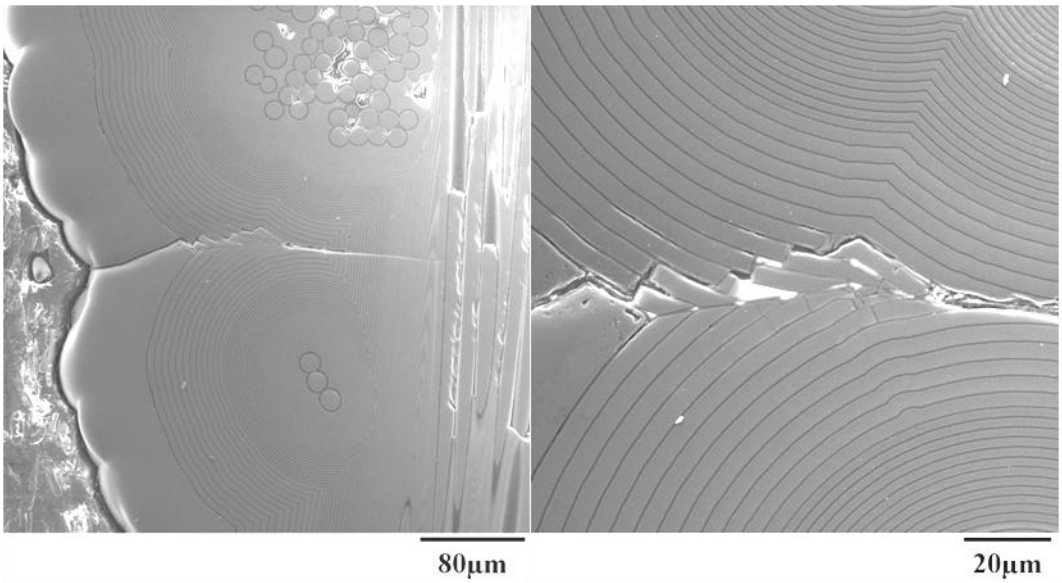

Figure 88: Higher magnification SEM micrographs of the specimen P6-3 tested in fatigue at 1.0 Hz at 1200°C in air showing an interior surface parallel to the specimen axis. Matrix cracks are seen to propagate along the matrix layers. σ_{max} = 140 MPa, N_f = 63,458, t_f = 17.6 h.

Figure 89 shows an SEM micrograph of a polished interior surface of specimen P6-4 subjected to the 140 MPa fatigue test at 1.0 Hz at 1200°C in steam. Specimen P6-4 was cut along the specimen axis (also the loading direction) in order to assess the damage development throughout the specimen. The amount of matrix cracking observed in Figure 89 is similar to that observed in Figure 85 for the specimen P6-3 tested in air. Figure 90A, B, and D show higher magnification views of the interior surface shown in Figure 89. Matrix cracks can be seen forming near the edges of the specimen in Figure 90A, B, and D. The glass deposits on the crack faces are also visible. The micrograph in Figure 90C shows a polished fracture surface of the specimen P6-4. This micrograph reveals that the fibers exposed to the steam environment no longer have fiber coating. Conversely, the fibers in the interior of the specimen that did not suffer significant oxidation maintained their fiber coating.

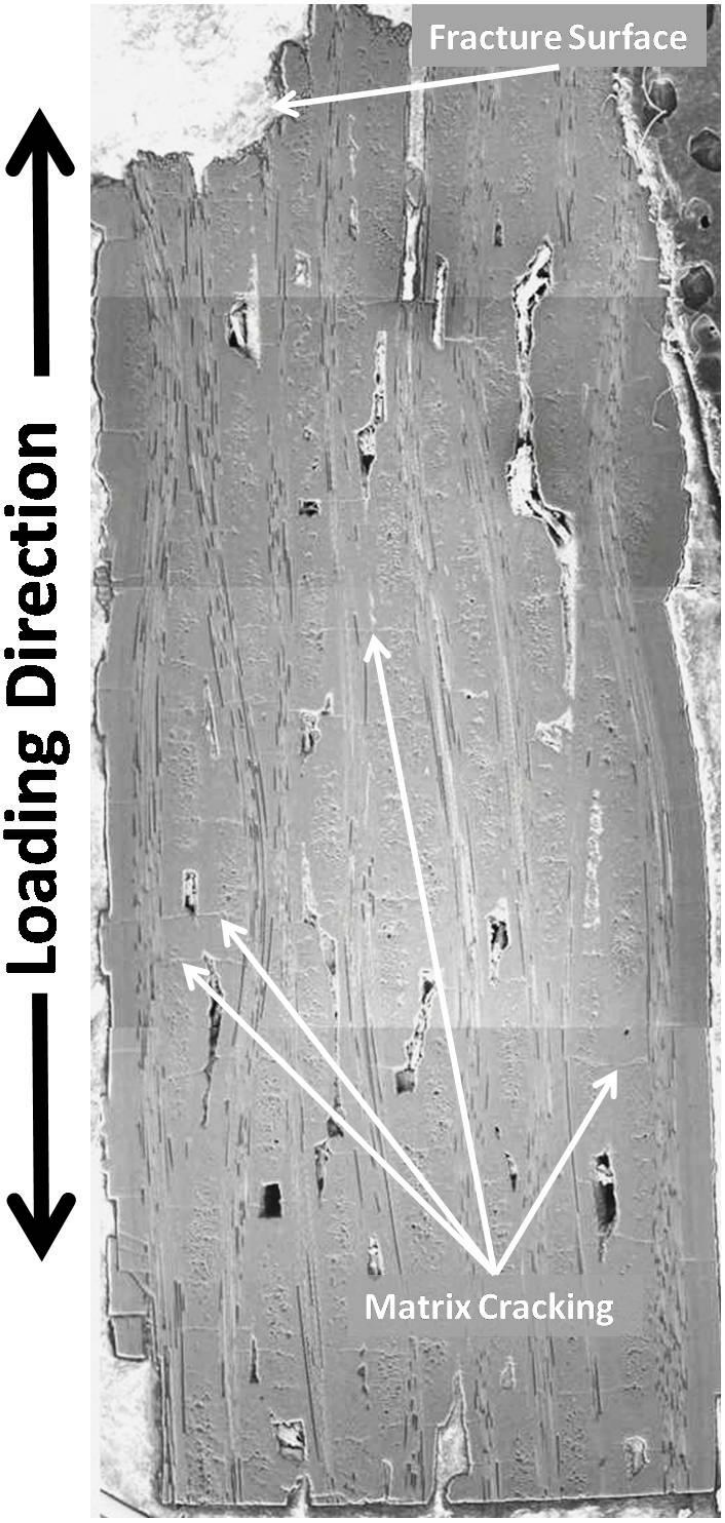

Figure 89: SEM micrograph of the specimen P6-4 tested in fatigue at 1.0 Hz at 1200°C in steam showing an interior surface parallel to the specimen axis. σ_{max} = 140 MPa, N_f = 36,679, t_f = 10.2 h.

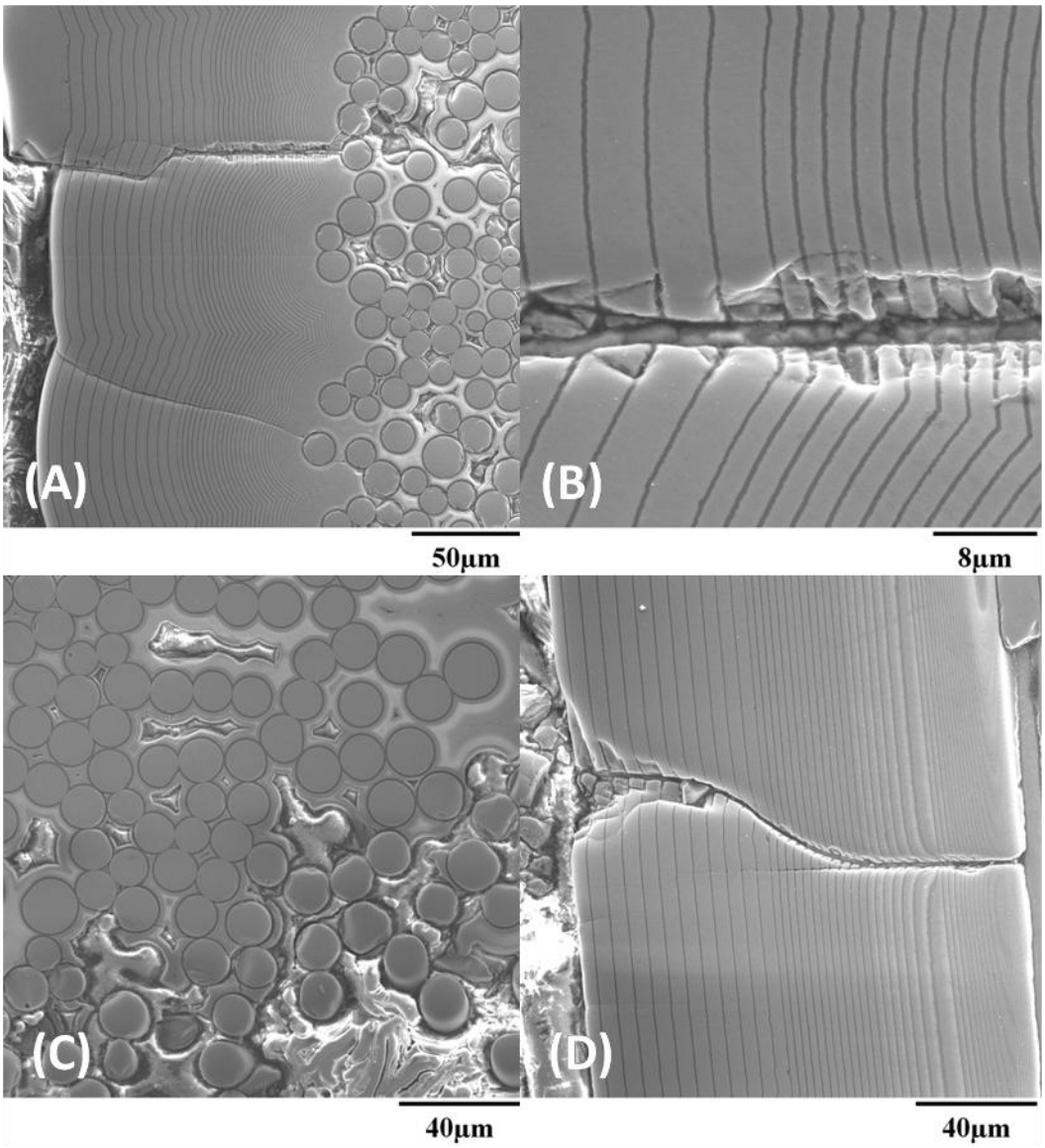

Figure 90: Higher magnification SEM micrographs of the specimen P6-4 tested in fatigue at 1.0 Hz at 1200°C in steam. σ_{max} = 140 MPa, N_f = 36,679, t_f = 10.2 h.

5.7.5 Microstructure of the Specimens Tested at 10 Hz

Optical micrographs of the fracture surfaces for specimens tested in fatigue with the maximum stress of 140 MPa at 10 Hz in air and in steam are presented in Figure 91 and Figure 92, respectively.

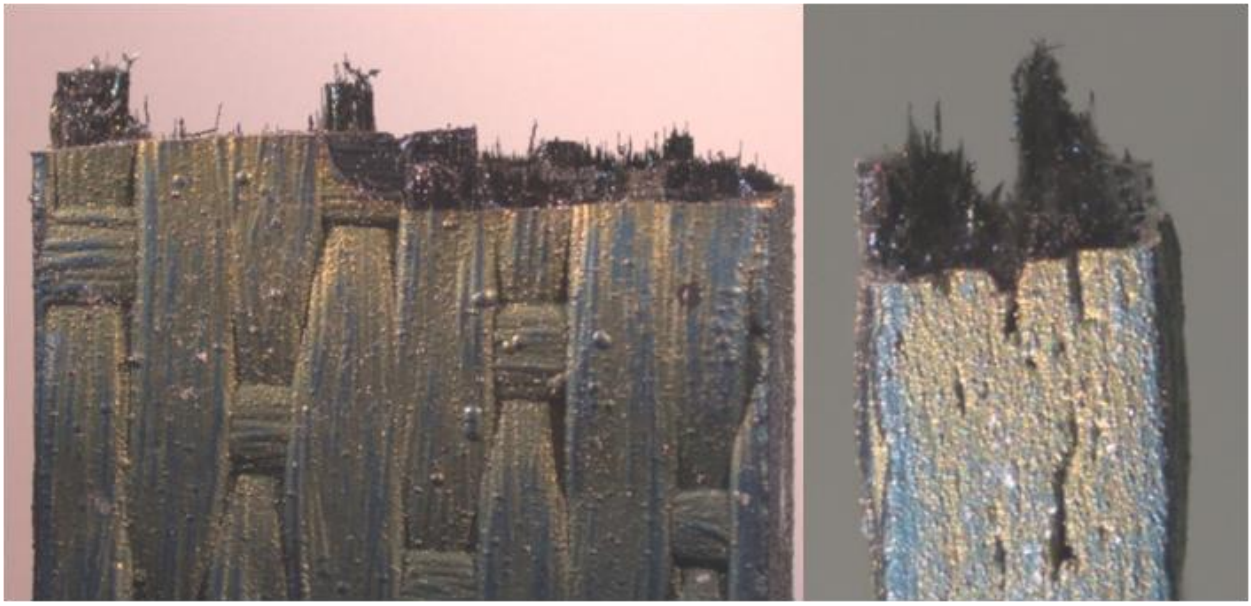

Figure 91: Optical micrographs of specimen P6-5 tested in fatigue at 10 Hz at 1200°C in air. σ_{max} = 140 MPa, N_f > 200,000, t_f > 5.6 h.

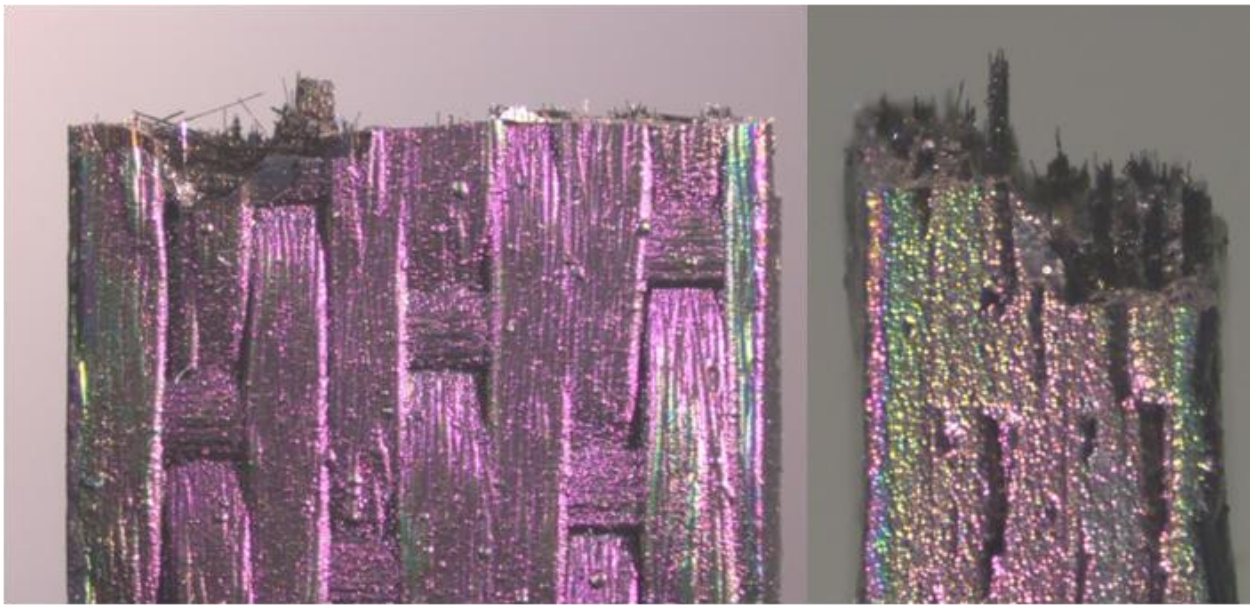

Figure 92: Optical micrographs of specimen P6-6 tested in fatigue at 10 Hz at 1200°C in steam. σ_{max} = 140 MPa, N_f = 39,849, t_f = 1.1 h.

The SEM micrographs of the fracture surfaces obtained in the 140 MPa fatigue tests conducted at 10 Hz at 1200°C in air and in steam are shown in Figure 93 and Figure 94,

respectively. The fracture surfaces of both specimens show signs of oxidation. For both specimens, the degree of oxidation was higher near the edges of the fracture surface. However, oxidation appears to be more pronounced in the case of the specimen tested in steam. Some fiber pull-out can be seen in the interior of the fracture surfaces in Figure 93A and D, and Figure 94C and D.

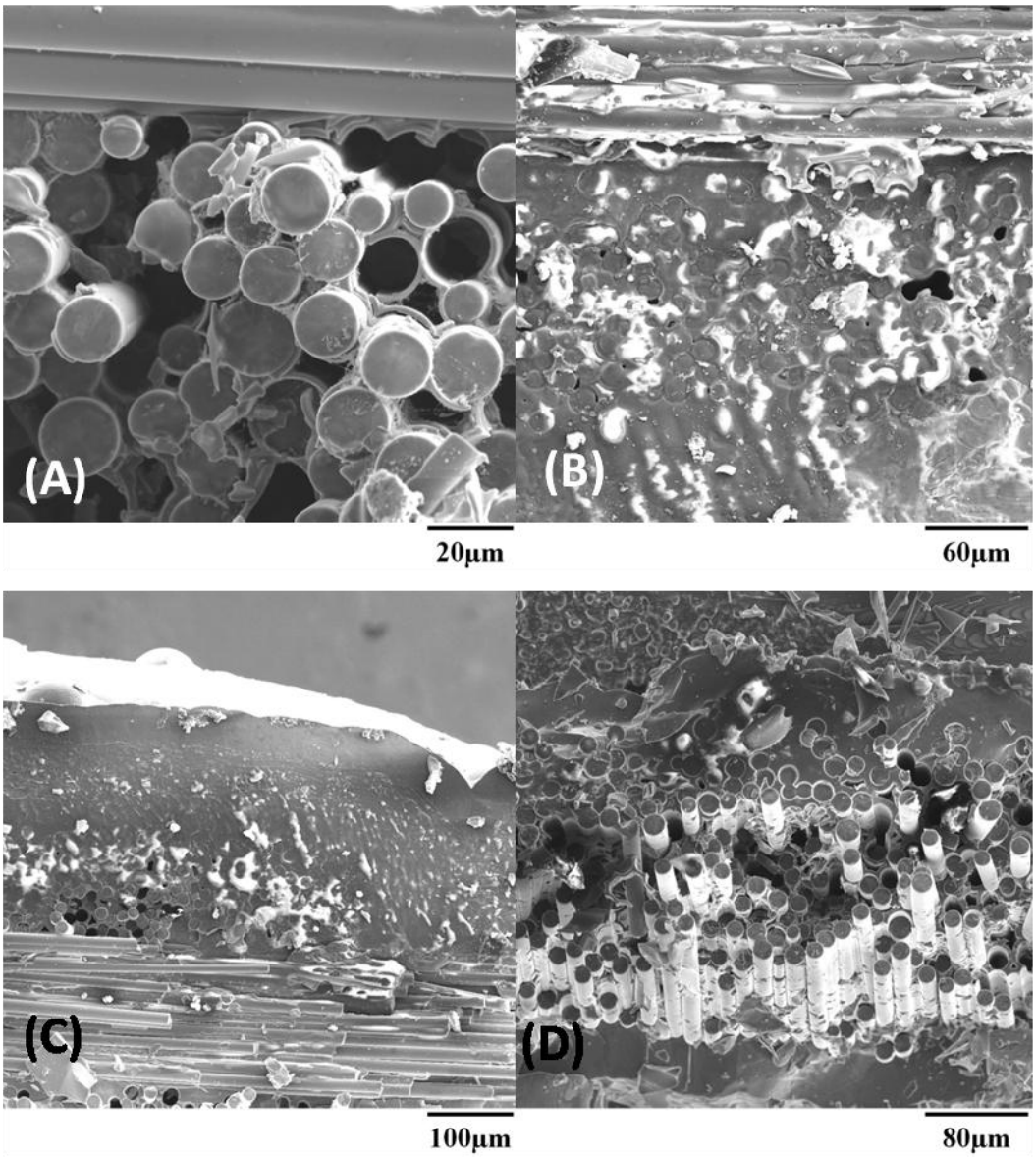

Figure 93: SEM micrographs of specimen P6-5 tested in fatigue at 10 Hz at 1200°C in air. σ_{max} = 140 MPa, N_f > 200,000, t_f > 5.6 h.

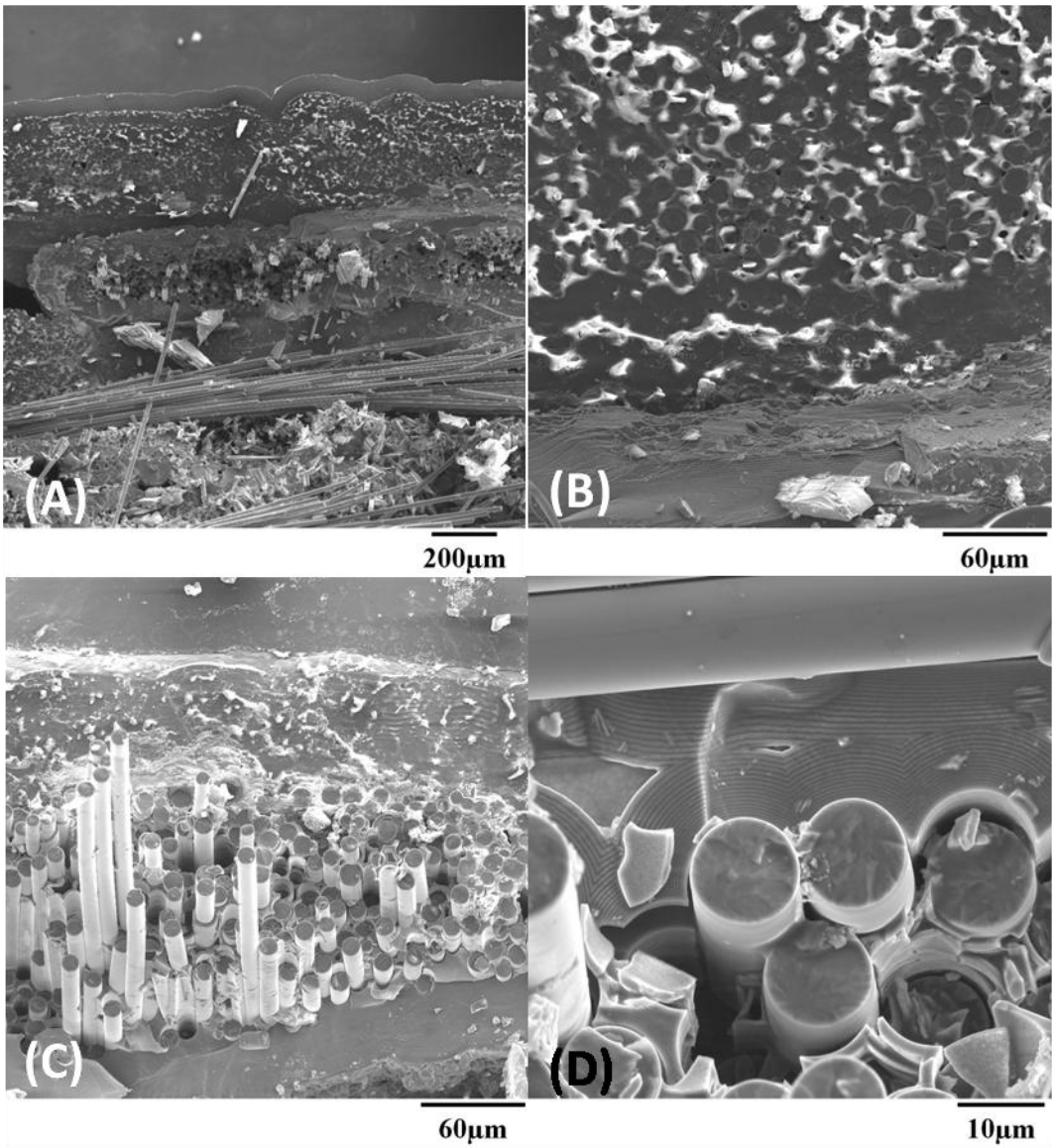

Figure 94: SEM micrographs of specimen P6-6 tested in fatigue at 10 Hz at 1200°C in steam. σ_{max} = 140 MPa, N_f = 39,849, t_f = 1.1 h.

Figure 95 shows an SEM micrograph of a polished interior surface of specimen P6-5 subjected to the 140 MPa fatigue test at 10 Hz at 1200°C in air. Specimen P6-5 was cut along the specimen axis (also the loading direction) in order to assess the damage development

throughout the specimen. A considerable amount of matrix cracking is observed in Figure 95. This is particularly noteworthy as this specimen achieved fatigue run-out. Note that more matrix cracking is seen in specimen P6-5 (Figure 95) than in specimen P5-4 (Figure 81), which also achieved a run-out in the 100 MPa fatigue test conducted at 1.0 Hz in air. This result is not surprising, as higher fatigue stress and higher fatigue frequency in the case of specimen P6-5 would cause more matrix cracks. Figure 96 shows higher magnification views of the interior surface shown in Figure 95. Matrix cracks are seen forming near the edges of the specimen.

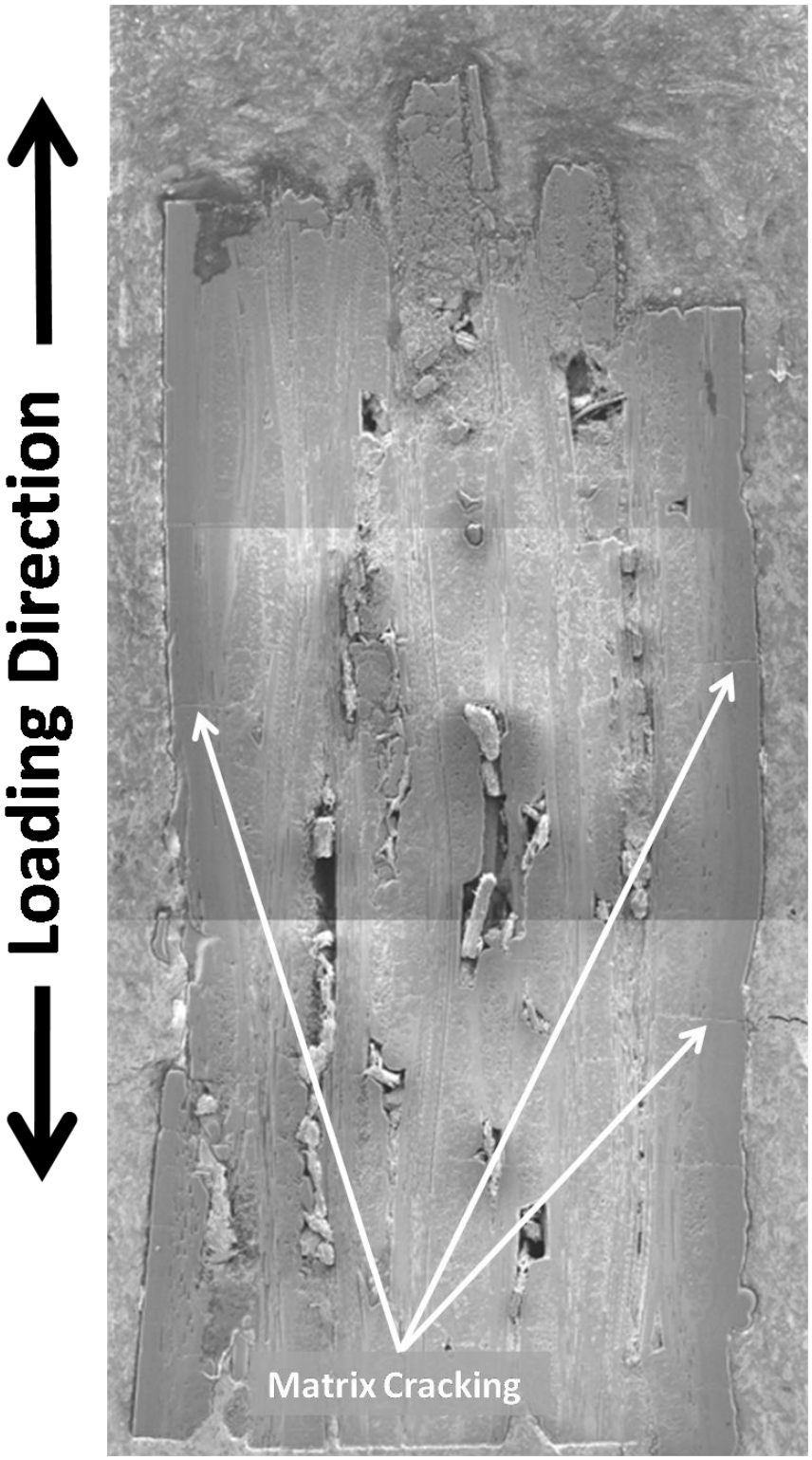

Figure 95: SEM micrograph of the specimen P6-5 tested in fatigue at 10 Hz at 1200°C in air showing an interior surface parallel to the specimen axis. σ_{max} = 140 MPa, N_f > 200,000, t_f > 5.6 h.

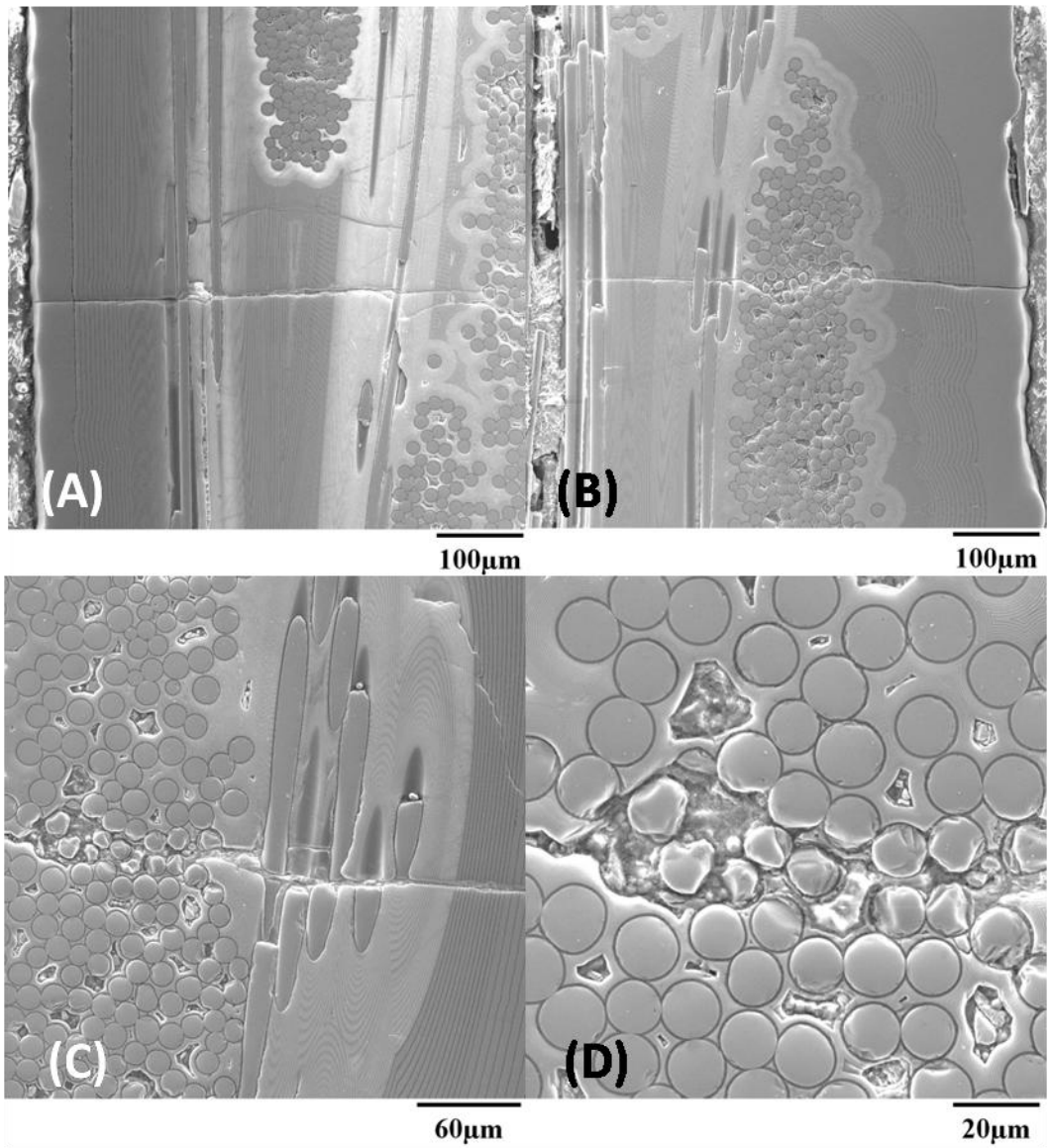

Figure 96: Higher magnification SEM micrographs of the specimen P6-5 tested in fatigue at 10 Hz at 1200°C in air. σ_{max} = 140 MPa, N_f > 200,000, t_f > 5.6 h.

Figure 97 shows an SEM micrograph of a polished interior surface of specimen P6-6 subjected to the 140 MPa fatigue test at 10 Hz at 1200°C in steam. Specimen P6-6 was cut along the specimen axis (also the loading direction) in order to assess the damage development throughout the specimen. An appreciable amount of matrix cracking is observed in Figure 97. Figure 98 shows higher magnification views of the interior surface shown in Figure 97. Figure

98 shows a crack propagating through the matrix and the fibers. In this case the weak fiber/matrix interface did not perform as intended. The matrix crack was not deflected around the fibers. When the highly oxidizing steam environment reached the fibers, oxidation occurred. As a result the fiber coating was degraded and replaced by the glass that formed due to oxidation. In this fashion, the weak fiber/matrix interface involving fiber coating was destroyed and fibers failed by fracture. Figure 99A shows a matrix crack initiating at the matrix void, while Figure 99B shows a crack propagating between the fibers. Micrographs in Figure 100 reveal that the fibers located near the fracture surface appear to have lost their fiber coating due to oxidation.

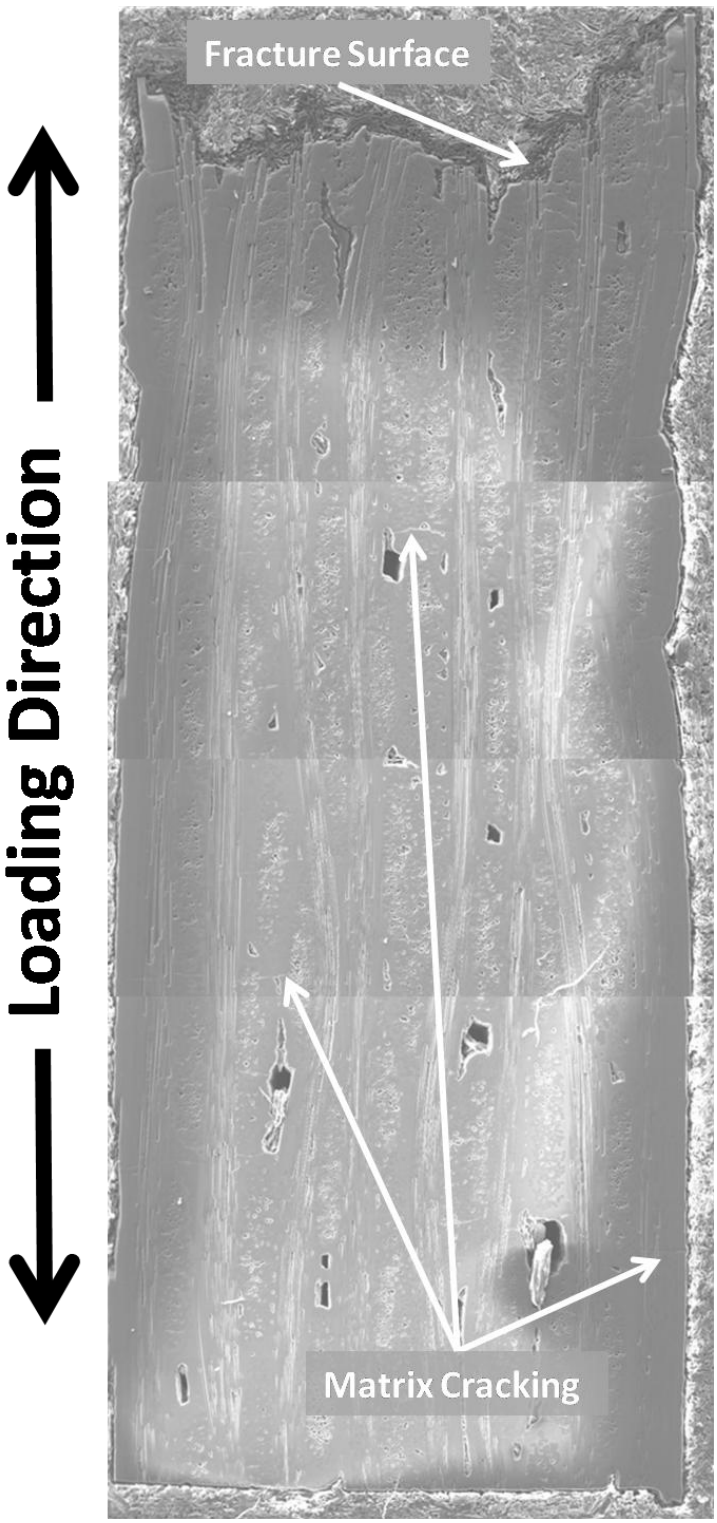

Figure 97: SEM micrograph of the specimen P6-6 tested in fatigue at 10 Hz at 1200°C in steam showing an interior surface parallel to the specimen axis. σ_{max} = 140 MPa, N_f = 39,849, t_f = 1.1 h.

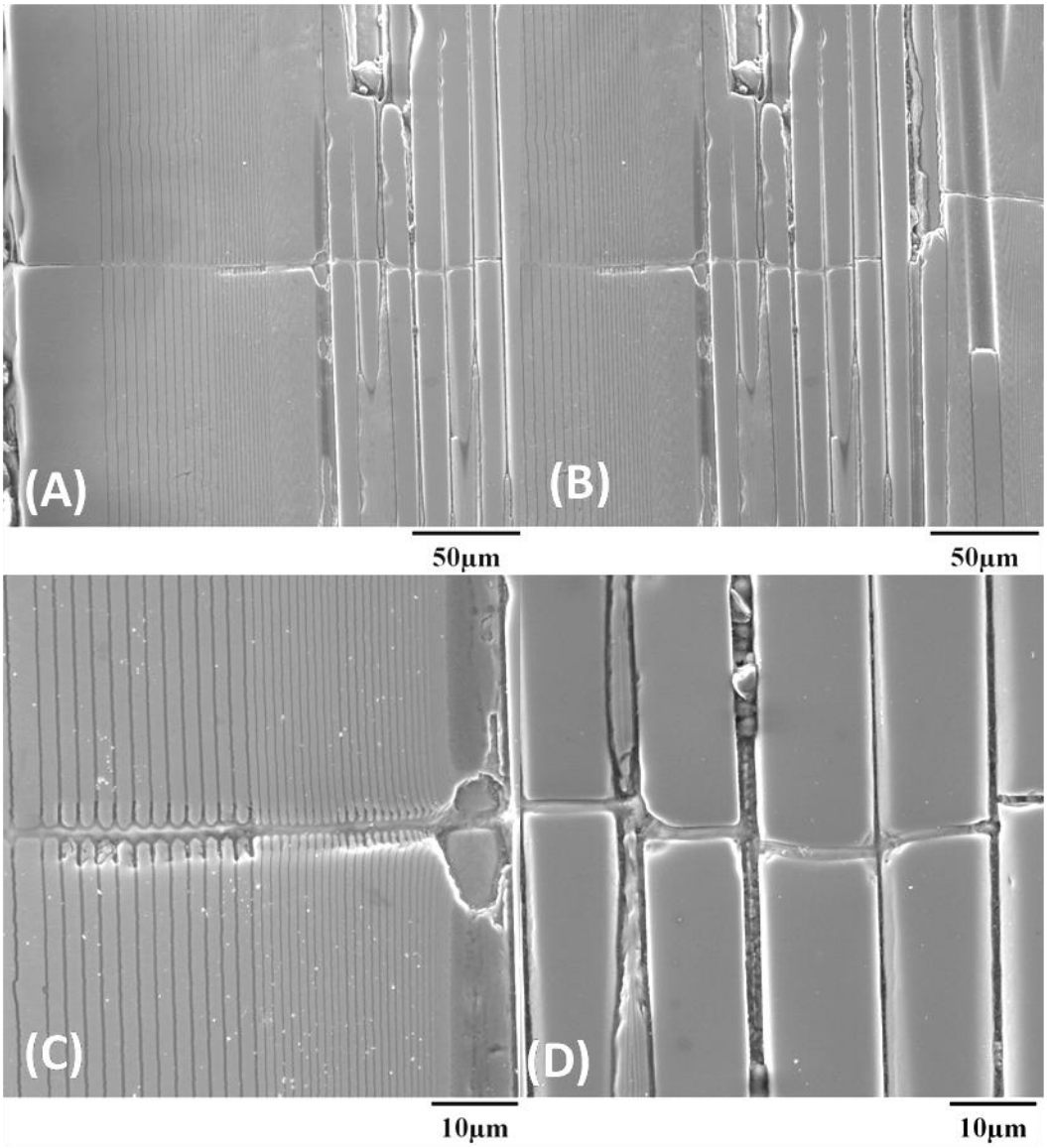

Figure 98: Higher magnification SEM micrographs of the specimen P6-6 tested in fatigue at 10 Hz at 1200°C in steam showing an interior surface parallel to the specimen axis. σ_{max} = 140 MPa, N_f = 39,849, t_f = 1.1 h.

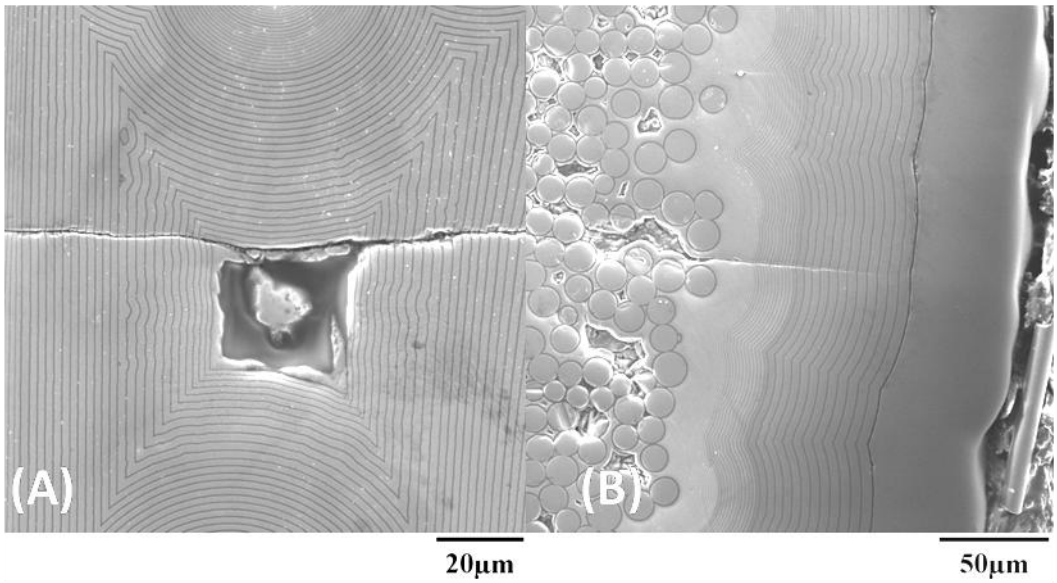

Figure 99: Higher magnification SEM micrographs of the specimen P6-6 tested in fatigue at 10 Hz at 1200°C in steam showing (a) a matrix crack initiating at the matrix void and (b) a crack propagating between the fibers. σ_{max} = 140 MPa, N_f = 39,849, t_f = 1.1 h.

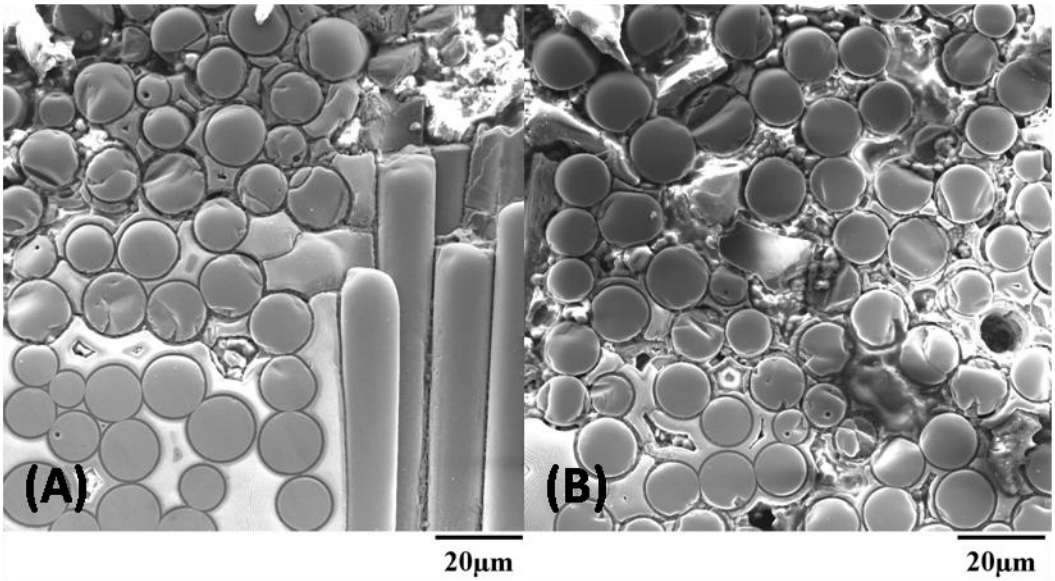

Figure 100: Higher magnification SEM micrographs of the specimen P6-6 tested in fatigue at 10 Hz at 1200°C in steam showing an interior surface parallel to the specimen axis. Fibers located near the fracture surface appear to have lost their fiber coating. σ_{max} = 140 MPa, N_f = 39,849, t_f = 1.1 h.

VI. Conclusion and Recommendations

6.1 Conclusion

The Hi-Nicalon/PyC/HyprSiC advanced CMC tested in this effort demonstrated excellent fatigue resistance in laboratory air at 1200°C. Fatigue life of the CMC decreased as the fatigue stress increased and the frequency decreased. The presence of steam degraded the fatigue resistance of the material at 0.1 Hz and 10 Hz. At 1.0 Hz, the presence of steam appeared to have little influence on the fatigue resistance for the fatigue stress levels < 140 MPa. The presence of steam degraded the fatigue performance of the CMC at 1.0 Hz for the fatigue stress level of 140 MPa. The Hi-Nicalon/PyC/HyprSiC CMC exhibited considerable strain ratcheting during fatigue testing. Furthermore, reduction in stiffness with increasing fatigue cycles was dramatic. Fatigue frequency and maximum stress level appeared to influence rate of reduction in stiffness and the rate of strain accumulation with cycling.

Prior fatigue appeared to have a large effect on the retained tensile strength of the Hi-Nicalon/PyC/HyprSiC. Specimens tested in air retained 42-61% of their tensile strength and specimen tested in steam retained 59-75% of their tensile strength. The modulus loss averaged 35% in steam and 52% in air.

Optical micrographs of the fracture surfaces of the specimens revealed that the specimens tested under the same loading conditions produced similar fracture surface regardless of testing environment. The SEM micrographs of the fracture surfaces of the failed specimens showed increased oxidization in specimens tested in a steam environment.

However, the oxidation was confined to a small region around the perimeter of the specimen's fracture surface. Little or no effects of oxidization were observed in the interior of the fracture surface, where some fiber pullout was also seen. The SEM micrographs of the polished interior surfaces parallel to the specimen axis of select specimens show that glass forming on the crack faces due to oxidation acts as a crack closing mechanism. The glass formation was found in specimens tested in air and in steam. However, the effect was more pronounced in specimens tested in steam.

6.2 Recommendations

The large strains produced at lower frequencies suggest that time-dependent deformation such as creep should be investigated for this material. It is recommended that the creep tests be conducted at multiple stress levels for Hi-Nicalon/PyC/HyprSiC CMC. Creep should also be investigated for the oxidation inhibited matrix alone. CVD flat plats of the oxidation inhibited matrix and pure SiC should be compared to investigate creep of the oxidation inhibited matrix used for this study. Additionally, to get more confidence in the data presented in this manuscript, multiple tests should be performed in air and in steam for each loading condition investigated in this research. Also, tests should be performed at additional maximum stress levels at 0.1 Hz, 1.0 Hz and 10 Hz to better define the S-N curves.

Appendix A

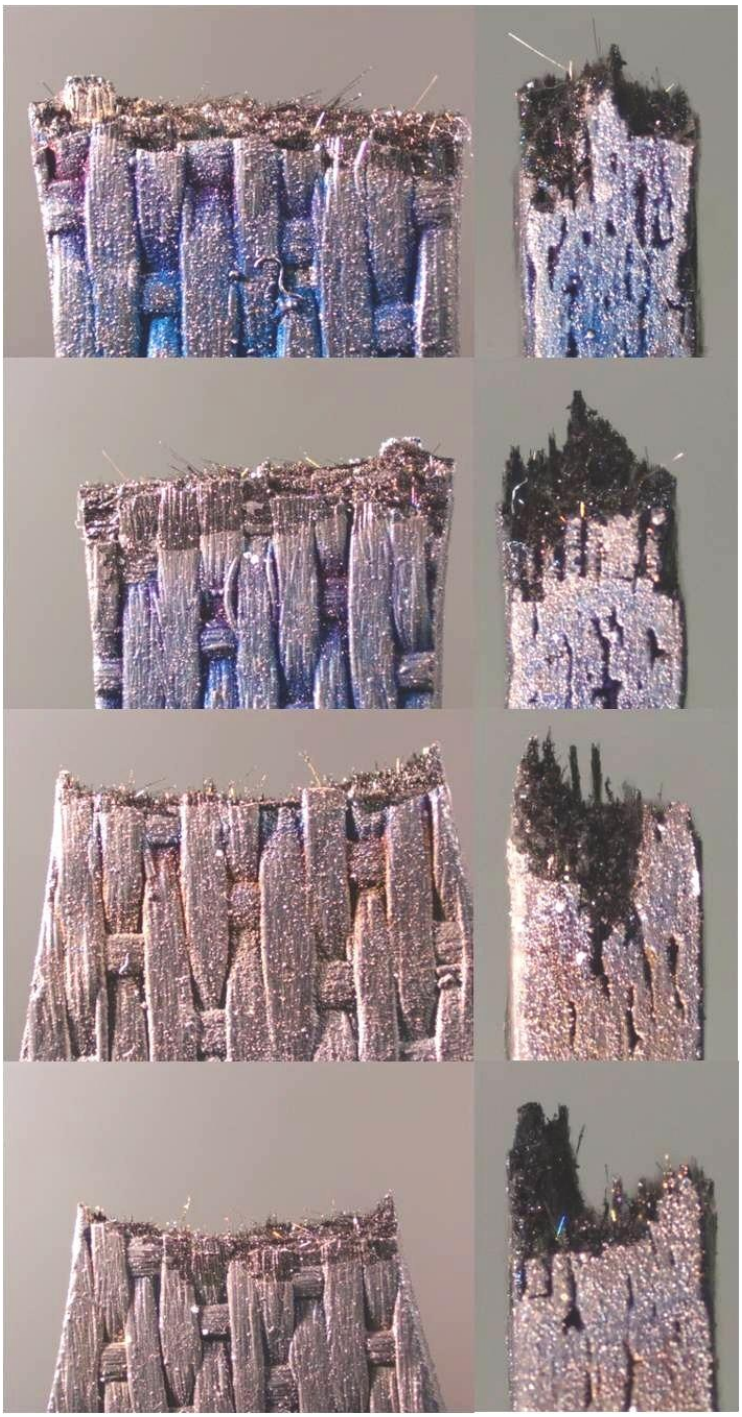

Figure 101: Optical micrographs of the fracture surface produced in tensile test to failure conducted at 0.05mm/sec at 1200˚C air on specimen P5-1.

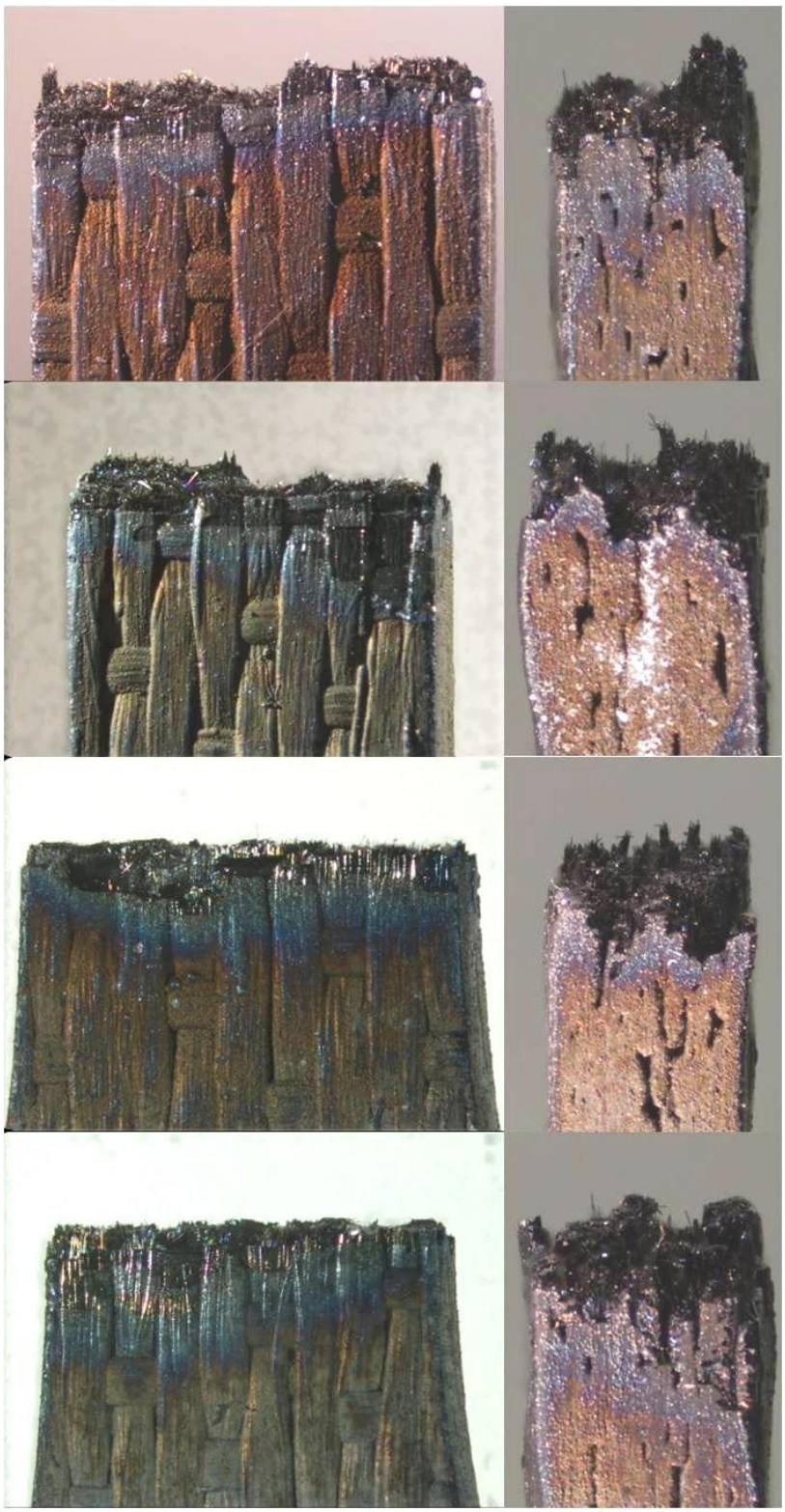

Figure 102: Optical micrographs of the fracture surface produced in tensile test to failure conducted at 0.05mm/sec at 1200˚C air on specimen P5-2.

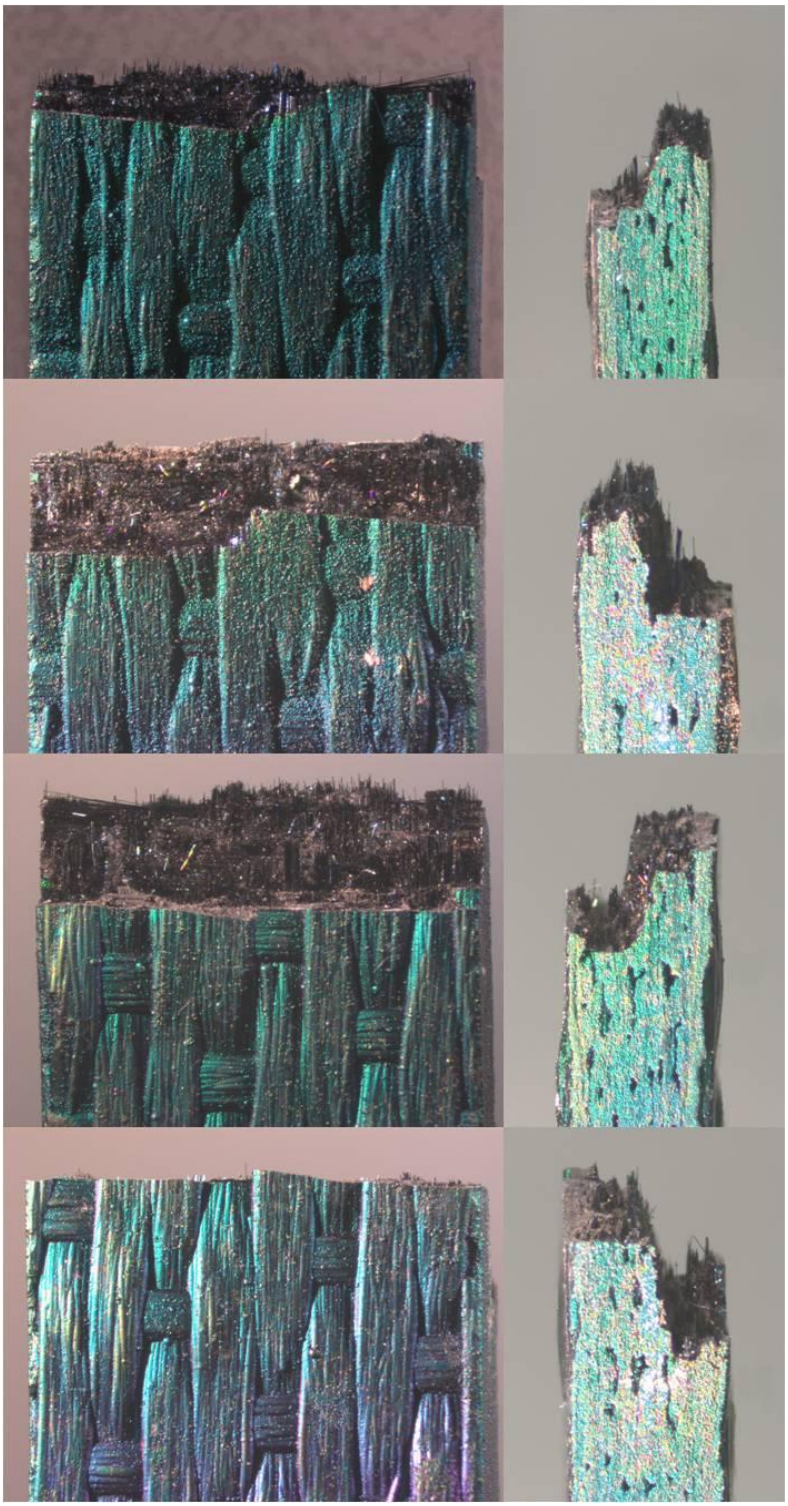

Figure 103: Optical micrographs of fracture surface of specimen P5-3 tested in fatigue at 1.0 Hz in air at 1200˚C. σ_{max} = 120 MPa, N_f = 92,468, t_f = 25.7 h.

Figure 104: Optical micrographs of fracture surface of specimen P5-4 tested in fatigue at 1.0 Hz in air at 1200˚C. σ_{max} = 100 MPa, N_f = 200,000, t_f = 55.6 h.

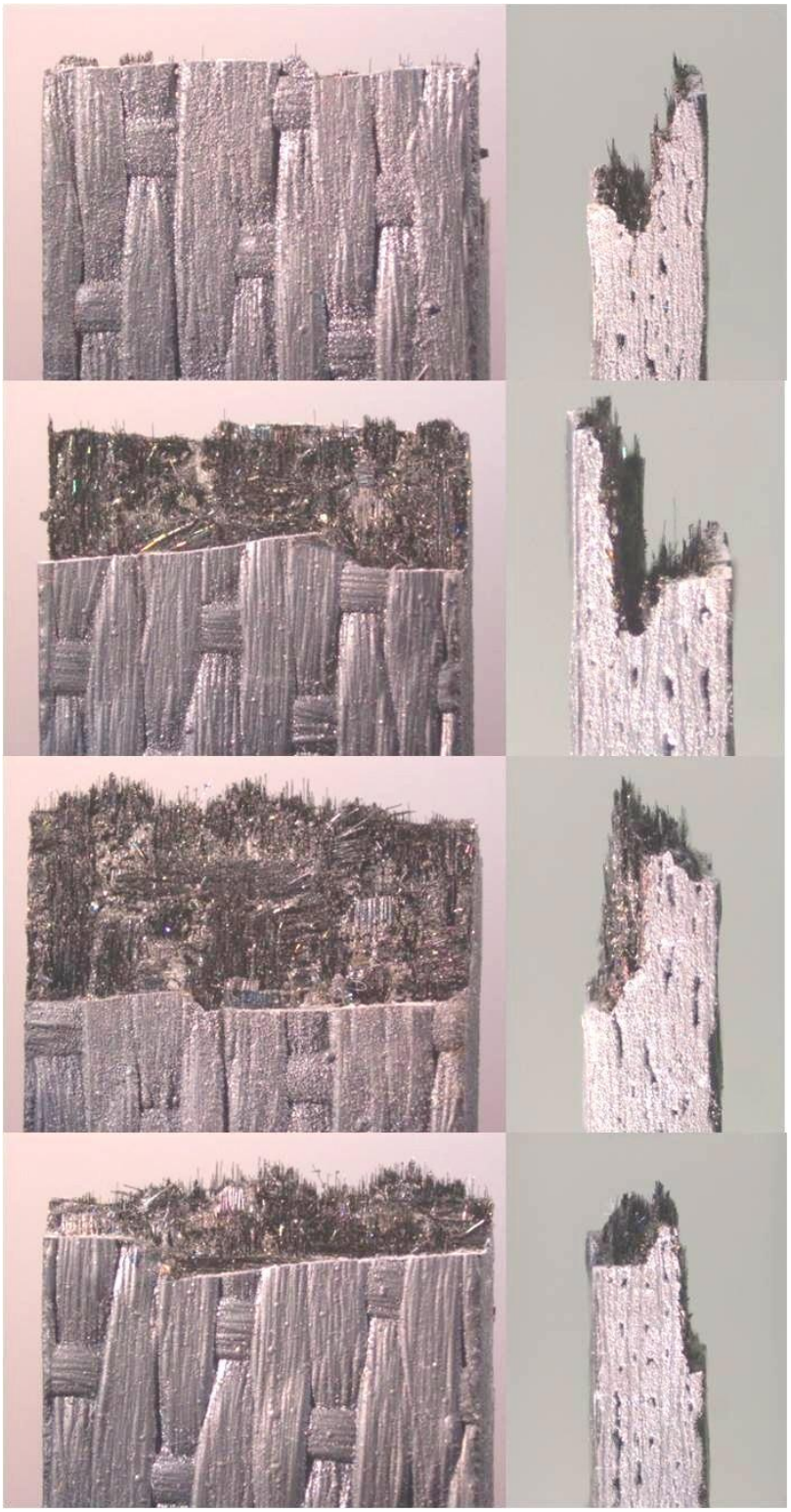

Figure 105: Optical micrographs of fracture surface of specimen P5-5 tested in fatigue at 1.0 Hz in steam at 1200˚C. σ_{max} = 100 MPa, N_f = 200,000, t_f = 55.6 h.

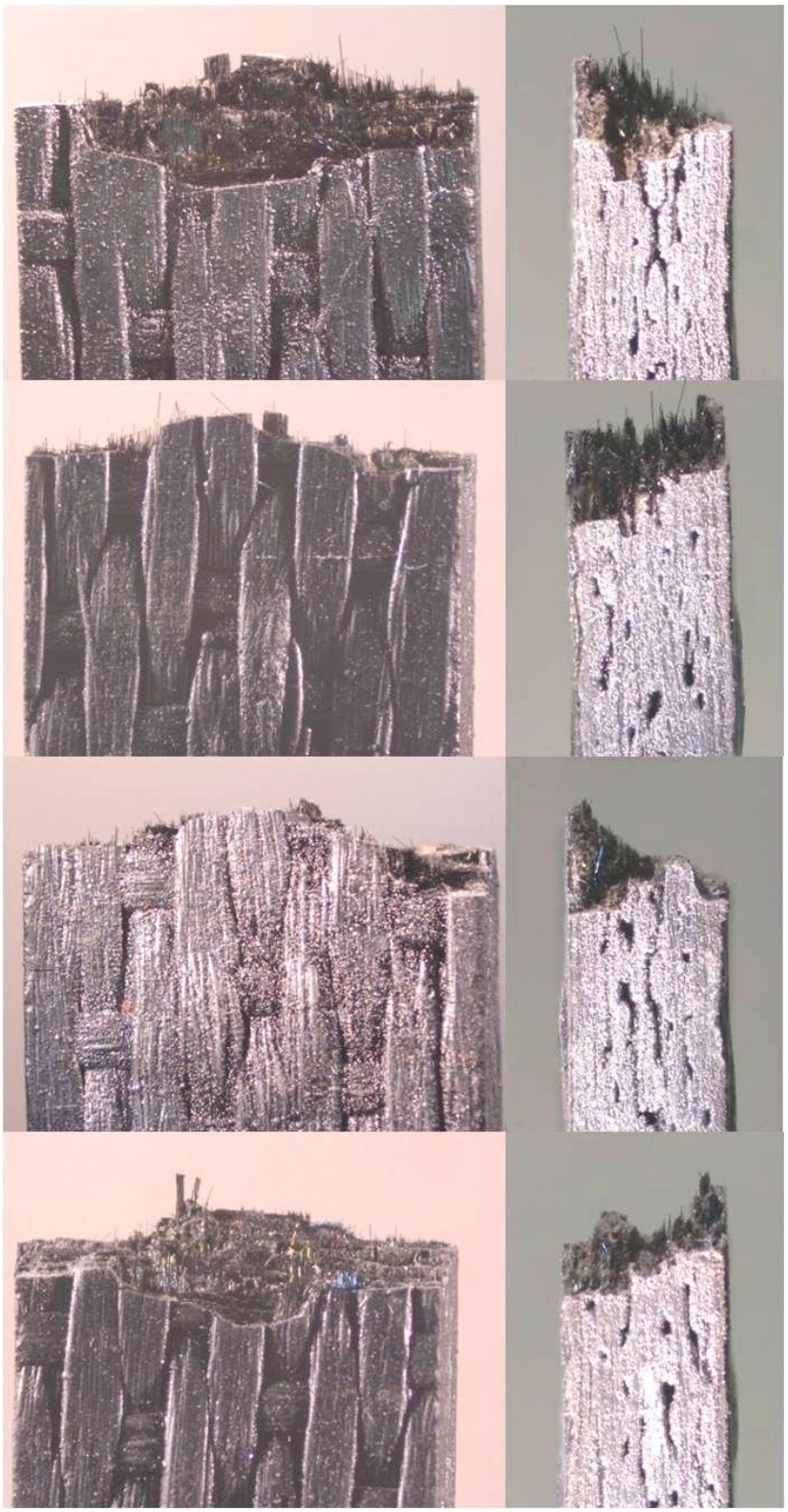

Figure 106: Optical micrographs of fracture surface of specimen P5-6 tested in fatigue at 1.0 Hz in steam at 1200˚C. σ_{max} = 120 MPa, N_f = 119,931, t_f = 33.3 h.

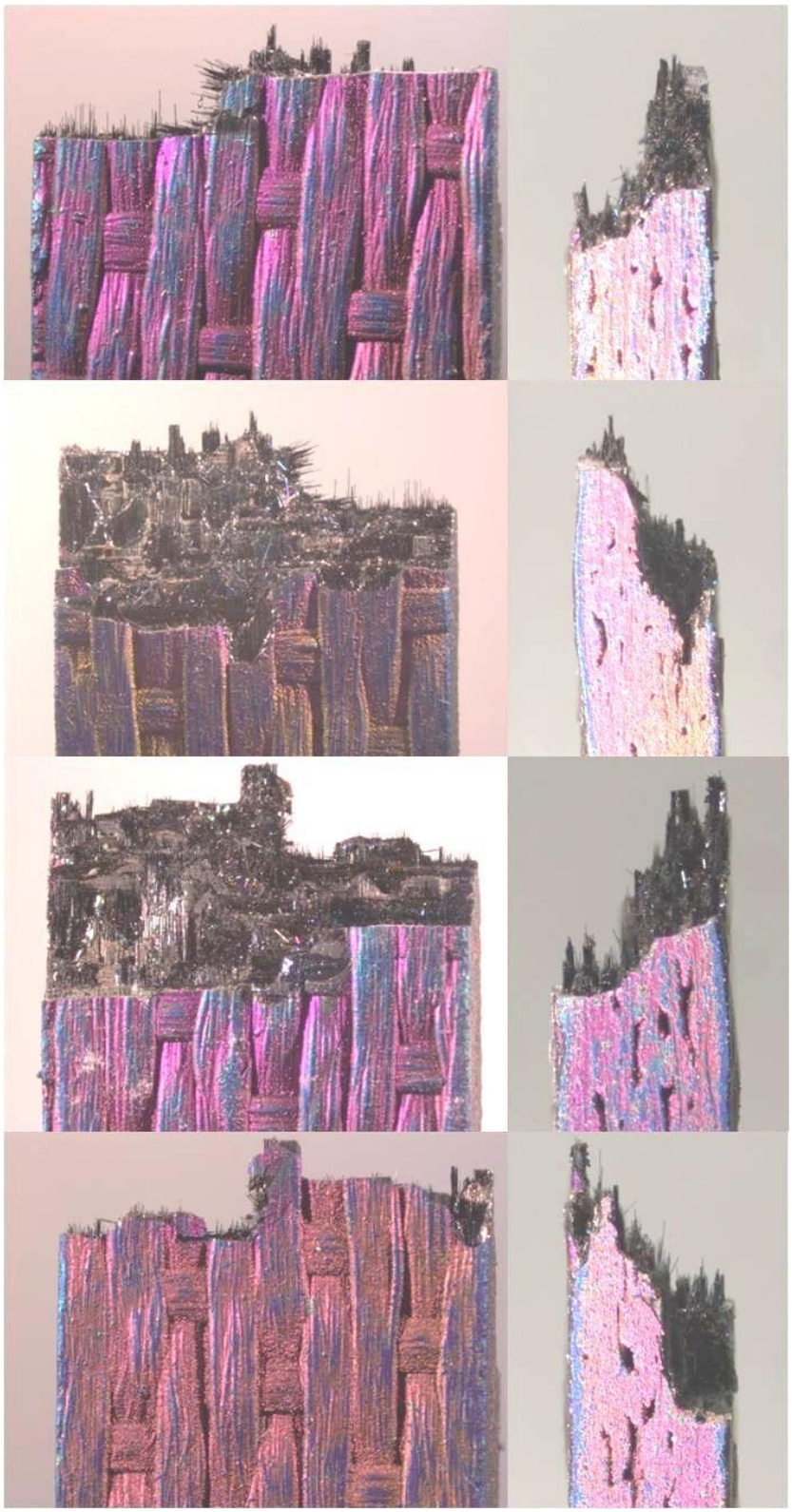

Figure 107: Optical micrographs of fracture surface of specimen P5-7 tested in fatigue at 1.0 Hz in air at 1200˚C. σ_{max} = 130 MPa, N_f = 70,309, t_f = 19.5 h.

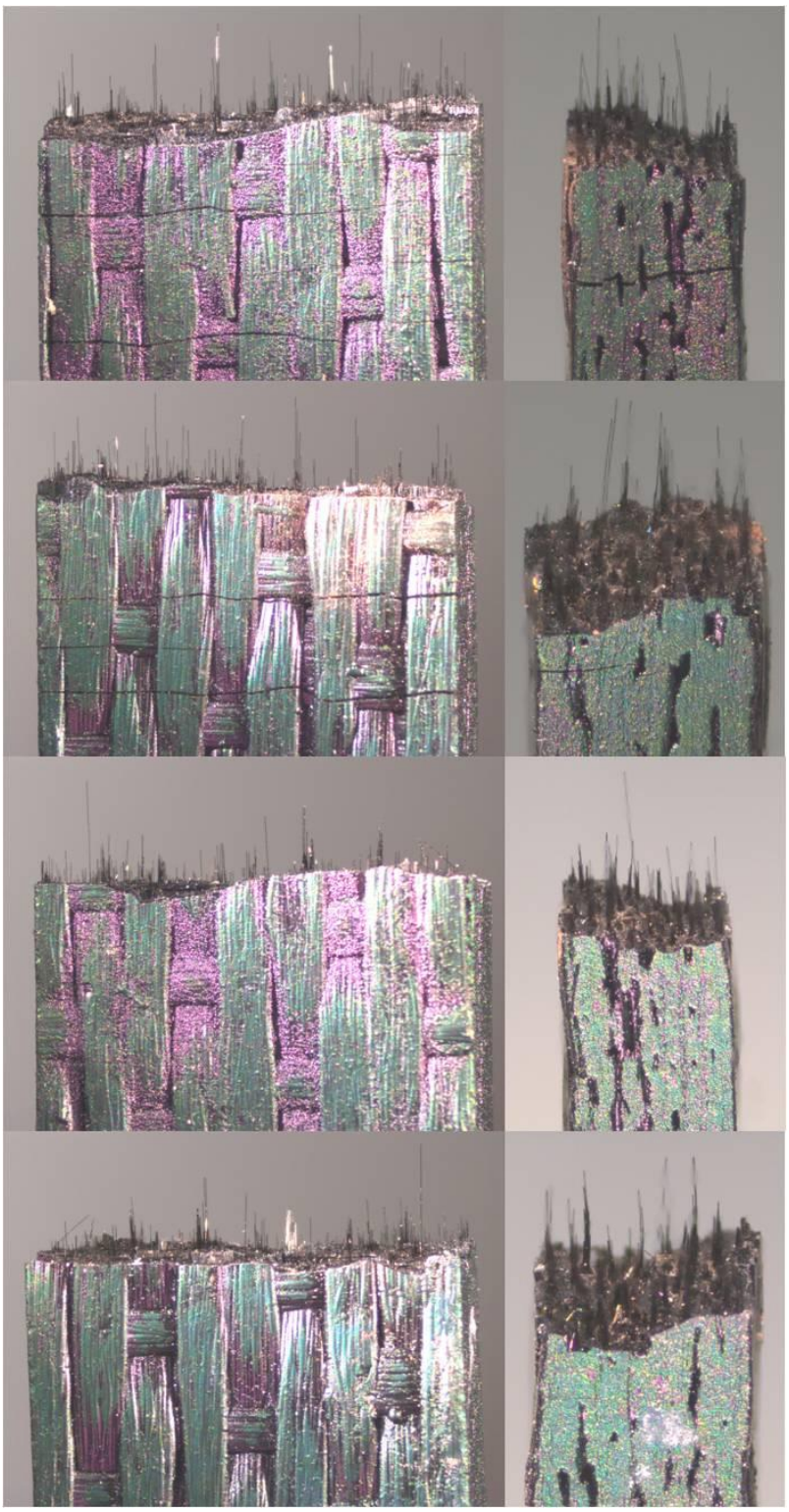

Figure 108: Optical micrographs of fracture surface of specimen P5-8 tested in fatigue at 0.1 Hz in air at 1200˚C. σ_{max} = 100 MPa, N_f = 24,925, t_f = 69.2 h.

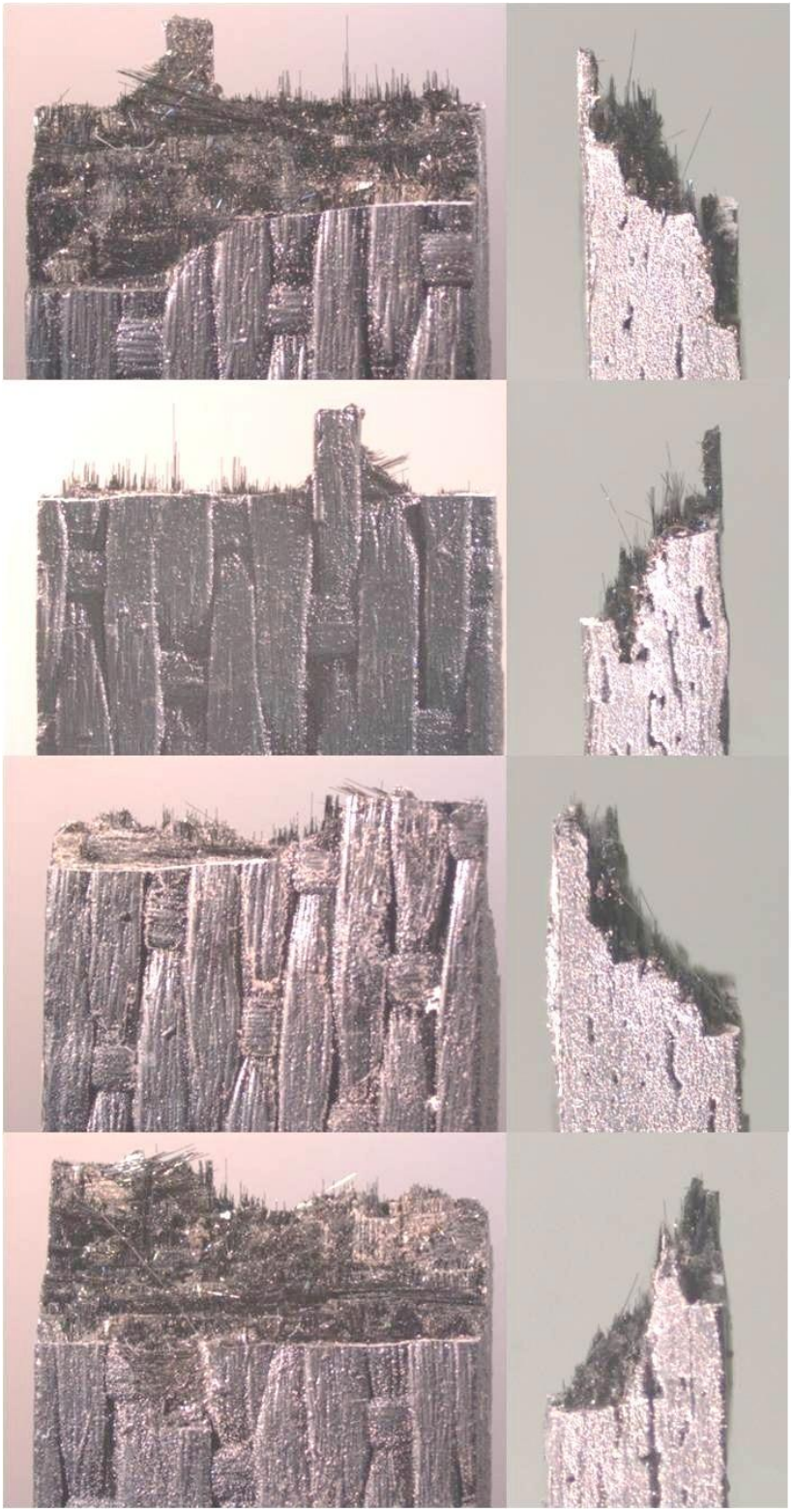

Figure 109: Optical micrographs of fracture surface of specimen P5-9 tested in fatigue at 1.0 Hz in steam at 1200˚C. σ_{max} = 130 MPa, N_f = 98,462, t_f = 27.4 h.

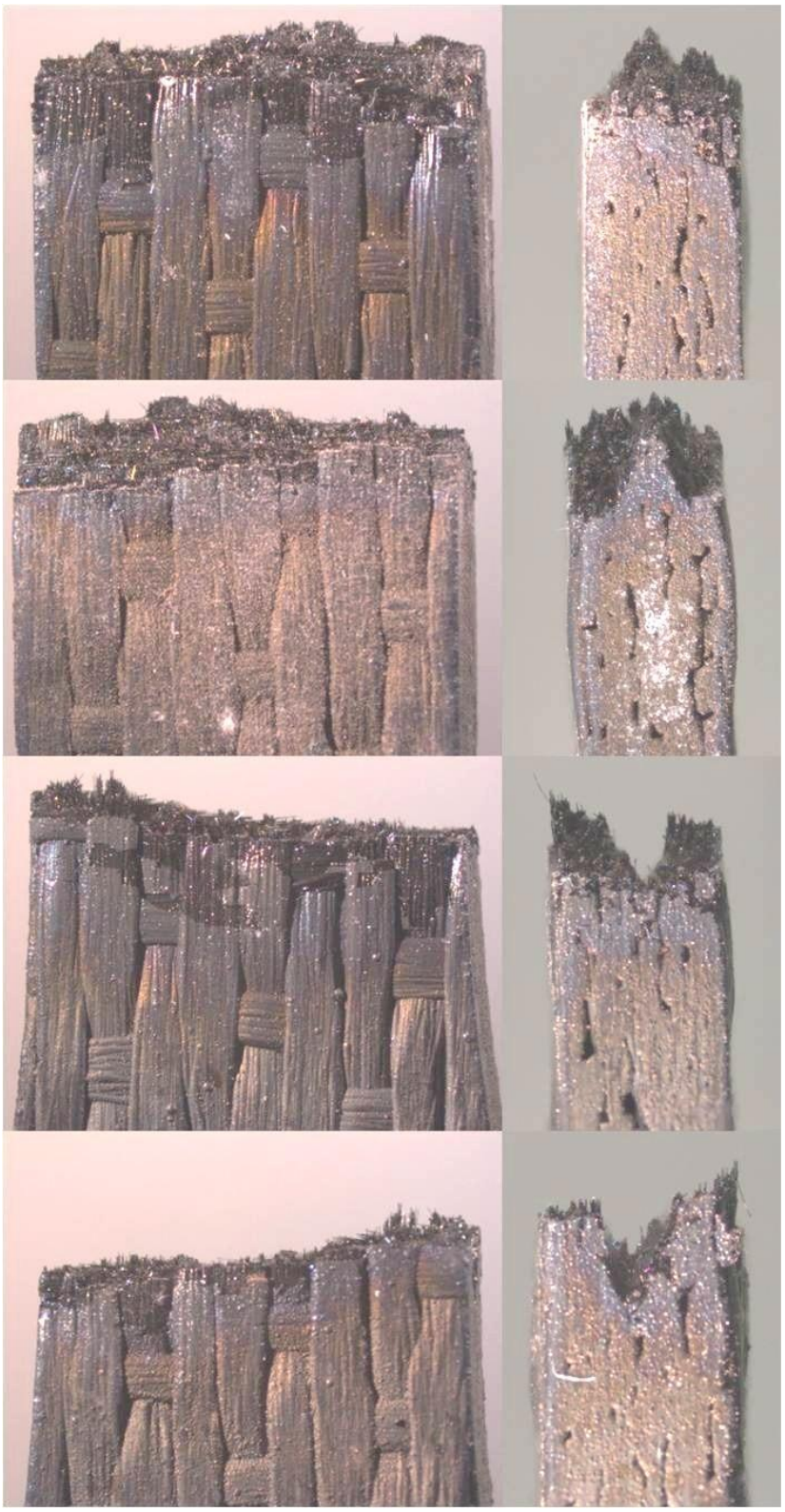

Figure 110: Optical micrographs of fracture surface of specimen P6-1 tested in tension to failure in air at 1200˚C.

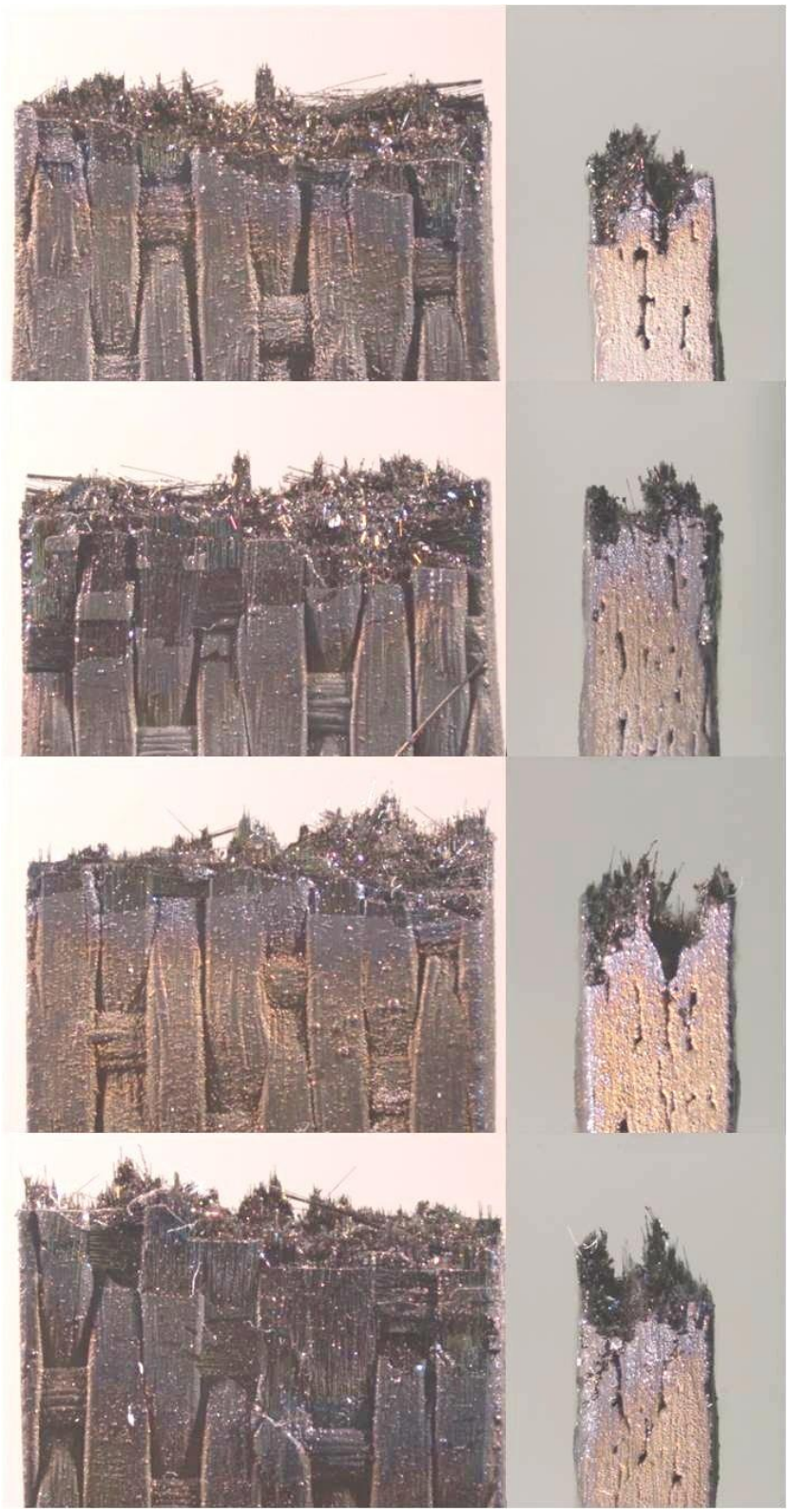

Figure 111: Optical micrographs of fracture surface of specimen P6-2 tested in tension to failure in air at 1200˚C.

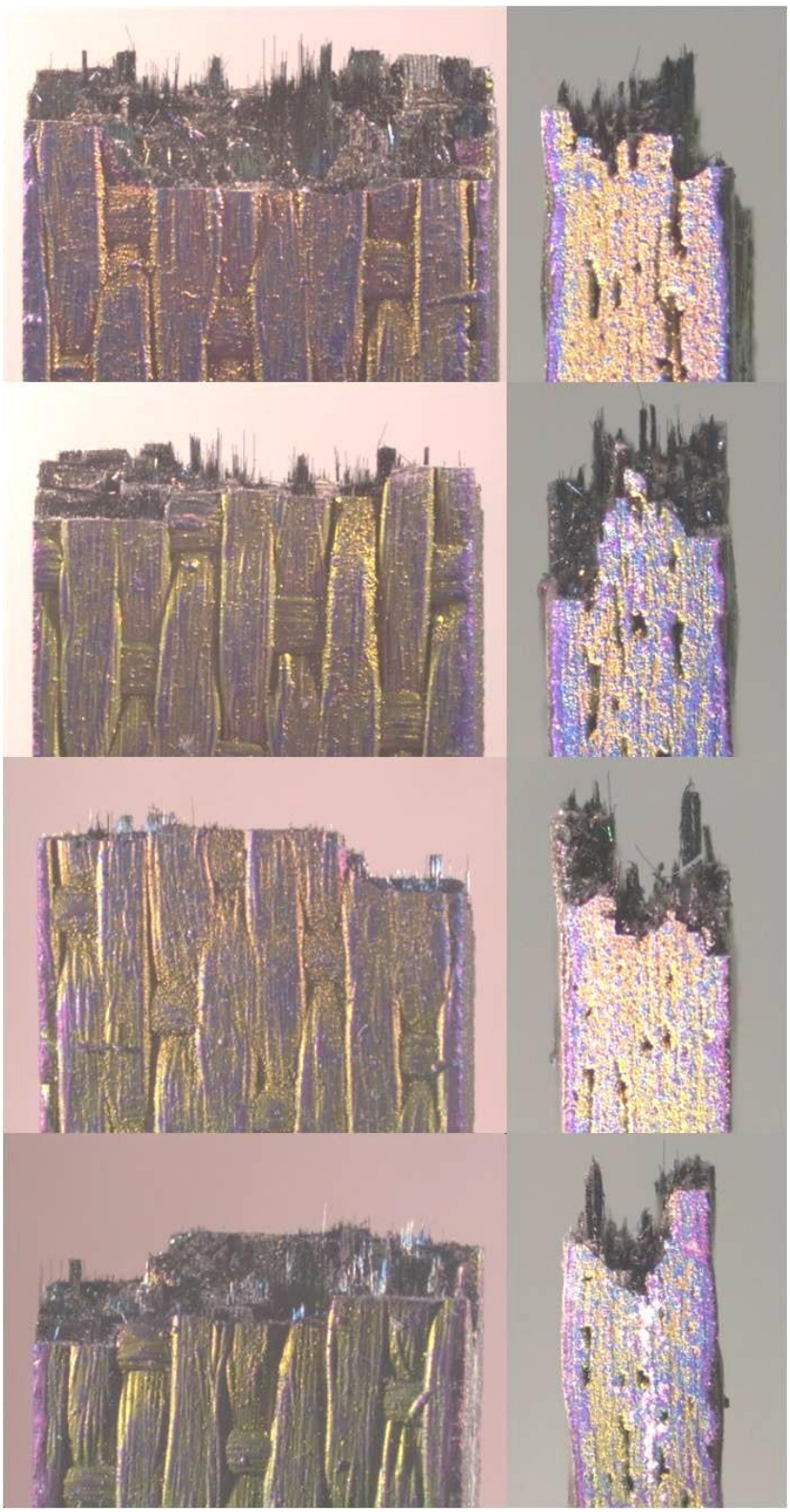

Figure 112: Optical micrographs of fracture surface of specimen P6-3 tested in fatigue at 1.0 Hz in air at 1200˚C. σ_{max} = 140 MPa, N_f = 63,458, t_f = 17.6 h.

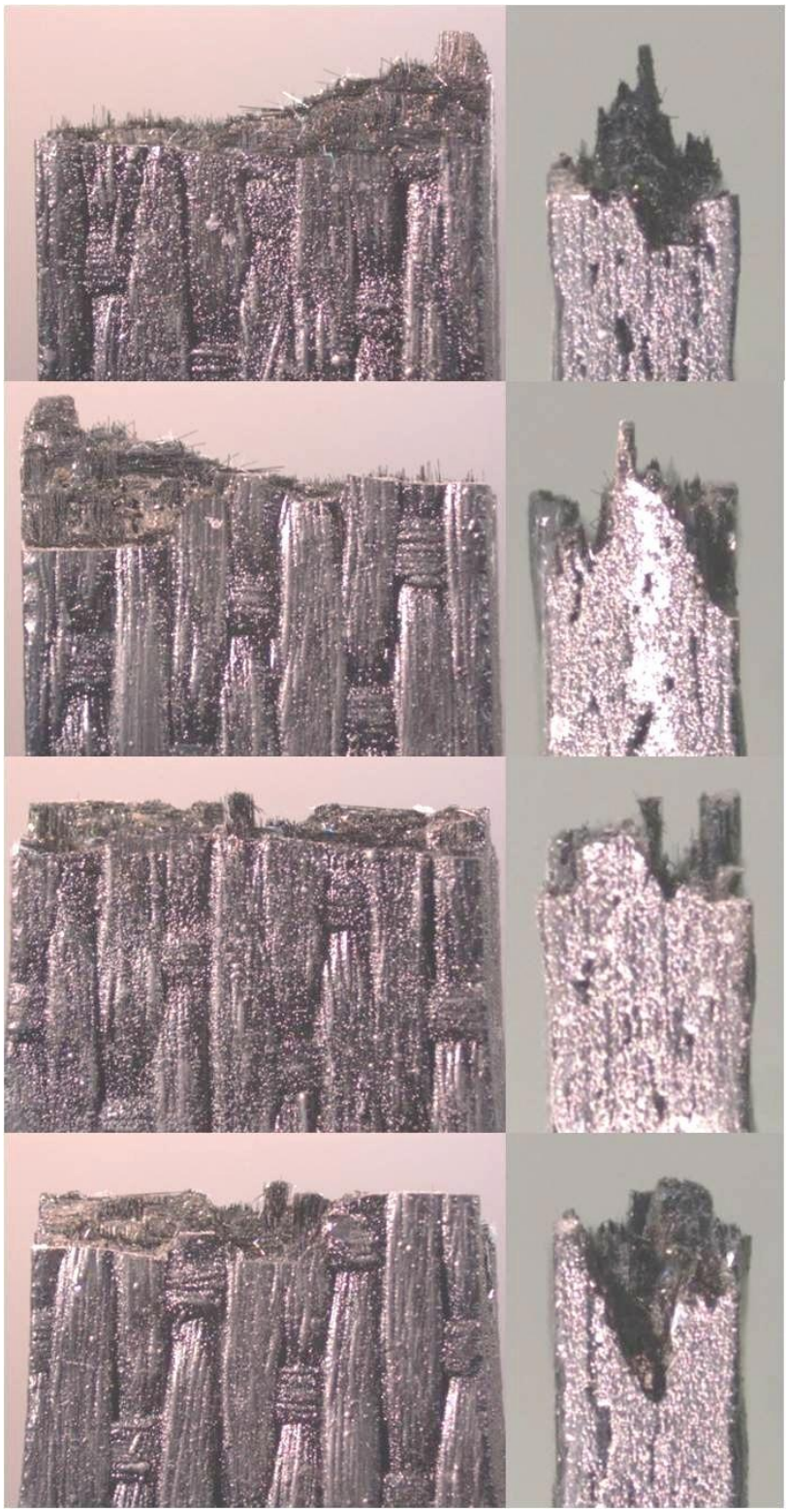

Figure 113: Optical micrographs of fracture surface of specimen P6-4 tested in fatigue at 1.0 Hz in steam at 1200˚C. σ_{max} = 140 MPa, N_f = 36,679, t_f = 10.2 h.

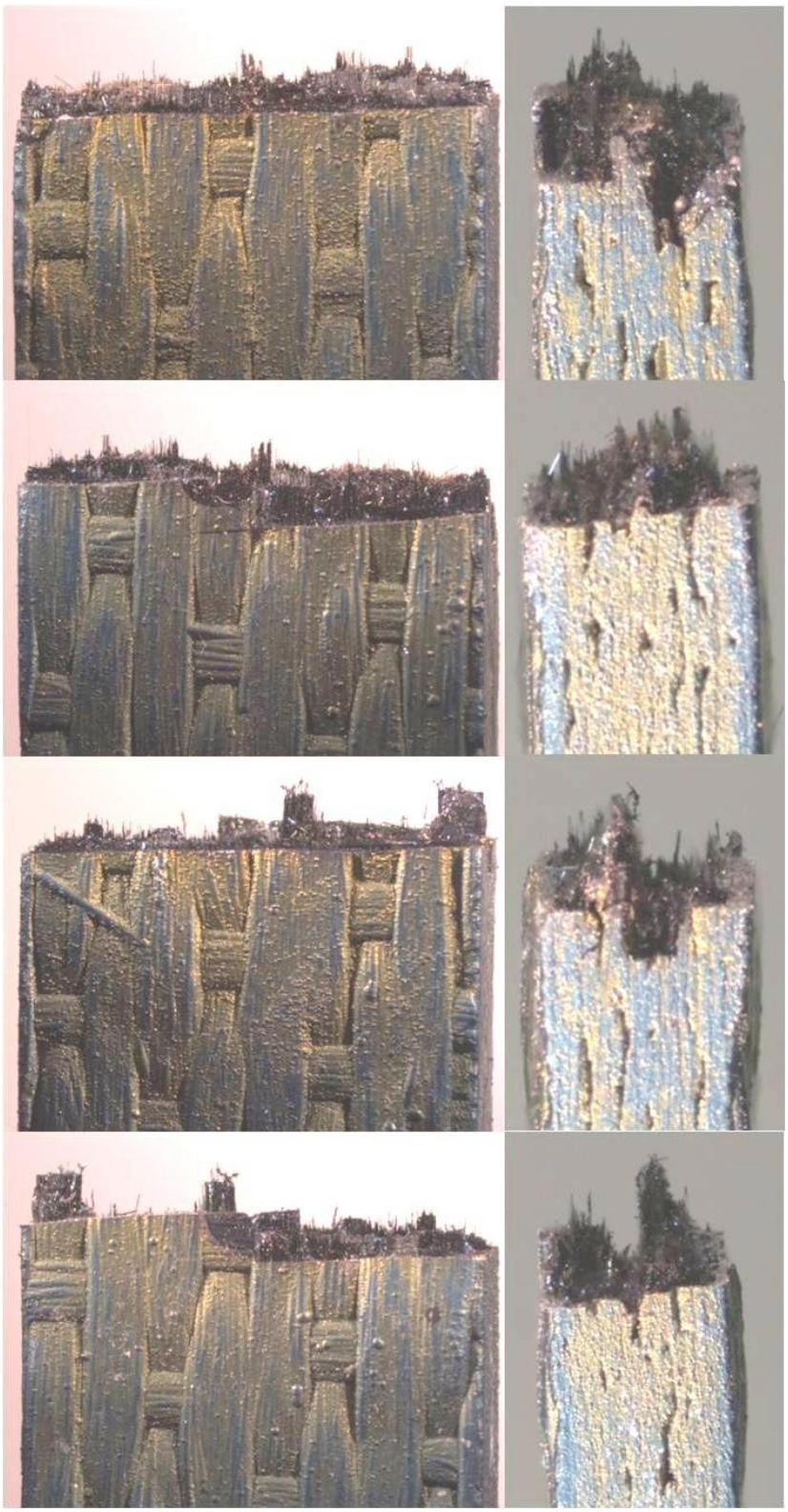

Figure 114: Optical micrographs of fracture surface of specimen P6-5 tested in fatigue at 10 Hz in air at 1200˚C. σ_{max} = 140 MPa, N_f = 200,000, t_f = 5.6 h.

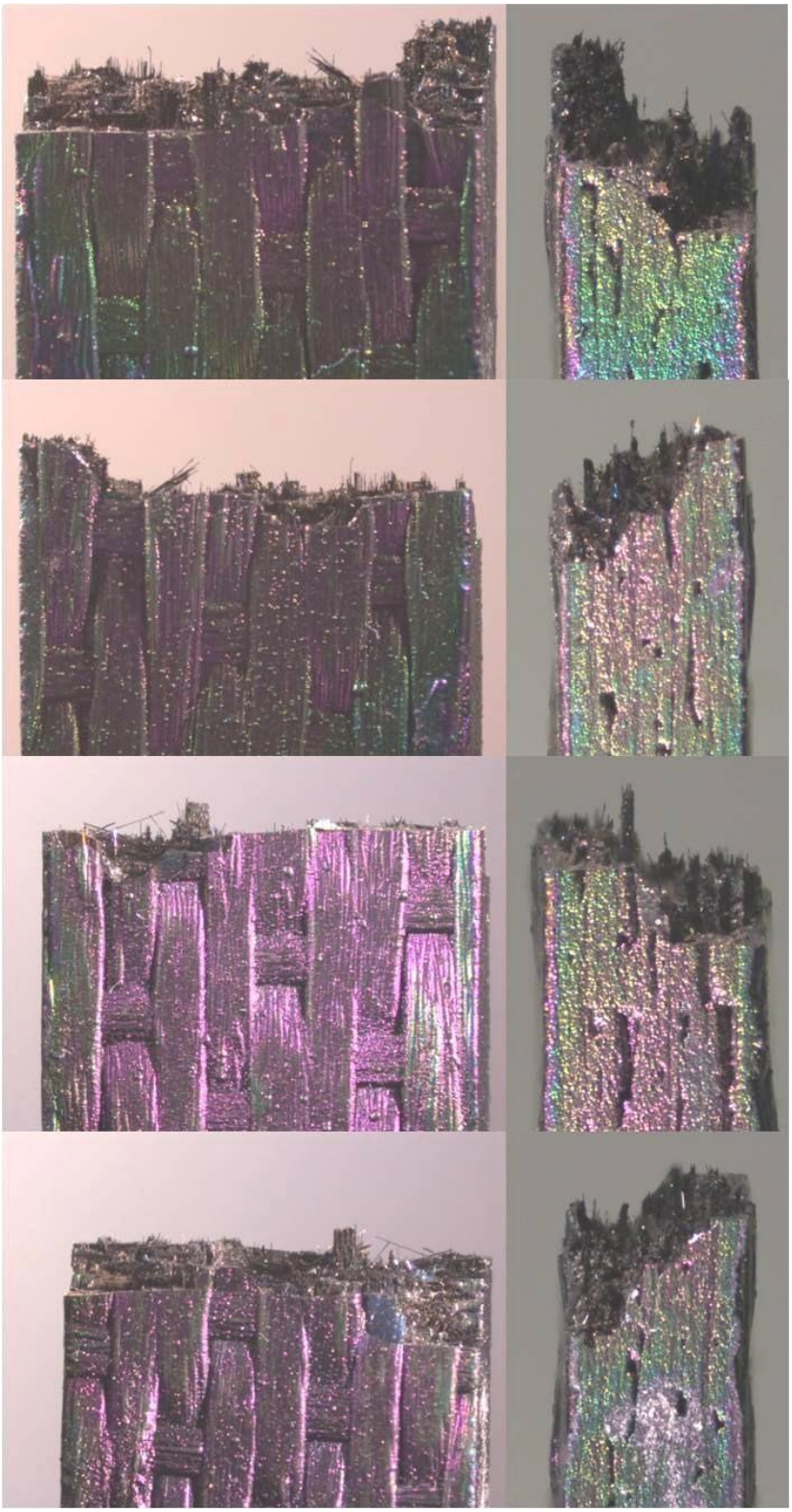

Figure 115: P6-6 Optical micrographs of fracture surface of specimen P6-6 tested in fatigue at 10 Hz in steam at 1200˚C. σ_{max} = 140 MPa, N_f = 39,849, t_f = 1.1 h.

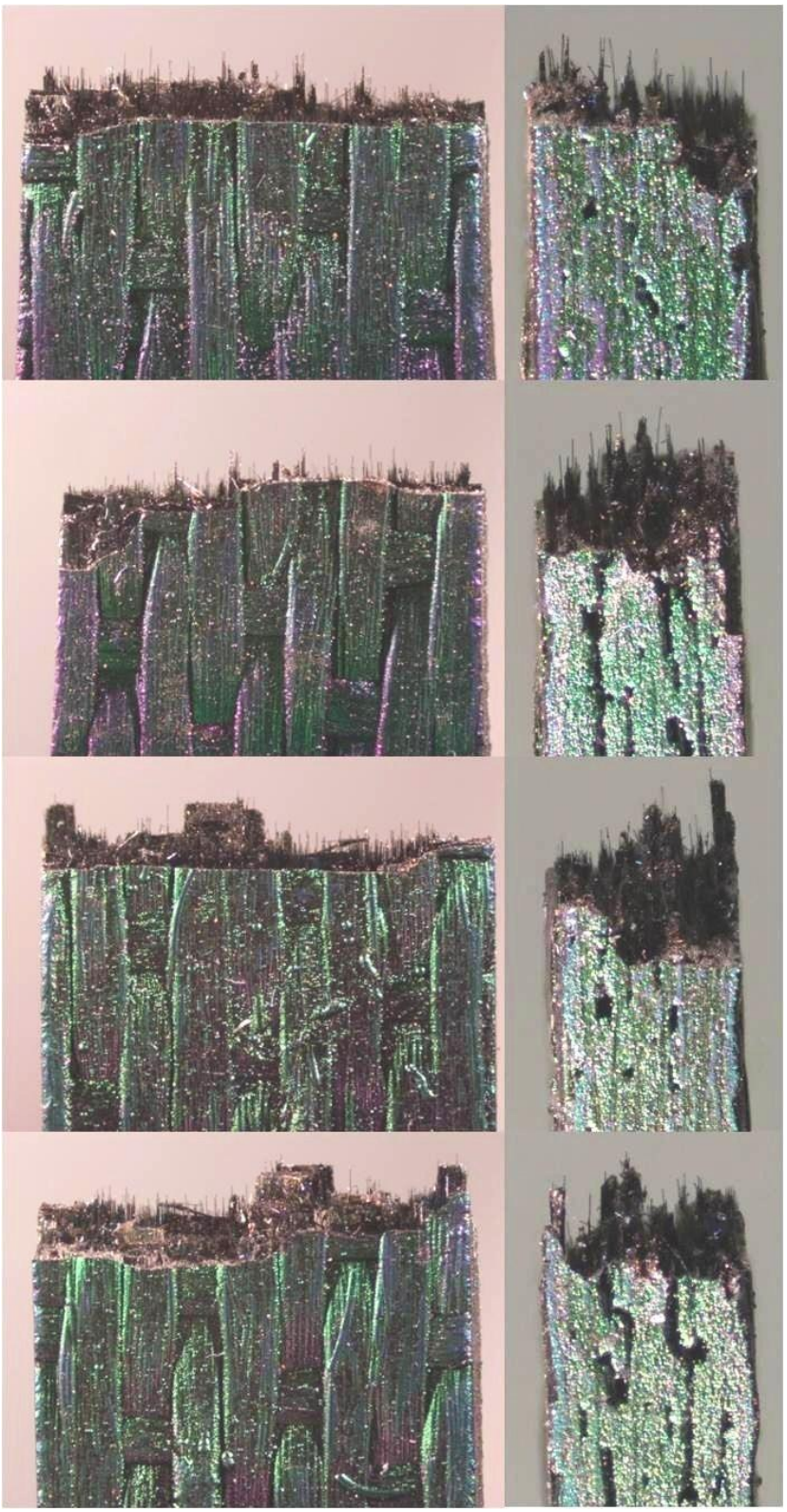

Figure 116: Optical micrographs of fracture surface of specimen P6-7 tested in fatigue at 0.1 Hz in air at 1200˚C. σ_{max} = 140 MPa, N_f = 30,712, t_f = 85.3 h.

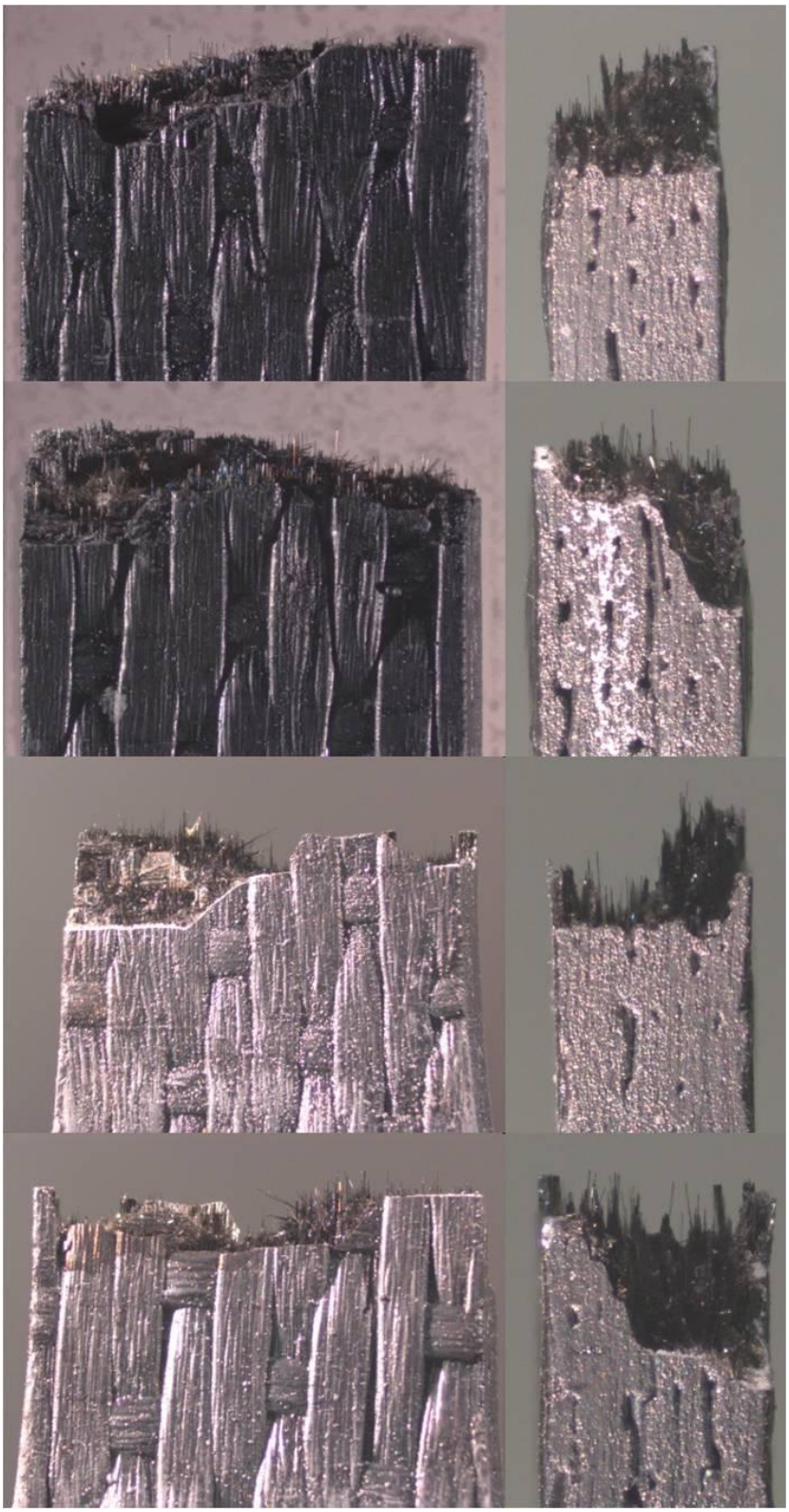

Figure 117: Optical micrographs of fracture surface of specimen P6-8 tested in fatigue at 0.1 Hz in steam at 1200˚C. σ_{max} = 140 MPa, N_f = 11,323, t_f = 31.5 h.

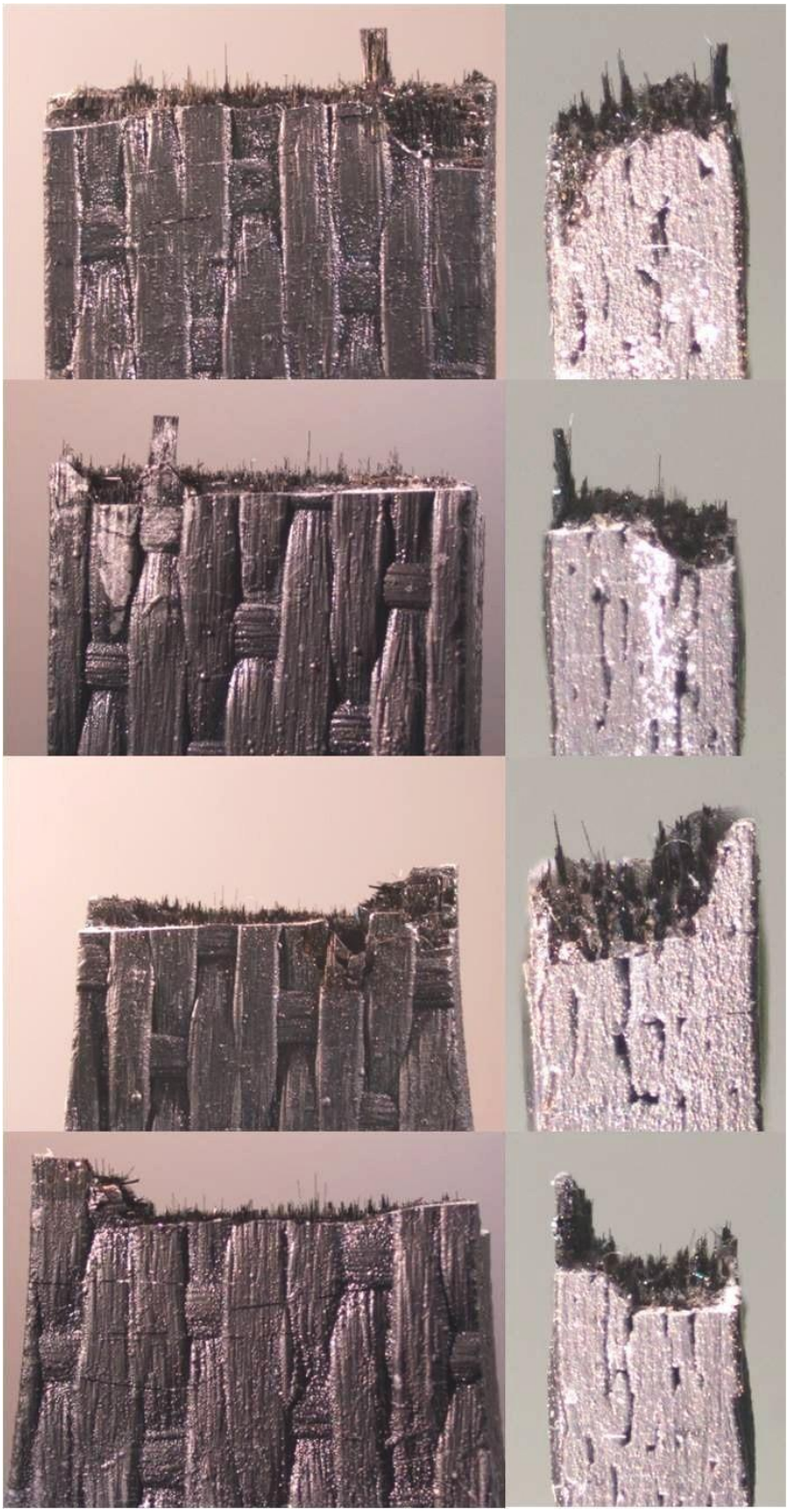

Figure 118: Optical micrographs of fracture surface of specimen P6-9 tested in fatigue at 0.1 Hz in steam at 1200˚C. σ_{max} = 130 MPa, N_f = 19,542, t_f = 54.3 h.

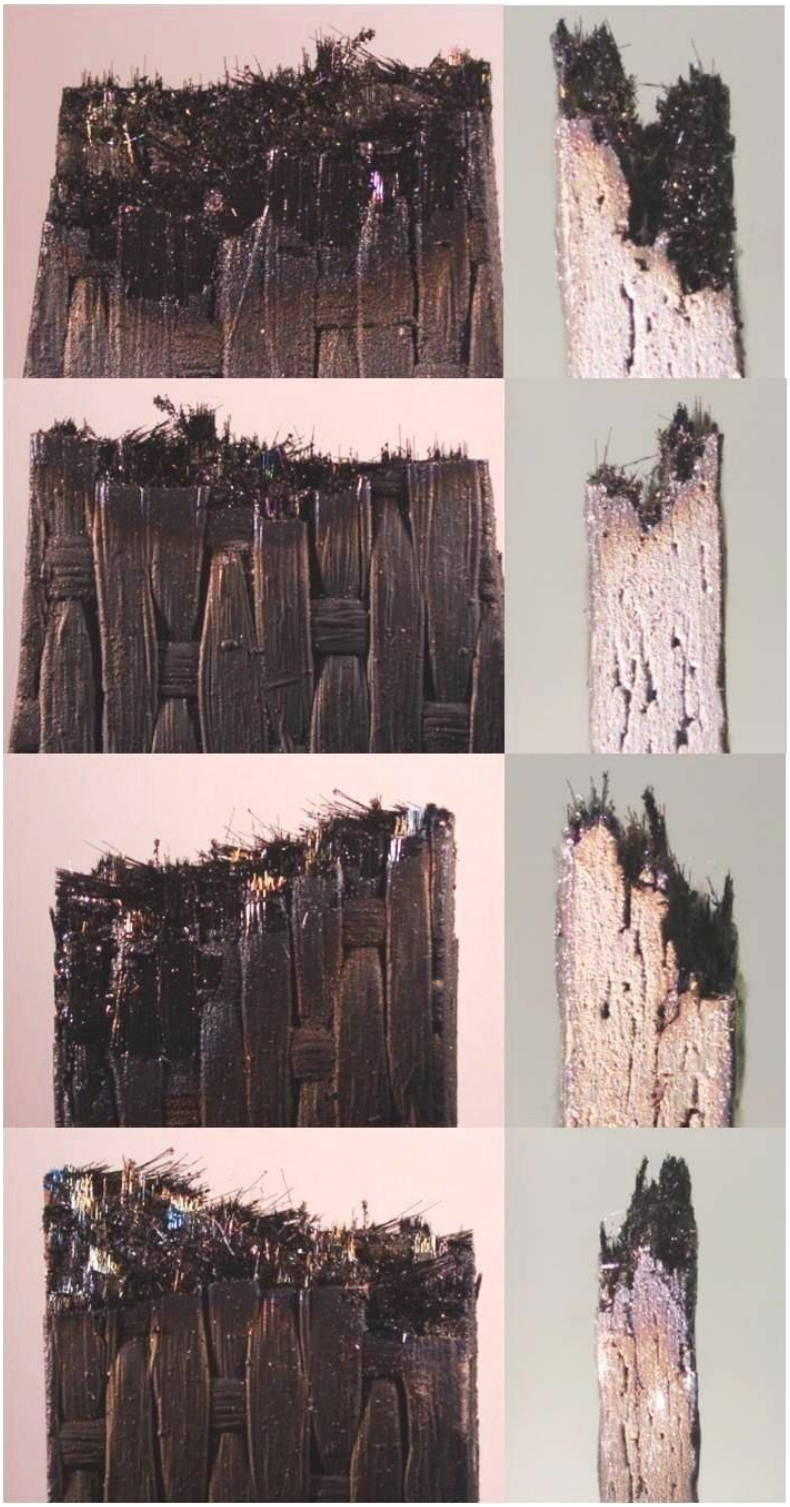

Figure 119: Optical micrographs of fracture surface of specimen P7-1 tested in tension to failure in air at 1200˚C.

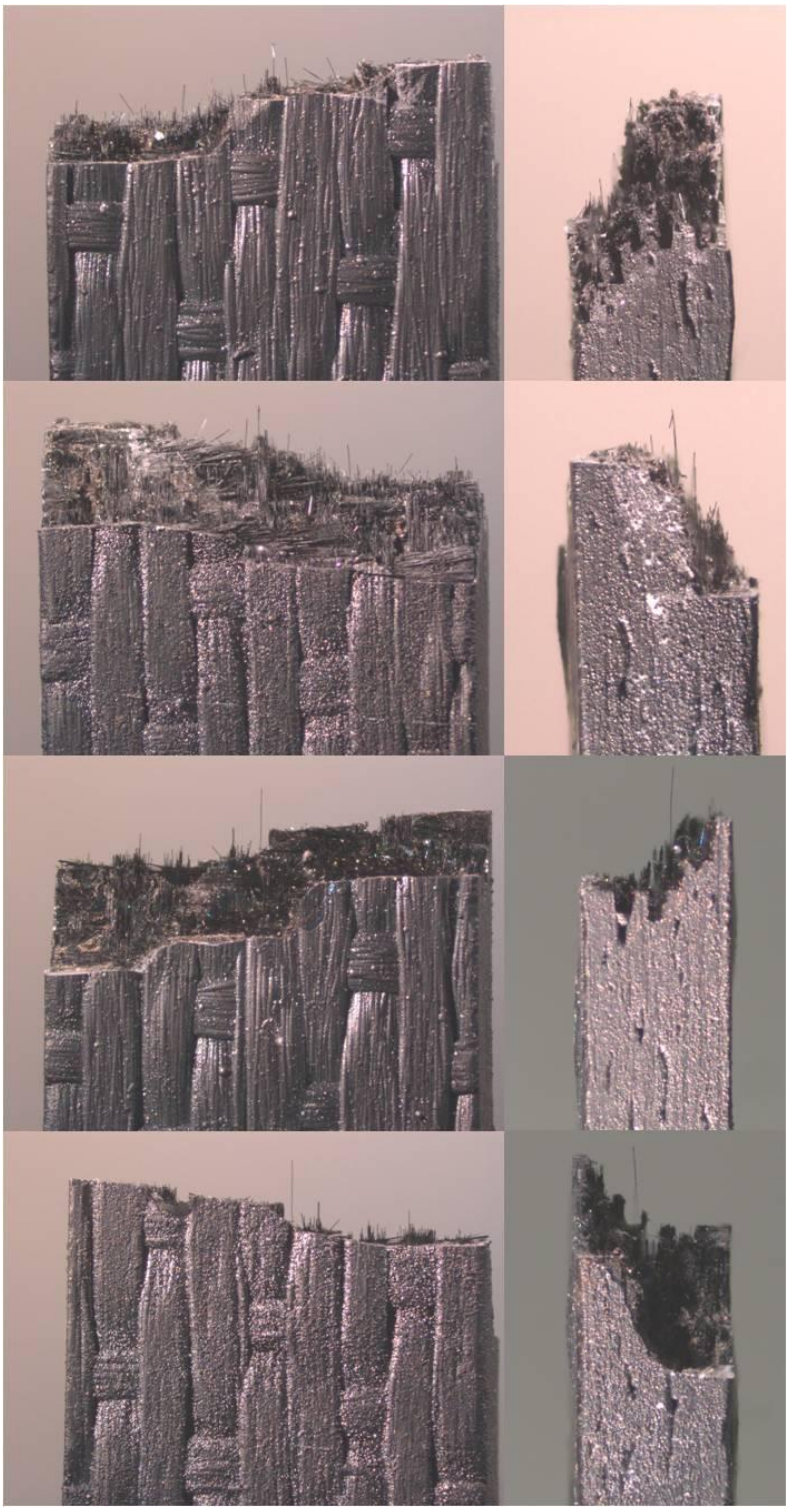

Figure 120: Optical micrographs of fracture surface of specimen P7-2 tested in fatigue at 1.0 Hz in steam at 1200˚C. σ_{max} = 120 MPa, N_f = 134,512, t_f = 37.4 h.

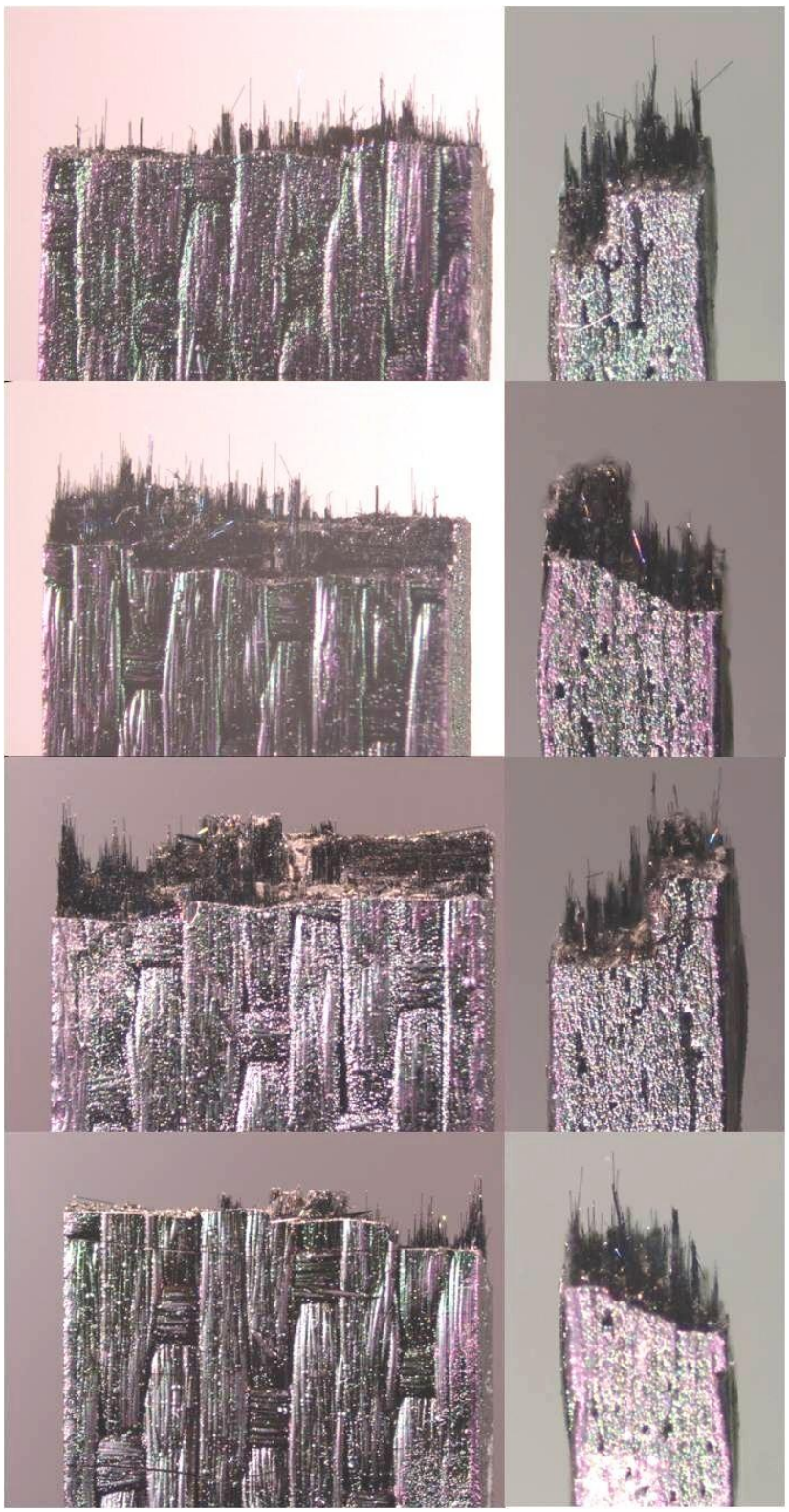

Figure 121: Optical micrographs of fracture surface of specimen P7-3 tested in fatigue at 0.1 Hz in air at 1200˚C. σ_{max} = 130 MPa, N_f = 42,449, t_f = 117.9 h.

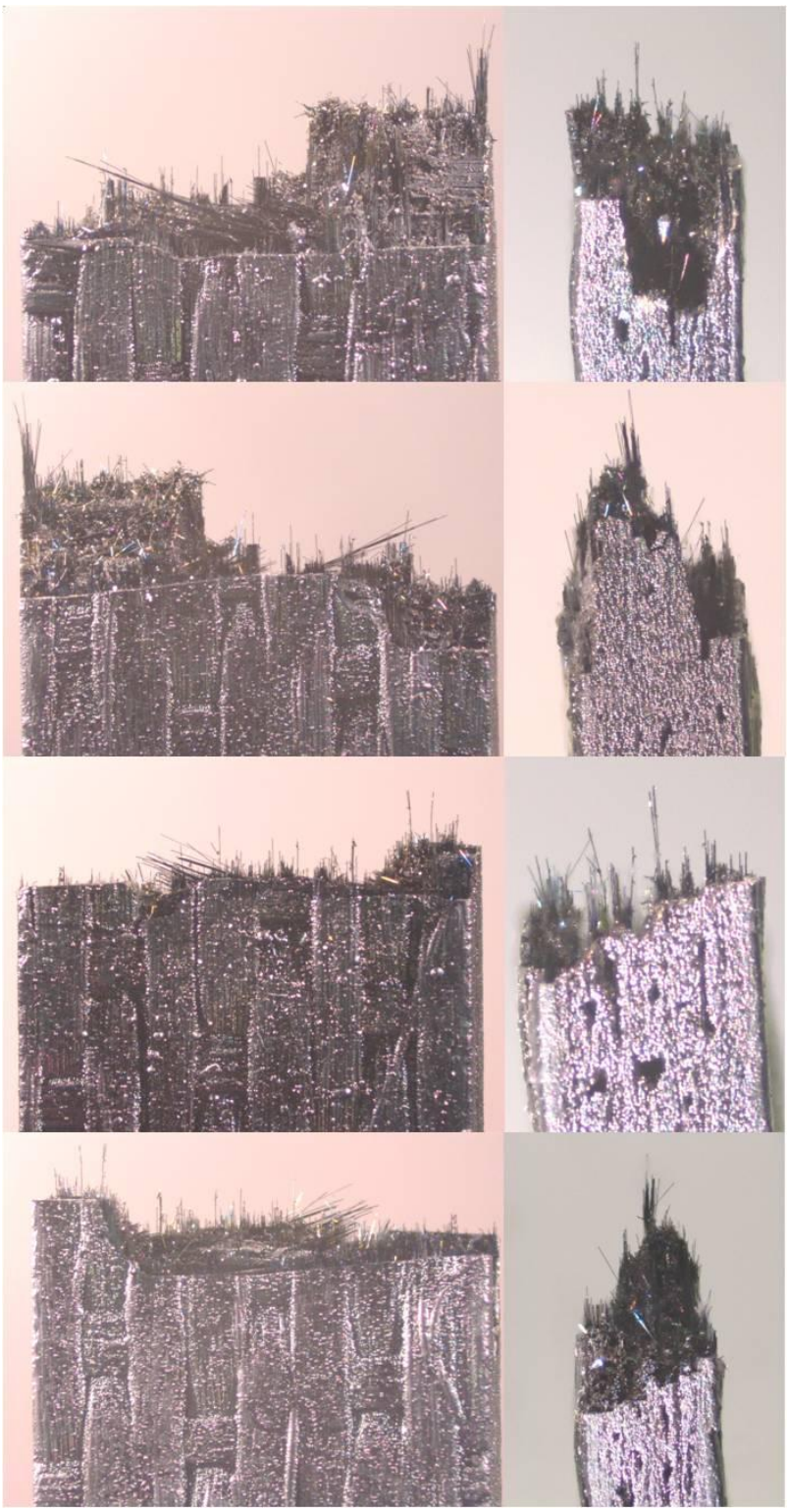

Figure 122: Optical micrographs of fracture surface of specimen P7-4 tested in fatigue at 0.1 Hz in air at 1200˚C. σ_{max} = 100 MPa, N_f = 67,607, t_f = 187.8 h.

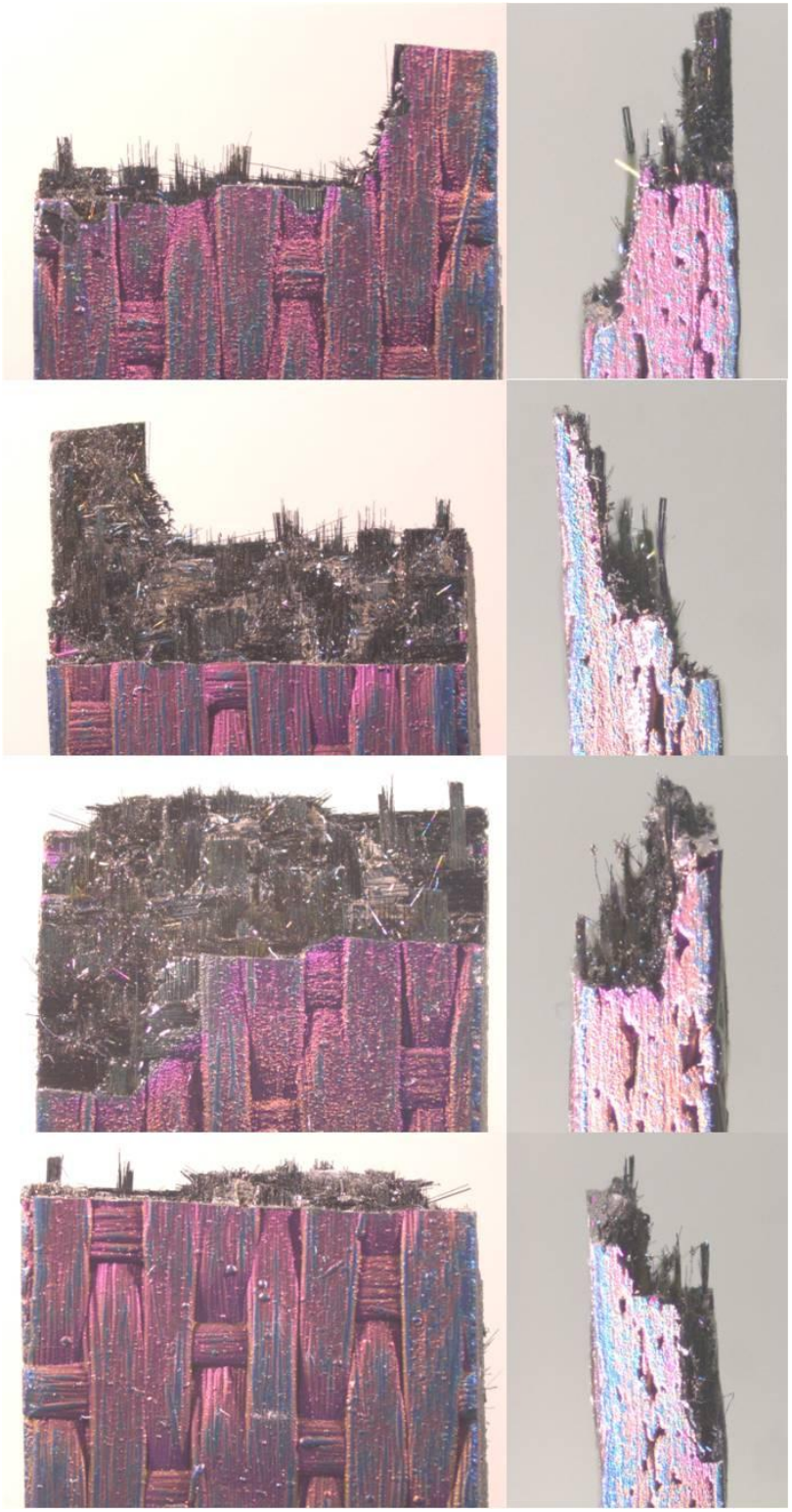

Figure 123: Optical micrographs of fracture surface of specimen P7-5 tested in fatigue at 1.0 Hz in air at 1200˚C. σ_{max} = 130 MPa, N_f = 95,712, t_f = 26.6 h.

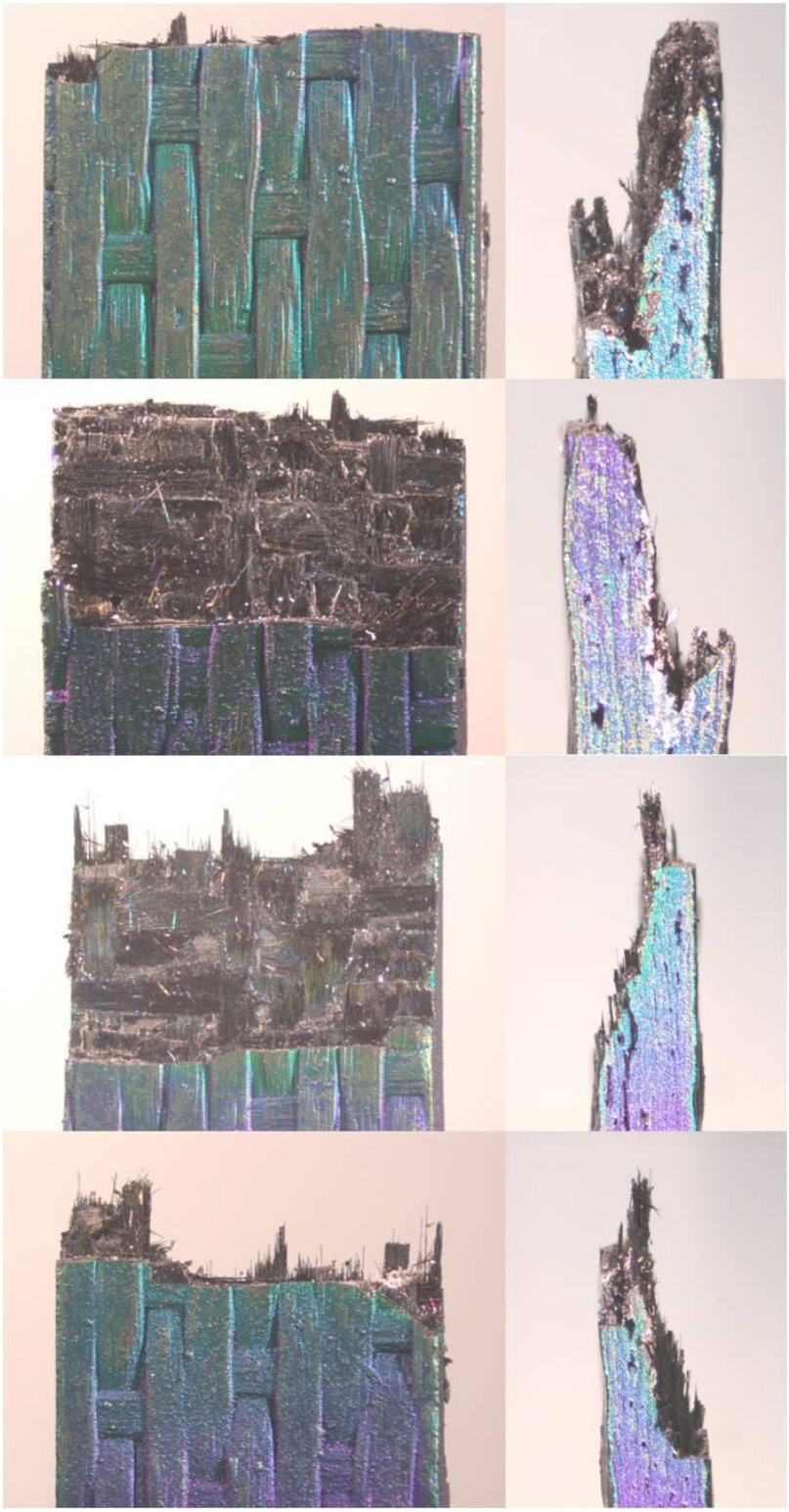

Figure 124: Optical micrographs of fracture surface of specimen P7-6 tested in fatigue at 1.0 Hz in air at 1200˚C. σ_{max} = 120 MPa, N_f = 92,468, t_f = 25.7 h.

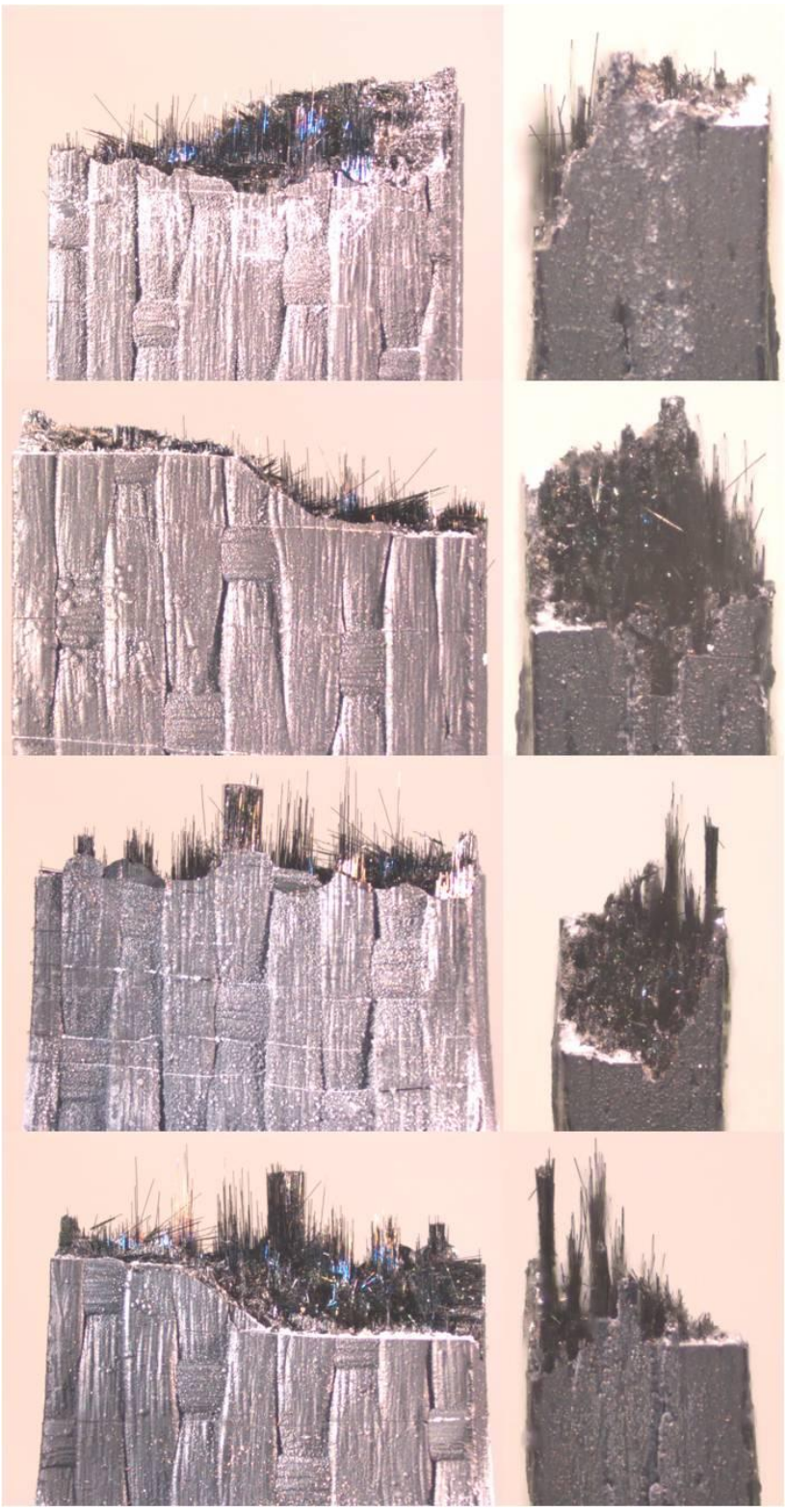

Figure 125: Optical micrographs of fracture surface of specimen P7-7 tested in fatigue at 0.1 Hz in steam at 1200˚C. σ_{max} = 120 MPa, N_f = 79,532, t_f = 220.9 h.

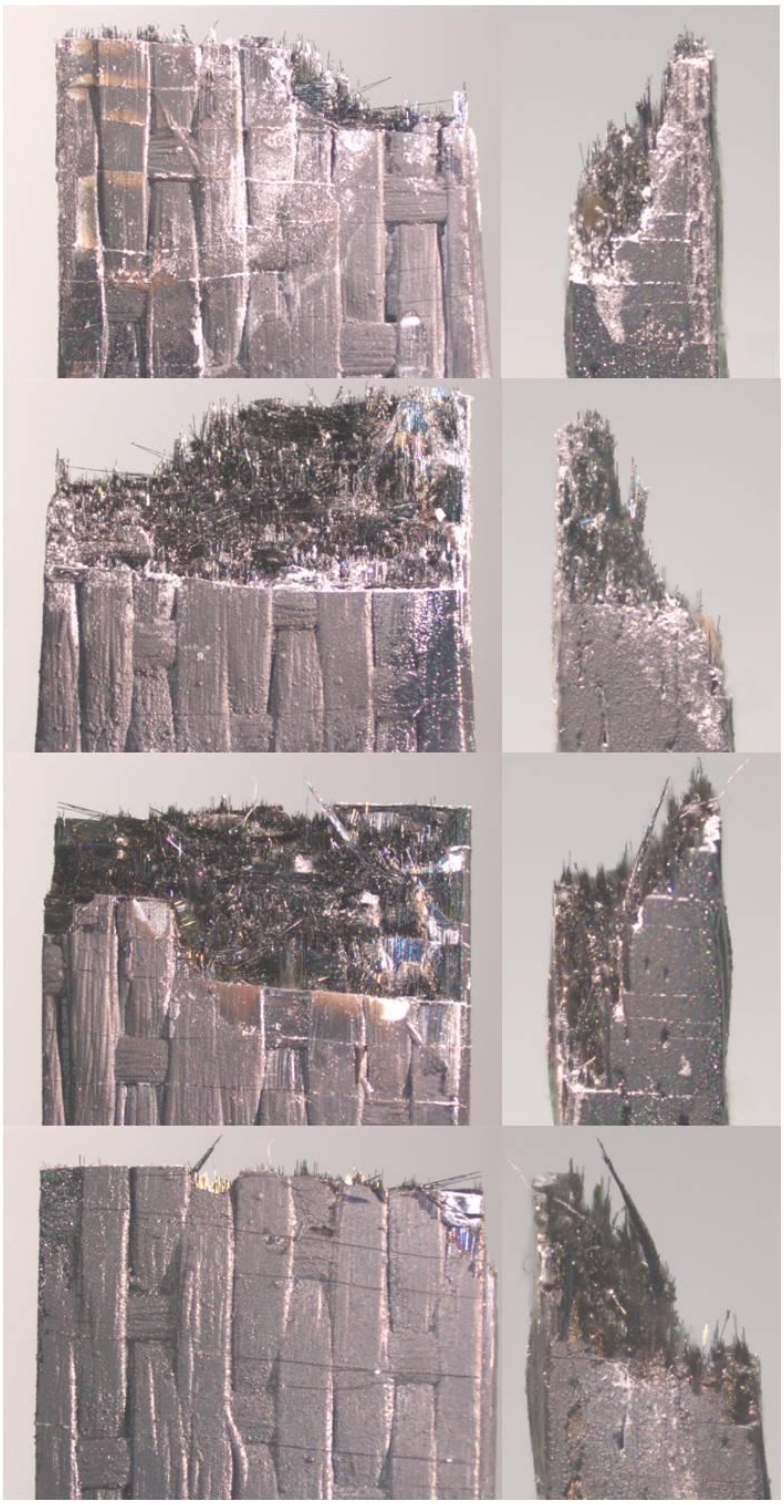

Figure 126: Optical micrographs of fracture surface of specimen P7-8 tested in fatigue at 0.1 Hz in steam at 1200˚C. σ_{max} = 100 MPa, N_f = 100,000, t_f = 277.8 h.

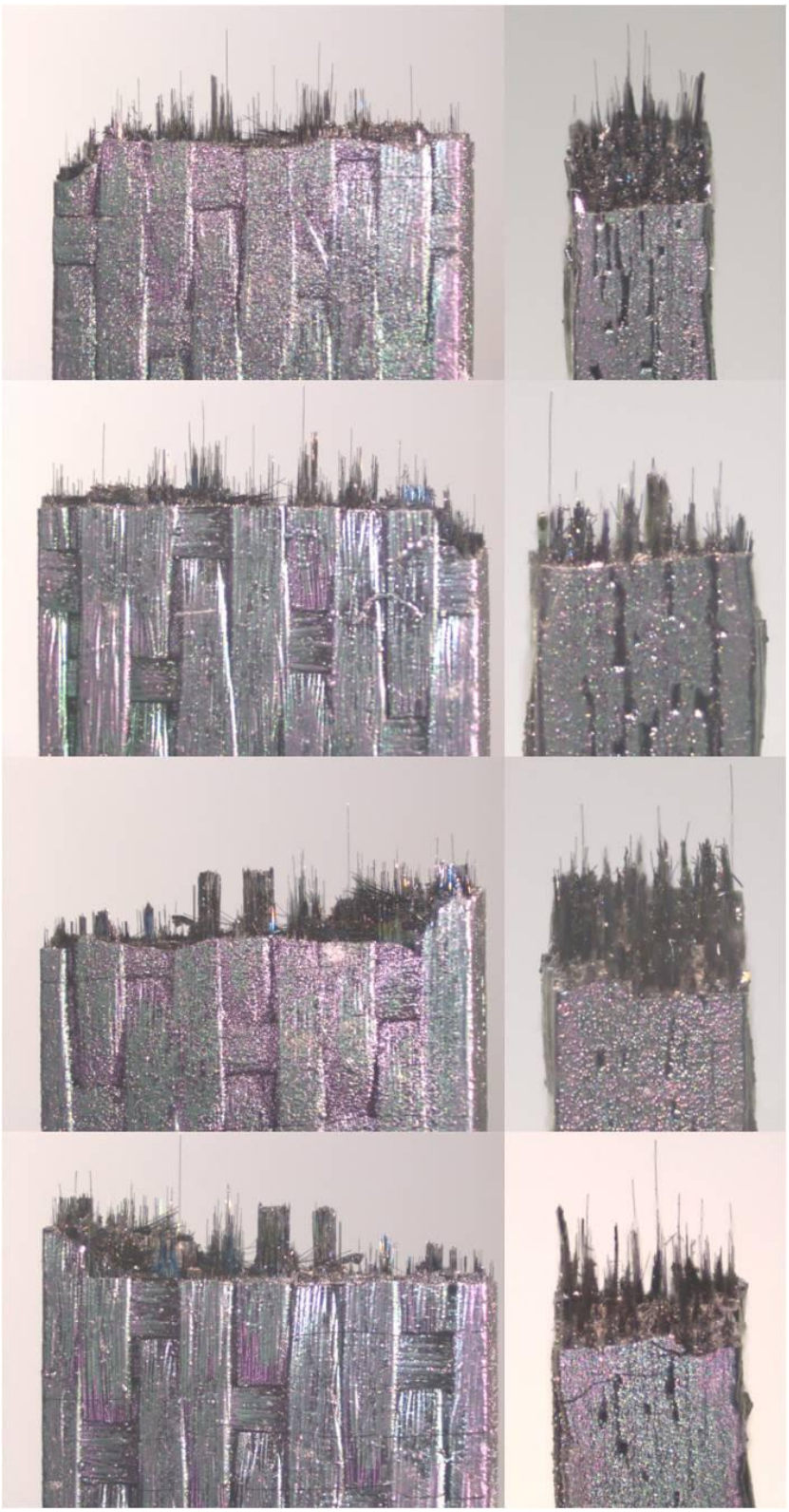

Figure 127: Optical micrographs of fracture surface of specimen P7-9 tested in fatigue at 0.1 Hz in air at 1200˚C. σ_{max} = 120 MPa, N_f = 41,918, t_f = 116.4 h.

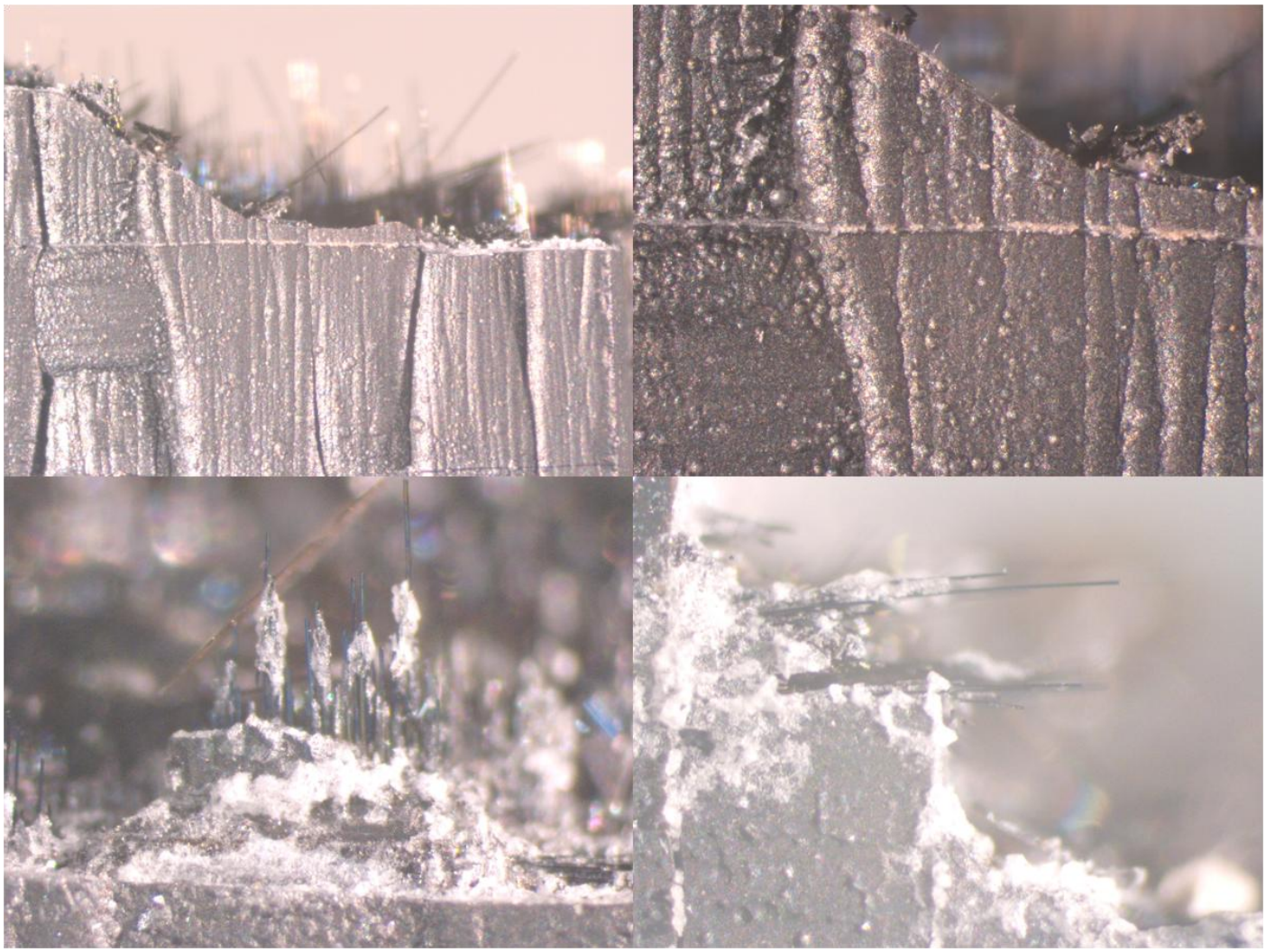

Figure 128: Optical micrographs of fracture surface of specimen P7-7 tested in fatigue at 0.1 Hz in steam at 1200˚C showing glass formation inside cracks and on fibers. σ_{max} = 120 MPa, N_f = 79,532, t_f = 220.9 h.

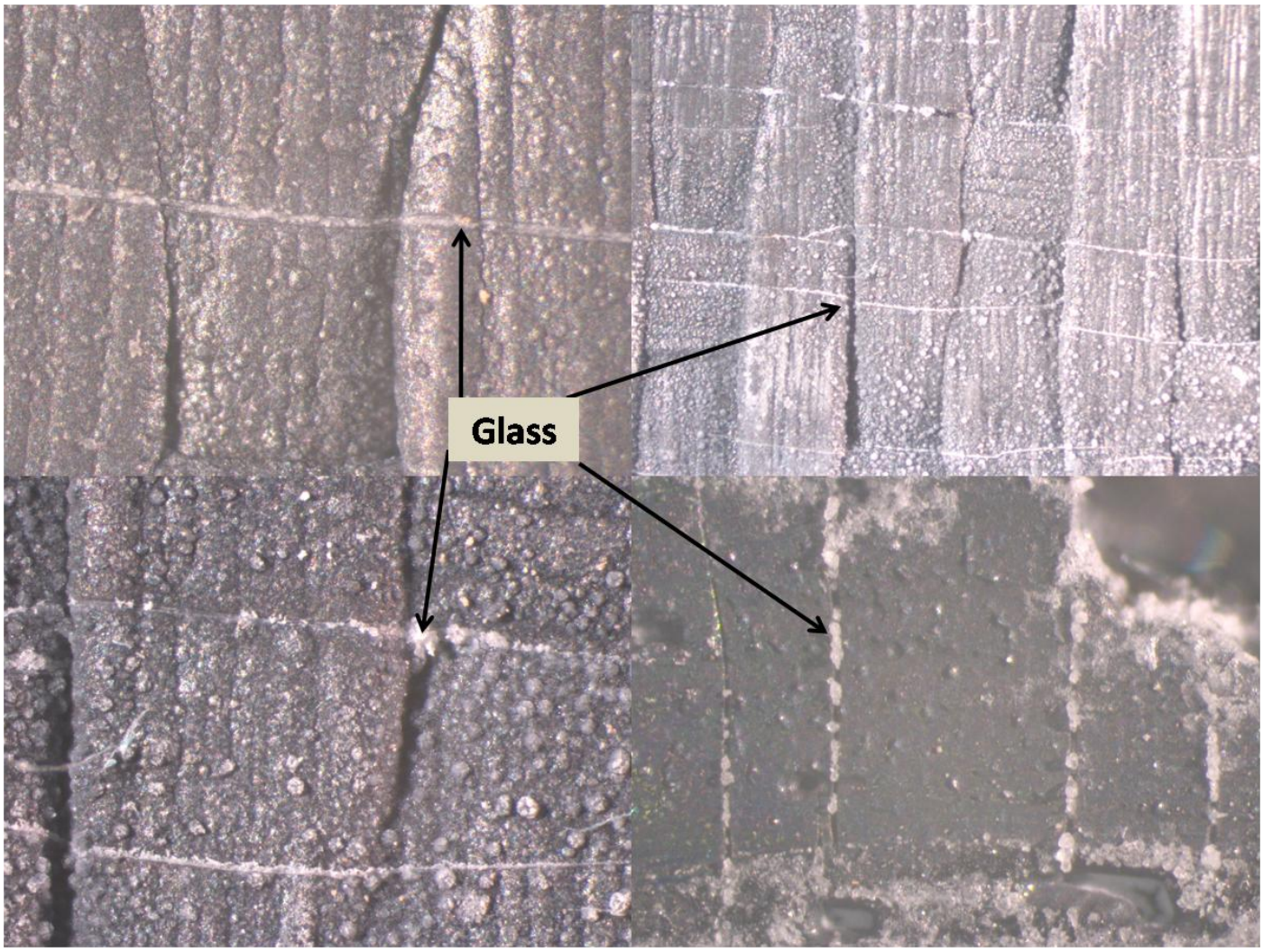

Figure 129: Optical micrographs of fracture surface of specimen P7-7 tested in fatigue at 0.1 Hz in steam at 1200˚C showing glass formation inside cracks. σ_{max} = 120 MPa, N_f = 79,532, t_f = 220.9 h.

Appendix B

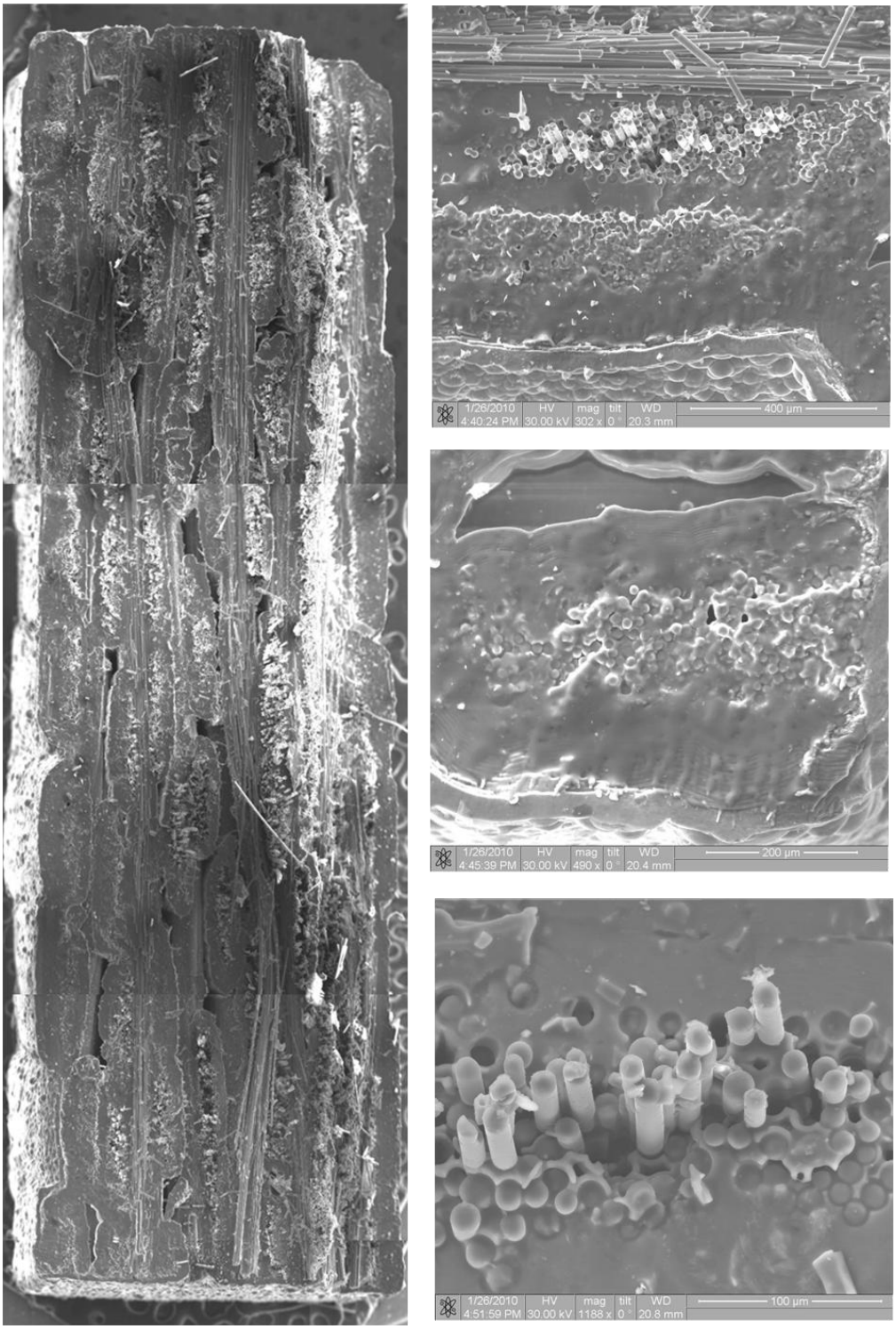

Figure 130: SEM micrographs of fracture surface of specimen P5-4 tested in fatigue at 1.0 Hz in air at 1200˚C. σ_{max} = 100 MPa, N_f = 200,000, t_f = 55.6 h.

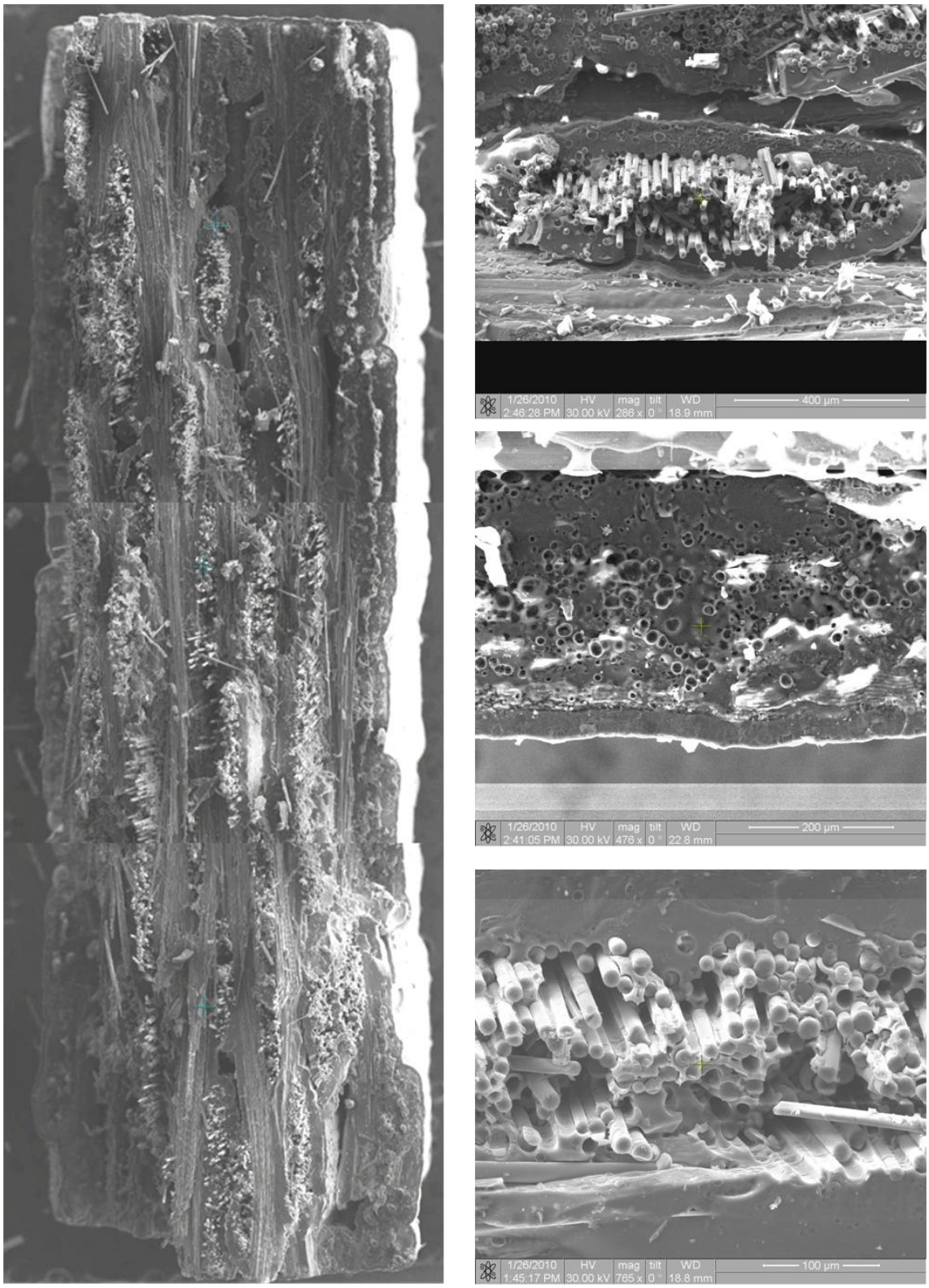

Figure 131: SEM micrographs of fracture surface of specimen P5-5 tested in fatigue at 1.0 Hz in steam at 1200˚C. σ_{max} = 100 MPa, N_f = 200,000, t_f = 55.6 h.

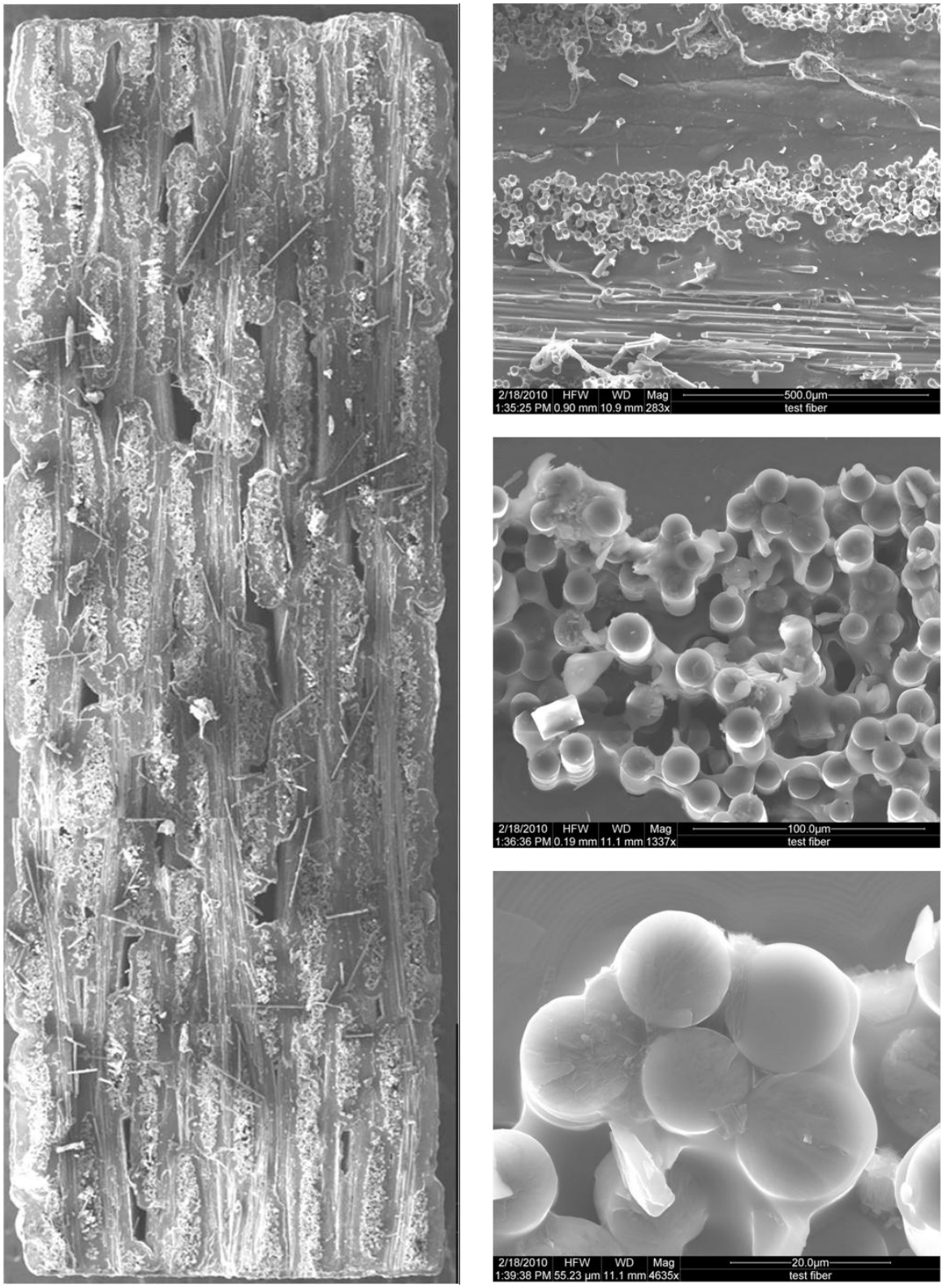

Figure 132: SEM micrographs of fracture surface of specimen P5-8 tested in fatigue at 0.1 Hz in air at 1200˚C. σ_{max} = 100 MPa, N_f = 24,925, t_f = 69.2 h.

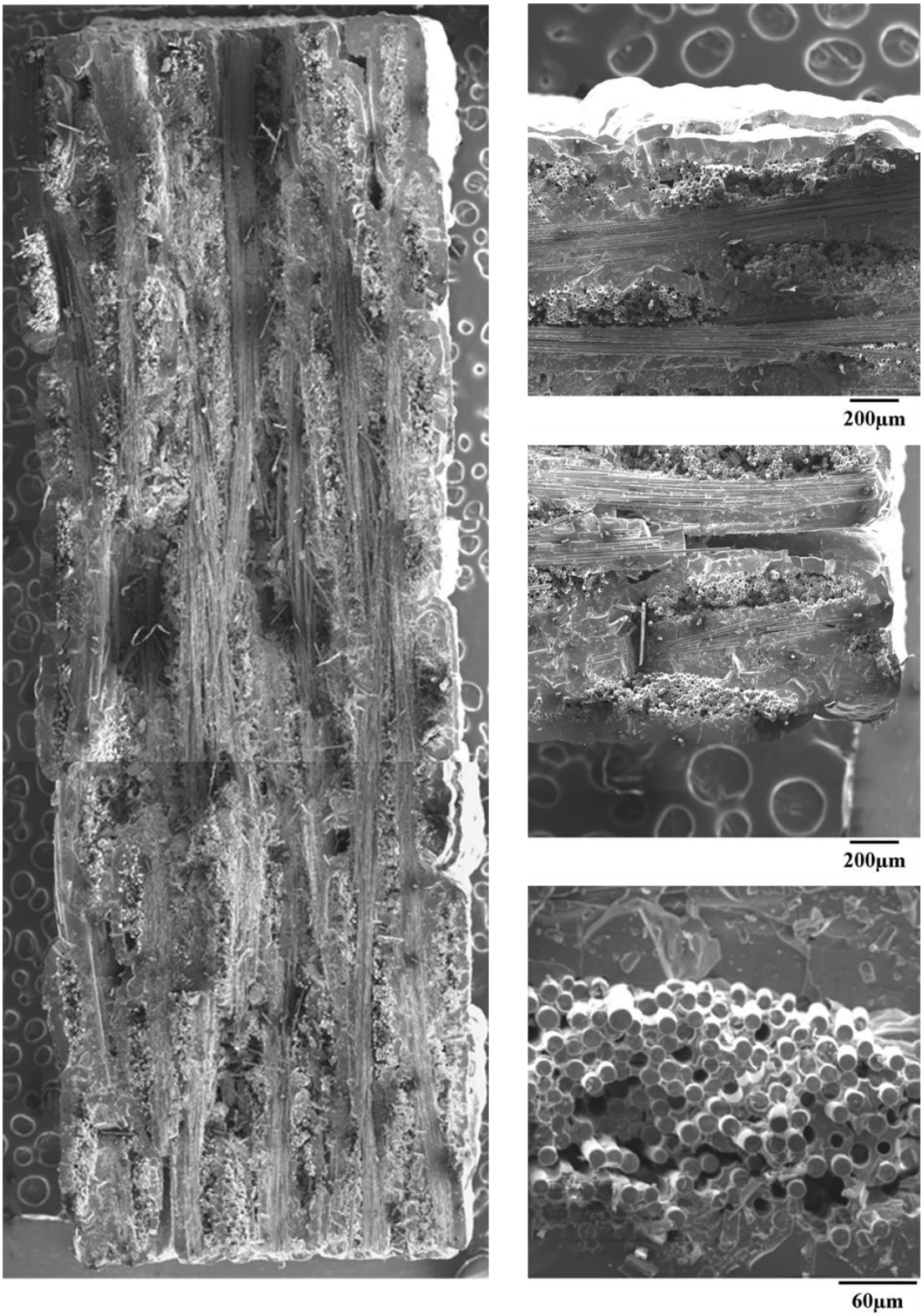

Figure 133: SEM micrographs of fracture surface of specimen P6-1 tested in tension to failure in air at 1200˚C.

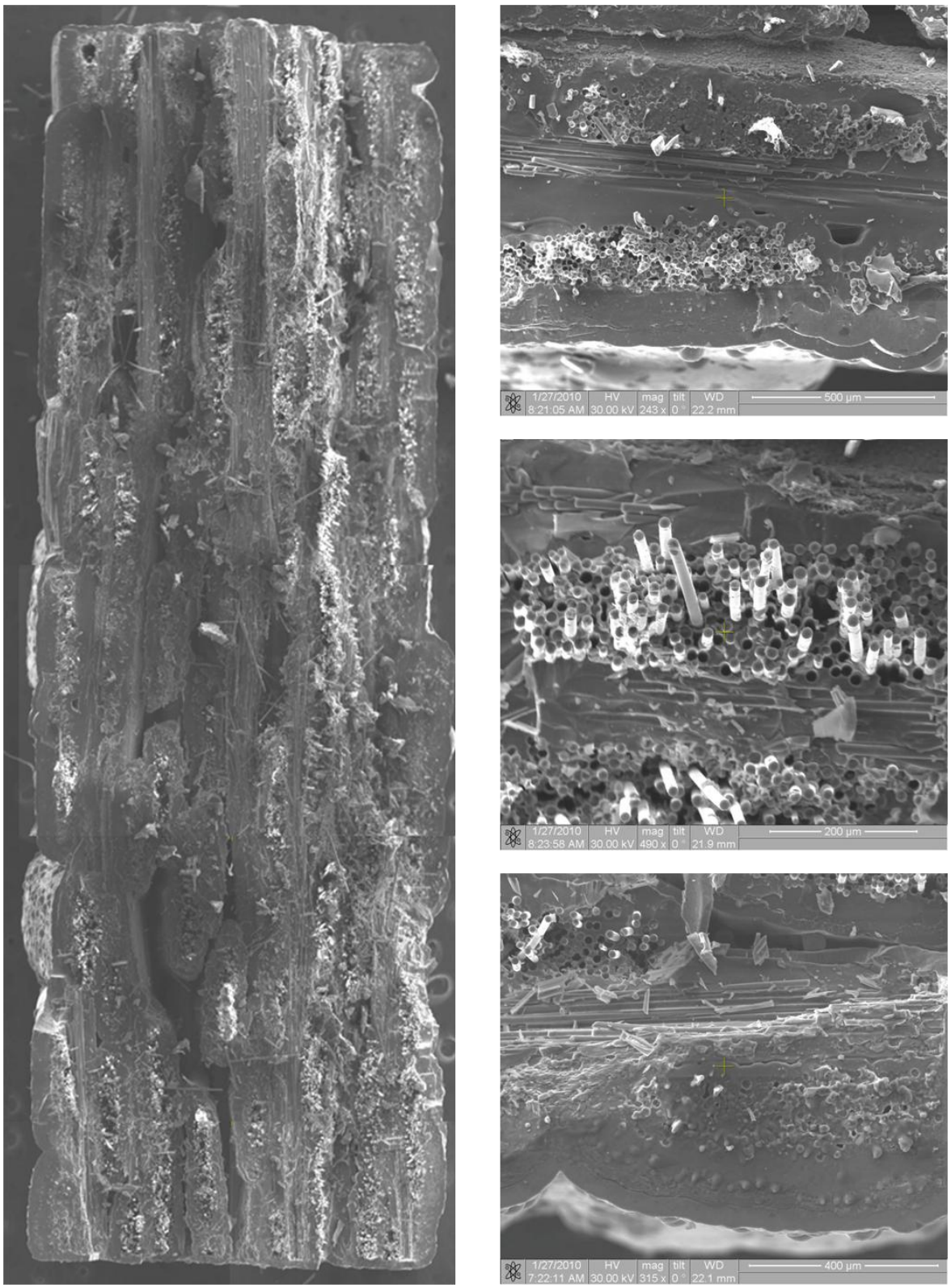

Figure 134: SEM micrographs of fracture surface of specimen P6-3 tested in fatigue at 1.0 Hz in air at 1200˚C. σ_{max} = 140 MPa, N_f = 63,458, t_f = 17.6 h.

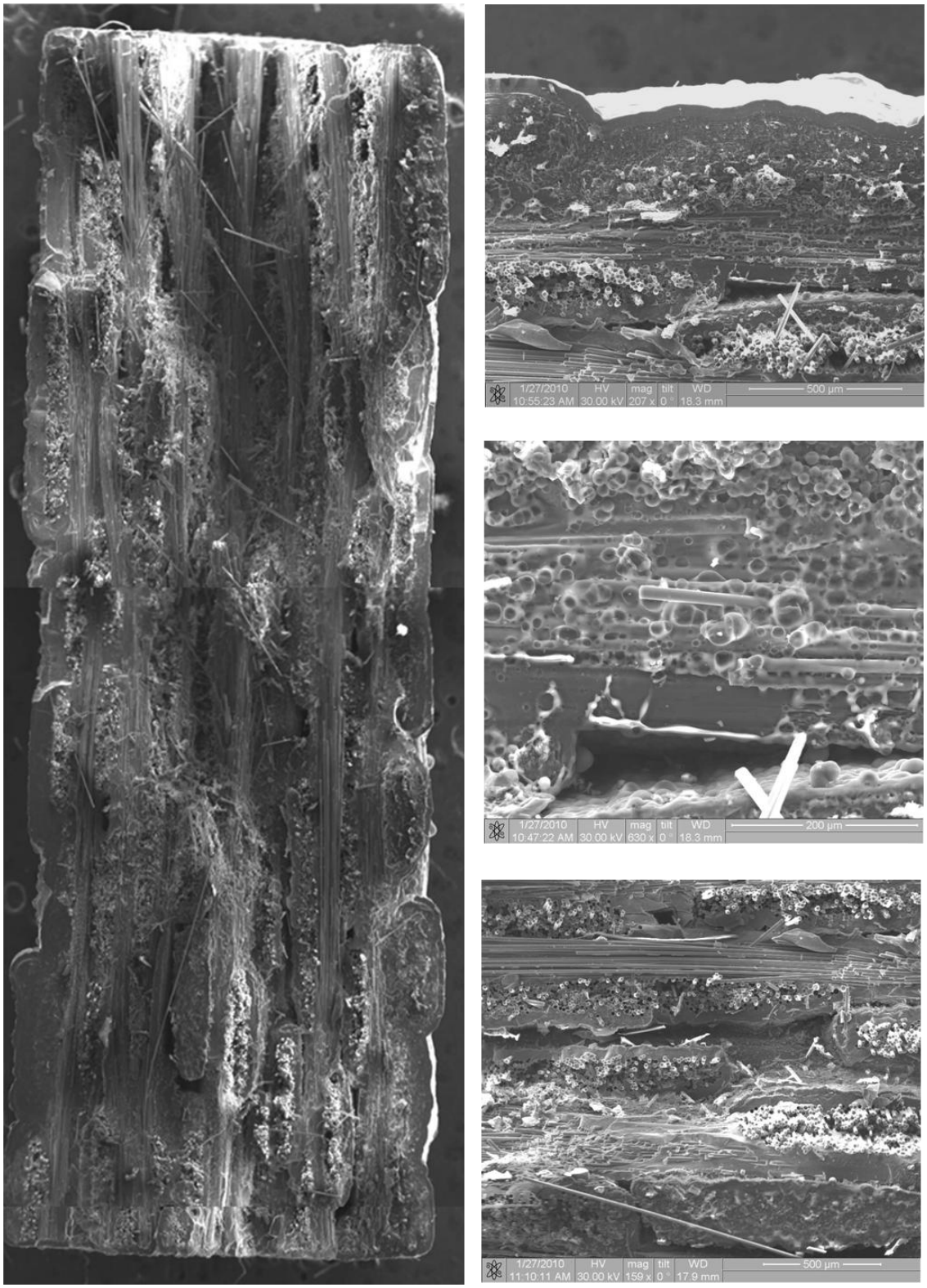

Figure 135: SEM micrographs of fracture surface of specimen P6-4 tested in fatigue at 1.0 Hz in steam at 1200˚C. σ_{max} = 140 MPa, N_f = 36,679, t_f = 10.2 h

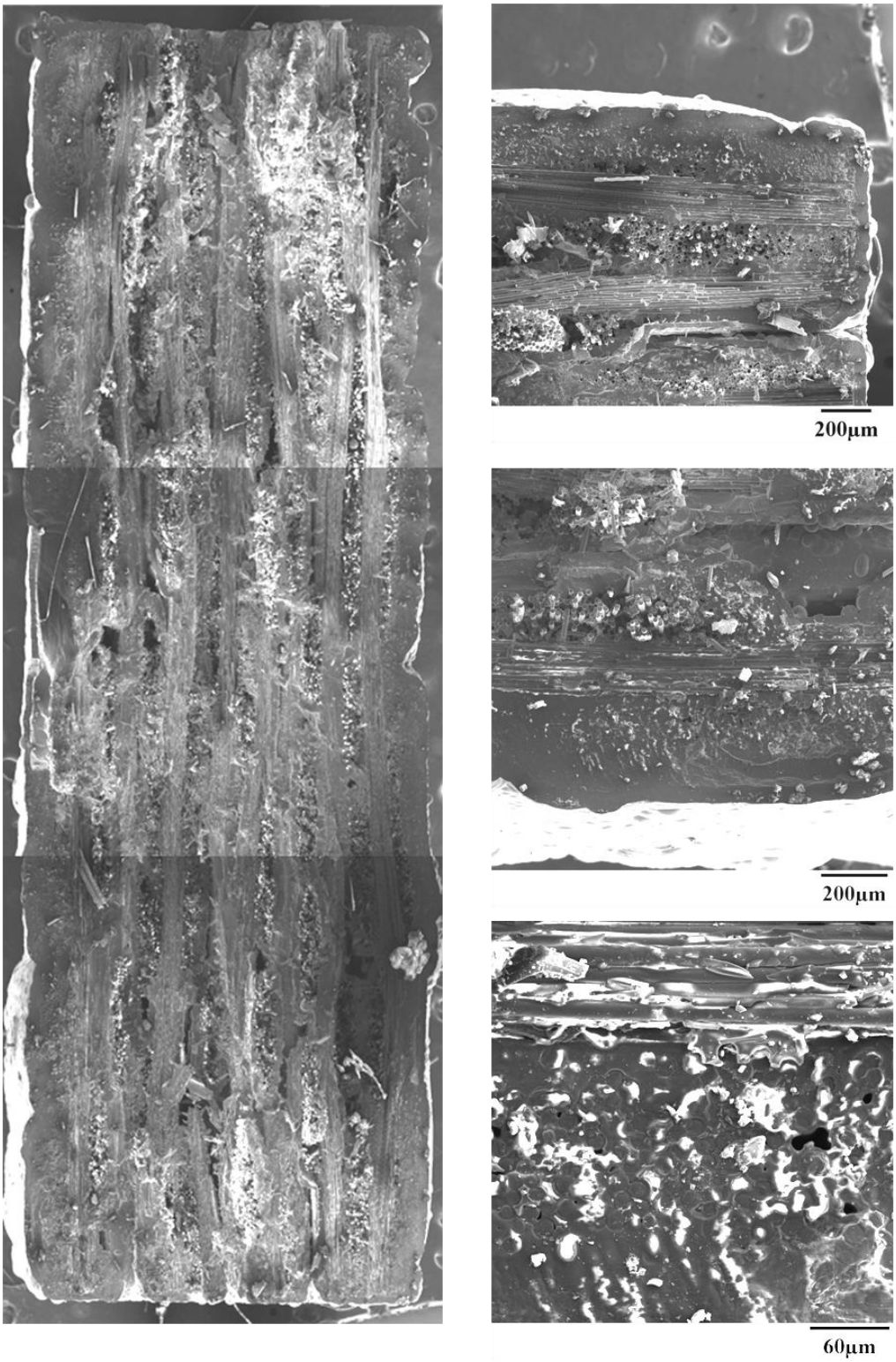

Figure 136: SEM micrographs of fracture surface of specimen P6-5 tested in fatigue at 10 Hz in air at 1200˚C. σ_{max} = 140 MPa, N_f = 200,000, t_f = 5.6 h.

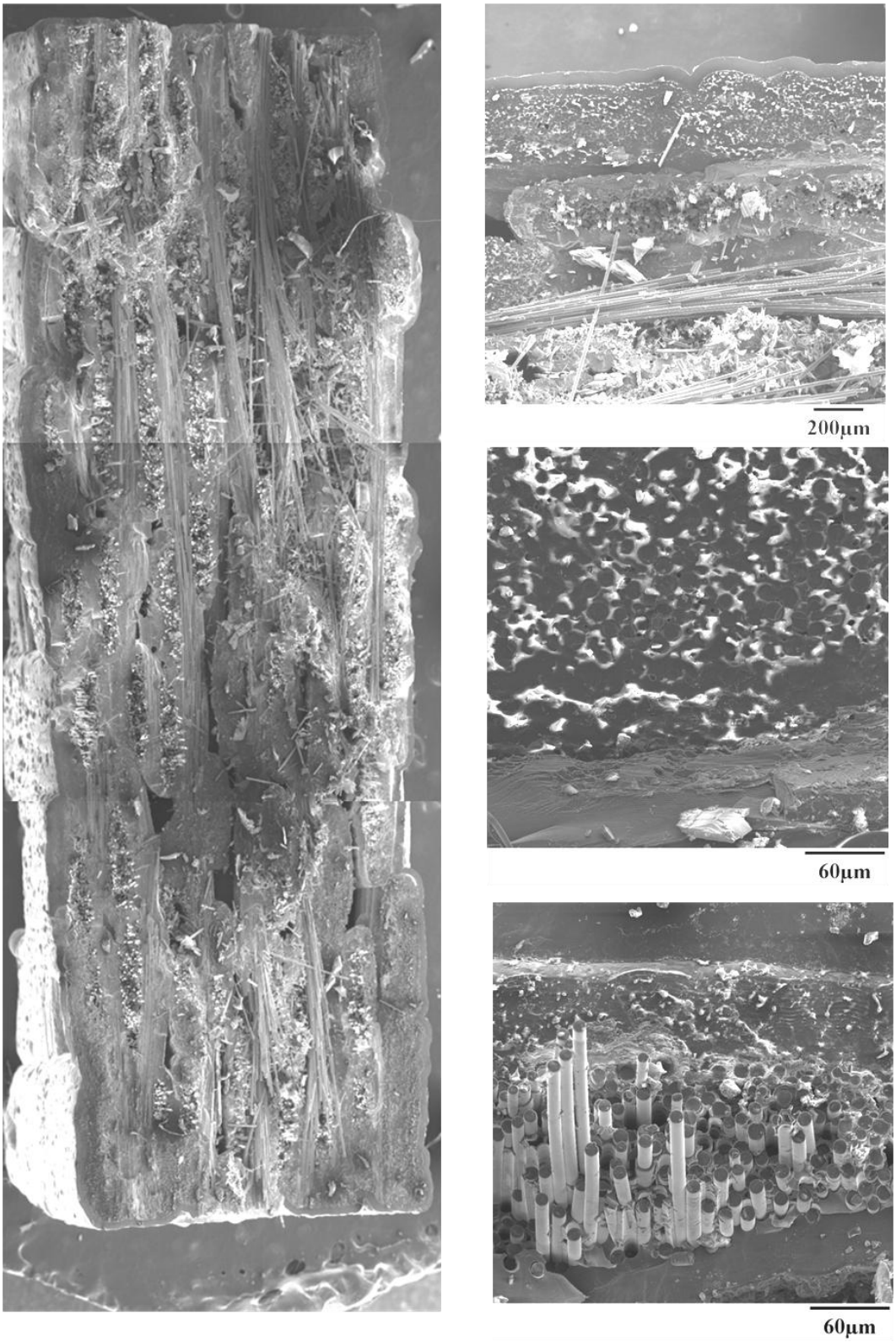

Figure 137: SEM micrographs of fracture surface of specimen P6-6 tested in fatigue at 10 Hz in steam at 1200˚C. σ_{max} = 140 MPa, N_f = 39,849, t_f = 1.1 h.

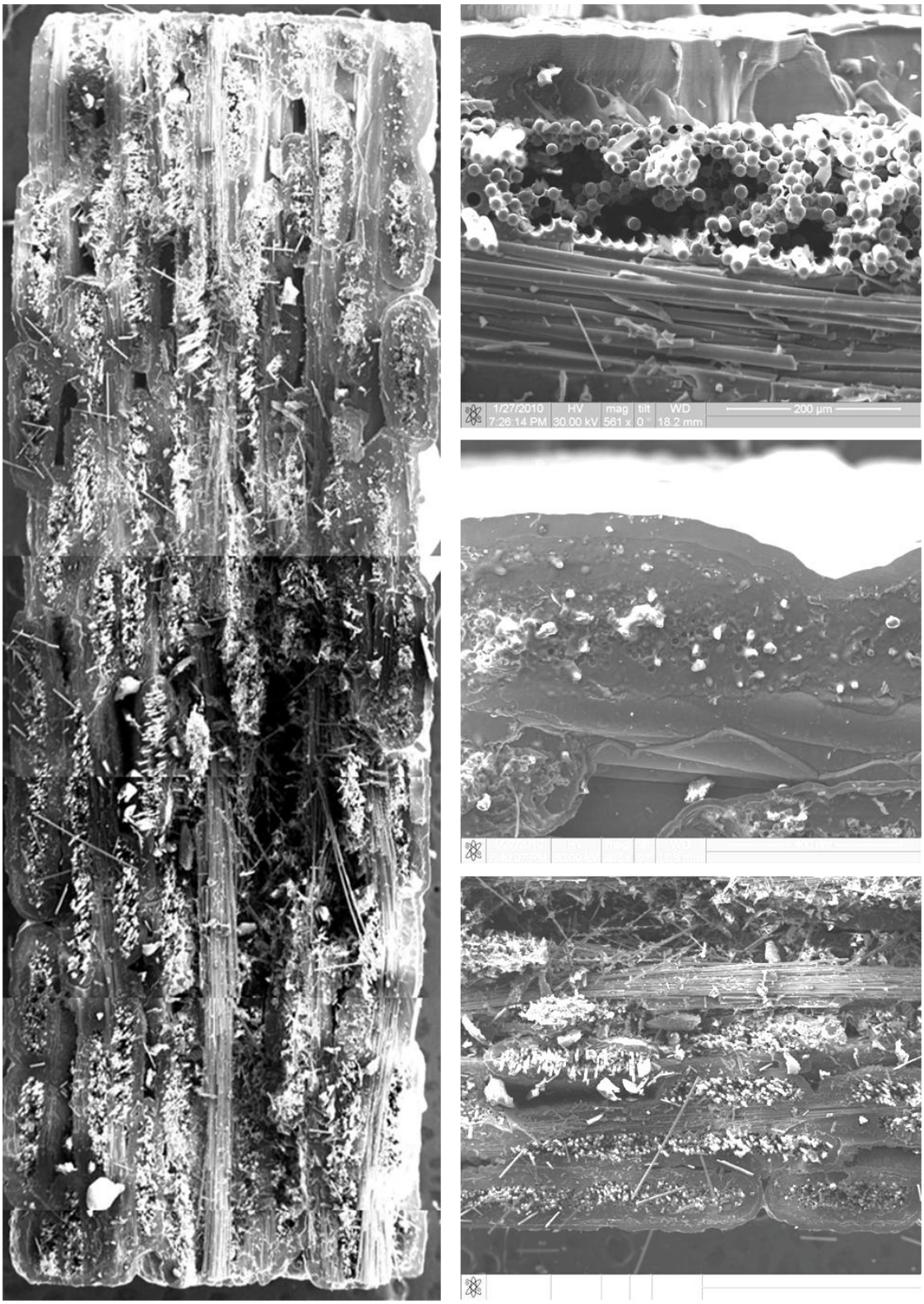

Figure 138: SEM micrographs of fracture surface of specimen P6-7 tested in fatigue at 0.1 Hz in air at 1200˚C. σ_{max} = 140 MPa, N_f = 30,712, t_f = 85.3 h.

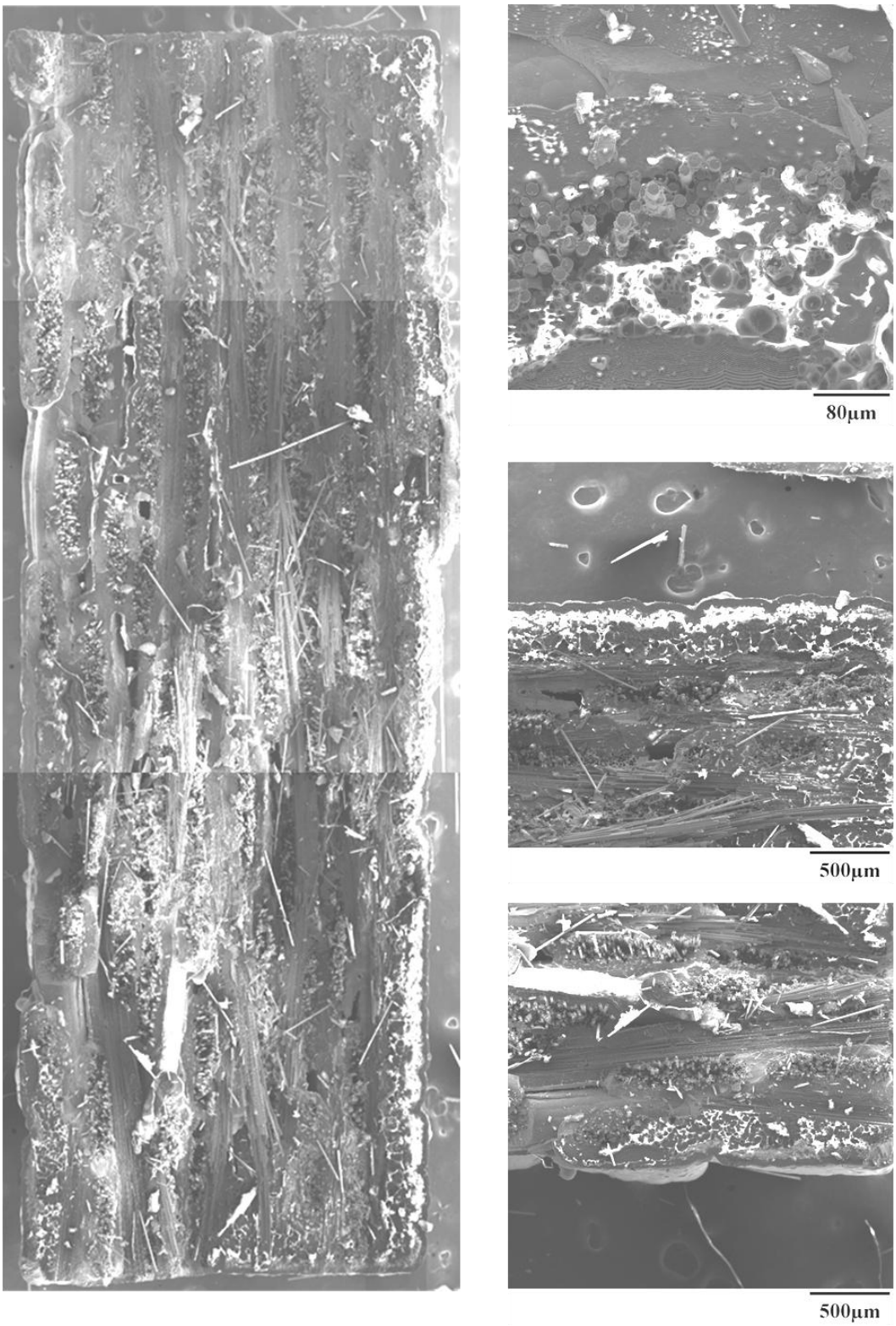

Figure 139: SEM micrographs of fracture surface of specimen P6-8 tested in fatigue at 0.1 Hz in steam at 1200˚C. σ_{max} = 140 MPa, N_f = 11,323, t_f = 31.5 h.

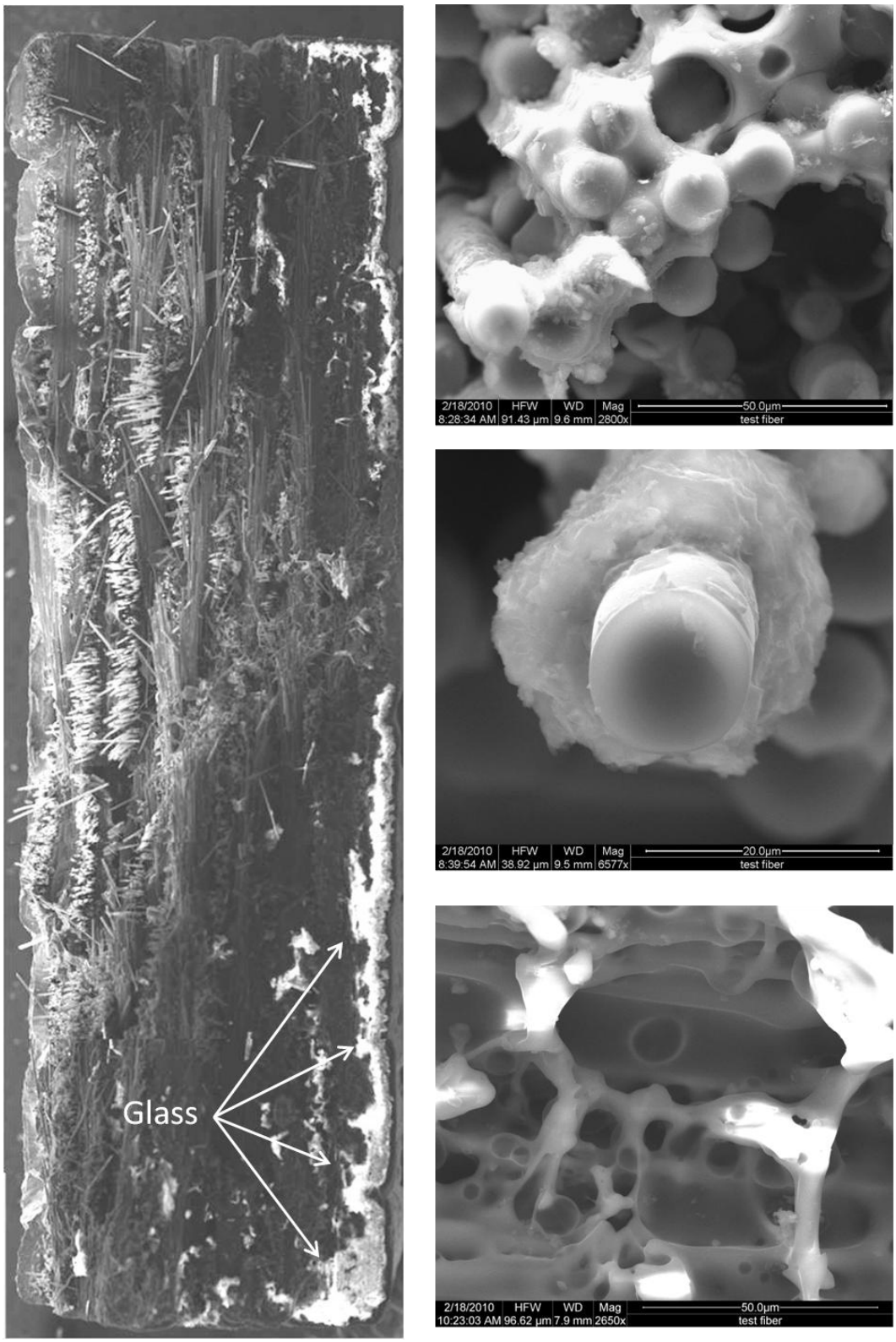

Figure 140: SEM micrographs of fracture surface of specimen P7-7 tested in fatigue at 0.1 Hz in steam at 1200˚C. σ_{max} = 120 MPa, N_f = 79,532, t_f = 220.9 h.

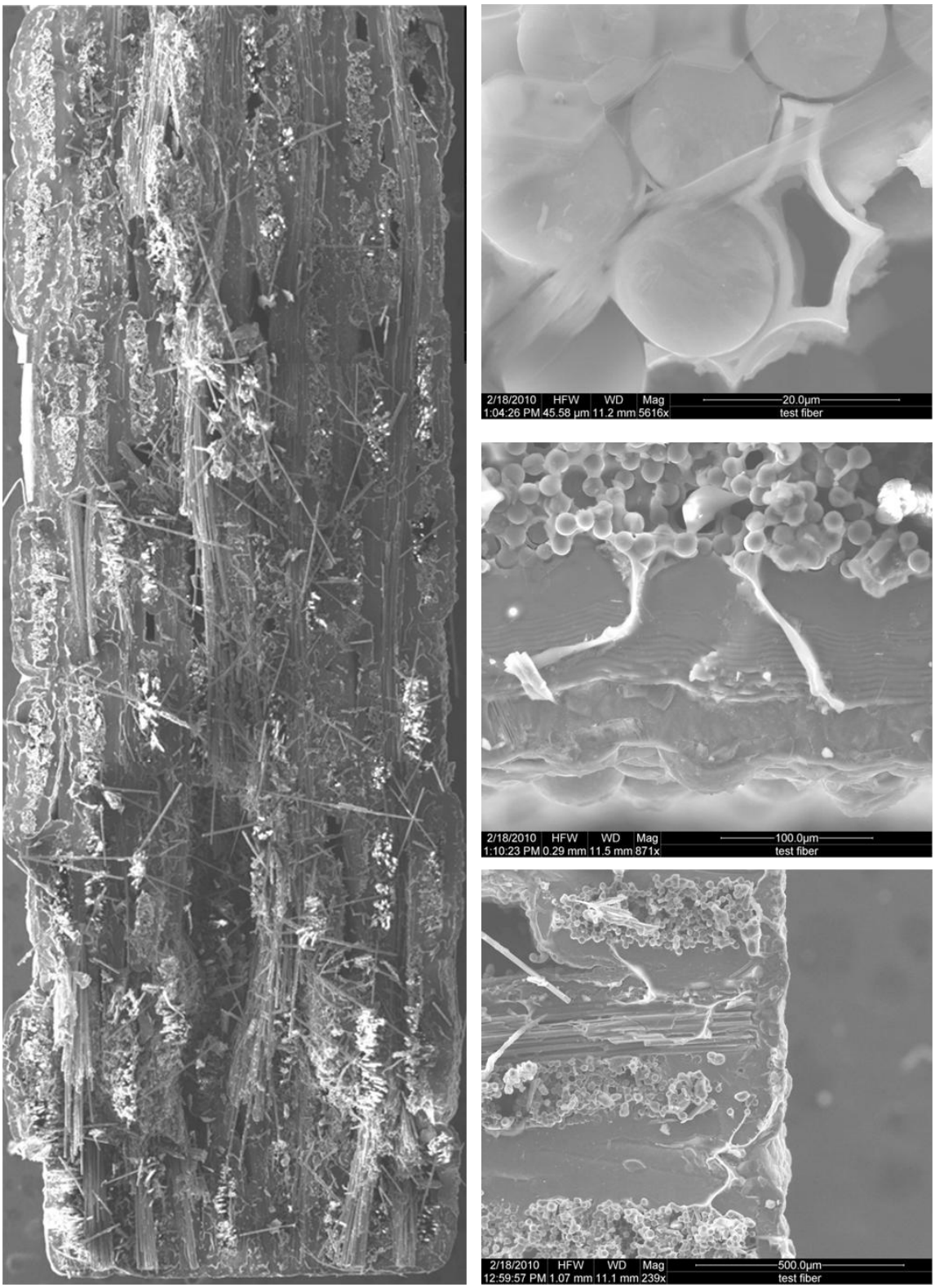

Figure 141: SEM micrographs of fracture surface of specimen P7-9 tested in fatigue at 0.1 Hz in air at 1200˚C. σ_{max} = 120 MPa, N_f = 42,918, t_f = 116.4 h.

Bibliography

1. Baker, Alan, Stuart Dutton, and Donald Kelly. *Composite Materials for Aircraft Structures (Second Edition).* Reston: American Institute of Aeronautics and Astronautics, inc, 2004.

2. Bansal, Narottam P. "Tensile Strength and Microstructure of Hi-Nicalon Fibers Extracted from Celsian Matrix Composites." In *Advances in Ceramic Matrix Composites IV*, by J.P. Singh and Narottam P. Bansal. Westerville: The American Ceramic Society, 1999.

3. Campbell, F.C. *Manufacturing Processes for Advanced Composites.* Oxford: Elsevier, 2004.

4. Campbell F.C. *Manufacturing Technology for Aerospace Structural Materials.* Amsterdam: Elsevier, 2006.

5. Cantor, B., H. Assender, and P. Grant. *Aerospace Materials.* Bristol: Institue of Physics Publishing, 2001.

6. Chawla, K. K. *Ceramic Matrix Composites.* Vol. Second Edition. Boston: Kluwer Acadmic Publishers, 2003.

7. Chawla, Krishah K. *Composite Materials Science and Engineering (Second Edition).* New York: Springer, 1998.

8. Christensen, Devon T. *Fatifue Behavior of an Advanced SiC/SiC Composite at Elevated Temperture in Air and Steam.* MS thesis, AFIT/GAE/ENY/09-D02. Schoool of Engineering and Management, Air Force Institue of Technology (AU), Wright-Patterson AFB, OH, December 2009.

9. Cowles, B.A. "High cycle fatigue in aircraft gas turbines-an industry perspective." In *International Journal of Fracture, 22*: 1996: 147-163.

10. Deve, H.E., and C. McCullough. "High Performance Aluminum/Alumina Composites." In *High Performance Metal and Ceramic Matrix Composites*. Upadhya: The Minerals, Metals, and Materials Society, 1994.

11. Droillard, Christine, Jacques Lamon, and Xavier Bourrat. "Strong Interface in CMCs, A Condition for Efficient Multilayered Interphases." In *Ceramic Matrix Composites - Advanced High-Temperture Structural Materials*, by Richard A. Lowden, Mattison Ferber, John R. Hellmann, Krishan K. Chawla and Stephen G. DiPietro, 371-376. Pittsburgh: Material Research Society, 1995.

12. Fair, G.E. private communications (2010).

13. Flower, Harvey M. *High Performance Materials in Aerospace.* London: Chapman & Hall, 1995.

14. Hermes, E.E., and R.J. Kerans. "Degradation of Non-oxide Reinforcement and Oxide Matrix Composites." *Material Resistant Society Symposium Proceedings, vol 125*, 1988: 73-78.

15. Hetrick, Griffin. *Effects of Frequency and Enviroment on Fatigue Behavior of an Oxide-Oxide Ceramic Matrix Composite at 1200C.* MS Thesis, AFIT/GAE/ENY/06-J05. School of Engineering and Management, Air Force Institue of Technology (AU), Wright-Patterson Air Force Base, OH, June 2006.

16. Kaw, Autar K. *Mechanics of Composite Materials.* Boca Raton: Taylor & Francis Group, 2006.

17. Krenkel, Walter. *Ceramic Matrix Composites.* Weinheim: Wiley-Vch Verlag Gmbh & Co. KGaA, 2008.

18. Kuhn, Jonathan L. *Mechanical Behavior of Woven Ceramics Matrix Composites.* Ann Arbor: A Bell & Howell Company, 1998.

19. Musikant, Solomon. *What Every Engineer Should Know About Ceramics.* New York: Marcel Dekker, Inc, 1991.

20. Ohnabe, H., S. Masaki, M. Onozuka, K. Muyahara, and T. Sasa. "Potential Applications of Cermic Matrix Compsites to Aero-engine Components." *Composites: Part A, 30*, 1999: 489-496.

21. Opila, E.J. "Variation of the Oxidation Rate of Silicon Carbide with Water Vapor Pressure." *Journal of American Ceramic Society*, 1999: 625-636.

22. Parlier, M., and M.H. Ritti. "State of the Art and Perspectives of Oxide/Oxide Composites." *Aerospace Science and Technology*, 2003: 211-221.

23. Ramulu, M., N.E. Prasad, G. Malakondaiah, and Z. Guo. "Secondary Processing Effects and Damage Mechanisms in Continuous-Fiber Ceramic Composites." In *Thermal and Mechanical Test Methods and Behavior of Continuous-Fiber Ceramic Composites*, by Michael G. Jenkins, Stephen T. Gonczy, Edgar Lara-Curzio, Noel E. Ashbaugh and Larry P. Zawada. American Society for Testing and Materials , 1997.

24. Ruggles-Wrenn, M.B., private communications (2010)

25. Ruggles-Wrenn, M.B., G. Hetrick, and S.S. Baek. "Effects of Frequency and Enviroment on Fatigue Behavior of an Oxide-Oxide Ceramic Composite at 1200C." *International Journal of Fatigue 30*, 2007: 502-516.

26. Schmidt, S., H. Knabe, H. Immich, R. Mestring, and A. Gessler. "Advanced Ceramic Matrix Composite Material fo Current and Future Propulsion Technology Applications." *Acta Astronautica, 55*, 2004: 409-420.

27. Sharma, Vipul. *Effects of Temperature and Steam Enviroment on Fatigue Behavior of Three Sic/Sic Ceramic Matrix Composites.* MS thesis, AFIT/GAE/ENY/08-S02. School of Engineering and Management, Air Force Institute of Technology (AU), September 2008.

28. "Standard Test Method for Monotonic Tensile Strength Testing of Continuous Fiber-Reinforced Advanced Ceramics with Solid Rectangular Cross-Section Specimens at Elevated Temperatures." *ASTM C 1359* (Reapproved 2000), West Conshohocken: ASTM International.

29. Zawada, L.P., R.S. Hay, S.S. Lee, and J. Staehler. "Characterization and High-Temperature Mechanical Behavior of an Oxide/Oxide Composite." *Journal of American Ceramic Society 86*, 2003: 981-990.

30. Zok, Frank W. "Mechanical Properties of Porous-matrix Ceramic Composites." *Advanced Engineering Materials*, 2001: 15-23.

Vita

Captain Jacob Delapasse was raised in Brusly, Louisiana. He graduated from Brusly High School in 2000 and entered the United Stated Air Force Academy in Colorado Springs, Colorado in the summer of 2000. In June of 2004, he graduated with a Bachelor of Science in Engineering Mechanics.

Captain Delapasse's first assignment was to the Warner Robins Air Logistics Center (WR-ALC) in Robins AFB, GA where he was a structural engineer for the EC-130J Commando Solo. From Robins AFB, he would deploy as a Depot Liaison Engineer to Southwest Asia. When he returned from his deployment, he became the Chief Aircraft Battle Damage Repair Engineer for the WR-ALC. His second assignment was to the Graduate School of Engineering and Management, Air Force Institute of Technology. Upon graduation he will take an assignment in the Air Force Research Lab (AFRL) propulsion lab at Wright-Patterson AFB, OH.

REPORT DOCUMENTATION PAGE

Form Approved
OMB No. 0704–0188

1. REPORT DATE (DD–MM–YYYY)	2. REPORT TYPE	3. DATES COVERED *(From — To)*
03-25-2010	Master's Thesis	Aug 2008-Mar 2010

4. TITLE AND SUBTITLE

Fatigue Behavior of an Advanced SiC/SiC Composite with an Oxidation Inhibited Matrix at 1200°C in Air and in Steam

5a. CONTRACT NUMBER

5b. GRANT NUMBER

5c. PROGRAM ELEMENT NUMBER
2009-075

6. AUTHOR(S)

Delapasse, Jacob, Capt., USAF

5d. PROJECT NUMBER

5e. TASK NUMBER

5f. WORK UNIT NUMBER

7. PERFORMING ORGANIZATION NAME(S) AND ADDRESS(ES)
Air Force Institute of Technology
Graduate School of Engineering and Management (AFIT/ENY)
2950 Hobson Way
WPAFB OH 45433-7765

8. PERFORMING ORGANIZATION REPORT NUMBER

AFIT/GAE/ENY/10-M07

9. SPONSORING / MONITORING AGENCY NAME(S) AND ADDRESS(ES)
Dr. Geoff Fair
Air Force Research Laboratory/Material and Manufacturing Directorate; Metals, Ceramics, and NDE Division
2230 Tenth Street, Bldg 655
WPAFB OH 45433-7765 DSN: 785-3232
geoff.fair@wpafb.af.mil

10. SPONSOR/MONITOR'S ACRONYM(S)
AFRL/RXLN

11. SPONSOR/MONITOR'S REPORT NUMBER(S)

12. DISTRIBUTION / AVAILABILITY STATEMENT
APPROVED FOR PUBLIC RELEASE; DISTRIBUTION UNLIMITED

13. SUPPLEMENTARY NOTES

14. ABSTRACT

The fatigue behavior of an advanced Silicon Carbide/Silcon (SiC/SiC) ceramic matrix composite (CMC) with oxidation inhibited matrix was investigated at 1200°C in laboratory air and in steam environments. The composite consisted of an oxidation inhibited SiC matrix reinforced with Hi-Nicalon fibers coated with pyrolytic carbon (PyC) with a boron carbide overlay woven into eight-harness-satin (8HS) weave plies. Tensile stress-strain behavior and tensile properties were evaluated at 1200°C. Tension-tension fatigue tests were conducted in both laboratory air and in steam at 1200°C at frequencies of 0.1 Hz, 1.0 Hz, and 10 Hz. The tension-tension fatigue tests had a ratio of minimum stress to maximum stress of R = 0.05, with maximum stresses ranging from 100 to 140 MPa in air and in steam. Fatigue run-out was defined as 10^5 cycles for the 0.1 Hz tests and as 2×10^5 cycles for the 1.0 Hz and 10 Hz tests. Strain accumulation with cycles and modulus evolution with cycles were analyzed for each fatigue test. The presence of steam degraded the fatigue resistance of the material at 0.1 Hz and 10 Hz. At 1.0 Hz, the presence of steam appeared to have little influence on the fatigue resistance for the fatigue stress levels <140 MPa. The presence of steam degraded the fatigue performance of the CMC at 1.0 Hz for the fatigue stress level of 140 MPa. Fatigue limit was 100 MPa (32.6% UTS) in air and steam at 1.0 Hz and in steam at 0.1 Hz. Fatigue limit was 140 MPa (45.6%) in air at 10 Hz. Specimens that achieved run-out were subjected to tensile tests to failure to characterize the retained tensile properties. Specimens tested in air retained 42-61% of their tensile strength and specimen tested in steam retained 59-75% of their tensile strength. The modulus loss in air and in steam was limited to 56%. The microstructural investigation revealed pronounced oxidation on the fracture surfaces of specimens tested in steam. The self sealing matrix cracks were also observed.

15. SUBJECT TERMS
Ceramic Matrix Composite (CMC), Silicon Carbide/Silicon Carbide Composite (SiC/SiC), Boron Carbide, Pyrolytic Carbon Chemical Vapor Infiltration (CVI), Fatigue Testing, Material Properties, Cyclic Loading, Environmental Testing

16. SECURITY CLASSIFICATION OF:			17. LIMITATION OF ABSTRACT	18. NUMBER OF PAGES	19a. NAME OF RESPONSIBLE PERSON
a. REPORT	b. ABSTRACT	c. THIS PAGE	UU	201	Dr. Marina Ruggles-Wrenn
U	U	U			19b. TELEPHONE NUMBER (Include Area Code) (937)255-3636, ext 4641 Email: marina.ruggles-wrenn@afit.edu

Standard Form 298 (Rev. 8–98)
Prescribed by ANSI Std. Z39.18